STABILITY, REACTIVITY, AND CONSTITUENT INTERACTION IN $TiSe_2$-BASED METASTABLE MISFIT LAYER COMPOUNDS SYNTHESIZED FROM DESIGNED AMORPHOUS PRECURSORS

by

DEVIN R. MERRILL

A DISSERTATION

Presented to the Department of Chemistry and Biochemistry
and the Graduate School of the University of Oregon
in partial fulfillment of the requirements
for the degree of
Doctor of Philosophy

December 2015

DISSERTATION APPROVAL PAGE

Student: Devin R. Merrill

Title: Stability, Reactivity, and Constituent Interaction in $TiSe_2$-Based Metastable Misfit Layer Compounds Synthesized from Designed Amorphous Precursors

This dissertation has been accepted and approved in partial fulfillment of the requirements for the Doctor of Philosophy degree in the Department of Chemistry and Biochemistry by:

Dr. Georgy Nazin	Chairperson
Dr. David C. Johnson	Advisor
Dr. Shannon W. Boettcher	Core Member
Dr. Ben McMorran	Institutional Representative

and

Dr. Scott L. Pratt	Dean of the Graduate School

Original approval signatures are on file with the University of Oregon Graduate School.

Degree awarded December 2015

DISSERTATION ABSTRACT

Devin R. Merrill

Doctor of Philosophy

Department of Chemistry and Biochemistry

December 2015

Title: Stability, Reactivity, and Constituent Interaction in $TiSe_2$-Based Metastable Misfit Layer Compounds Synthesized from Designed Amorphous Precursors

A series of intergrowth compounds with the basic formula $[(MSe)_{1+\delta}]_m(TiSe_2)_n$ are reported. The compounds are prepared from modulated elemental reactants and display interesting structural and electronic behavior. Section 1 of this dissertation outlines initial attempts to characterize constituent interaction. The first member of the SnSe based subclass is reported and displays the highest Seebeck coefficient of any m = n = 1 compound reported to date, and a surprising amount of order is observed, compared to previously reported compounds. With properly established deposition parameters, the synthesis was extended to included the m = 2-4 compounds. These compounds display interesting electronic behavior that suggests the band structure shifts considerably as the SnSe block is expanded, affecting the interaction between the constituent layers. The first compound based on BiSe is then reported, suggesting that the Bi structure donates more conduction electrons to the band structure.

Targeted substitution through kinetic control is the focus of Section 2, and a family of $(Pb_xSn_{1-x}Se)_{1+\delta}TiSe_2$ is reported over the entire range of x, even though a miscibility gap exists in the bulk $Pb_xSn_{1-x}Se$ system. The resulting alloyed intergrowth compounds also display equal or higher mobility than the end members, suggesting modulation doping

could be used to affect transport properties. As a proof of principle, the analogous system based on a $Bi_xSn_{1-x}Se$ constituent was prepared to attempt to systematically affect carrier concentration. It was found that while carrier concentration can be controlled, the evolving structure affects the doping efficiency of the Bi atoms and mobility in the structure.

Section 3 outlines attempts to form higher order $TiSe_2$-based heterostructures and the important chemical considerations observed during the preparation of these materials. The 3 component systems in the Pb-Sn-Ti-Se system can be formed at low temperature, with $SnSe_2$ rather than SnSe. While at higher temperatures, topotactic reactions occur, causing rearrangement to the alloyed rocksalt structure. Compounds within the alloy system with $m > 1$ are presented which show surface segregation of Pb atoms, and a designed experiment suggests this is a thermodynamic effect.

This dissertation includes previously published and unpublished coauthored material.

CURRICULUM VITAE

NAME OF AUTHOR: Devin R. Merrill

GRADUATE AND UNDERGRADUATE SCHOOLS ATTENDED:

University of Oregon, Eugene
Whitworth University, Spokane, Washington
Whatcom Community College, Bellingham, Washington

DEGREES AWARDED:

Doctor of Philosophy, Chemistry, 2015, University of Oregon
Bachelor of Science, Chemistry, 2011, Whitworth Universtiy
Associate of Arts and Science, 2008, Whatcom Community College

PROFESSIONAL EXPERIENCE:

Materials Analysis Intern, Intel Corporation, 2015
Teaching assistant, Department of Chemistry, University of Oregon, 2011-2013

GRANTS AND AWARDS:

Graduate Teaching Fellowship, Chemistry, 2011 to Present

PUBLICATIONS:

Merrill, D. R.; Sutherland, D. R.; Ditto, J.; Bauers, S. R.; Falmbigl, M.; Medlin, D. L.; Johnson, D. C. Kinetically Controlled Site-Specific Substitutions in Higher-Order Heterostructures. *Chem. Mater.* **2015**, *27*, 4066–4072.

Merrill, D.; Moore, D.; Bauers, S.; Falmbigl, M.; Johnson, D. Misfit Layer Compounds and Ferecrystals: Model Systems for Thermoelectric Nanocomposites. *Materials (Basel)*. **2015**, *8*, 2000–2029.

Merrill, D. R.; Moore, D. B.; Ditto, J.; Sutherland, D. R.; Falmbigl, M.; Winkler, M.; Pernau, H.; Johnson, D. C. The Synthesis, Structure, and Electrical Characterization of $(SnSe)_{1.2}TiSe_2$. *Eur. J. Inorg. Chem.* **2015**, *2015*, 83–91.

Wood, S. R.; Merrill, D. R.; Falmbigl, M.; Moore, D. B.; Ditto, J.; Esters, M.; Johnson, D. C. Tuning Electrical Properties through Control of $TiSe_2$

Thickness in $(BiSe)_{1+\delta}(TiSe_2)_n$ Compounds. *Chem. Mater.* **2015**, *27*, 6067–6076.

Bauers, S. R.; Merrill, D. R.; Moore, D. B.; Johnson, D. C. Carrier Dilution in $TiSe_2$ Based Intergrowth Compounds for Enhanced Thermoelectric Performance. *J. Mater. Chem. C* **2015**, *3*, 10451-10458.

Falmbigl, M.; Alemayehu, M. B.; Merrill, D. R.; Beekman, M.; Johnson, D. C. In-Plane Structure of Ferecrystalline Compounds. *Cryst. Res. Technol.* **2015**, *50*, 464–472.

Merrill, D. R.; Moore, D. B.; Coffey, M. N.; Jansons, A. W.; Falmbigl, M.; Johnson, D. C. Synthesis and Characterization of Turbostratically Disordered $(BiSe)_{1.15}TiSe_2$. *Semicond. Sci. Technol.* **2014**, *29*, 064004.

ACKNOWLEDGMENTS

This work would not have been possible without the help of many along the way. I would like to thank my coworkers in the Johnson Lab past and present for both guidance and help. This includes Dr. Dan Moore, Jeff Ditto, Sage Bauers, Suzzie Wood, Marco Esters, Richard Westover, Dr. Matti Alemayehu, Dr. Noel Gunning, and Dr. Ryan Atkins, Gavin Mitchson, Kyle Hite, and Erik Hadland. I would also like to thank post-doctoral researcher Dr. Matthias Falmbigl, for his patience, direction, and help on several projects, and for all that he taught me. I am especially grateful to Professor Dave Johnson, for providing me with the opportunity to work in his group, and for his time and guidance, which has allowed me to produce this dissertation and the publications within. I owe a special thanks to Duncan Sutherland, an undergraduate student who worked with me for most of my time in the Johnson Lab. Thank you for all of your help along the way. I would also like to thank undergraduate students Mark Coffey, Alex Lygo, Matt Stolt, Zack Jones, Daniel Berg, and Chun Lee for their help. Thank you to the Adam Jansons for his contribution during his rotation.

Collaborators were instrumental in providing analyses above and beyond our capabilities and expertise. I would like to thank Dr. Doug Medlin from Sandia National Laboratory for his excellent work with electron microscopy. I would also like to Dr. Sven Rudin from Los Alamos National Laboratory, as well as Joshua Gabriel and Professor Richard Hennig from the University of Florida for they contributions to this work through DFT calculations.

I would also like to thank Kris Johnson for his time and effort to help us with our technical difficulties, and the staff of CAMCOR, specifically Julie Chouinard, Josh

Razink, and John Donovan for their aid in materials characterization. I also owe many thanks to the staff at the Advanced Photon Source at Argonne National Laboratories (beamline 33-BM) for their assistance with diffraction experiments.

I would like to acknowledge funding from the National Science Foundation under grant DMR-1266217 and through the Chemical Center of Innovation (CCI) from CHE-1102637. Use of the Advanced Photon Source, an Office of Science User Facility operated for the U.S. Department of Energy (DOE) Office of Science by Argonne National Laboratory, was supported by the U.S.DOE under contract no. DE-AC02-06CH11357.

To my parents, and all of those who have helped and supported me along the way.

TABLE OF CONTENTS

Chapter Page

Chapter Page

Chapter Page

LIST OF FIGURES

Figure Page

Figure Page

Figure Page

Figure Page

Figure Page

Figure Page

Figure Page

LIST OF TABLES

Table Page

CHAPTER I

INTRODUCTION: MISFIT LAYER COMPOUNDS AND FERECRYSTALS: MODEL SYSTEMS FOR THERMOELECTRIC NANOCOMPOSITES

This work was published in volume 8, issue 4 of *Materials* in 2015 with coauthors Daniel B. Moore, Sage R. Bauers, Matthias Falmbigl, and David C. Johnson. Daniel B. Moore assisted with sample synthesis, Sage R. Bauers and Matthias Falmbigl assisted with writing and reference compilation, David C. Johnson is my advisor and research group leader, and I am the primary author.

I.1. Background

Thermoelectric research dates back to the 1820's when Seebeck discovered that a current flows in a closed circuit made of two different metals when the two junctions between the metals are at different temperatures.[1] Peltier discovered the reverse effect a decade later, setting the stage for both heating and cooling thermoelectric modules.[2] Initial devices were based on metal thermocouple junctions. The first significant breakthrough to improve performance was by Ioffe in the 1930's, who discovered that heavily doped semiconductors were more efficient than metals.[3] The ability to make them n doped and p doped enabled the development of useful thermoelectric modules. Later Ioffe introduced the concept of the figure of merit for thermoelectric materials.[4] A material's dimensionless figure of merit is given by,

$$zT = \frac{\alpha^2 \sigma T}{\kappa}$$

where T is the temperature, α is the Seebeck coefficient, σ the electrical conductivity and κ the total thermal conductivity. κ is the sum of the electrical thermal conductivity, κ_e, and the lattice thermal conductivity, κ_l. α, σ and κ are all temperature dependent. To obtain high values of zT, the goal is to maximize the numerator (power factor) and minimize the denominator (total thermal conductivity) simultaneously to increase the zT. This requires decoupling of the above three key transport related properties in solids - α, σ and κ_e. As discussed by Spaldin, these are "contraindicated" properties.[5] The electrical

conductivity and Seebeck coefficient vary in opposite directions with the density of states at the Fermi level. The electrical and the electrical thermal conductivity vary together, resulting in the Wiedemann-Franz relationship.[6] This interrelationship between these properties presents one of the grand challenges in materials chemistry and physics - engineering new materials to obtain "contraindicated" properties. Three separate challenges need to be met. One needs to design new materials in which the scattering mechanisms and band structure can be altered to allow simultaneous increases in electrical conductivity and Seebeck coefficient, or at least to minimize the trade-off between them. One also needs to design chemical structures in which phonons and electrons move independently so as to minimize lattice thermal conductivity without reducing electron mobility. Third, one needs to be able to synthesize the designed materials to determine if the design criteria are correct and result in the targeted compounds having the expected properties.

I.1.1. Overview

This paper begins with a historical overview of thermoelectric research, starting with a short summary of the research focus during the 1950's when thermoelectric materials first became interesting from a device perspective. A summary of some of the highlights of the past 20 years is given, where a significant increase in the figure of merit occurred due to an understanding of how to decrease the lattice thermal conductivity without adversely affecting electrical transport. A short section then summarizes suggestions in the literature for enhancing the power factor and some experimental results to date. Misfit layered compounds are introduced as a potential platform to understand enhancements observed in nanocomposites, which have been a major focus of researchers in the past decade. The repeating interfaces in misfit layer compounds enable their structure to be determined more accurately than randomly oriented composite materials, enabling structure function relationships to be understood. The peculiar incommensurate structural features, composed of two different building blocks with distinct properties, allows for structural manipulations which are challenging in conventional materials. Due to the versatile properties of their constituents, MLCs (in particular TiX_2-based MLCs with X = S, Se) also qualify as promising candidates for thermoelectric applications. The

discussion includes a brief summary of the synthesis, structure, thermal conductivity and electrical properties of misfit layer compounds. The literature on the structure and physical properties of turbostratically disordered polytypes of misfit layer compounds - ferecrystals - which can be prepared with a broad range of constituents, constituent thicknesses, and various layer sequences is then summarized. Following this overview of the literature we present new results on the synthesis, structure and electrical properties for a sequence of new ferecrystals, the ten possible $[(PbSe)_{1+\delta}]_m(TiSe_2)_n$ compounds with m and n less than or equal to 3.

I.2. Historical Context

I.2.1. The First Wave of Thermoelectric Materials Research

Ioffe and others started the first wave of thermoelectric materials research in the 1950's based on several design concepts.[7,8] This decade and the 60's focused on preparing and characterizing narrow band gap semiconductors and on making solid solutions to reduce the lattice thermal conductivity via mass difference (or alloy) scattering. There was a focus on using heavy elements from the right hand side the periodic table with small electronegativity differences under the assumption that this would result in high carrier mobility. These efforts resulted in finding thermoelectric materials such as bismuth telluride, with zT's around 1, which still are the dominant materials in commercial thermoelectric devices today. Thermoelectric materials research activity subsequently declined during the 1970's and 1980's, being limited in part by the lack of new semiconducting materials to be explored and also by the lack of new strategies that might significantly increase zT.

I.2.2. The Second Wave - Minimizing Lattice Thermal Conductivity

Starting in the mid 1990's, there has been a tremendous surge of interest in the search for new thermoelectric materials with enhanced performance resulting from two new ideas. In 1993, Hicks and Dresselhaus proposed that it might be possible to increase zT of certain materials by preparing them as part of quantum-well superlattice structures.[9,10] The idea was that the lower dimension of a two dimensional slab would introduce sharp features in the density of states that could result in an increased power factor. Two years

later, Slack proposed the concept of a “phonon- glass electron-crystal” for designing efficient thermoelectric materials.[11] The idea was to lower the lattice thermal conductivity, which is independent of electrical transport properties, without degrading the electrical properties. The lowest thermal conductivities are commonly found in glasses due to the short mean free paths of phonons, hence the phonon glass in Slack's concept. High zT values also require maximizing the numerator, which is commonly referred to as the power factor. The power factor is typically largest in materials with large mobility values, which are found in single crystals - the electron crystal part of Slack's concept. Importantly, Slack suggested several types of structures where “phonon-glass electron-crystal” behavior might be found. These centered around structures that contain large vacancies where dopant atoms could be incorporated without disturbing the electronic crystal component. The concept was that dopant atoms would "rattle" around in the large cavity at operating temperatures, acting as an Einstein-like scatterer of phonons. The atoms forming the valence band would be matrix atoms, only weakly coupled to the dopant atoms, and therefore the compounds would maintain their large mobility values.

With these ideas introduced, the experimentalists quickly found very promising initial systems to explore. While there were several very promising early reports of extraordinarily high zT values from layered systems prepared to test the prediction of Hicks and Dresselhaus, the main cause of increased performance was a significant reduction in lattice thermal conductivity rather than an increase in the power factor.[12,13] Unfortunately, other research groups have not been able to reproduce the exceptionally high zT values in these initial reports.[14] The “phonon- glass electron-crystal” concept, on the other hand, has produced two major classes of materials, skutterudites[15] and clathrates[16], that now have compounds that rank in the top 10 of the highest zT's reported.

The renewed research efforts have also resulted in several other proposed mechanisms to increase zT and have been used as foundations to search for exceptional zT performance. It was noted that compounds with complex unit cells often have very low lattice thermal conductivities, and a very promising new thermoelectric material $Yb_{14}MnSb_{11}$ was discovered by Kauzlarich in 2007.[17,18]Lee and later Morelli both

showed that compounds near phase transitions can have very low lattice thermal conductivity and reasonable zT's.[19,20] Kanatzidis and others have shown that nanocomposites are another way to achieve exceptionally high zT values, with the inclusions of A in B resulting in very low lattice thermal conductivity and hints that the ability to control carrier concentration in part through charge transfer between the matrix and the inclusion and selective scattering of carriers might result in higher power factors.[21]

To summarize the efforts in the last 20 years, there are now quite a few avenues to reduce lattice thermal conductivity without seriously impacting the power factor. This has led to several materials reported by more than one research group having ZT's of ~1.5. There have even been reports of thermal conductivity values well below the previously assumed "predicted minimum thermal conductivity" as a result of efforts to optimize thermoelectric performance.

I.2.3. The Third Wave - Enhancing Power Factors through Nanocomposites and Band Engineering

To find materials with even higher zT values, the community is challenged to find avenues to increase the power factor above that which can be obtained by optimizing the carrier concentration (Figure I.1).[22,23] There are several promising leads as to how this might be accomplished and the community is poised for a breakthrough that would lead to a third wave of increased research activity. Large power factors require both large conductivities and simultaneously large Seebeck coefficients. While the search in the 1950's focused on narrow gap semiconductors, high performance thermoelectric materials generally have electrical resistivity values less than 1×10^{-5} Ωm at 300 K which is considerably more conductive than Mott predicted[24,25] for his minimum metallic conductivity. Compounds with metallic conductivity generally have low Seebeck coefficients, but high power factors violate this principle. A recent review highlighted how infrequently metallic conductivity is found with large Seebeck coefficients as shown in Figure I.2, adapted from work by Gaultois et al.[26] High power factors result from interesting physics that make the compounds unusual. For bismuth and lead telluride compounds, a high band degeneracy perhaps with band asymmetry results in an

unusually high Seebeck coefficient despite their metallic behavior.[27] Skutterudite structured compounds can have unusually high mobility values, leading to high conductivities at lower carrier concentrations.[28,29] Correlated electron and electron spin interactions in layered cobalt oxides, perhaps combined with an unusual band structure, results in very high Seebeck coefficients for a metallic compound.[30-32] High power factors are often found in compounds having correlated electron behavior, for example heavy Fermion materials[33,34] and compounds with large electron-phonon coupling often associated with charge or spin density wave behavior.[35]

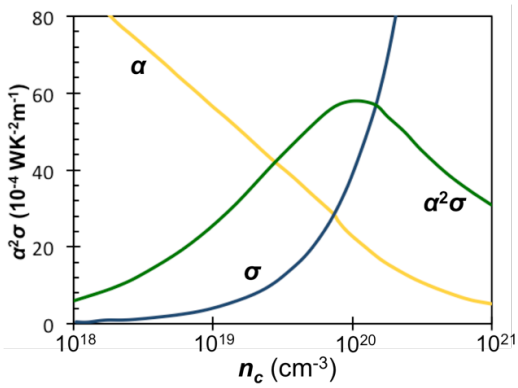

Figure I.1: General relationship between Seebeck coefficient (α), conductivity (σ), and power factor ($\alpha^2\sigma$) as a function of carrier concentration (n_c). Curves generated based on Bi_2Te_3,[22,23] and can be expected to change in shape and magnitude based on material system.

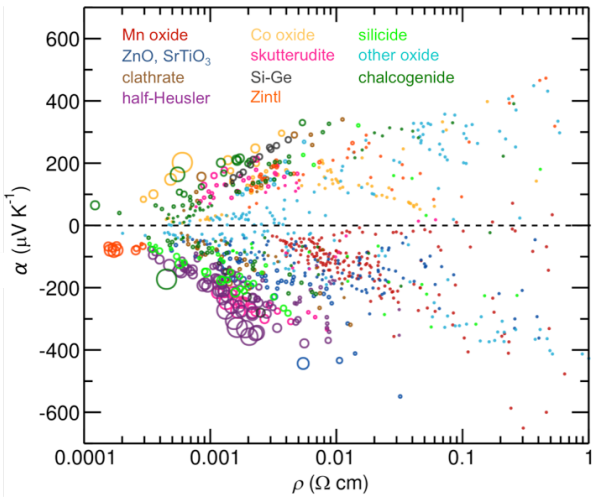

Figure I.2: Transport properties of thermoelectric compounds reported to date, organized by class of compound. Marker radius is proportional to the reported power factor. Figure adapted from work by Gaultois et al.[26]

There are relatively few reports of taking a high performing material and enhancing the power factor and they generally fall into two categories. One successful approach has been to dope PbTe with either sodium or thallium in a manner that both controls the doping and alters the band structure.[36,37] The second strategy involves creating a nanocomposite, with material A present as nanoinclusions within a matrix of an already high performing thermoelectric material B. The nanoinclusions of A act as a dopant and scatter phonons, but also have been suggested to increase the power factor either by scattering electrons of different energy at different rates or by doping in a manner that preserves high carrier mobility.[38] This second approach has become the focus of considerable effort, although the main contribution to enhanced zT still arises from a lowering of the lattice thermal conductivity through the scattering of heat carrying phonons.

I.2.4. Nanocomposites

A challenge in the efforts to optimize nanocomposites has been to find that part of the nanocomposite that is enhancing performance. Each of the constituents of the composite have their own band structures, and charge transfer will occur between them to lower the total energy. The surfaces of one or both constituents are likely to distort, changing the band structure from that of the bulk material. The charge transfer between the nanoinclusion and the matrix, equivalent to modulation doping in semiconductor superlattices, can control the carrier concentration without significant lowering of the carrier mobility due to impurity scattering.[39] The techniques available to characterize the nanostructure, including the local compositions and local structures at interfaces, are limited and provide only local views of what is likely to be a broad distribution of structural configurations at the interfaces. Understanding how to modify the structure at interfaces and tuning the Fermi energy of the nanoinclusions via alloying to control doping remains a challenge. It offers opportunities to adjust parameters in ways not available to a single constituent system. An apprehension remains concerning the long-term stability of these nanoengineered systems under the high temperatures and temperature gradients during operation as part of a thermoelectric device. Hopefully a

balance can be found that maintains the gains in performance while preserving the long-term stability and reliability of thermoelectric devices.

I.3. Misfit Layer Compounds

Misfit Layer Compounds (MLCs) are an interesting class of precisely ordered thermodynamically stable nanocomposites and the discovery of high ZT in $[Ca_2CoO_3]_p$ CoO_2 resulted in examining chalcogenide compounds with similar structures. We will not discuss the oxide materials here, as very good overviews already exist.[40,41] The misfit layered chalcogenides are composed of a layered dichalcogenide and a rocksalt like structure as seen in Figure I.3 with the general formula $[(MX)_{1+\delta}]_m(TX_2)_n$, where M is Sn, Pb, Sb, Bi or a rare earth, T is Ti, V, Nb, Ta or Cr, and X is S or Se. There are several excellent reviews of these compounds and their unusual structures and properties.[42-45] They provide an interesting potential opportunity to study the effect of interface structure and local distortions on thermoelectric properties, because the precisely periodic structure enable the structure to be solved using higher dimensional crystallography to take into account the mismatch in in-plane area of the two constituents.[46] Unfortunately it is only possible to prepare compounds with small m and n due to synthetic limitations.

I.3.1. Structure

Initial reports misidentified the misfit layer chalcogenide compounds as MTX_3, until single crystal diffraction experiments showed the complex superlattice structure with two unique constituents, the history of which is nicely summarized by Wiegers.[42] The unit cell is generally defined with the c-axis normal to the constituent layers, which typically consists of a bilayer of rocksalt interleaved between dichalcogenide layers, with only van der Waals bonding thought to occur between the two structures. [42-45] Compounds reported to date have generally been discovered through high temperature synthesis routes, with most of the reported compounds having m=n=1 or m=1, n=2. There is one report of a m=1, n=3 compound. The relative displacement between the constituents, the distortions of each of the constituents discussed below, and different stacking arrangements of the dichalcogenide layers produce a considerable number of different unit cell symmetries as has been extensively reviewed by Wiegers in 1996.[42] The two constituents display large

distortions from the expected bulk structures, as the two lattices conform to one another typically yielding a commensurate *b* lattice parameter, as shown in Figure I.3. The *a* lattice parameters, however, are typically not commensurate and result in a difference in the in-plane packing density of the two constituents, expressed by the 1+δ term, and calculated as shown in Figure I.3. The incommensurate structure between the distinct lattices results in a modulation function that reflects the changes in the local environment in the crystal structure.[46] A simple 2-D depiction of this phenomenon is given in Figure I.4, where the proximity of M cations and X anions in the rock salt structured constituent with respect to the neighboring X atoms in the TX_2 layer varies with position. The termination of the 3 dimensional rock salt structure causes a puckering distortion of the MX layer. Charge transfer between the constituents and local charges on different atoms result in electrostatic interactions that affect the puckering distortions in the MX layer. The complexity of the crystal structure, the lack of distinct bonds between constituents, and the anharmonic potentials for atoms at the interfaces has lead to suggestions that this structural motif could provide an ideal platform for a phonon-glass electron-crystal behavior, with potentially large zT values if the proper material system could be identified.

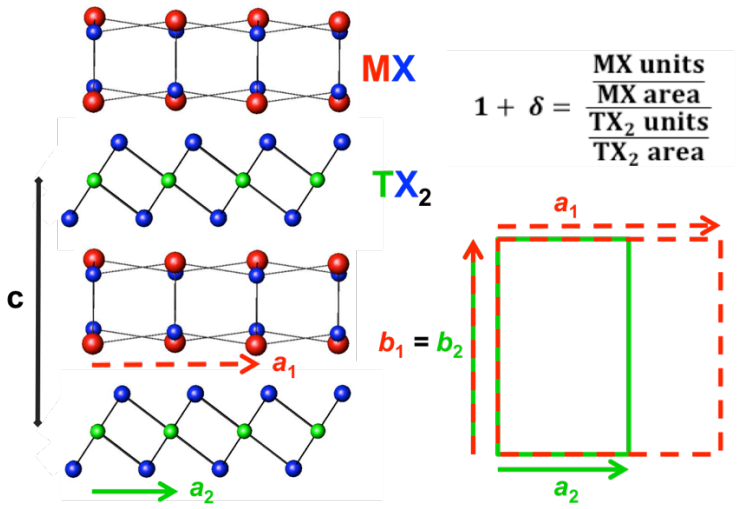

Figure I.3: Structural summary of misfit layer compounds. General Superlattice structure (left) with in-plane lattice depiction (bottom right) and calculation of misfit parameter based on difference in in-plane packing density (top right).

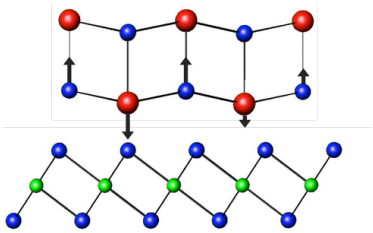

Figure I.4: Two-dimensional representation of modulation in the *a*-direction and the resulting changes in local environment. The black arrows represent coulombic interactions expected based on proximity to X atoms in the adjacent TX_2 layer.

I.3.2. Thermal Transport Properties

Misfit compounds have been proposed as potentially ideal thermoelectric materials, with the dichalcogenide layer providing a region of high-mobility that provides the electron-crystal electronic structure, interwoven with the *M*X layer between the dichalcogenide layers acting as a phonon-glass by suppressing the transport of phonons by the structural mismatch between the MX layer and TX_2 layer which disrupts the periodicity of dichalcogenide perpendicular to the layers.[47] It should be noted that these two interactions are orthogonal to one another in the structure. The first thermal conductivity study of a misfit layered chalcogenide that we could find a report of was done on $(Yb_{0.95}S)_{1.24}NbS_2$ in 2004 in response to the high performance discovered in the structurally related layered cobalt oxides.[48] A very low total thermal conductivity of 0.80 $WK^{-1}m^{-1}$ was measured at 300 K. Subsequent measurements on $(LaS)_{1.20}CrSe_2$ and $(LaS)_{1.14}NbS_2$ measured total thermal conductivity values between 1.2 and 1.5 $WK^{-1}m^{-1}$.[49] Thermal conductivity values of 2.8 $WK^{-1}m^{-1}$, 2.4 $WK^{-1}m^{-1}$ and 2.8 $WK^{-1}m^{-1}$ respectively have been reported by Koumoto for the misfit compounds containing two $TiSe_2$ layers per unit cell, $(BiS)_{1.2}(TiS_2)_2$, $(SnS)_{1.2}(TiS_2)_2$ and $(PbS)_{1.18}(TiS_2)_2$ and are further enhanced by stacking faults.[47,50]

I.3.3. Electrical Transport Properties

The transport properties of misfit layer compounds are generally thought to be dominated by the dichalcogenide layer, and can vary from semimetallic (Ti) to metallic (V, Ta, Nb) based on the number of d-electrons of the transition metal and the coordination environment.[45] The presence of the MX layers result in vastly different

properties from the bulk TX_2 compounds with reported carrier concentrations varying drastically from the bulk values of the parent dichalcogenide, due to charge transfer from the MX constituent.[45] The distortion of the constituent lattices undoubtedly also affects the transport properties, particularly the mobility of the carriers. If electrons are indeed transferred from the rocksalt to the dichalcogenide to fill lower energy states, this results in partially filled bands in both constituents, with the higher mobility carriers in the dichalcogenide layer responsible for the transport properties. This proposed mechanism of conduction explains the change in sign of both measured Hall and Seebeck coefficients for a number of misfit layered compounds when compared to the pristine bulk dichalcogenide, and their intercalates.[45,51-53] This suggests that selection of the two proper constituents could lead to a method of optimizing the carrier concentration through modulation doping, to maximize the power factor while maintaining a low κ_L. Most of the studies in metallic Nb and Ta based sulfide compounds have been reported to have Seebeck coefficients less than $|50|\ \mu VK^{-1}$ due to high carrier concentrations.[42] While it should be possible to control carrier concentration via doping of the rock salt structure, this has not been reported, presumably due to the difficulty of obtaining single phase products from the high temperature synthesis approaches commonly used.

Compounds based on a single layer of TiS_2, $(MS)_{1+\delta}TiS_2$, were reported to have lower carrier concentrations than the Nb and Ta based compounds, approximately 10^{21} cm^{-3} compared to 10^{22} cm^{-3}, producing higher Seebeck coefficients (as high as $|70|\ \mu VK^{-1}$) with still reasonably high conductivity values.[47,54]The group of Koumoto reported the synthesis of $(MS)_{1+\delta}(TiS_2)_2$, where n = 2 with M = Bi, Pb and Sn.[47] The addition of the extra layer of TiS_2 per unit cell in the PbS and SnS resulted in nearly a factor of 2 increase in the Seebeck coefficient when compared to the n = 1 compounds. The Bi compound showed a marked increase in both carrier concentration and conductivity, presumably because it is donating it's additional valence electron to the TiS_2, and a corresponding decrease in α. $(PbSe)_{1.16}(TiSe_2)_2$ reported by Giang and Cava is the only misfit layer based on $TiSe_2$ with a reported Seebeck coefficient in the literature to date.[53] This compound has a lower electrical conductivity and comparable Seebeck coefficient to the sulfur analog prepared by Koumoto.[47] The difference in measurement techniques (single crystal versus pressed pellet) and the variability inherent in solid state synthesis

makes it difficult to draw conclusions from the comparison. Combined with the thermal conductivity values discussed earlier, these TiX_2 based compound reach zT values of ~0.3 at room temperature, similar to that reported for $[(Yb_{0.95}S)_{1.24}]NbS_2$.[48] It is important to note that none of these compounds have been optimized to have the carrier concentration that yields the highest power factor.

The chemical flexibility of misfit layer compounds provides an interesting platform to explore structure-function relationships, to explore the phonon glass-electron crystal concept of Slack, and to understand phenomena of importance to improving performance of thermoelectric materials. The pseudo-independent band structures in these layered materials offer the opportunity to adjust one layer to affect the other through modulation doping. To date, the extent to which this class of compounds has been explored is limited by the constraints of thermodynamic stability at the high temperatures used in traditional solid-state chemistry synthesis approaches. Their potential flexibility remains relatively unexplored. The discovery of the layered cobalt oxide based compounds suggests that misfit type compounds, consisting of two unique constituent lattices, provide a flexible structural motif that has relatively low thermal conductivity and potential new avenues to improving the power factor.[40,41] Controlled substitution, alteration of layering schemes, and identification of constituent pairings that result in optimum materials properties remain to be explored.

I.4. Ferecrystals

A thermodynamically stable $(MX)_{1+\delta}TX_2$ misfit layer compound implies that the interface between the constituent layers must lower the free energy of the misfit layer compound below that of a mixture of the two binary compounds. Hence, it is straightforward to postulate that increasing the thickness of one or both of the constituent layers in the repeating unit, depicted in Figure I.5 should yield a compound that is at least a local free energy minimum. The challenge is coming up with a kinetically controlled route to any specific compound within the very large set of potential compounds $[(MX)_{1+\delta}]_m(TX_2)_n$.

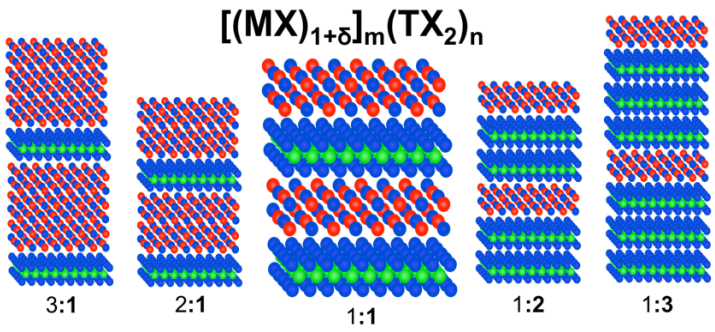

Figure I.5: The thermodynamic stability of the reported MLCs suggests that local free energy minima must exist for other values of m and n.

I.4.1. Synthesis

A kinetically controlled synthesis approach has been developed over the past 25 years to access metastable compounds under conditions where they are kinetically trapped via the self assembly of vacuum deposited amorphous precursors containing designed sequences of ultrathin modulated elemental layers.[55-59] In the last 10 years, it has been shown that precursors prepared with local composition profiles similar to that found in a misfit layer compound will self assemble in a short time (minutes) at low temperatures 300-400°C because only short -range diffusion is required. By preparing designed sequences of binary layers, it has been possible to trap kinetically stable compounds with specific m and n values not obtainable through traditional methods.[55-59] This approach requires the precise calibration of the elemental layers to provide the correct composition of each of the precursor's elemental bilayers corresponding to the constituent's stoichiometry, the correct ratio of composition between the two constituents as defined by the misfit parameter, and the correct total amount of material per constituent layer (either M-X or T-X) to allow for the formation of a single structural repeating unit of each of the targeted constituents. This procedure has been previously described in considerable detail.[57] Typically precursors are prepared with ≤ 5% excess chalcogen to account for any losses during annealing. The synthesis of specific compounds in the system is done by repeating the deposition of the elemental M-X and T-X bilayers the desired number of times to achieve the targeted m and n values. Low temperature annealing self-assembles the precursors into the targeted kinetically stable intergrowth structures.

I.4.2. Structure

This approach has been used to prepare metastable compounds of the general formula $[(MX)_{1+\delta}]_m(TX_2)_n$ with M = Bi, La, Pb, or Sn; T = Ti, V, Cr, Mo, Nb, W, or Ta; and X = Se or Te that contain an integer number m bilayers of MX separating blocks of TX_2 that are n X-T-X trilayers thick. The difference in the synthesis approach results in several important structural differences between the thermodynamic and metastable misfit layer compounds. First, the constituent structures do not distort to make a common in-plane lattice parameter resulting in independent in plane diffraction patterns for the two constituents.[60] The metastable compounds also exhibit turbostratic disorder, or rotational disorder about the c-axis (Figure I.6).[55-61] This disorder disrupts the 3-D crystallinity in the material, and these metastable compounds are referred to as ferecrystals, from the latin root *fere*, meaning almost.

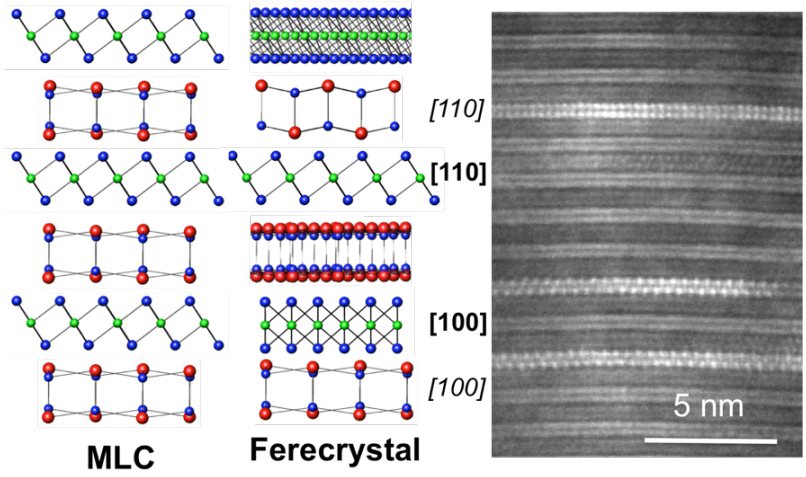

Figure I.6: Comparison of 3-D crystals observed in misfit layer compounds and the turbostratic disorder observed in the metastable ferecrystals (left). HAADF-STEM image of ferecrystalline $(SnSe)_{1.2}TiSe_2$ showing turbostratically disordered layers (right). Zone axes are visible that help identify the constituents.

In most ferecrystal families, the TX_2 structures can be fit to the bulk structure types. Systems containing Ta, Nb, Mo and W typically have trigonal prismatic coordination of the transition metal, while those containing Ti and V have octahedral coordination. A useful discussion of the structure of these binary compounds based on electron configuration was presented by Kertesz and Hoffman.[62] Zone axes for the expected

structures (chevrons for trigonal prismatic and dumbbells for octahedral (see Figure I.7) have been observed in electron microscopy studies of ferecrystals, and the in-plane structures have displayed reflections consistent with the bulk structures, with lattice parameters generally very close to those reported in bulk compounds.[55-61]

Different stacking arrangements of TX_2 layers result in a large number of polytypes in the bulk binary compounds.[62,63]Octahedrally coordinated systems such as TiX_2 and VX_2 form 1-T polymorphs, where the layers stack in an A-A repeating sequence, yielding a c-axis lattice parameter equal to the distance between transition metal atoms in two adjacent layers. Compounds containing Ta, Nb, Mo and W in trigonal prismatic and/or octahedral coordination form more complex stacking sequences by varying the synthesis conditions. Ferecrystal containing TiX_2 and VX_2 have each block of n trilayers forming as a 1-T polymorph, but the orientation of the 1T blocks varies between blocks. Ferecrystals containing Ta, Nb, Mo and W show mostly trigonal prismatic coordination and typically have a random stacking sequence both in and between dichalcogenide blocks.[55-61,64]

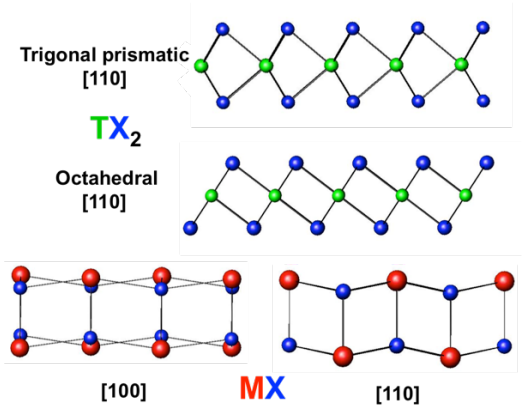

Figure I.7: Structure types observed for TX2 layers. Compounds based on Ti and V are octahedrally coordinated, and those based on Ta and Nb are trigonal prismatically coordinated. The rocksalt like structure is also shown, with puckering distortions in the c-direction.

The structure of the MX constituents in ferecrystals varies with the thickness of the block, as surface and volume free energies compete to create the lowest energy structure. PbSe layers adopt a square basal plane structure, but there is a pairing distortion with alternating long and short distances between the rock salt planes along the c axis. This

distortion decreases as m increases, and when m~6 the structure appears to be bulk, with a puckering distortion of the surface layer.[65] SnSe is either square or displays a slight distortion from a square basal plane, at low values of m. At higher values of m, SnSe shifts towards the orthorhombic (GeS structure) for α-SnSe.[58] A more complete summary of the in-plane structures of ferecrystalline compounds and a comparison with the thermodynamic compounds is available elsewhere.[60]

I.4.3. Thermal Conductivity

The lack of long-range order in ferecrystals prevents the formation of phonons, which are present in the crystalline misfit layer compounds. This results in incredibly low thermal conductivity, including the lowest lattice thermal conductivities every measured for a full dense solid, on the order of 0.05 - 0.10 $Wm^{-1}K^{-1}$ along the c-axis.[66,67]The cross plane thermal conductivity is the sum of the series thermal conductivity of the individual components. Along the constituent planes, the thermal conductivity is higher, 0.4-0.5 $Wm^{-1}K^{-1}$ measured on a number of free-standing films annealed under a variety of conditions. These very low lattice thermal conductivities are very advantageous for potential thermoelectric applications, as it reduces the loss of efficiency due to heat flow through the module. Turbostratic disorder is currently the most effective strategy known to realize a "phonon glass".

I.4.4. Transport Properties

The absolute value of the electrical resistivity of ferecrystals and misfit layer compounds with the same composition and nanoarchitecture are within a factor of 10 of one another. The resistivities of the metastable compounds have very little temperature dependence when compared to their thermodynamic analogs. Interestingly, the low residual resistivity ratio is not due to an increased resistivity at low temperatures, which may be expected from impurity or other fixed defect scattering. For systems where both thermodynamic and metastable compounds are reported, the resistivity at low temperatures is similar in magnitude.[68-71] Misfit layer compounds with high carrier concentrations show behavior expected for a metal, with resistivity increasing linearly with temperature due to increased electron-phonon scattering. The metastable analogs,

while showing similar magnitudes of resistivity below 50 K, do not show the increase at higher temperatures. This lack of temperature dependence has been attributed to the lack of electron-phonon scattering at higher temperatures.

In general, ferecrystals have a higher mobility than the misfit layer compounds. The lack of distortions in the TX_2 constituents in the ferecrystals may play a role in the enhanced mobility observed. Improving mobility in materials is one way to improve the conductivity of a material, without significantly affecting the Seebeck coefficient. The Seebeck coefficients of ferecrystals of similar resistivity to misfit layer compounds tend to be larger, due to the higher mobility.

I.4.5. Charge Transfer Between Constituents

The ability to synthesize ferecrystalline compounds with a much broader range of m and n has provided a mechanism to systematically study constituent interaction. Two series of metallic compounds, $[(PbSe)_{1+\delta}]_mNbSe_2$ and $[(SnSe)_{1+\gamma}]_mNbSe_2$, have systematically decreasing carrier concentration when normalized to the $NbSe_2$ layer as m increases.[69,71] $NbSe_2$ itself is a metal with a half filled band, and the Hall coefficient for both these series is positive and systematically increases as m increases. This suggests an increasing transfer of electrons from the rocksalt to the dichalcogenide as m increases. Work on $TiSe_2$ containing ferecrystsals also suggests charge transfer, with the m = 1, n = 2 compounds displaying similar trends to that observed for the Sn, Pb and Bi MLC analogs with TiS_2. The BiS and BiSe containing MLCs and ferecrystals have a higher carrier concentration, consistent with the donation of one electron to TiX_2 for each Bi atom, and hence a higher conductivity than the SnX and PbX compounds. This charge transfer between constituents might account for the stability of these compounds. Calculations of the energetic gain through coulombic interactions, which can be thought of as energy stored in an atomic scale capacitor, suggest that significant stabilization may be gained through charge transfer. The varying level of charge transfer based on constituent suggests that adjustments to the rocksalt layer could be used to affect carrier concentration in the conducting dichalcogenide layers in a manner similar to modulation doping in III-V superlattice systems grown via molecular beam epitaxy.[72]

I.4.6. Thermoelectric Potential

The extremely low lattice thermal conductivities of ferecrystals and the ability to tune their structure make them attractive test systems and potentially useful thermoelectric materials. Turbostratically disordered compounds containing $NbSe_2$, $TaSe_2$, and VSe_2 as the dichalcogenide constituent layered with either PbSe and SnSe have metallic behavior with carrier concentrations too high to produce large Seebeck coefficients.[57,69,71,73] As with the misfit layered compounds, it would be interesting to explore the properties of these group V transition metal dichalcogenides with rare earth monochalcogenides. Turbostratically disordered compounds containing $MoSe_2$ and WSe_2 with either PbSe and SnSe can have very high Seebeck coefficients, but they also have resistivity values that are much to high, leading to low power factors.[59,74] As with the thermodynamically stable misfit compounds, however, materials based on $TiSe_2$ have shown to produce carrier concentrations on the order of 10^{21} cm^{-3}, with high Seebeck coefficients and resistivity values on the order of 10^{-5} Ωm. To date, $(SnSe)_{1.2}TiSe_2$, $(PbSe)_{1.16}(TiSe_2)_n$ (n = 1,2) and $(BiSe)_{1.15}TiSe_2$ have all been reported.[68,70,75,76] For $TiSe_2$ based compounds, the only direct comparison between a ferecrystal and a misfit compound is for $[(PbSe)]_{1.16}(TiSe_2)_2$.[53,68] Interestingly, the ferecrystal has an order of magnitude higher conductivity at room temperature as shown in Figure I.8 and α that is twice as large as the misfit layer compound.

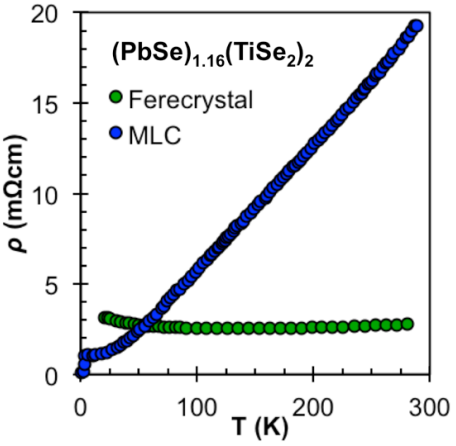

Figure I.8: MLC[53] and ferecrystal (from set A in this work) temperature dependent resistivity. The turbostratically disordered compound is found to be almost temperature independent due to the disruption of phonons in the out of plane direction.

Such an increase in Seebeck coefficient and conductivity in unison is rare, and results in a factor of approximately 30 increase in the power factor. Although no Hall data were reported for either compound, the simplest explanation is that the ferecrystal has a lower carrier concentration and a significantly higher mobility.

I.5. Synthesis and Properties of $[(PbSe)_{1+\delta}]_m(TiSe_2)_n$ with m,n ≤ 3

The significant difference in properties between the ferecrystal and misfit compound $[(PbSe)]_{1.16}(TiSe_2)_2$ lead us to investigate other members of this family of ferecrystalline compounds. Fortunately, the modulated elemental reactants synthetic technique provides an avenue to systematically prepare compounds with specific values of m and n. We decided to prepare all 10 compounds with m and n less than or equal to 3 - i. e. m:**n** = 1:**1**, 1:**2**, 1:**3**; 2:**1**, 2:**2**, 2:**3**; 3:**1**, 3;**2** :3:**3** and the 1:**1**:2:**2** structural isomer of 3:**3,** with sets of compounds summarized in Figure I.9. This sequence of compounds provides the

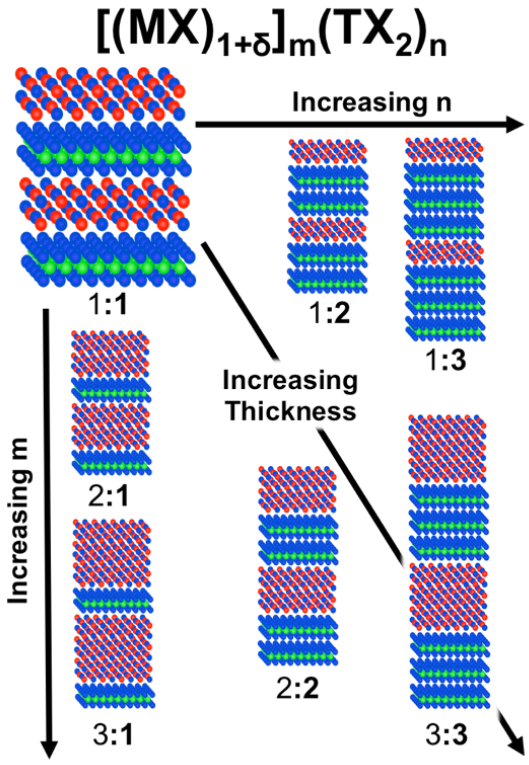

Figure I.9: The ability to synthesize compounds with a variety of m and n values offers the opportunity to identify structure property relationships. Some of the first 10 compounds are given here with m,n ≤ 3.

opportunity to look for trends indicative of charge transfer between constituents. If the PbSe layer behaves as an electron donor and the $TiSe_2$ layer as an acceptor, the carrier concentration for a series of constant m and increasing n should decrease, as the charge donated is spread over more layers.

I.5.1. Synthesis

The modulated elemental reactant synthesis approach is based on preparing a precursor that has local composition and overall nanoarchitecture similar to that of the desired final product. Gently annealing this precursor results in its self assembly into the desired product as shown in Figure I.10 for a 1:**1** compound. Depositing two layers of the Ti:Se layer instead of one layer as depicted in Figure I.10 would result in the self assembly of the 1:**2** compound. The calibration of the deposition system to prepare the precursors involves three steps. First, the ratio of the elements in the Pb:Se and Ti:Se layers have to be adjusted to correspond to the stoichiometry of the PbSe and $TiSe_2$ layers desired in the final product. Second, the ratio of Pb to Ti has to be made to correspond to the misfit parameter, 1.16. Third, the absolute thickness of the Pb:Se and Ti:Se layers has to be adjusted while maintaining relative compositions such that the number of atoms in each layer corresponds to the structural unit that will self assemble: a bilayer of PbSe and a Se-Ti-Se trilayer, respectively. A systematic procedure for accomplishing this using XRR and electron probe microanalysis[77] to determine thickness and composition respectively has been described in detail previously.[57]

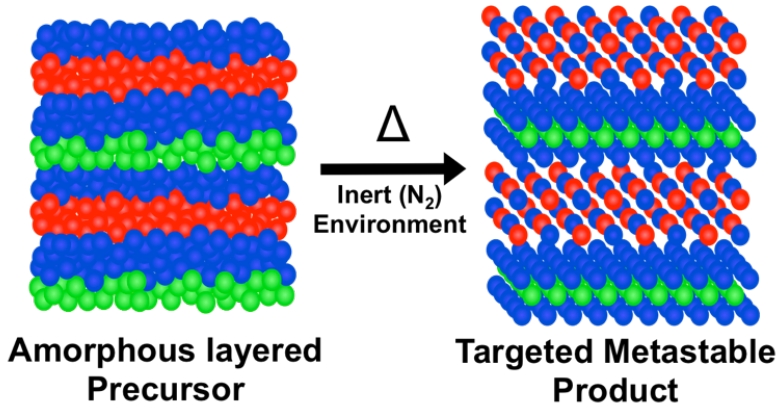

Figure I.10: Modulated elemental reactant synthesis. Control of local composition and structure allows for the self-assembly of amorphous precursors into targeted metastable products.

I.5.2. Structure

Figure I.11 contains the diffraction patterns obtained from the 9 compounds made with a simple A:B structure. All of the reflections can be indexed as 00l reflections of the targeted structures and the c-axis lattice parameters for each compound are given in Table I.1. Several of the compounds were made several times, and the table contains the lattice parameters for each attempt. For each of the three series of compounds, 1:n; 2:n and 3:n, there is a systematic increase in the c-axis lattice parameter of 0.60(1) nm, corresponding to the thickness of the added Se-Ti-Se trilayer. This value is consistent with that reported for the binary compound $TiSe_2$, 0.6004 nm and that found in the known $[(PbSe)]_{1.16}(TiSe_2)_2$ misfit layered compound. [53,78] The systematic increase of the c-lattice parameter as m is increased by 1 is 0.62(1) nm, which is also consistent with that reported for the binary compound PbSe and the estimated thickness of PbSe layers in known misfit compounds.[53,68,79]

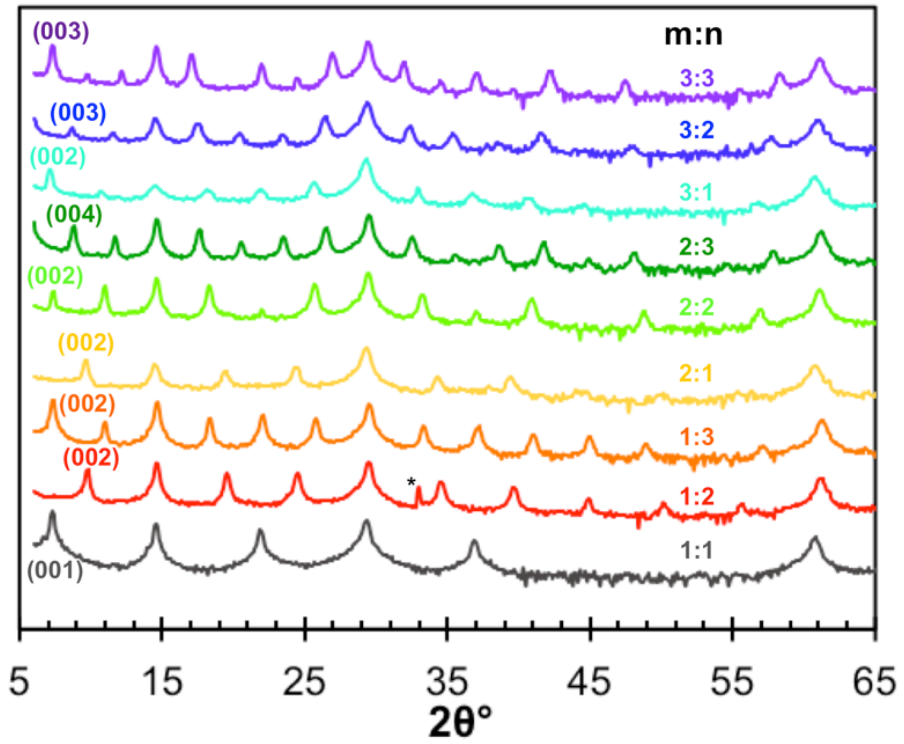

Figure I.11: Diffraction patterns for the unique combinations of m:n (Cu kα). All maxima can be indexed to 00l reflections (* = substrate peak).

Table I.1: C-lattice parameter, electrical resistivity (ρ) and Seebeck coefficient (α) for compounds in the $[(PbSe)_{1+\delta}]_m(TiSe_2)_n$ family synthesized for this study. The samples are organized by vacuum cycle in deposition equipment (black = set A, green = set B, blue = set C).

m : **n**	c-lattice (nm)	ρ (10^{-5} Ωm)	α (μV/K)
1 : **1**	1.218(1)	1.6	-
	1.2183(5)	2.7	-69
	1.218(1)	1.5	-57
1 : **2**	1.817(4)	1.3	-
	1.822(5)	3.7	-92
	1.817(1)	1.7	-79
1 : **3**	2.418(7)	1.1	-
	2.429(5)	4.3	-100
2 : **1**	1.832(4)	5.2	-68
	1.829(5)	1.6	-49
2 : **2**	2.430(2)	2.1	-
	2.432(3)	3.9	-89
	2.421(5)	3.3	-78
2 : **3**	3.033(4)	2.9	-103
3 : **1**	2.455(8)	1.5	-67
3 : **2**	3.091(7)	4.5	-94
3 : **3**	3.636(7)	2.2	-
	3.637(9)	4.3	-102
	3.637(6)	2.4	-85
1:**1**:2:**2**	3.643(4)	3.8	-74

Figure I.12 contains the diffraction patterns of the two structural isomers, 3:**3** and 1:**1**:2:**2**. As can be seen, the 00l reflections are at the same angles, reflecting the similar c-axis lattice parameters of these compounds. The intensities of the reflections differ from one another as expected, because of the difference in the modulation of their electron densities along the c-axis. The lattice parameter of the 1:**1**:2:**2** isomer is slightly larger due to the additional interface between PbSe and $TiSe_2$ in the unit cell.

To get more information about the structure of these compounds, in plane diffraction scans were collected on a subset of samples and are shown in Figure I.13. Only hk0 reflections are observed due to the crystallographic alignment of the compounds with the substrate, forming a '2-D' powder along the in-plane direction. The reflections can be indexed as independent patterns of PbSe and $TiSe_2$. The position of the reflections and their linewidths are similar in all 4 compounds, indicating that the in-plane lattice

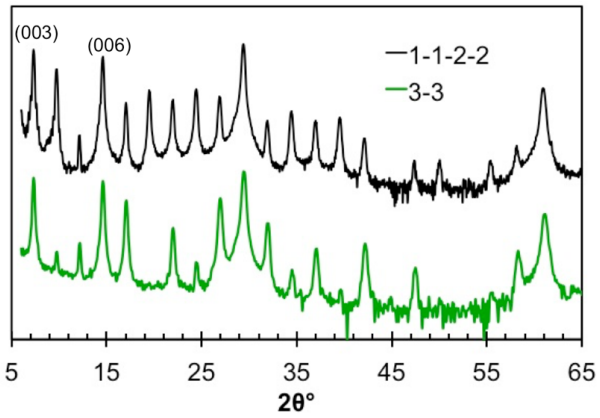

Figure I.12: 00*l* Diffraction pattern for the 3:3 compound and its structural isomer 1:1:2:2. Differences in layering scheme result in changes to the relative intensity of diffraction maxima.

parameters do not change significantly as m and n are varied and that the PbSe lattice remains square and the $TiSe_2$ lattice remains hexagonal in the plane as m and n are varied. The PbSe a-axis lattice parameter was found to be between 0.6109(4) nm and 0.6140(1) nm for these compounds. The $TiSe_2$ a-axis lattice parameter was found to be between 0.3561(6) nm and 0.357(1) nm. These values are similar to those reported previously for PbSe-$TiSe_2$ ferecrystals and misfit layer compounds.[53,68,70,75,76]

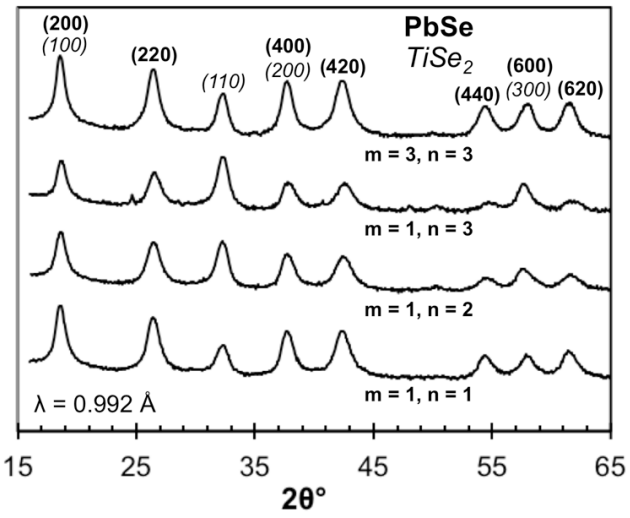

Figure I.13: In-plane diffraction patterns for 1:n and 3:3 compounds. Only *hk*0 reflections for the two constituent structures are observed (labeled on the 3:3 scan). The relative intensity of peaks change as expected for the varying ratio of constituent layers.

HAADF-STEM images were obtained on a subset of samples prepared for this study, and Figure I.14 contains a close up image of the 3:**3** and 1:**1**:2:**2** isomers. Both compounds have unit cells containing 3 structural units of each constituent, but a different sequence of layers resulting in an additional interface in the 1:**1**:2:**2** isomer. The structures of the different layers can be seen to be different and different layers of PbSe and $TiSe_2$ can be seen to have different orientations. However, within one block of each constituent the orientation remains the same. As observed in $[(PbSe)_{1+y}]_m[MoSe_2]_n$ compounds, the PbSe layer consists of pairs of planes, separated by slightly larger distances.[65] This distortion is thought to result from a competition between surface and volume free energy, with the observed distortion being the lowest energy state. The overall structure is consistent with that expected from the observed diffraction patterns and the designed nanoarchitecture of the precursors.

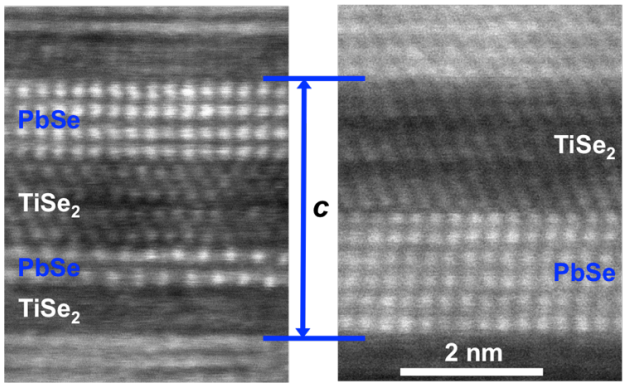

Figure I.14: HAADF-STEM data for the 3:3 and its structural isomer 1:1:2:2. The expected repeating units are observed, and turbostratic disorder is clearly visible in both compounds.

I.5.3. Electrical Transport Properties

The temperature dependent resistivity for the samples in black in Table I.1, which were all made in the same period of time with the same chamber calibration, are shown in Figure I.15. The resistivity increases as m increases in the series 1:**n** and surprisingly the 2:2 and 3:3 compounds have higher resistivity than the 1:1 compound. All compounds show the same basic temperature dependent behavior, with resistivity decreasing very slightly as temperature is decreased before either leveling out or slightly increasing at temperatures below 50 K. The two samples with higher resistivities also show a larger

upturn at lower temperatures from room temperature. The lack of temperature dependence is consistent with prior reports of the resistivity of ferecrystals, and has been attributed to the turbostratic disorder which prevents organized vibrations with an out of plane component. The slight upturn at low temperatures has been attributed to electron-electron interactions leading to localization of carriers.[80] The magnitude of the resistivity depends on both, the number of charge carriers, and their mobility through the lattice, both of which can be expected to change between compounds, and due to slightly different compositions, between samples prepared in different deposition cycles. Slight changes in the composition would be expected to affect both the carrier concentration and carrier mobility, as impurity scattering and grain sizes change.

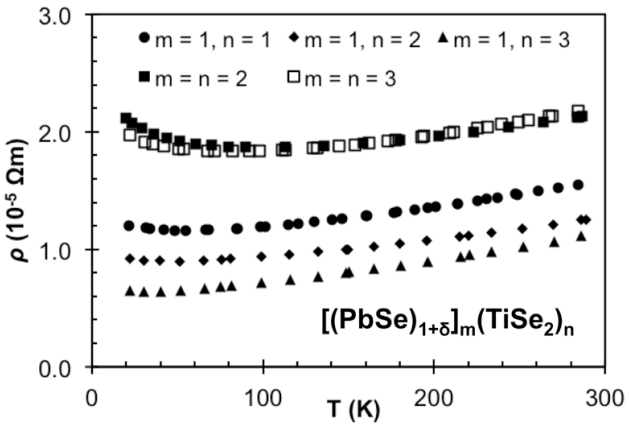

Figure I.15: Temperature dependent resistivity for compounds from set A (black text in Table I.1).

In order to determine if carrier concentration or mobility differences are responsible for the different resistivity values of the compounds in Figure I.15, Hall measurements were conducted and carrier concentration and Hall mobility were calculated assuming a single band model. For all samples the Hall coefficient was negative, indicating that electrons are the predominant charge carriers. This is in agreement with the prior work on TiS_2 containing misfit compounds, where the TiS_2 was assumed to be the predominant conducting layer and charge donation from the MS constituent resulted in the observed carrier concentration.[47,54] The room temperature results are summarized in Table I.2. The carrier concentration systematically decreases as n is decreased, and compounds with the same $TiSe_2$ thickness but different PbSe thickness have similar carrier concentrations. The systematic decrease in carrier concentration with increasing thickness of $TiSe_2$ is

consistent with charge transfer from the PbSe to $TiSe_2$, with the same amount of charge being spread across more $TiSe_2$ layers. The lack of a change in carrier concentration as m increases is more difficult to understand. The explanation is probably related to the structural distortions of the PbSe seen in the STEM images, which will change the band structure and perhaps leading to less charge transfer per layer as the number of PbSe layers increase. The mobility systematically increases in the 1:n compounds, varying inversely with the carrier concentration. The mobility remains relatively consistent within the m = n class of compounds. Figure I.16 contains the temperature dependence of the carrier concentration for the 2:**2** and 3:**3** compounds, which indicates that the upturn in the resistivity is a result of a decrease in carrier concentration. This variation of the carrier concentration might also be a result of assuming a single band model.

Table I.2: Carrier concentration and mobility for compounds in set A. Carrier concentrations calculated from the Hall coefficient suggest that charge transfer is occuring between constituents.

m	n	n_e (10^{21} cm^{-3})	μ_e ($cm^2V^{-1}s^{-1}$)
1	1	2.3	1.7
1	2	1.9	2.6
1	3	1.6	3.5
2	2	1.9	1.5
3	3	1.5	2.0

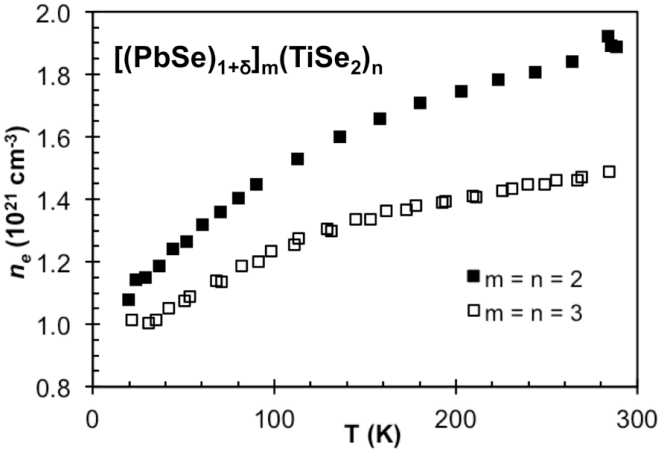

Figure I.16: Temperature dependent carrier concentration (n_e) for the m = n = 2 and 3 compounds, suggesting that the upturn in resistivity is in part due to a decrease in carriers.

Figure I.17 shows the variation of the room temperature Seebeck coefficient as a function of the number of $TiSe_2$ layers in the compounds for two sets of samples prepared in different deposition cycles. For all samples the Seebeck coefficient is negative, implying that electrons are the predominant carriers in agreement with the Hall measurements. The Seebeck coefficient is seen to increase in absolute magnitude as the number of $TiSe_2$ layers is increased but changes only slightly in each set of samples as m is varied. This is consistent with the changes in carrier concentration calculated from the measured Hall coefficients. There is a larger difference between the two sets of samples prepared in different deposition cycles. This is consistent with prior investigations of samples prepared via self-assembly in our group, where samples synthesized within a given deposition cycle are relatively consistent and there is more variation between samples prepared in different deposition cycles. The variation between cycles likely arises from slight changes to composition and thickness of the precursor layers that result in differences in the type and density of defects. These subtle changes in defect density have proven difficult to quantify through structural characterization techniques, with nearly all the samples having very similar diffraction patterns. Differences in defect densities have been observed via electron microscopy studies, but the small areas investigated make it difficult to say that these observations are representative. Table I.1

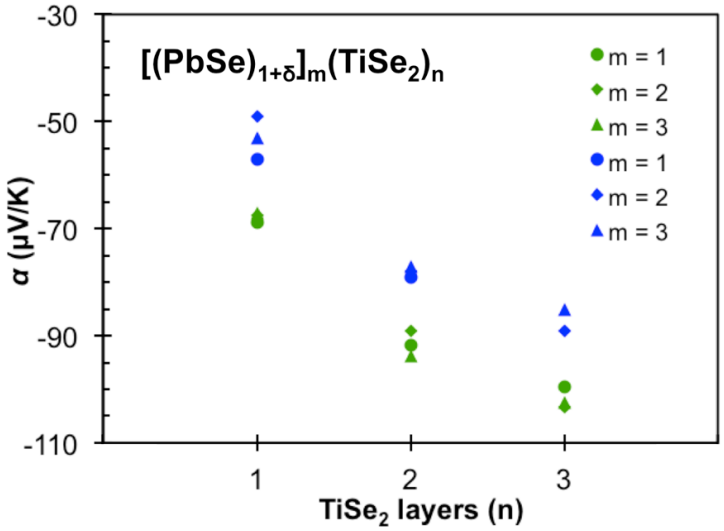

Figure I.17: Seebeck coefficient (α) as a function of number of $TiSe_2$ layers (n). The magnitude of α is seen to increase with n, independent of m.

contains a summary of all of the samples investigated color coded by the deposition cycle in which they were prepared.

Table I.1 also contains room temperature resistivity and Seebeck coefficients for the 3:**3** and 1:**1**:2:**2** sample. The resistvity of the 3:**3** compound was found to be slightly higher than that of the 1:**1**:2:**2** isomer, 4.3 x 10^{-5} Ωm compared to 3.8 x 10^{-5} Ωm. The Seebeck coefficient for the 3:3 compound was -102 μV/K while that for the 1:**1**:2:**2** compound was found to be -74 μV/K, respectively. This is consistent with the discussion of the transport data for the other compounds, where thicker blocks of $TiSe_2$ have lower carrier concentration, higher mobility and higher Seebeck coefficients. The data for the isomers, along with the other compounds with m,n ≤ 3 suggests that increased numbers of adjacent $TiSe_2$ layers might be an avenue to increase the power factor. Additional studies on structural isomers, especially where more isomers are possible such as the 6 possible isomers containing 4 structural units of each constituent, might provide more insights to the role of the interfaces in these compounds.

I.6. Conclusions and Outlook

Misfit layer and similar compounds may provide a useful platform for the and creation of high performance thermoelectric materials due to their low lattice thermal conductivity and potential for modulation doping on a sub-nanometer length scale. Like other material approaches to thermoelectric applications, understanding materials properties on a deeper level requires understanding reproducibility and the underlying affects on observed properties. In the case of bulk materials synthesized at high temperatures, it is generally assumed that thermodynamic equilibrium is achieved and can be reproduced. The variation of properties in the literature for nominally the same compound demonstrates that reproducibility is a challenge. Metastable compounds represent an opportunity to test materials properties over a wider range of composition and structure. Improving control in the preparation of precursors would improve reproducibility. The preferred orientation found in ferecrystals made via designed precursors makes structural characterization possible at a much more detailed level than a random mixture of a material in a matrix, The ability to synthesize the metastable variants of misfit layer compounds offers the opportunity to probe constituent interaction

on a deeper level, by changing the thickness of the constituent blocks with constant or varying composition, and identifying trends in the resulting transport properties. The synthetic control offers the opportunity to make new compounds and explore new material systems, providing the chance to observe trends in material behavior and potentially discovering properties not achievable through traditional approaches.

I.7. Dissertation Overview

The following dissertation can be broken down into three main sections. The first section, (Chapters II-VI) describe the synthesis of ternary compounds and seeks to understand the constituent interaction in $TiSe_2$ based compounds. Chapter II outlines the synthetic and characterization approaches used throughout this thesis. Chapter III outlines the synthesis and characterization of $(SnSe)_{1.2}TiSe_2$ which was published in collaboration with Daniel B. Moore, Jeffrey Ditto, Duncan R. Sutherland, Matthias Falmbigl, Markus Winkler, Hans-Fridtjof Pernau, and David C. Johnson. Chapter IV expands upon the structural studies of the compound reported in Chapter III, and was done in collaboration with Jeffrey Ditto, Sven Rudin, and David C. Johnson. Chapter V describes the synthesis of $[(SnSe)_{1+\delta}]_m(TiSe_2)_1$ compounds, with $m \leq 4$. This work was done in collaboration with Sage R. Bauers, Jeffrey Ditto, and David C. Johnson, and provides evidence for a more complicated band interaction in the SnSe based family of compounds. Chapter VI is the first report of a BiSe-based ferecrystal, and was published in collaboration with Daniel B. Moore, Mark N. Coffey, Adam W Jansons, Matthias Falmbigl, and David C. Johnson. The substitution of Sn with Bi suggests that changes in the rocksalt structure can affect the transport properties of the material, and suggests that $TiSe_2$ based compounds could be designed which optimize their thermoelectric performance.

Section two (Chapters VII, and VIII) reports attempts to demonstrate the formation of alloyed rock salt structures. Chapter VII reports the synthesis of compounds based on a $Pb_xSn_{1-x}Se$ alloyed constituent, and was published in collaboration with Duncan R. Sutherland, Jeffrey Ditto, Sage R. Bauers, Matthias Falmbigl, Douglas L. Medlin, and David C. Johnson. This chapter serves as proof of principle that metastable constituent structures can be formed robustly, even when bulk phase segregation would be expected. Chapter VIII presents the analogous Bi series, as proof of principle that modulation

doping is a viable approach to adjusting materials properties, and was done in collaboration with Suzannah R. Wood, Alex Lygo, Jeffrey Ditto, and David C. Johnson.

The final section of this dissertation (Chapter IX-XI) explores the metastability of compounds in the Pb-Sn-Ti-Se system. Chapter IX was done in collaboration with Duncan R. Sutherland, Jeffrey Ditto, Daniel B. Moore, Matthias Falmbigl, Douglas L. Medlin, and David C. Johnson and outlines the formation of a family of metastable multi-consituent heterostructures. Chapter X presents a topotactic reaction as the multi-constituent heterostructures decompose to form the alloy structure reported above, resulting from a collaborative effort with Duncan R. Sutherland, Jeffrey Ditto, Douglas Medlin, and David C. Johnson. Finally, chapter XI presents surface segregation observed in the alloyed structures, and was accomplished in collaboration with Jeffrey Ditto and David C. Johnson. This section provides a context for the understanding of both material formation and transformation, as well as the driving forces responsible for the observed behavior.

CHAPTER II
SYNTHETIC AND CHARACTERIZATION METHODS

The compounds presented herein were prepared via the modulated elemental reactants (MER) method, which uses low temperatures and therefore diffusion limitation to nucleate metastable products. This approach relies on controlling local composition of a precursor film which is close to the targeted structure of the desired intergrowth compound. A low temperature annealing step allows the mostly amorphous precursors to self-assemble in the local free energy minima provided by the precursor structure, without supplying sufficient energy to overcome the diffusion barriers that prevent the formation of thermodynamic products. This approach has been demonstrated for several systems with the same basic structural motif as their thermodynamic counterparts, misfit layer compounds,[1] with the basic formula $[(MSe)_{1+\delta}]_m(TSe_2)_n$.[2–5] The kinetic approach allows for the formation of several compounds that were previously not accessible through high temperature synthesis routes (i.e. values of m > 1, and n >3). What follows is an explanation of the experimental setup for the deposition of precursor films, the subsequent formation of the metastable intergrowth compounds, and their structural and electrical characterization.

Precursors are synthesized using physical vapor deposition, at pressures below $5x10^{-7}$ Torr. A custom built deposition chamber is used to deposit 3 (ternary compounds) or 4 (quaternary compounds) elements simultaneously. Each deposition source is isolated by a baffle system, with deposition pathways defined to reach the corresponding quartz crystal microbalance (QCM), and the substrate holder. The rates are monitored continuously by the QCM, and maintained between 0.1-0.3 Å/s at the substrate. In order to form the layered precursor, the path to the substrate is covered by a pneumatically controlled shutter. A custom designed Labview program is used to control the shutters for the sources used in the deposition, which opens the shutters in the sequence desired, and for the specified thickness for each source. The result is the ability to vary the thickness of individual elemental layers, and the sequence in which they are deposited.

The formation of targeted intergrowths require that precursor have close to the target composition, and repeating unit thickness expected for the metastable product. Achieving

deposition parameters that yield these conditions require an iterative calibration procedure, and the Sn-Ti-Se system is given as an example here. The first requirement is the stoichiometry of the metal cations, which is defined by the expected in-plane packing density. This is achieved by maintaining the one cation's parameters, while systematically varying the other. The appropriate ratio deposition parameters is then selected based on the composition results from electron microprobe analysis (EPMA), using a thin film method described elsewhere.[6] Figure II.1 shows the calculation of the M:T ratio at the end of this iterative cycle, which appears as the slope in the figure.

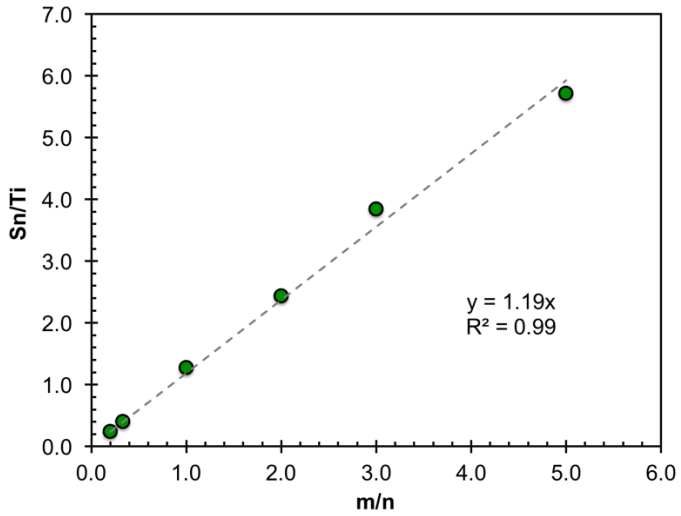

Figure II.1: Calculation of the Sn:Ti ratio. The measured Sn:Ti ratio (EPMA) is plotted versus the ratio of the number of SnSe repeats (m) to $TiSe_2$ repeats (n). The slope gives the ratio of the cations. The target in this case is 1.21, within the error of the measurement.

The ratio of Se in each layer is then adjusted by preparing compounds over a variety of m and n and comparing the ratio with the target 1Se : 1M and 2Se : 1T. Figures II.2 and II.3 give the Se:Sn and Se:Ti ratios, respectively, and are from the end of the iterative process. From these data points, the final ratio of deposition parameters are selected, to give the appropriate ratio of reactants, with slight excess Se (3-5%). Once the proper composition is achieved, the thickness of the precursor repeat unit is adjusted to give the correct total amount of reactants to form one structural unit, by measuring the thickness via x-ray reflectivity (XRR) and adjusting the thickness of the elemental layers while maintaining the ratio of the deposition parameters. If there is too much, or too little

reactant present, the structure has to rearrange in order to self assemble, often resulting in large defect regions, or a lack of formation of the targeted structure in general.

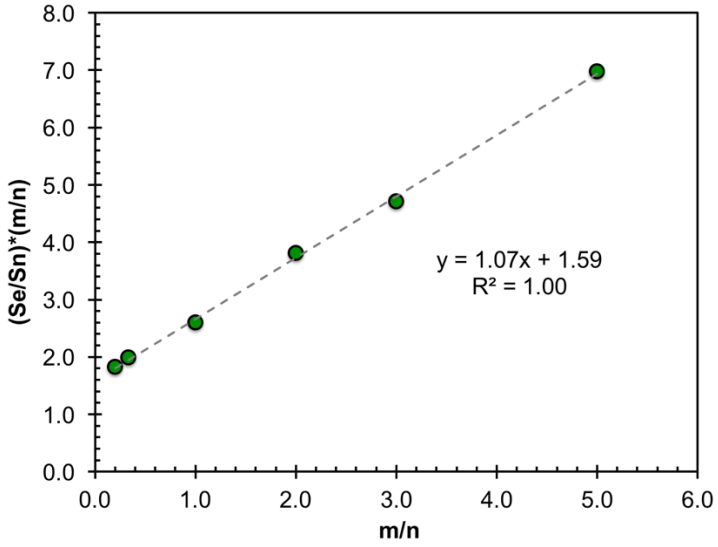

Figure II.2: Plot of normalized Se/Sn ratio versus the m/n. The slope gives the ratio of Se:Sn in the SnSe precursor layer. The target is 1.03-1.05 to meet the slight excess in Se requirement.

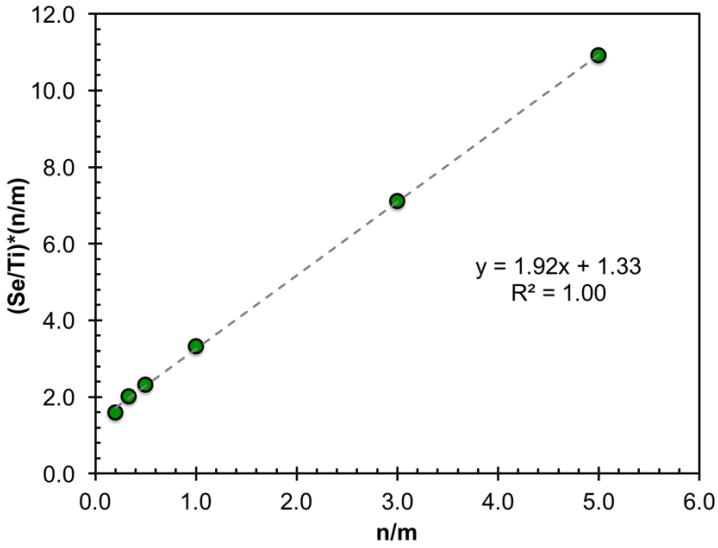

Figure II.3: Plot of the normalized Se/Ti ratio versus n/m. The slope gives the Se:Ti ratio in the $TiSe_2$ precursor layer. The target is 2.06-2.10 to provide the slight excess in Se.

Annealing is carried out on a calibrated hot plate in a N_2 environment ($[O_2],[H_2O] \leq$ 0.8 ppm). Once precursors with the appropriate composition and repeat thickness are established, annealing studies are performed for the various systems reported in the is

dissertation. The formation of the targeted metastable product can be tracked as a function of temperature and time through x-ray diffraction (XRD) experiments, which is commonly reported in the following chapters. The optimum temperature is determined by the maximum intensity and minimum full width at half maximum (FWHM). Above this temperature, the decomposition of the metastable structure is observed. Figure II.4 shows the O and Se content for the Bi-Ti-Se system as a function of annealing temperature. The data suggests that the decomposition of the structure is inpart due to the oxidation of the material, even though the concentration of oxidizing agents is low.

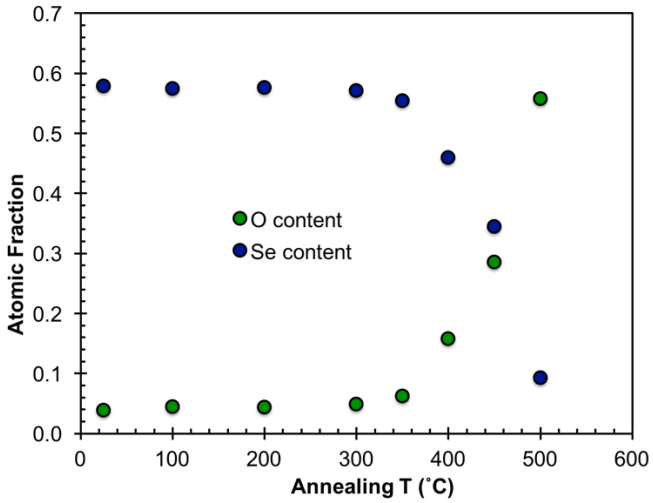

Figure II.4: The Se and O content measured for the Bi-Ti-Se m = n = 1 compound. At high temperatures, the film decomposes, with O replacing Se throughout much of the film.

Films are generally deposited with a targeted total thickness of approximately 50 nm, for the ease of characterization. Si (<100> oriented) substrates are used for structural characterization. X-ray diffraction experiments are reported in both locked couple (θ/2θ) and in-plane geometry. The textured nature of the films result in the observation of 00*l* and hk0 reflections in the two different geometries, respectively, which provides structural information about both the superstructure and the constituents individually. High angle annular dark field scanning transmission electron microscopy (HAADF-STEM) is used to understand the self assembly on a local level, and provides chemical information where intensity scales with atomic number. The resulting images compliment the global measurements made with EPMA and XRD.

For transport measurements, films are simultaneously deposited on fused silica substrates, using shadow masks to provide a cross-like geometry for van der Pauw resisitivity measurements. Temperature dependent resistivity and Hall effect measurements are performed using a lab-built system with a closed cycle He cryostat to measure in between 20-295 K. Carrier concentrations are calculated from the Hall coefficient (R_H) assuming a single band model. In-plane Seebeck effect measurements were performed using a lab-built system, which heats one contact to provide a small temperature gradient.

CHAPTER III

THE SYNTHESIS, STRUCTURE, AND ELECTRICAL CHARACTERIZATION OF $(SnSe)_{1.2}TiSe_2$

This material appeared in volume 2015, issue 1 of *European Journal of Inorganic Chemistry* (2015) with coauthors Daniel B. Moore, Jeffrey Ditto, Duncan R. Sutherland, Matthias Falmbigl, Markus Winkler, Hans-Fridtjof Pernau, and David C. Johnson. Daniel B. Moore and Duncan R. Sutherland assisted with sample synthesis, Jeffrey Ditto provided scanning transmission electron microscopy analysis, Matthias Falmbigl provided Rietveld refinement and le Bail analysis, Markus Winkler and Hans-Fridtjof Pernau assisted with the electrical characterization, David C. Johnson is my advisor and research group leader, and I am the primary author.

III.1. Introduction

Over the last two decades the search for compounds with enhanced thermoelectric performance was motivated to a large degree by a paper by Hicks and Dresselhaus that predicted enhanced power factors for structures of reduced dimensionality and the phonon glass electron crystal concept introduced by Slack.[1-3] The power factor, $\alpha^2\sigma$, where α is the Seebeck coefficient and σ is the electrical conductivity, is typically optimized as a function of carrier concentration through doping, to give the largest thermoelectric figure or merit, zT. Most thermoelectric materials are semiconductors resulting in an optimized carrier concentration of typically around 10^{19} carriers cm^{-3}. While not directly conforming to the original idea put forth by Hicks, there are a number of layered materials that have unusually high Seebeck coefficients with higher carrier concentrations ~10^{20} - 10^{21} carriers cm^{-3}. These include the layered cobalt oxides, Na_xCoO_2 and the misfit compound $[Ca_2CoO_3]_{0.62}[CoO_2]$, and a number of compounds containing titanium dichalcogenide layers, $(MS)_{1+x}(TiS_2)_2$ (M.Pb, Bi, Sn), $Ti_{1+x}Se_2$, and Cu_xTiS_2.[4-6]

Titanium dichalcogenide TiX_2 compounds themselves exhibit interesting transport properties. $TiTe_2$ is generally agreed to be semimetallic, TiS_2 is generally agreed to be semiconducting and $TiSe_2$, while debated over the years, is thought to be a small bandgap semiconductor.[7-9] TiS_2 and $TiSe_2$ have anomalously large Seebeck coefficients, which has been attributed to an unusually large phonon drag effect.[10] While the binary

compounds have thermal conductivities that are too large for them to be effective thermoelectric materials, recent reports have shown that inserting cations or incorporating structural layers into the van der Waal gaps reduces thermal conductivity while preserving the unusual electrical properties.[5,6,11,12] For the misfit layered TiS_2 containing compounds, the group of Koumoto has shown that changing the identity of the intercalated rock salt structure changes the amount of charge transfer.[5] There have only been three reports of misfit layered compounds containing $TiSe_2$. Crystalline $[(PbSe)_{1.16}]_1(TiSe_2)_2$ was reported to be a superconducting metal below 2.3 K by Giang, et al. Turbostratically disordered $[(PbSe)_{1.18}]_1(TiSe_2)_2$ and $[(PbSe)_{1.18}]_1(TiSe_2)_1$ were reported by Moore, et. al. to have a lower room temperature resistivity and a Seebeck coefficient that was almost double that of the crystalline analog reported previously.[13-15]

The synthesis approach used by Moore, et al. opens opportunities to prepare both new compounds and different polymorphs of existing compounds within the $TiSe_2$ containing family of compounds.[14,15] Turbostratic disorder, a common feature of compounds prepared using this approach, has been shown to result in remarkably low lattice thermal conductivities.[16,17] Since in the crystalline misfit sulfides reported by Wan the SnS containing compound had better thermoelectric performance than the lead analog, we were motivated to synthesize $(SnSe)_{1.2}TiSe_2$.[5] Here we present the synthesis of this new compound, its structure, and its electrical transport properties. The power factor was found to be almost a factor of two larger than reported for $(PbSe)_{1.18}TiSe_2$.[14] Reducing the carrier concentration, through doping of the SnSe layer or by incorporating a larger band gap partner for $TiSe_2$, are suggested as avenues to further increase the performance of these interesting materials.

III.2. Experimental Section

Designed precursors containing modulated elemental reactants were synthesized in a custom built high vacuum system at pressures below 5×10^{-7} torr. Tin and titanium metal were deposited using electron beam guns and Se was deposited using an effusion cell, with rates maintained between 0.2-0.3 Å/s at the substrate and monitored by quartz crystal microbalances. Elemental layers were deposited in calibrated thicknesses in the sequence of Ti, Se, Sn, Se and repeated 43 times to give total film thickness of approximately 50 nm. Films were deposited on Si and fused silica substrates for

structural and electrical measurements, respectively. Samples were annealed in a nitrogen atmosphere ($[O_2],[H_2O] \leq 0.7$ ppm) for 30 minutes at different temperatures to determine the optimum formation conditions.

X-ray reflectivity and diffraction measurements were conducted on a Bruker D8 Discover (Cu Kα radiation) and used to measure total film thickness and as-deposited repeat unit thickness, as well as to follow the self-assembly of the precursor into the superlattice. Refinement of the atomic planes along the c axis was performed using the Rietveld method and the Full Prof Suite software package.[18] Composition was monitored with electron probe microanalysis (EPMA) using a Cameca SX50 to follow O, Se, Sn, and Ti content using a process described elsewhere.[19] Samples were cleaved in vacuum for XPS analysis by epoxying a post to the sample surface and knocking the post off in the sample introduction chamber. TEM cross-section Samples were prepared on a FEI Helios 600 Dual-Beam FIB with a Sidewinder ion column using methods developed by Schaffer et al .[40] High angle annular dark field scanning transmission electron microscopy (HAADF-STEM) images were obtained using an FEI Titan 80-300 TEM at 300keV. Temperature dependent resistivity and Hall effect measurements were performed in the van der Pauw geometry on cross-shaped samples deposited on quartz substrates using shadow masks. Lab built measurement systems were used for electrical characterization. Low temperature measurements were performed under high vacuum conditions (University of Oregon) and high temperature measurements were conducted in a 100mbar nitrogen environment (Fraunhofer Institute for Physical Measurement Techniques).

III.3. Results and Discussion

The synthetic approach used to prepare the title compound requires that precursors are prepared which contain constituent layers with compositions close to the stoichiometry of the desired components to induce them to nucleate, and that the total amount of material deposited in each constituent layer is close to that required to form a structural unit of the desired constituent.[20-22] The deposition parameters for $TiSe_2$ that result in a one to two Ti:Se ratio and the proper thickness to form a single Se-Ti-Se trilayer had been established previously, and were used as a starting point for the calibration.[14,15] The misfit parameter δ was initially estimated to be 0.20 using the

analogous sulfide misfit layer compound[23] and was used as a target Sn:Ti ratio until the true value could be determined experimentally from the in-plane packing density calculated from the constituent lattice parameters. In order to establish the necessary deposition parameters to get the correct stoichiometric ratio of Sn to Ti, a series of films were created in which the thickness of the elemental Sn-Se precursor bilayer was varied while the previously determined $TiSe_2$ parameters were maintained. The resulting films were then analyzed with EPMA to determine the elemental composition.[19] The Sn:Se ratio was next optimized by varying the thickness of the elemental Se layer while maintaining the Sn parameter and checking composition with EPMA. Finally, while maintaining established elemental ratios, the thickness of the repeating unit was varied to be just slightly thicker than the c-lattice parameter of the target compound, which was determined by least squares refinement of superlattice diffraction observed in some of the annealed samples from the initial depositions. Samples prepared using the calibrated deposition parameters had the desired Sn:Ti ratio for the targeted misfit parameter. The Ti:Se and Sn:Se ratios were calibrated to be 3-5% selenium rich compared to the idealized 1:2 and 1:1 ratios respectively, to compensate for Se loss during the annealing process.

III.3.1. Structural Analysis

The initial sets of samples were annealed at 350°C, the temperature determined to be optimal for the formation of the Pb analog.[14,15] Once precursors with correct composition and repeat unit thickness that formed the title compound on annealing at 350°C were prepared, 00*l* diffraction patterns were taken as a function of annealing temperature to probe the formation of the superlattice as a function of annealing conditions (Figure III.1). The as-deposited precursor contains weak and broad low angle Bragg reflections due to the periodic electron density in the films. Intense, sharp peaks are not observed due to the composition gradients that likely exist across the mostly amorphous interfaces and local variations in the thickness of the elemental layers. As the annealing temperature increased, the superlattice reflections intensify and a clear decrease in the full width at half maximum (FWHM) of the Bragg peaks is observed as the temperature is increased from 200-350°C, which is consistent with the formation of the targeted compound. Maximum intensities are obtained for the 350°C annealed sample.

A shoulder on the 004 peak begins to appear at 400°C, suggesting the growth of another phase, probably SnSe. At T > 400°C, the shoulder intensifies, unidentified phases grow in, and the diffraction peaks from the superlattice structure decay suggesting the decomposition of the target structure. From this study, 350° C was chosen as an optimal annealing temperature.

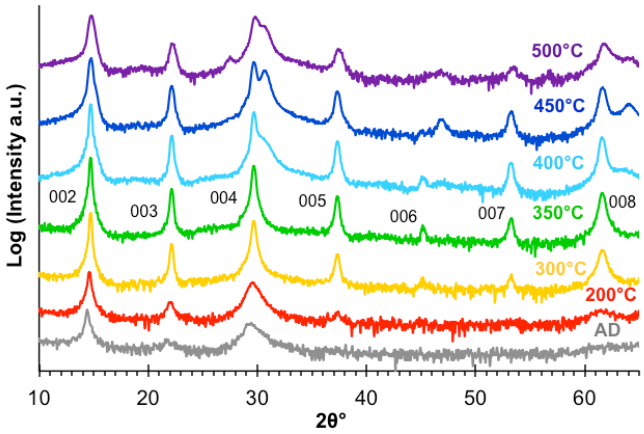

Figure III.1: 00*l* Diffraction as a function of annealing temperature (offset for clarity). Observed superlattice maxima are indexed for the pattern at the optimum temperature (350°C)

During the calibration process, annealed films with a surprisingly large range of composition and precursor repeat unit thicknesses (summarized in Table III.1) had diffraction patterns consistent with the target superlattice structure. The ratio of Sn to Ti varied between 1.0 and 1.39 and the thickness of the repeating unit in the precursor varied between 12.1 and 13.2 Å. The c-parameters varied little (12.04 Å to 12.08 Å), suggesting that there is a defined structure. One possible explanation is the occurrence of conformal inclusions, regions where one layer substitutes for the other, observed previously in MER synthesized films.[24] These conformal inclusions allow composition to be varied without a disruption of the long-range superlattice structure of the material. In an attempt to characterize the relative amount of the target product formed, the defect level of the structure and the variability of the layer stacking, the intensity of the 003 reflection (counts per seconds, CPS), the FWHM of the 003 reflection and the ratio of the 003 to 002 reflection intensities were tabulated (Table III.1). The films can be sorted into two distinct groups. The first (Samples A-E, bold, Table III.1) contains films that show high intensity, low FWHM, and a small range of 003/002

intensity ratios, suggesting the formation of a similar product in each case. Samples in the second group (Samples F-M, Table III.1) have one or more of the following features: low intensity, larger FWHM, more variability in the ratio of 003/002 reflection intensities, and a wider range of annealed c-parameters. Since sample thickness and the sample area illuminated were held constant, the low intensity results from less superlattice material in the sample volume. The increase in the FWHM is likely caused by higher defect concentrations and/or smaller grain size. The larger range of the ratio of the 003 and 002 reflections is likely caused by different concentrations of volume defects, regions where one layer substitutes for the other. It is clear that the formation of ferecrystalline products from the amorphous precursors is surprisingly robust and the details of the resulting defects formed require further investigation. For the remainder of this paper, however, we will focus our attention on the samples in group 1.

EPMA data was collected as a function of annealing temperature to determine if changes in the composition of the film with annealing time or temperature were responsible for the decrease in superlattice diffraction above 350°C. The atomic percent of oxygen increased from approximately 3% for as-deposited films, to 4-5% for films annealed at 350°C despite annealing in a nitrogen atmosphere with ~0.5 ppm oxygen. The oxygen signal in the as-deposited sample is in part due to the native oxide layer on the Si substrate. Additional oxygen in the as-deposited sample could come from incorporation during the deposition process or from surface oxidation after removal from the deposition chamber. To distinguish between surface oxidation and a distribution of oxygen throughout the sample, samples were cleaved in the XPS vacuum chamber and a comparison of the exfoliated regions to original surface regions was performed. The resulting spectra show that the original surface of the film had a strong oxygen signal, while the freshly exposed interior layers displayed no observable oxygen signal, suggesting that oxygen is not incorporated in the sample during deposition and surface oxidation is the major factor in the increase in oxygen level during annealing. Further support for surface oxidation comes from HAADF-STEM experiments, where 2-3 bilayers of SnSe could be identified adjacent to one another at the surface of the film, suggesting that $TiSe_2$ is oxidized in the uppermost unit cells, forming independent TiO_x and SnSe layers not associated with the intergrowth compound. At temperatures above

350°C, the oxygen content of the films increased dramatically to 15-20 atomic percent after annealing at 400°C, even though the annealing was done in an inert atmosphere, suggesting that there is sufficient energy at this temperature to overcome any kinetic barrier towards oxidation. The decomposition of $(SnSe)_{1+\delta}TiSe_2$ is therefore in part due to it's instability with respect to oxidation.

Table III.1: Table of samples synthesized during the calibration process that displayed superlattice diffraction maxima. Composition is reported from EPMA and represents global film composition. The composition of the superstructure is given by the in-plane packing density of each constituent (calculated from in-plane lattice parameters below). Samples given in bold (A-E) are considered representative of the title compound.

Sample	Precursor c (Å)	Sn/Ti	Annealed c (Å)	FWHM (003)	Normalized Intensity (CPS-003)	003/002 Intensity Ratio
A	**12.1(1)**	**1.25(1)**	**12.04(1)**	**0.24**	**82.2**	**0.067**
B	**12.1(1)**	**1.20(1)**	**12.04(1)**	**0.25**	**61.3**	**0.070**
C	**12.4(1)**	**1.16(1)**	**12.05(1)**	**0.24**	**100.0**	**0.062**
D	**12.1(1)**	**1.25(1)**	**12.04(1)**	**0.26**	**80.1**	**0.064**
E	**13.2(1)**	**1.14(1)**	**12.04(1)**	**0.26**	**81.8**	**0.059**
F	12.5(1)	1.00(1)	12.06(1)	0.28	22.5	0.085
G	12.2(1)	1.21(1)	12.06(1)	0.27	17.2	0.145
H	12.1(1)	1.23(1)	12.04(1)	0.27	46.8	0.075
I	12.6(1)	1.13(1)	12.05(1)	0.38	16.8	0.166
J	12.7(1)	1.33(1)	12.05(1)	0.29	6.4	0.202
K	12.8(1)	1.15(1)	12.08(1)	0.78	0.9	0.088
L	12.3(1)	1.21(1)	12.04(1)	0.28	24.0	0.069
M	12.4(1)	1.39(1)	12.061(1)	0.68	13.1	0.050

A high quality θ/2θ diffraction scan of sample can be seen in Figure III.2a. The films are highly textured, with the c-axis normal to the substrate, so diffraction data taken in the conventional θ/2θ geometry show only 00*l* diffraction maxima. The presence of Kiessig fringes (the high frequency oscillations between Bragg reflections) to relatively high two theta values suggests that the air/film and film/substrate interfaces are smooth and parallel. The Parratt relationship (inset Figure III.2b) describes the extent to which these interfaces are parallel and smooth, where Δt is the film roughness, θ_c is the critical angle, and θ_i represents the angle at which fringes can no longer be resolved.[25] Based off the pattern shown in Figure III.2b, θ_i was estimated to be 7.5°, leading to a calculated roughness of 0.9 Å. This suggests that the top and bottom interfaces are very parallel and near atomically smooth. Further insight about the evolution of the film during annealing

can be gained from the number of fringes appearing between Bragg reflections. In theory, the number of fringes (n_f) between Bragg reflections is $n_f = n_{r.u.} - 2$, where $n_{r.u}$, is the number of repeating units present in the film. In the pattern in Figure III.2 $n_f = 39$, and in the designed precursor $n_{r.u.} = 43$, yielding $n_f = n_{r.u.} - 4$. This indicates that two of the deposited repeating units were lost, probably due to surface oxidation as suggested by the EPMA and XPS results, during the annealing process.

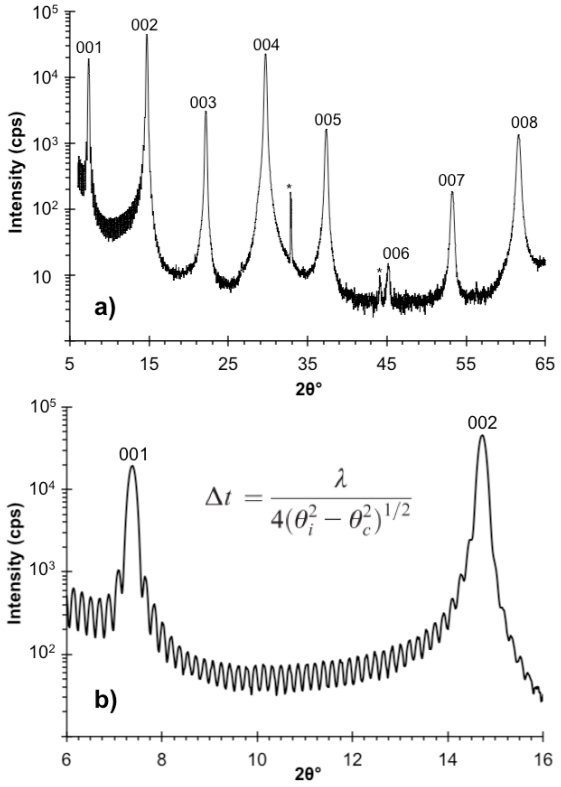

Figure III.2: A diffraction pattern of sample A **(a)** displaying Kiessig fringes to more than 15° 2θ **(b)**. The Parratt relationship is inset. Superlattice maxima are indexed, * denotes substrate or stage peaks.

Cross-sectional HAADF-STEM data was obtained on sample A to probe the structure and the frequency of defects. The lower magnification image shown in Figure III.3a clearly shows the alternating SnSe (bright) and $TiSe_2$ (dark) layers throughout the film, confirming the formation of the superlattice unit cell consisting of 1 structural unit of each constituent. Interestingly, there are several regions of higher order within the film that have not been observed previously in compounds synthesized by modulated elemental reactants. The bulk structures for each constituent compound can be seen in Figure III.3b, and a higher magnification HAADF-STEM image of a particularly ordered

region in Figure III.3c. $TiSe_2$, like other dichalcogenides, consists of Se-Ti-Se trilayers with a van der Waal gap separating adjacent layers, The Se-Ti-Se layers are stacked in an a-b-c pattern resulting in Ti being octahedrally coordinated to 6 Se atoms. The Se-Ti-Se layers stack in an A-A stacking sequence, with the trilayers identically aligned in each layer, resulting in the 1T polytype.[26] The 110 zone axes observed in the STEM image shows that the Ti atoms are octahedrally coordinated.α-SnSe, the thermodynamically stable phase at room temperature and ambient pressure, crystallizes in the GeS structure,

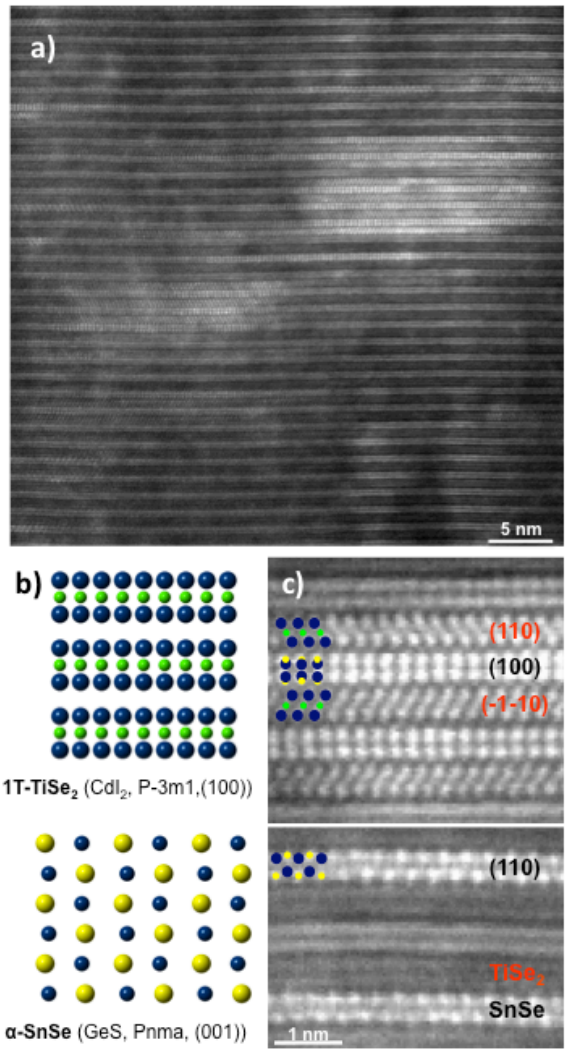

Figure III.3: (a) Low magnification HAADF-STEM images displaying alternating layers of SnSe and $TiSe_2$ throughout the entirety of the film. **(b)** Bulk structures for the constituent compounds. **(c)** High magnification HAADF-STEM displaying two unique lattices intergrown. Crystal faces and structure representations are specified for hexagonal $TiSe_2$ and square-basal SnSe, as seen with other ferecrystal systems.

which is a distorted variant of the cubic rock salt structure.[27] In previously reported SnSe containing misfit layer compounds, SnSe is significantly distorted from the bulk structure, and was reported to have a = b, or a square basal-plane structure for single bilayers of SnSe.[20-22,28,29] In Figure III.3c, both 100 and 110 zone axes are clearly visible, but the extent of the distortion cannot be determined from the images. The indices assigned in Figure III.3c are consistent with the square basal plane SnSe and 1T-$TiSe_2$ structures reported for the constituents in previously reported misfit layer compounds.[14,15,20-22,28,29] The images clearly confirm the independent constituent structures of the intergrowth compound.

The presence of clearly defined crystallographic planes offers the opportunity to calculate the in-plane lattice parameters from the HAADF-STEM images. Line profiles in the hk0 direction were analyzed to determine the distance between atomic columns, from which the lattice parameters were calculated for each constituent, assuming a square basal plane for SnSe and the CdI_2 structure for $TiSe_2$. The lattice parameters for both SnSe (a = 6.2(1)Å) and TiSe2 (a = 3.7(1) Å) are both within the error bars of those reported for other ferecrystalline and misfit layered compounds containing SnSe (generally a = 6.0 (1) Å)[20-22,28,29] or $TiSe_2$ (a = 3.55(5) Å).[13-15] The calculated misfit parameter, from our STEM derived lattice parameters was found to be 0.2, which is the same value previously reported for the analogous sulfide compound.[23]

Further details of the structure were obtained by refining the 00*l* diffraction pattern using the Rietveld method to determine the location of atomic planes in the c direction, as shown in Figure III.4 and tabulated refinement parameters can bee seen in Table III.2.[18] The refinement converged to a lattice parameter c = 12.050(1) Å, with residuals, R_F and R_B of 0.0159 and 0.00781 respectively. Further details of the results are tabulated and a depiction of the resulting model and the calculated distortions are given in Figure III.4. Within the SnSe layer, the Sn and Se atoms are not in the same plane. This puckering of what would be a single 100 plane in an ideal rock salt structure is nearly double that observed in the PbSe layer in the $(PbSe)_{1.16}TiSe_2$ ferecrystal reported previously.[14] The 27 pm distortion is larger than that found in $[(SnSe)_{1.15}]_1[VSe_2]_1$ (19(3) pm) Sn-Se but smaller than that found in $[(SnSe)_{1.06}]_1[MoSe_2]_1$, (40(1)pm).[21,28] The refined distance between the Ti and Se planes in the $TiSe_2$ constituent (1.54Å) is significantly larger than

the 1.45 Å reported for the analogous Pb compound.[14] The distance between the Se plane in $TiSe_2$ and the puckered Sn plane in the Sn-Se layers is 2.98 Å compared to 3.13 Å for the analogous distance reported for $(PbSe)_{1.16}TiSe_2$.[14] The model and the refined distances are all consistent with the conclusions drawn from the STEM images in Figure III.3.

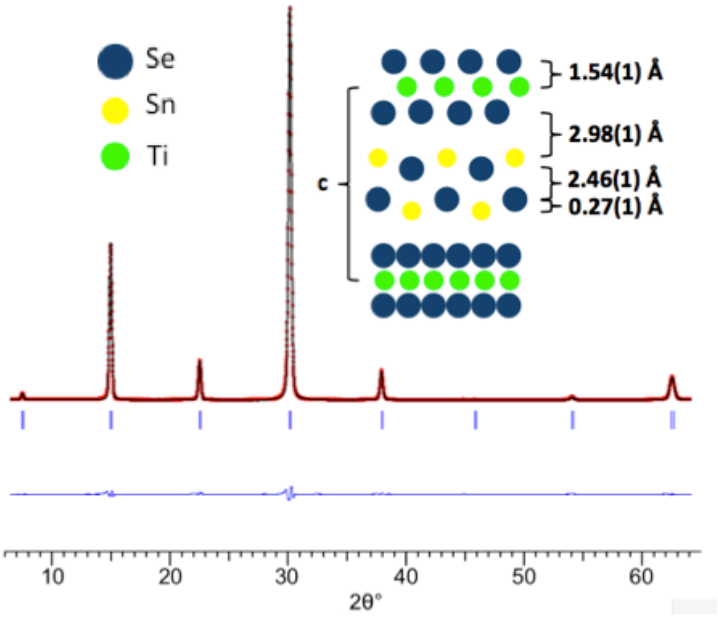

Figure III.4: Rietveld refinement of sample A. The red dots represent the measured pattern, the black line the modeled intensity, the blue line the difference between experimental and calculated intenstity, and the blue ticks indicate the Bragg positions (only 00l). Spacings between interatomic planes in the c direction are also given.

III.3.2. Electrical Characterization

Table III.3 contains the room temperature transport data for both samples A and B studied here, and a summary of prior published values for both $TiSe_2$ and TiS_2 containing misfit layered compounds. The magnitude of the conductivity of samples A and B is consistent with that of a low conductivity metal, a semimetal or a heavily doped semiconductor. The magnitude is slightly higher than prior reported values for $TiSe_2$ containing misfit layer compounds and ferecrystals[13-15] but smaller by a factor of 3 than the values reported for TiS_2 containing misfit layer compounds.[5,30] In these prior reports, it was suggested that the TiX_2 layers dominate the electrical properties as substitution of Sn for isoelectronic Pb did not significantly alter the electrical properties.

Table III.2: Refinement parameters for interatomic plane spacing along the c-axis associated with the fit plotted in Figure III.4.

Compound Parameters	
Composition from refinement	$(SnSe)_{1.14}TiSe_2$
Radiation	Bruker D8, Cu
2θ range (degrees)	$6 \leq 2\theta \leq 65$
c (Å)	12.050(1)
Reflections in refinement	16
Number of variables	13
$R_F = \Sigma \mid F_o - F_c \mid / \Sigma F_o$	0.0160
$R_I = \Sigma \mid I_o - I_c \mid / \Sigma I_o$	0.0079
$R_{wP} = [\Sigma w_i \mid y_{oi} -$	0.0826
$R_P = \Sigma \mid y_{oi} - y_{ci} \mid / \Sigma \mid y_{oi} \mid$	0.0403
$R_e = [(N-P+C)/(\Sigma w_i y^2_{oi})]^{1/2}$	0.0186
$\chi^2 = (R_{wP}/R_e)^2$	19.7
Atom parameters	
Ti in 1a(0), B_{eq} (B_{iso})	
Occ.	1.0
Se1 in 2c (z), z	0.1268(1)
Occ.	1.0
Sn in 2c (z), z	0.3754(2)
Occ.	1.14(1)
Se2 in 2c (z), z	0.3977(3)
Occ.	1.14(1)

The resistivity as a function of temperature for samples A and B are shown in Figure III.5, along with the isoelectronic $(PbSe)_{1.16}TiSe_2$ analog. The slight difference in resistivity between heating and cooling in the high temperature data for sample A is a consequence of surface oxidation of the top layers due to prolonged exposure to elevated temperatures, resulting in a slight decrease in the conducting film thickness. The resistivity shows relatively little temperature dependence, with the overall magnitude of the resistivity changing by less than a factor of two from 20 K to 295K, with a slight upturn at low temperatures. This change in the resistivity with temperature is a factor of 12 less than reported for $(PbSe)_{1.16}(TiSe_2)_2$ by Giang et. al,[13] and a factor of 5 and 10 less than that of $(PbS)_{1.16}TiS_2$ and $(SnS)_{1.20}TiS_2$ reported by Wiegers[30] respectively. The smaller -magnitude of the temperature dependence of the resistivity has been attributed to the turbostratic disorder observed in compounds synthesized from modulated elemental reactants. The turbostratic disorder results in a very different phonon distribution and very low cross plane lattice thermal conductivities.[16,17] The room temperature electrical

resistivity of $(SnSe)_{1.2}TiSe_2$ is a factor of two smaller than that reported for single crystals of $(PbSe)_{1.16}(TiSe_2)_2$,[13] suggesting that the decreased temperature dependence is not a result of a high residual resistivity, but rather due to less phonon scattering at higher temperatures. The upturn at low temperatures, found in all $TiSe_2$ containing intergrowths with significant rotational disorder between layers is thought to result from electron-electron correlations leading to weak localization.[33]

Table III.3: Electrical properties of TiX_2 based compounds are shown. Those given in bold are compounds synthesized from modulated elemental reactants.

Material	σ_{ab} (S/cm)	n_e ($10^{21}cm^{-3}$)	α_{ab} (μV/K)	$\alpha^2\sigma$ x10^{-4} (W/K^{2}m)
Sample A	**660**	**2.0**	**-75**	**3.7**
Sample B	**860**	**2.4**	**-77**	**5.1**
$(PbSe)_{1.16}TiSe_2$[14]	**650**	**2.3**	**-66**	**2.8**
$(PbSe)_{1.16}(TiSe_2)_2$[15]	**360**	**-**	**-91**	**3.0**
$(PbSe)_{1.16}(TiSe_2)_2$[13]	50	-	-50	0.13
$(SnS)_{1.20}TiS_2$[30]	2000	1.8	-36	2.6
$(PbS)_{1.18}TiS_2$[30]	6300	3.8	-29	5.3
$(SnS)_{1.2}(TiS_2)_2$[5]	1700	1.9	-70	8.3
$(PbS)_{1.18}(TiS_2)_2$[5]	1900	2.4	-56	6.0
$(BiS)_{1.18}(TiS_2)_2$[5]	2700	5.3	-45	5.5
$TiSe_2$[31]	$1.0x10^{-3}$	-	+15	2.3 x 10-7
$Ti_{1.1}Se_2$(MER)[32]	280	3.4	-134	5.0
$Cu_{0.1}TiS_2$[6]	4000	3.7	-45	10
$Cu_{0.11}TiSe_2$[12]	3000	0.2	-50	8

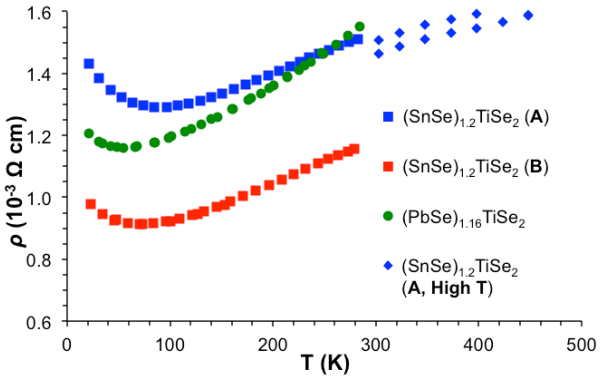

Figure III.5: Temperature dependent resistivity for the compounds synthesized from modulated elemental reactants.

To further understand the electrical behavior of the $(SnSe)_{1.20}TiSe_2$ compounds, Hall effect measurements were performed. The Hall coefficients were found to be negative, indicating electrons are the majority charge carriers. Following previous reports, the carrier concentration was calculated using $R_H = 1/n_e e$ where n_e is the concentration of conducting electrons and e is the elementary charge (Figure III.6 and III.7). The carrier concentration measured for samples A and B are very similar to that reported for other isoelectronic $(MX)_{1+\delta}TiX_2$ intergrowth compounds. The carriers are thought to arise from the rock salt constituent donating electrons to the 3d band of the TiX_2 constituent, which is responsible for the majority of the conductivity.[34] The carrier concentration decreases linearly for the Sn compounds below room temperature, and are very similar in magnitude and behavior to the previously reported PbSe analog, synthesized by methods previously reported and measured for comparison (Figure III.7a).[14] There is a significant increase in carrier concentration as the temperature is raised above 300 K, which may be a consequence of the thermal excitation of carriers or increased contribution from the carriers in the SnSe layer. The calculated single band mobility (Figure III.7b) of the carriers in $(SnSe)_{1.2}TiSe_2$ and $(PbSe)_{1.18}TiSe_2$ have nearly identical temperature dependent behavior and magnitudes, as may be expected for the isoelectronic systems. Similar temperature dependence was also found for $(BiSe)_{1.15}TiSe_2$ synthesized from modulated elemental reactants and reported elsewhere,[35] though the magnitude of the carrier

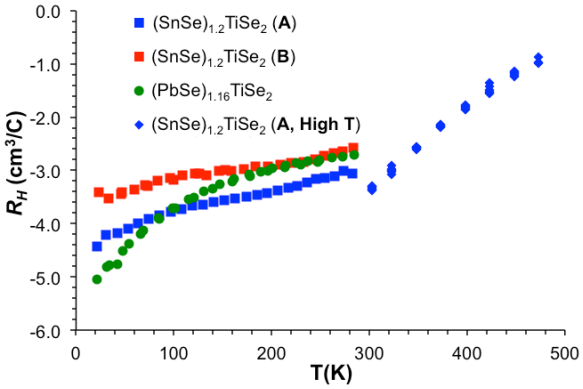

Figure III.6: Temperature dependent Hall coefficient for the compounds synthesized from modulated elemental reactants.

concentration coincided with the addition of an extra carriers, consistent with reports of the TiS_2 compounds, and further suggesting that a $TiSe_2$ band is responsible for conduction.[5,14,35] The increase in mobility as temperature decreases is likely due to a decrease in in-plane phonon scattering and decreased magnitude of the atomic vibrations. The carrier mobility found in single crystals of the analogous sulfides is a factor of 3 larger. Prior studies on semiconducting $[(PbSe)_{1.0}]_m[MoSe_2]_n$ and $[(PbSe)_{1.0}]_m[WSe_2]_n$ compounds suggests that the mobility of $(SnSe)_{1.2}TiSe_2$ might be increased by extended low temperature annealing in a selenium partial pressure.[36,37]

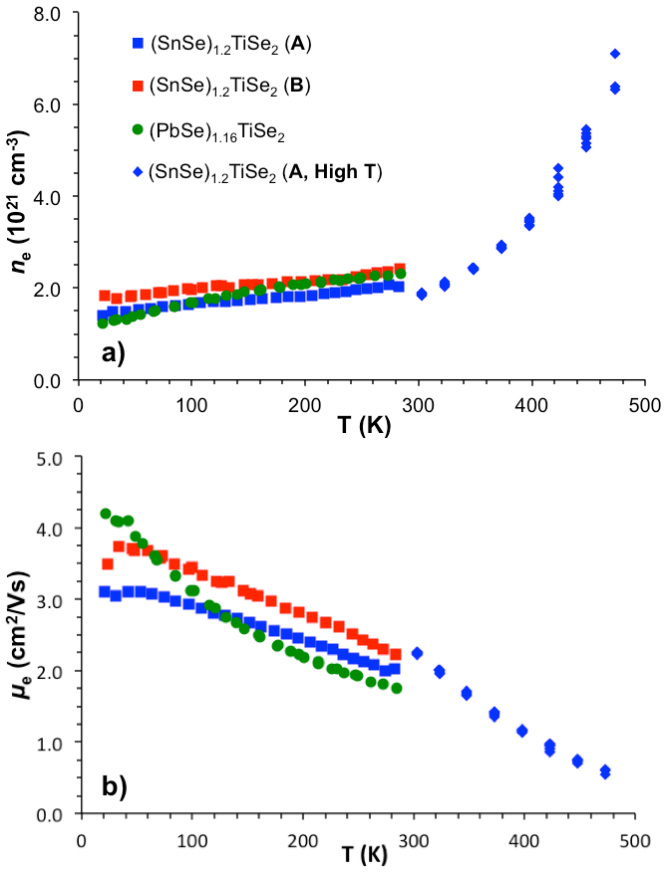

Figure III.7: (a) Calculated carrier concentration (n_e) and **(b)** electron mobility (μ_e) based on a single band model, as a function of temperature.

The Seebeck coefficients (S) of samples A and B were -75 μVK^{-1} and -77 μVK^{-1} at room temperature, respectively. The negative sign of S agrees with the negative Hall coefficient, also indicating that electrons are the predominant charge carriers. The Seebeck coefficients of samples A and B are greater in magnitude than the -66 μVK^{-1} previously reported for the $(PbSe)_{1.16}TiSe_2$ ferecrystal just as S is larger in $(SnS)_{1.2}(TiS_2)_n$

than $(PbS)_{1.18}(TiS_2)_n$.[5,14,30] The Seebeck coefficients of the selenide compounds $(SnSe)_{1.2}TiSe_2$ and $(PbSe)_{1.16}TiSe_2$ are about than a factor of 2 higher than that reported for the sulfide compounds $(SnS)_{1.2}TiS_2$ and $(PbS)_{1.18}TiS_2$ with similar carrier concentrations.[30]

Formal valence arguments suggest that $(MX)_{1+\delta}TiX_2$ compounds should be semiconductors ($[M^{2+}X^{2-}]_{1+\delta}[Ti^{4+}X^{2-}_2]$). Prior literature explains the metallic behavior of these compounds as resulting from an overlap of the valence band of the MX constituent with the formally empty d band of TiX_2 leading to charge transfer from MX to TiX_2.[34] For the $(SnSe)_{1.2}TiSe_2$ compounds reported here, an average carrier concentration of 0.3 electron per Ti was calculated by considering the density of Ti atoms and assuming the Hall voltage can be converted to carrier concentration using a single band model where the carriers are in a Ti 3d conduction band. This value is approximately double of that reported for $(SnS)_{1.2}(TiS_2)_2$, as expected because the Sn/Ti ratio is half of that in $(SnSe)_{1.2}TiSe_2$.[5]

Figure III.8 contains a schematic band structure diagram illustrating the proposed relative band energy and Fermi level of the two constituents and the stabilization of the material due to charge transfer. The energy contained in the capacitance resulting from electrons in the $TiSe_2$ layer and the corresponding number of holes left in the adjacent SnSe constituent is appreciable, between 7 and 9 kJ/mol depending on the value used for the distance of the charge separation (6 Å between the Ti layer in $TiSe_2$ to center of the SnSe layer or 4.5 Å from the Ti to the closest Sn/Se average plane position, respectively), the approximation used for permittivity (vacuum), and assuming a Madelung constant of 2 for the superlattice structure. This suggests that charge transfer between constituents may help explain the somewhat unexpected thermodynamic stability of the intergrowth compound compared to the individual constituents when prepared using solid-state synthesis methods.[34] The data presented here, in agreement with prior literature results, show that electrons dominate the electrical conduction. This implies that the mobility of the holes in SnSe is significantly smaller than that of the electrons in $TiSe_2$.

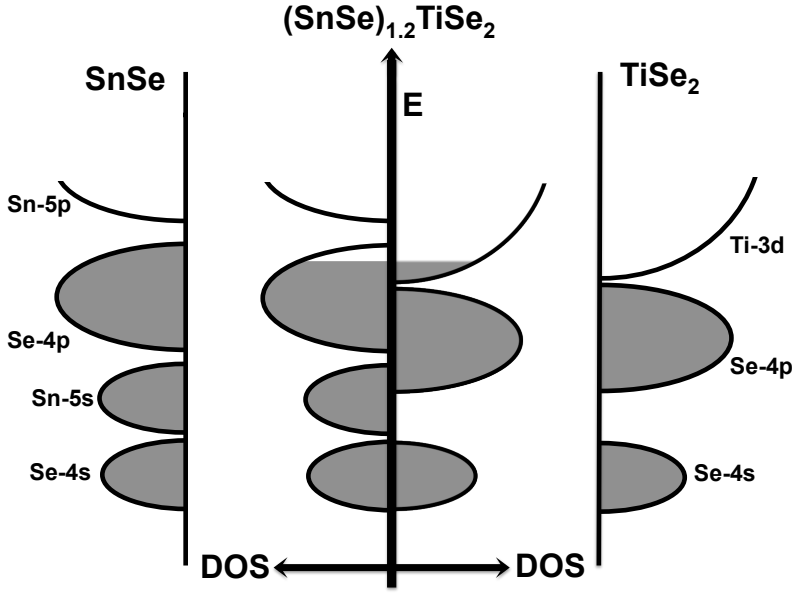

Figure III.8: Proposed band structures of the constituent materials (left and right) and the ferecrystal product (center).

The effective mass of samples A and B were calculated to be 6.1 and 7.1 times that of a free electron from α and n_e measured at room temperature, respectively, assuming a single band and carrier type are responsible for conduction. The relationship used for the calculation is given below, where kB is Boltzmann's constant, e is the elementary charge, h is Planck's constant, m* is the effective mass, and T is temperature.[38]

$$\alpha = \frac{8\pi^2 {k_B}^2}{3eh^2} m^* T \left(\frac{\pi}{3n}\right)^{2/3}$$

As a first approximation, one can estimate the power factor as a function of n_e by assuming a constant effective mass and using the Pisarenko relationship.[39] Not surprisingly, lowering the carrier concentration in $(SnSe)_{1.2}TiSe_2$ should result in an increased power factor. The proposed band diagram suggests that there are several mechanisms possible for lowering the carrier concentration in the material. A series of compounds $(SnSe)_{1+\delta}(TiSe_2)_n$ would lower the carrier concentration in each $TiSe_2$ layer as n increases, if the amount of charge transfer remains relatively constant. Substituting a monovalent cation for Sn^{2+} in the rocksalt layer would lower the amount of charge transfer, potentially without lowering the carrier mobility in the $TiSe_2$ layer.

III.4. Conclusions

Intergrowth compounds represent an opportunity to study buried interfaces and the bonding between two different structures. The different band structures of the components provide opportunities to controllably adjust the properties of one material with one carrier type by choosing the other constituent to provide the correct band alignment and therefore provide carriers by charge transfer. In an ideal situation, the "donor" layer would contribute the amount of carriers required to maximize the power factor of a thermoelectric material, while not providing detrimental effects from the holes left after charge transfer. Such a system would effectively allow for a controlled doping with little or no effect on carrier mobility as demonstrated above.

III.5. Bridge

The synthesis of the m = n = 1 compound in the Sn-Ti-Se system provides a comparison to the Pb analog. It is also the foundation from which this dissertation is built. In the coming chapters, the observed long range order in this compound, and other compounds with increased m are explored.

CHAPTER IV

THE OBSERVATION OF LONG RANGE ORDER IN $[(SnSe)_{1.2}]_1(TiSe_2)_1$

This work is unpublished but was coauthored with Jeffrey Ditto, Sven Rudin, and David C. Johnson. Jeffrey Ditto assisted with HAADF-STEM and electron diffraction data, Sven Rudin supplied the DFT calculations, David C. Johnson is my advisor and research group leader, and I am the primary author.

IV.1. Introduction

Misfit layer compounds represent an interesting class of thermodynamically stable superlattice materials, which have been reviewed extensively.[1–3] They are composed of interleaved rocksalt-like and transition metal dichalcogenide structures with the basic formula $(MX)_{1+\delta}(TX_2)_n$ where X is a chalcogen (S or Se) and n is the number of dichalcogenide layers in the unit cell, generally n = 1, 2, or 3. The rocksalt structure consists of a bilayer structure with the cations (M = Sn, Pb, Bi, or a rare earth) displaying a puckering distortion along the c-lattice vector toward the neighboring dichalcogenide layer. To date, compounds have been prepared with T = Ti, V, Nb, Ta, and Cr. It is generally hypothesized that the transport properties are dominated by the choice of dichalcogenide, and subsequent charge transfer between constituents in the intergrowth compound. The structure of the constituents are known to distort, forming a common b axis, while the a-lattice vectors remain incommensurate. The result is a 3-dimensional crystal with a difference in in-plane packing density, which results in the misfit parameter (1+δ) for which the compounds are named. These compounds have been studied extensively, but the high temperature synthesis routes lead to thermodynamic products, and has limited the ability to form designed materials to affect materials properties.

Recently, a new approach to synthesizing metastable compounds with the same basic structural motif has been developed.[4,5] It employs the use of modulated elemental reactants (MER) in a layered amorphous precursor which displays local compositions close to that of the targeted structure, and a low temperature annealing step to nucleate the constituent structures. The MER method has enabled the synthesis of a multitude of compounds not previously available through control of the thickness of each of the constituent layers and compounds containing new constituents, for example $MoSe_2$ and WSe_2.[6–8] This has enabled systematic studies of constituent interaction[9,10] and size

dependent structural effects.[7,8,11,12] The metastable variants show several important distinctions when compared the MLCs. The most influential is the presence of turbostratic (rotational) disorder, which results in the compounds behaving as a stack of 2-D layers, rather than as 3-D crystals. This interesting disorder has resulted in the term "ferecrystal" from the latin root *fere*, meaning "almost". It also results in the structure of the constituents having lattice parameters closer to those of the bulk materials, with no distortions to create common axes between them. While the self-assembly of the precursors into ferecrystals is still not understood, early evidence suggests that templating occurs between adjacent dichalcogenide layers[13], with the preferred orientation disrupted by the presence of the rocksalt intergrowth.[14,15]

The recently reported $(SnSe)_{1.2}TiSe_2$ compound prepared using modulated elemental reactants, however, displayed large areas containing aligned adjacent layers, not previously observed compounds using this synthesis approach.[16] This lead us to investigate the structure in greater detail, to understand if constituent interaction could be resulting in template growth. STEM data suggests there are preferred orientations between the layers, with similar combinations of zone axes present. The *hk*0 structure of SnSe also displays a distortion that is not present in other SnSe based ferecrystals. We also present initial calculations comparing the Sn-Ti and Sn-V systems, which seems to support a larger discrepancy between orientational stability in the Sn-Ti system. The data seems to support the formation of a compound with template growth, that generally displays longer range order than previously observed, with rotational disorder still present, but to a smaller degree.

IV.2. Results and Discussion

High angle annular dark field scanning transmission electron microscopy (HAADF-STEM) data was collected on several m = n = 1 compounds, and some representative images can be seen in Figure IV.1. The contrast difference between the layers allows for the unambiguous identification of the SnSe bilayers (bright) and $TiSe_2$ trilayers (dark). In a large number of the images, crystallographically aligned layers can be observed, confirming the basic structural motif of the compound, and constituents. Surprisingly, there are regions where several adjacent layers show similar crystallographic alignment. This is something not previously observed in compounds prepared using the MER

approach, where turbostratic disorder has been observed in all systems to date. The statistical improbability of seeing so many adjacent layers oriented in a consistent manner suggests that these regions are not the result of random chance.

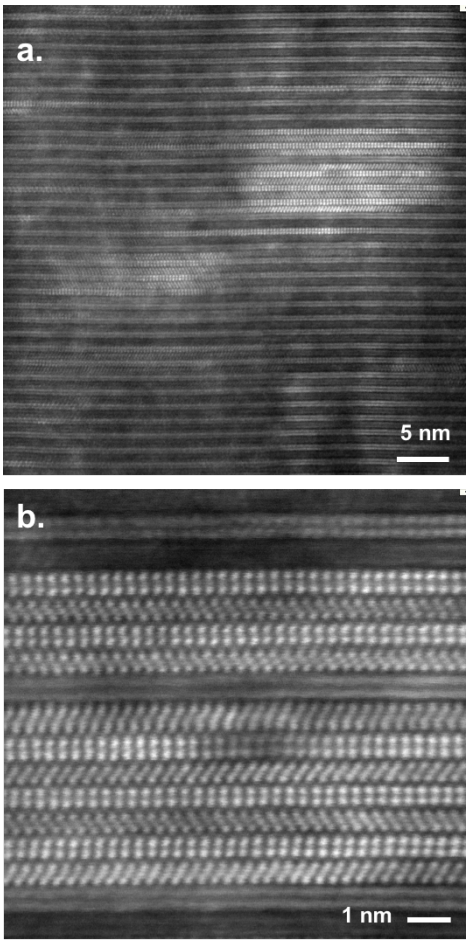

Figure IV.1: Representative HAADF-STEM data at **(a)** low and **(b)** high magnification. There are several regions were multiple adjacent layers display consistent orientation, not previously observed in compounds synthesized byt the MER technique.

The hk0 patterns for two Sn-Ti-Se compounds can be seen in Figure IV.2, with indices for both constituents provided for the observed reflections. The structure for $TiSe_2$ is consistent with all previous reports for $TiSe_2$ containing ferecrystals, and matches the CdI_2 bulk structure and lattice parameter (3.55 Å).[17–20] Compounds containing SnSe have displayed either a square basal plane, or the expected orthorhombic distortion consistent with α-SnSe.[21] In $(SnSe)_{1.21}TiSe_2$, the reflections cannot be indexed to either of these space groups. Split peaks are observed, ruling out the square basal plane structure, while the splitting of reflections does not match the reduced symmetry of α-

SnSe. The structural can be fit using a 2-D space group *p*2*gg*. This is the first report of this distortion in a SnSe based metastable intergrowth compound synthesized from modulated elemental reactants. The only SnSe containing MLC reported to date is $(SnSe)_{1.16}NbSe_2$. The constituent structure was fit to the *Cm*2*a* space group with a = 0.5928 nm and b = 0.5970 nm. Interestingly, the distortion observed in the metastable compound is larger than the thermodynamic compound.

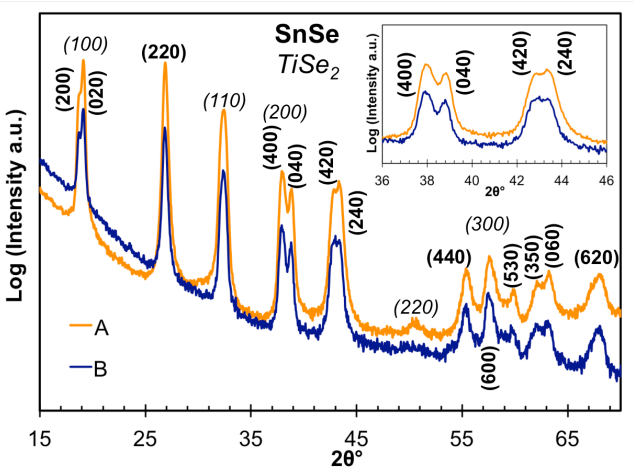

Figure IV.2: In-plane diffraction pattern for 2 m = n = 1 compounds. The in-plane distortion can be fit to the 2D space group *p*2*gg*, and is unlike any other reported for a SnSe based compound.

A reciprocal space map (RSM) was collected at the ESRF in an attempt to identify long range order, and can be seen in Figure IV.3, with the expected position of the *l* = 1,4 based on the known c-lattice parameter given for reference. Ferecrystalline films in the past have displayed streaking along in the *l* direction for each family of *hk* reflections, due to a decoherence in the structure across layers due to rotational disorder. The RSM in Figure IV.3 displays broad but discreet maxima in the *l* direction in both the (22*l*) SnSe and (11*l*) $TiSe_2$ families of reflections. The position of the maxima correlate with the c-lattice parameter determined from the (00*l*) reflections, which is highlighted in the integrated profile comparison of the (00*l*) and SnSe (22*l*) set of reflections. The presence of discreet maxima which correspond to the c-lattice parameter suggests that there are regions in the film which show greater coherence than previously observed for this class of metastable intergrowths. This is consistent with the preferred orientation observed in the STEM data, which suggests that there should be increased coherence across multiple adjacent unit cells.

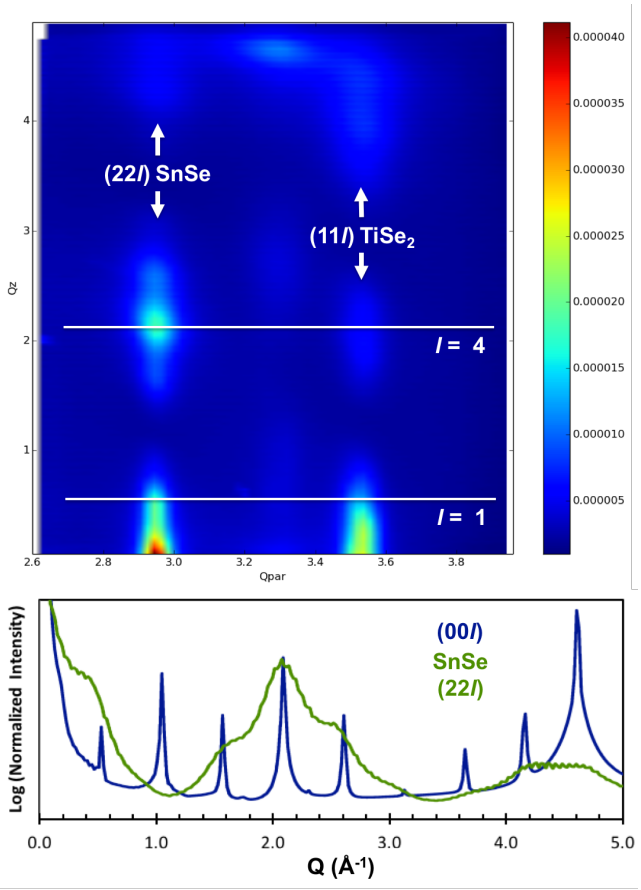

Figure IV.3: Reciprocal space map from the ESRF, with expected *l* positions given. Discreet maxima in the *l*-direction suggest more long range order in the compound than previously observed. Inegrated profiles of the (00*l*) and SnSe (22*l*) family of reflections show that the spacing in the *l*-direction is consistent with the c-lattice parameter.

To gain additional information about the coherence between unit cells, electron diffraction data was collected from the especially ordered regions of the cross section and shown in Figure IV.4. The streaks along *hkl* directions normally observed in ferecrystals show modulation that in some cases can be resolved into discreet maxima. The modulations suggest that there is coherence across multiple unit cells in the Sn-Ti-Se system. Figure IV.4 shows line profiles through the (00*l*) set of reflections, and a set of *hkl* reflections (profile locations noted in Figure IV.4, center). It is clear from the profiles that discreet maxima exist and that the period is increased in the *hkl* data, suggesting that there is a supercell in the volume being probed by the beam. Further study of reciprocal space is required, where both global (XRD) and local (electron diffraction) structure experiments are used to further understand the nature and extent of the long range order.

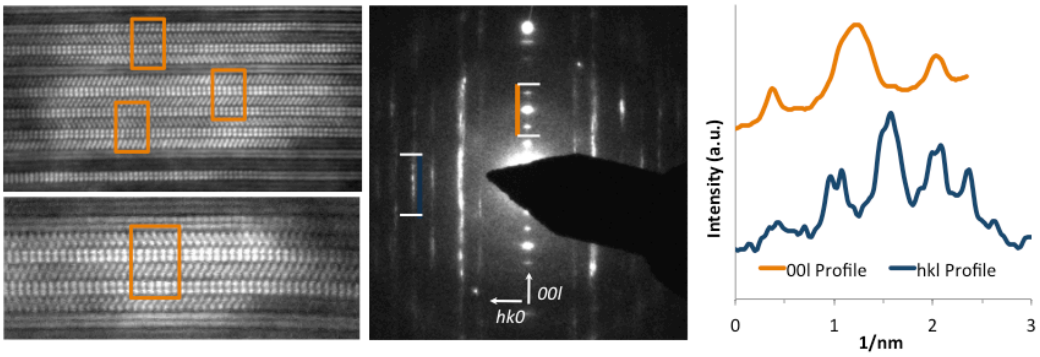

Figure IV.4: STEM (left) and SAED (center) for the m = n = 1 compound. The discreet maxima in the *l* direction suggest there may be local regions were a supercell is present, as highlighted by the line profiles (right).

The constituent structures of misfit layer compounds are known to distort to one another, to form a commensurate b lattice vector. Such distortions must provide a drop in free energy, as they present themselves over nearly all of the materials systems explored in the thermodynamic compounds explored to date. The observed distortion in the Sn-Ti-Se compound is reminiscent of the structural interaction observed in the thermodynamically stable compounds. An overlay of the two in-plane lattice structures shows surprising alignment of atomic planes, when the a axes are aligned perpendicular to one another. The presence of such a distortion and congruent atomic plane along one of the lattice vectors suggests that the alignment observed in the STEM data and the distortion in the lattice parameters results in significant stabilization.

Calculations were performed in order to understand if the two structures may be expected to show preferred orientation. Figure IV.5 shows the basic approach for the calculations, with two islands of SnSe surrounded by dichalcogenide layers. In this case, we chose to compare the Sn-Ti-Se system with the similar previously reported Sn-V-Se system where the long range order is not observed. The islands were placed in 6 combinations of locations between the trilayers structures, and the islands. Table IV.1 shows the results of the calculations. The most stable configuration for both systems is listed first, and the other 5 combinations listed below. Interestingly, the favorable position in the Sn-Ti-Se system was found to have a lower overall energy, and perhaps even more interesting is that the other orientations showed a far more marked increase than the Sn-V-Se system. While these calculations are preliminary, they suggest that the

two constituent structures, due to their size and shape, may provide conditions that favor specific interlayer orientations, seemingly supporting the observations from the STEM and in-plane diffraction data.

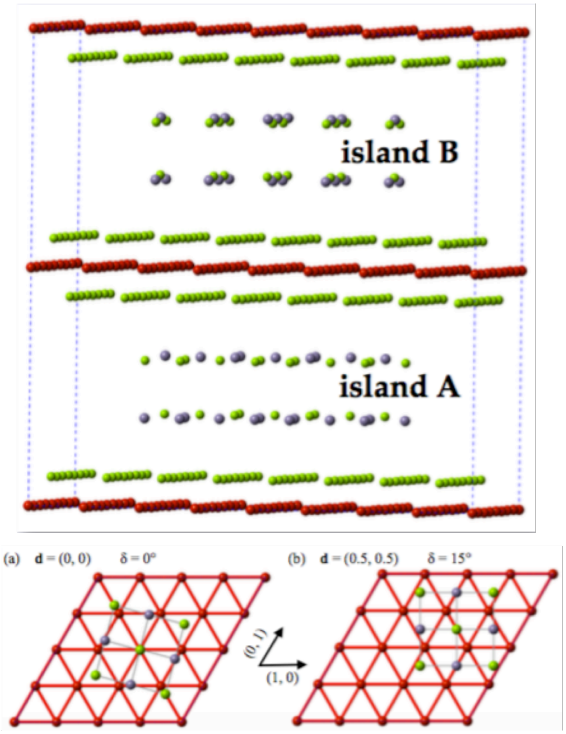

Figure IV.5: Calculations of interlayer orientation, with two specific orientations given in **(a)** and **(b)**.

Table IV.1: Calculation of 6 different island orientations for the Sn-V-Se and Sn-Ti-Se systems. The large difference observed in the Sn-Ti-Se system supports the notion that significant stabilization could be gained in the system through preferred interlayer orientation.

			Sn-V-Se System		Sn-Ti-Se system	
Island	Angle	Origin	E_{total} (eV)	ΔE_{total} (meV/atom)	E_{total} (eV)	ΔE_{total} (meV/atom)
A	15	0,0	-2728.94	0	-2738.16	0
B	15	0,0				
A	0	0,0	-2718.97	21	-2712.05	56
B	0	1/2,1/2				
A	0	0,0	-2719.43	20	-2712.5	55
B	15	0,0				
A	0	0,0	-2718.61	22	-2711.74	56
B	15	1/2,1/2				
A	15	0,0	-2719.14	21	-2712.19	55
B	15	1/2,1/2				
A	15	1/2,1/2	-2718.3	23	-2711.4	57
B	15	1/2,1/2				

IV.3. Conclusions

The in-plane unit cell of SnSe in $(SnSe)_{1.2}TiSe_2$ prepared using modulated elemental reactants is distorted in a manner not previously observed. The distortion results in a lattice match, when the *a*-axis lattice vector to SnSe is oriented perpendicular to the *a*-axis lattice vector of $TiSe_2$. STEM, electron diffraction data and x-ray diffraction reciprocal space maps data all show that long range order between the constituents is present. Calculations suggests that the superstructure as a whole gains significant stabilization from preferred orientation between the layers, perhaps driving the slight distortion of the SnSe structure to provide lattice match. Further electron diffraction studies need to be conducted to understand the long range ordering.

IV.4 Bridge

The long range order observed in the m = n = 1 compound is unique among compounds synthesized from modulated elemental reactants. It represents a hybrid material between the turbostratically disordered ferecrystals and the thermodynamic misfit layer compounds. This compound is the baseline for the comparison of the compounds with increasing rocksalt thickness (m) in the following chapter.

CHAPTER V

COMPLEX CONSTITUENT INTERACTION IN $[(SnSe)_{1+\delta}]_m(TiSe_2)_1$ COMPOUNDS: CONVERSION FROM N-TYPE TO P-TYPE BEHAVIOR

This work is to be submitted for publication with coauthors Sage R. Bauers, Jeffrey Ditto, and David C. Johnson, prior to the submission of this dissertation. Sage R. Bauers assisted with sample synthesis and structural data collection, Jeffrey Ditto provided scanning transmission electron microscopy analysis, David C. Johnson is my advisor and research group leader, and I am the primary author.

V.1. Introduction

Multi-phase composite materials have garnered a large amount of recent interest for applications that require optimizing contradictory properties, for example electronic transport, magnetic, thermal or mechanical properties. Multiferroic composites, for example, have more than three orders of magnitude higher magnetoelectric coupling coefficients compared to single phase materials.[1–3] Electrochemical applications such as fuel cells have mass transport, electrical conductivity, and catalytic requirements which, while difficult to optimize in a single phase material, can be independently tuned in a composite.[4–6] Thermoelectric materials represent another application where the simultaneous optimization of the Seebeck coefficient, electrical, and thermal conductivity is hindered by contradictory properties.[7,8] The presence of interfaces between phases can enhance performance by providing diffusion paths, active catalysis sites, phonon scattering, and interfacial magnetoelectric coupling. As the size of the composite crystallites decreases, interface density increases, and these effects are magnified. In the nanoscale regime, new properties can immerge.[9] Understanding how constituent structures change with size and interact with one another is critical to enable materials design in these complex systems and applications.

Titanium dichalcogenides and compounds containing the layered TiX_2 structural motif are an example of a material system with potentially interesting thermoelectric properties where optimizing properties has been challenging. TiS_2 and $TiSe_2$ are small band gap semiconductors with unusually large Seebeck coefficients relative to their density of carriers, making them an interesting target for thermoelectric optimization.[10–12]

Intercalation has been shown to dramatically decrease thermal conductivity, increasing the dimensionless thermoelectric figure of merit to around 0.5.[11,13] Misfit layer compounds based on TiS_2 and $TiSe_2$ have been synthesized with m = 1, and n = 1,2.[14–16] The sulfide based, n = 2 compounds[14] displayed promising thermoelectric behavior for an unoptimized material. Making related derivatives of these compounds and optimizing carrier concentrations have been unsuccessful and challenging respectively, due to the lack of tools to control products in the high temperature vapor transport reactions used to produce crystals. Designed precursors that self assemble at low temperatures while maintaining the precursor architecture have recently enabled layering schemes previously not achievable in $[(MX)_{1+\delta}]_m(TSe_2)_n$ materials to be synthesized.[17–20] The presence of turbostratic (rotational) disorder between and within the constituent layers in these materials results in very low lattice thermal conductivity.[21,22] Several layering schemes involving $TiSe_2$ have been reported and the data suggests that charge transfer is occurring between the constituents, with electrons the majority carriers.[17] The carrier concentration can be diluted by increasing the ratio of $TiSe_2$ layers to PbSe layers leading to enhanced power factors.[17] This suggests that nanoarchitecture and the ratio of constituents can potentially be used to control carrier concentration to improve power factors.

To probe the effect of nanoarchitecture on both structure and properties we synthesized a family of compounds $[(SnSe)_{1+\delta}]_mTiSe_2$ where $m \leq 4$. SnSe was chosen as the constituent to pair with $TiSe_2$ due to the higher performance of SnS-TiS_2 misfit compounds reported by Wan, and the behavior of the m = n = 1 selenide compounds.[14,18,19,23] The compounds form even if there is excess Sn or Se in the precursors, with the excess leaving the targeted structures during the low temperature self assembly. As the thickness of the SnSe layer is increased, the structure changes significantly, from a rectangular in plane unit cell when m = 1, to a square in plane unit cell for m = 2 and 3, to a different rectangular unit cell that is related to the bulk α-SnSe orthorhombic structure for m = 4. The unusual in-plane unit cell of the m=1 compound results from the formation of long range order, which is the first time this has been observed from compounds prepared via low temperature self assembly from designed precursors. Electrical transport measurements indicate that a simple single band is inappropriate for these compounds, as the sign of the Hall coefficient and Seebeck

coefficient change sign as m is increased. The complex electrical transport behavior is intertwined with the structural changes that occur as m is increased, making the previously applied rigid band model with charge transfer between constituents insufficient do describe the transport properties.

V.2. Experimental

Precursors were synthesized in a high vacuum physical vapor deposition system, with deposition occurring at pressures below 5 x 10^{-7} Torr. Tin and titanium metals were deposited using electron beam guns, and selenium was deposited using an effusion cell. A PC controlled pneumatic shutter system was used to control the sequence and thickness of the elemental layers. The rate of deposition, and thickness of elemental layers were measured using quartz crystal microbalances, with rates maintained at 0.1-0.3 Å/s at the substrate. The elemental layers were deposited in a Ti-Se-m[Sn-Se] sequence, with the Sn-Se precursor layer repeated m times to form the targeted compounds. The sequence was repeated to get a total film thickness of approximately 50 nm for ease of characterization. Precursors were annealed in an inert environment (N_2, [O_2,H_2O] ≤ 0.8 ppm) at 350°C for 30 minutes.

The structure of the precursors and products were determined using x-ray diffraction and electron microscopy. Locked couple X-ray diffraction (XRD) and reflectivity (XRR) were used to determine the superstructure and the total film thickness, respectively, using a Bruker D8 Discover. Constituent structures were characterized using in-plane diffraction geometry on a Rigaku SmartLab diffractometer. All diffraction patterns are reported using a Cu Kα radiation source. Composition measurements used for the calibration of deposition parameters was performed using a method described elsewhere.[24] High angle annular dark field scanning transmission electron microscopy (HAADF-STEM) data was collected at Pacific Northwest National Laboratory using a probe aberration-corrected Titan 80-300™ STEM and EDX maps were acquired using a probe aberration corrected JEOL ARM200CF. Hall effect and van der Pauw resistivity measurements were conducted on a lab-built closed cycle He low temperature system.

V.3. Results and Discussion

The modulated elemental reactant approach was used to prepare the targeted compounds. The deposition parameters required to prepare layered amorphous precursors

that closely resemble the targeted structure in both local composition and layer thickness were determined using an iterative approach. This approach involves preparing a series of precursors with varying n and m values, measuring composition via EPMA and amorphous repeat thickness via XRR, and interpolating to obtain desired compositions and thicknesses as described previously. [25] Once deposition parameters were calibrated, precursors for each of the targeted $[(SnSe)_{1+\delta}]_mTiSe_2$ compounds were prepared by repeating the elemental Sn and Se bilayer m times and the Ti|Se bilayer once to obtain a total thickness of approximately 50 nm. 350°C was used as an annealing temperature during the optimization process to correlate the composition and precursor thickness to superstructure formation based on a previous investigation.[23] Once calibration was complete a brief study confirmed that 350°C for 30 min was the optimum annealing temperature and time, which was used for all of the compounds reported here.

V.3.1. Structural Characterization

The diffraction patterns of the compounds prepared in this investigation can be seen in Figure V.1. The layered nature of the precursor, and the subsequent superlattice structure results in films with the c-axis normal to the Si substrate, therefore only 00*l* reflections are present in the patterns. The narrow and sharp reflections, without the presence of impurity phase maxima, and the changes in the position and frequency of 00*l* maxima

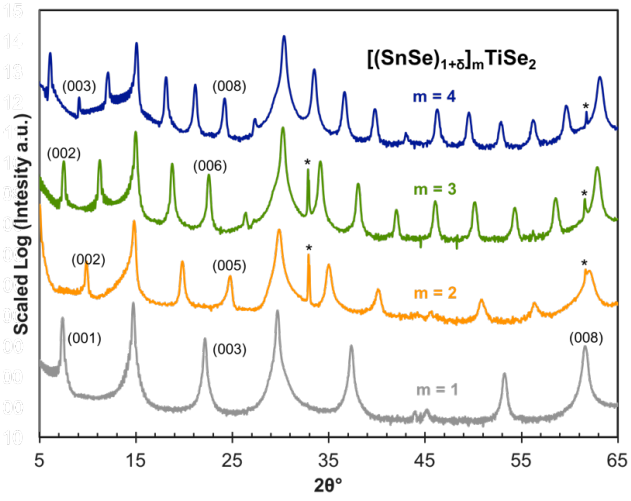

Figure V.1: Out of plane diffraction for the compounds with m ≤ 4. All reflections can be indexed to 00*l* reflections of the superstructure. Offset for clarity.

suggest that the targeted structures were prepared. The calculated *c*-axis lattice parameters are summarized in Table V.1. The *c*-axis lattice parameter increases by 0.579(1) nm per bilayer of SnSe, which is consistent with the 0.577(5) nm reported for SnSe-$NbSe_2$ based compounds,[26] and 0.5806(2) reported for SnSe-$MoSe_2$ compounds.[27]

Table V.1: Lattice parameters for the title compounds. The space group used to fit the SnSe structure is also given.

m	SnSe space group	SnSe a (nm)	SnSe b (nm)	$TiSe_2$ a (nm)	1+ δ	c (nm)
1	p2gg	0.6094(3)	0.5974(4)	0.356(1)	1.21	1.204(1)
2	p4gm	0.602(1)	-	0.352(3)	1.18	1.784(1)
3	p4gm	0.605(1)	-	0.353(3)	1.18	2.364(1)
4	Pcmn	0.436(1)	0.423(1)	0.352(3)	1.16	2.942(2)

In-plane diffraction patters were collected to characterize the constituent structures and are shown in Figure V.2a. The observed reflections can be indexed as either SnSe or $TiSe_2$ reflections, except for a reflection which is consistent with $SnSe_2$. STEM experiments discussed later indicate that the $SnSe_2$ is present on the surface of the films. The in-plane lattice parameters for each constituent were calculated from least squares fits and are summarized in Table V.1. In all of the compounds, $TiSe_2$ could be fit using the CdI_2 structure type (*P-3m1*) with an *a*-axis lattice parameter ranging between 0.352(3) and 0.354(3) nm. This is consistent with previously reported metastable compounds containing $TiSe_2$ and the bulk structure of $TiSe_2$.[17–20,28,29] The relatively large error on the $TiSe_2$ lattice parameter results from overlapping reflections, with only the (110) reflection free from interference from other phases.

The SnSe in-plane structure varies considerably as a function of its thickness as highlighted in Figure V.2b, with the appropriate symmetry groups and resulting lattice parameters given in Table V.1. The m = 1 compound displays a unique distortion identified previously,[29,30] which can be fit using the 2-D space group *p2gg*. This distortion results in a lattice match with the $TiSe_2$ structure. The compound also displays long range order with the *a*-axis lattice vectors of $TiSe_2$ and SnSe being perpendicular to one another. This data, along with supporting STEM data, indicates that the m = n = 1

compound is better described as a metastable misfit layer compound, with a large number of rotational defects present.

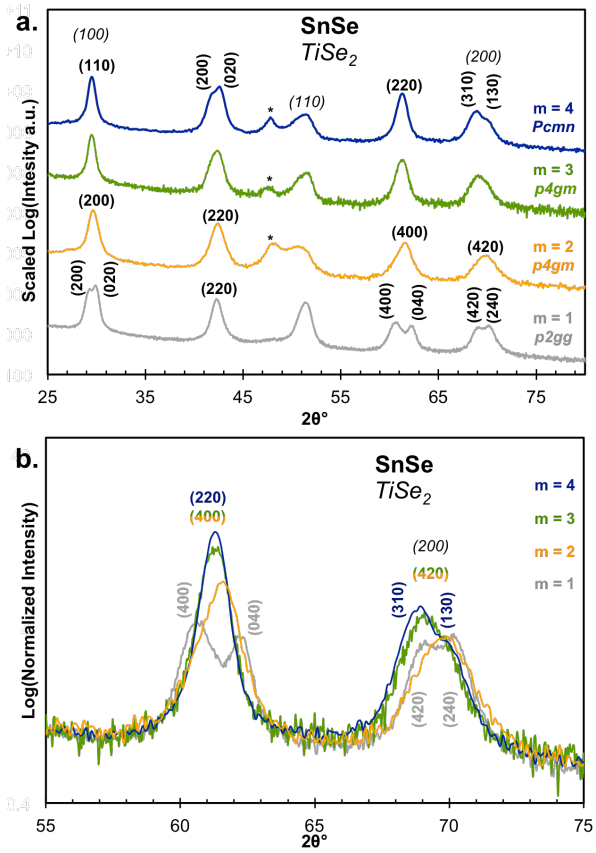

Figure V.2: (a) In-plane diffraction patterns of the title compounds. **(b)** Maxima displaying the structural evolution of the SnSe constituent as a function of thickness.

The rectangular distortion of the SnSe constituent is no longer observed in the m = 2 and 3 compounds. The SnSe reflections in these compounds can be indexed to the 2-D space group *p4gm*, which is consistent with the structures reported in the SnSe-$TaSe_2$ and SnSe-$MoSe_2$ systems.[25,31] No evidence for long range order is observed. The *a*-axis lattice parameter of the m = 3 compound is slightly larger than that observed in the m=2 compound. The increase in lattice parameter is likely due to a decrease in the puckering distortion as the volume to surface ratio changes.[31] The SnSe in-plane structure changes again in the m=4 compound, with the reflections now indexing to a rectangular in plane unit cell based on the bulk α-SnSe orthorhombic structure. This structural change with thickness was observed previous in the SnSe-$TaSe_2$ and SnSe-$MoSe_2$ systems.[25,31]. The change in the surface to volume ratio as m increases is the likely cause of the structural

evolution with thickness, with thicker layers favoring the bulk SnSe constituent structure.[30,31]

HAADF- STEM investigation shows that the majority of the film has the targeted structure, although small regions with substitutional defects where $TiSe_2$ replaces a portion of a SnSe bilayer were observed. This has been observed previously in ferecrystalline compounds,[32] and is likely due to deviations in composition in the precursor. $SnSe_2$ was observed at the surface and the film/substrate interface as a high Z CdI_2 structured phase. The $SnSe_2$ likely forms from excess Sn and Se migrating out of the sample as the superstructure self-assembles. As seen in Figure V.3, a high magnification HAADF STEM image of a representative area of the m = 3 compound, the layers of SnSe and $TiSe_2$ have the contrast expected for the relative Z of the constituents, and the monoselenide is the Sn containing phase in the superstructure. Extensive turbostratic disorder is observed for the $m \geq 2$ compounds, supporting the decoupling of the layers suggested by the *hk*0 diffraction. This is consistent with the other SnSe containing compounds synthesized from modulated elemental reactants. [25,31] Atomically abrupt and smooth interfaces between the different constituents are observed, reflecting the extent of

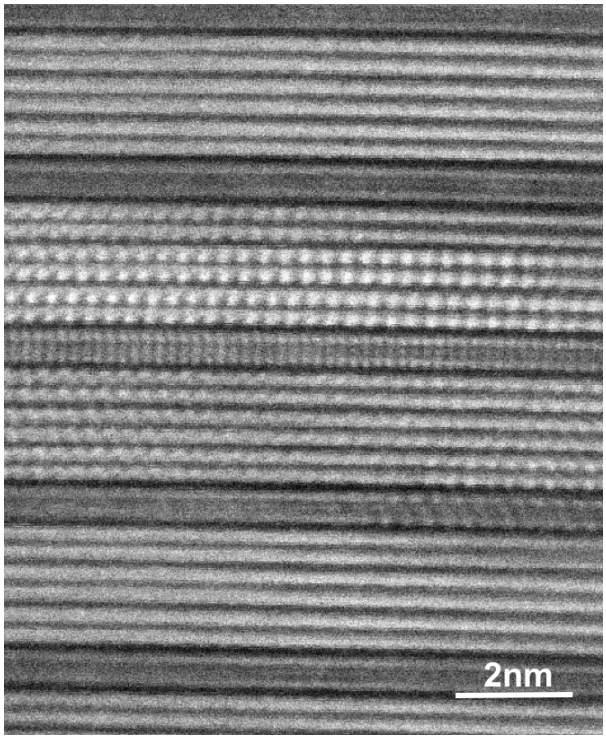

Figure V.3: High magnification HAADF-STEM image. The expected crystal faces are observed for the two constituents, with turbostratic disorder observed between the layers.

diffusion during the self-assembly process which corrects for local variation in both thickness and composition. Where zone axes are observed for the darker Se-Ti-Se layers, they are those expected for a CdI_2 structured $TiSe_2$ with Ti octahedrally coordinated. The SnSe layer is based on a distorted rocksalt structure best described as 3 pairs of bilayers, with longer interplane distances between the more closely spaced bilayers. A similar distortion into bilayers was observed for thin PbSe layers and rationalized as an interplay between volume and surface free energy.

Where zone axes are observed for the SnSe layers, each of the bilayers has the expected patterns for a distorted rock salt layer, but surprisingly several different relative orientations are observed. The majority of the layers have the anticipated rock salt structure where the cations alternate with the anions in a face centered arrangement. In some of the areas along the [100] zone axis, however, occasionally the bilayers stack with the cations aligned above each other as highlighted in Figure V.4. This unexpected stacking arrangement may reflect the mechanism of formation, as the crystallographic alignment of the two constituent structures suggests that the layers template off of each other.[33] Calculations are required to determine if there is a significant energy difference between the different configurations and if processing conditions influence the frequency this is observed.

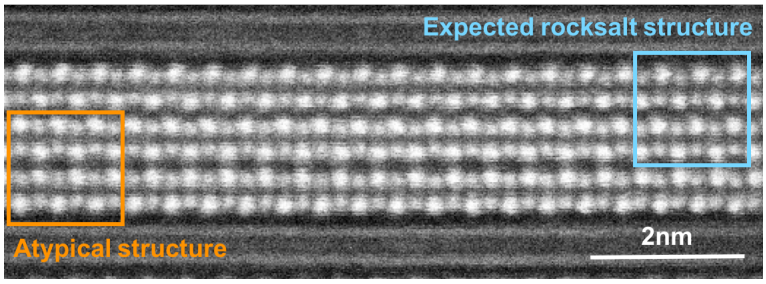

Figure V.4: HAADF-STEM data showing interesting atypical structure in thicker SnSe layers. The presence of such structural variation may be a reason for the unexpected transport behavior.

V.3.2. Transport Properties

Temperature dependent resistivity was measured for the compounds and can be seen in plotted in Figure V.5. The resistivity of the m=2, 3 and 4 compounds are all higher than that previously reported m = n = 1 compound. Adding additional layers of SnSe, a wider band gap constituent than $TiSe_2$ might be expected to increase the resistivity, but

surprisingly, the highest resistivity is measured for the m = 2 compound, with subsequent increases in m resulting in lower resistivity. This behavior is different than that observed previously for $(SnSe)_m(NbSe_2)_n$, where an increase in the thickness of nominally semiconducting phases resulted in a systematic increase in resistivity.[26] The resistivity increases as temperature is decreased for all of the compounds at low temperature, with the overall magnitude of the increase scaling with the room temperature resistivity. The temperature dependence is not exponential as expected for a traditional semiconductor, but is consistent with a metal where carrier localization is occurring at low temperatures.

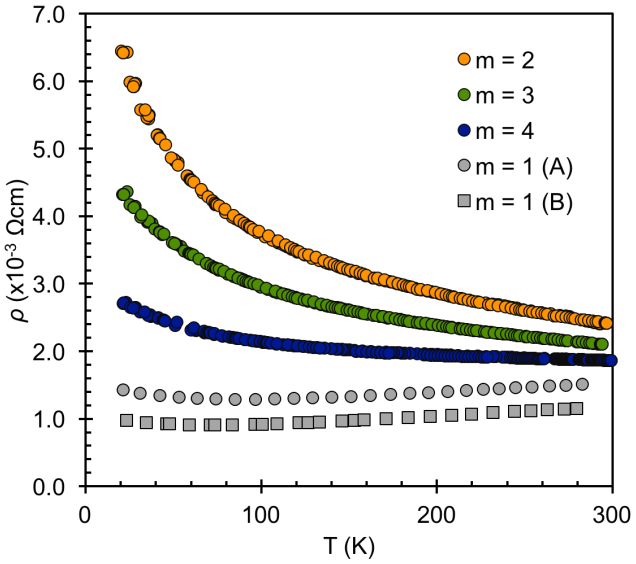

Figure V.5: Temperature dependent resistivity of the compounds plus the two previously reported m = 1 compounds. The decreasing resistivity with increasing SnSe thickness is unexpected, based on previously reported $TiSe_2$ based compounds.

Hall effect measurements were made to provide additional data to understand the surprising resistivity results, and the temperature dependence of the Hall coefficient for the compounds can be seen in Figure V.6. For all of the compounds, the Hall coefficient changes very little as temperature is varied, consistent with metallic behavior. The m=1 compound has a negative Hall coefficient at all temperatures, indicating electrons are the majority carrier. This is consistent with electrons in SnSe transferring to lower energy Ti 3d states in $TiSe_2$.[refs] The compounds with m > 1, however, all display positive room temperature Hall coefficients, suggesting holes are the majority carriers. The Hall coefficient for the m = 2 compound switches sign at approximately 160 K, suggesting a change in majority carrier type. The Hall coefficients systematically become more

positive as m is increased, suggesting that the changes in resistivity with m do not reflect changes in carrier concentration. This suggests that the average carrier mobility must significantly increase as m is increased, and that the mobility for electrons is significantly different than for holes.

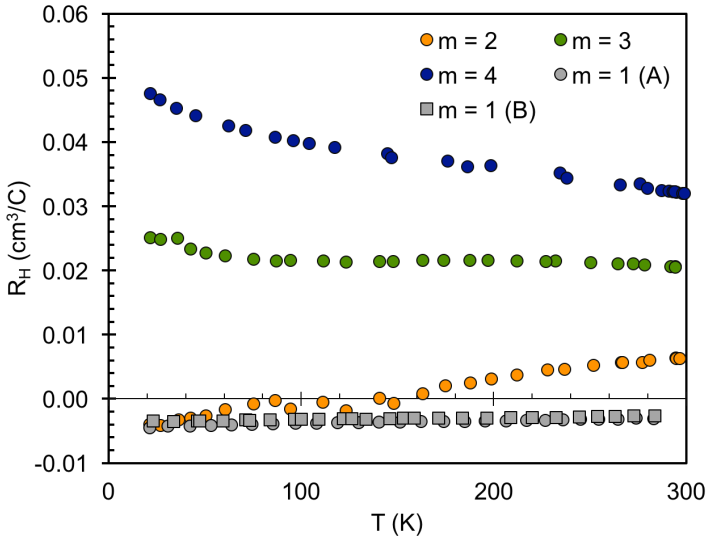

Figure V.6: Temperature dependent Hall coefficient (RH) measurements for the title compounds plus the previously reported m = 1 compounds. The Hall coefficient switches sign as a function of SnSe thickness.

Room temperature Seebeck coefficients were measured for all of the compounds to gain more information of the electronic structure and are summarized in Table V.2. Like the Hall coefficient, the Seebeck coefficient also changes sign as m is increased. The m = 2 compound displays a positivie Hall coefficient and a negative Seebeck coefficient, which is consistent with the change in the Hall coefficient as a function of temperature and indicates that both carrier types contribute to the observed conductivity. The difference in the magnitudes of the resistivities, Hall coefficients and Seebeck coefficients suggest that the holes have higher mobility than the electrons. The magnitude of the Seebeck and Hall coefficients for the m=1 and 4 compounds indicate that effective masses of the electrons and holes must also be different, with the electrons having a higher effective mass. This complex behavior is inconsistent with the simple rigid band model with charge transfer between constituents used to rationalize the electrical properties of analogous m ≤ n compounds.[14–16] The band structure of these compounds can conceptually be thought of as consisting SnSe bands and $TiSe_2$ bands, both perturbed

by the interface and the charge transfer between SnSe and $TiSe_2$ which depends on the band offsets and the Fermi level. The diffraction and TEM data indicates that the structure of the SnSe constituent is changing with the thickness of the SnSe layer, so a rigid band model is certainly not appropriate. The complex variation of the electrical properties indicate that these compounds cannot be thought of as simple composites where the properties of the individual constituents can be summed to obtain the properties of the intergrowth.

Table V.2: Room temperature electrical data for the title compounds and the previously reported m = 1 compounds.

m	ρ (mΩcm)	R_H ($x10^3$ cm^3C^{-1})	α (μVK^{-1})
1 (A)	1.5	-4.4	-75
1 (B)	1.2	-3.4	-77
2	2.4	6.4	-28
3	2.1	20.6	+3
4	1.9	32.2	+22

V.4. Conclusions

Three new $[(SnSe)_{1+\delta}]_m(TiSe_2)_1$ compounds were synthesized from modulated elemental reactants. As the SnSe block thickness is increased, the structure evolves from orthorhombic (m = 1) to cubic (m = 2,3) to a structure that is related to the bulk orthorhombic phase (m = 4). The distortion of SnSe in the m=1 compound results from the formation of an extended commensurate lattice. The compounds also display unexpectedly complex electrical properties, with resistivity decreasing as the thickness of the SnSe layer is increased and the carrier type changing as m is varied and as a function of temperature. The evolving structure and interesting electrical properties suggest the constituent interaction is complicated and the previously used models based on rigid bands and charge transfer between the constituents is not appropriate for these compounds. The complex electrical behavior observed for the title compounds indicates that two carriers contribute have different mobility values and effective masses.

V.5. Bridge

The $m \leq 4$ compounds displayed interesting structural and electronic evolution as a function of SnSe thickness. The interesting behavior observed suggests the simple band

diagram give in Chapter III falls apart as the structure evolves as a function of m. This suggests that complex behaviors, and interesting thermoelectric behavior may be observed at high values of m.

CHAPTER VI

SYNTHESIS AND CHARACTERIZATION OF TURBOSTRATICALLY DISORDERED $(BiSe)_{1.15}TiSe_2$

This work appeared in volume 29 issue 6 of Semiconductor Science and Technology in 2014 with coauthors Daniel B. Moore, Mark N. Coffey, Adam W Jansons, Matthias Falmbigl, and David C. Johnson. Daniel B. Moore and Mark N. Coffey assisted with sample synthesis, Adam W Jansons assisted with electrical characterization, Matthias Falmbigl provided Rietveld and le Bail analyses, David C. Johnson is my advisor and research group leader, and I am the primary author.

VI.1. Introduction

Over the last several years, increasing attention has been paid to the properties of two dimensional sheets of materials, with the initial focus on graphene leading to a Nobel Prize awarded to Novoselov and Geim in 2010 for the discovery of truly extraordinary mechanical and electronic properties of this two dimensional new material.[1,2] The expectation is that there will be an emerging field of applications, especially in the arena of electronics, using two-dimensional materials that offer high mechanical and chemical stability complemented by a wide range of electronic properties.[3-6] The transition metal dichalcogenides, composed of a range of transition metals (T = Mo, W, Re, Nb, Ti etc.) and chalcogens (X = S, Se, Te) with a stoichiometry TX_2, may either be metallic or semiconducting with a variety of band gaps and structurally contain two-dimensional X-T-X trilayers. Stacking two-dimensional building blocks of different materials in designed sequences creates opportunities for many applications, including enhanced solar energy conversion and electronic device performance, by taking advantage of unique combinations of electrical and optical properties found in the building blocks.[3,7-10] For thermoelectric materials, the presence of two crystalline constituents shows promise for increasing phonon scattering while not sacrificing electrical conductivity, both of which are crucial for maximizing the thermoelectric figure of merit. Intergrowth structures might permit the tailoring of properties via nanoarchitecture to achieve a "phonon glass - electron crystal".

One class of compounds that naturally consist of stacked two dimensional layers with different structures are misfit layer compounds (MLCs) composed of a transition metal

dichalcogenide and a rocksalt-like structure interleaved to create a superlattice.[11] The presence of two crystalline constituents results in low thermal conductivity, presumably from the anharmonic atomic potentials at the interfaces created by the mutual distortion of the two constituent layers. [12,13] Exceptionally low thermal conductivity has been observed if there is turbostratic disorder between the layers that eliminates the 3-D periodicity. [14] The turbostratic disorder, while scattering phonons effectively, does not appear to decrease electrical conductivity. Where both ordered and turbostratically disordered polymorphs of the same compound are known and the electrical conductivity measured, the disordered compound has similar or higher conductivity.[15]

Recently, the synthesis of the new MLC $(BiSe)_{1.13}TiSe_2$ via vapor transport methods was reported.[16] The MLC was found to consist of a BiSe layer interleaved with $TiSe_2$ in alternating layers. A coherent superstructure was reported with common lattice parameters of b = 6.2 Å and c = 23.748 Å but differing a lattice vectors a = 3.5 Å ($TiSe_2$) and a = 6.2 Å (BiSe). Like other MLCs reported previously, the b lattice parameters of the two constituents conform to one another, while the a parameters do not, resulting in different in-plane packing density and thus the "misfit", or non-integer stoichiometry between constituent layers.[11] The temperature dependent resistivity displays metallic behavior, with increasing resistivity as a function of temperature.

Herein we report the synthesis and characterization of $(BiSe)_{1.15}TiSe_2$ from modulated elemental reactants with a similar interleaved structure containing layers of BiSe and $TiSe_2$, but without the presence of a coherent supercell. The structural characterization shows significant differences in both in-plane lattice parameters of the BiSe constituent and long-range order in the c-direction in the film due to the turbostratic disorder. The $(BiSe)_{1.15}TiSe_2$ compound we report also shows metallic resistivity behavior, but different temperature dependence than the 3-D crystal. The lack of long-range order appears to make the material behave more like 2-D layers rather than a 3-D compound. Comparison to previously synthesized $(PbSe)_{1.16}TiSe_2$ offers a chance to understand the effect of electron configuration of the rocksalt cation on the electrical properties of the resulting films, and suggests a method for controlled doping.[17]

VI.2. Experimental

Samples were prepared using a custom-built physical vapor deposition system, at pressures below 5 x 10^{-7} Torr. Bi and Ti were deposited using electron beam guns and Se was evaporated using an effusion cell. Rates of deposition and thickness deposited were monitored by quartz crystal microbalances with rates maintained between 0.2-0.3 Å/s at the substrate. Films were deposited on both <100> Si substrates and masked, fused silica substrates for structural and electrical characterization, respectively. Elemental layers were deposited in the order of Ti, Se, Bi, Se at calibrated thicknesses using personal computer controlled pneumatic shutters. The shutters were opened sequentially until the desired thickness for each element was achieved. The thickness of the elemental layers was scaled to match the composition of the previously synthesized misfit layer compound as an initial target, and the total thickness of the repeat unit was scaled to the expected c-lattice parameter of approximately 1.2 nm.[16] The desired layer sequence was repeated 42 times to give approximately 50 nm total film thickness. Electron probe microanalysis (EPMA) and x-ray diffraction and reflectivity were used to determine the composition, and layer thickness, and total film thickness, respectively.[18] X-ray diffraction and reflectivity measurements were carried out using a Bruker D8 Discover diffractometer (Cu Kα radiation). Films were annealed in an inert environment (N_2, with [O_2, H_2O] ≤ 0.5 ppm) at the experimentally determined optimal temperature for 30 minutes to induce the formation of the target compound.

High angle annular dark field scanning transmission electron microscopy (HAADF-STEM) and selected area electron diffraction (SAED) data were obtained using an FEI Titan transmission electron microscope at 300 kV accelerating voltage. In-plane structural studies were carried out at the Advanced Photon Source (APS), beamline 33-BM-C using a wavelength of 1.1272(1) Å, and in-plane goniometer geometry resulting in *hk*0 diffraction maxima in the patterns. Lattice parameters were obtained from least squares fits. Electrical resistivity measurements were made on films deposited on fused silica substrates in the van der Pauw geometry using a custom built system with a closed system He cryostat for temperature dependent studies. Hall effect measurements were made in the same system and geometry by varying the magnetic field while supplying a

constant current. The resulting hall voltage (R_H) was used to calculate both carrier concentration and mobility using a single band model, discussed in greater detail below.

VI.3. Results and Discussion

VI.3.1. Synthesis and Structural Characterization

The synthesis of the target compound was accomplished using a method described elsewhere.[19,20] The deposition parameters for $TiSe_2$ had been previously established during the preparation of $[(PbSe)_{1+\delta}]_m[TiSe_2]_n$ compounds and were held constant while the parameters used for the BiSe layer were adjusted.[15,17] The ratio of the Bi:Ti was adjusted by changing the thickness of the Bi layer to match the misfit parameter reported for the previously reported MLC as a starting point. Once the correct ratio of Bi:Ti had been achieved, the Se in the BiSe layer was adjusted to give approximately 5% excess Se to account for Se loss during processing steps. When the proper composition was realized, the total thickness of the repeating unit was scaled to be 1.2 nm, slightly greater than the expected unit cell thickness.[16] During the process several films were synthesized with *c*-axis lattice parameters near 11.77 Å and the films were remarkably well ordered on deposition with 5 orders of 00*l* Bragg diffraction maxima. The structural information on several films is summarized in Table VI.1. The formation of the target structure over a wide compositional range suggests that the structure can accommodate defects to compensate for excess reagents without greatly affecting the supercell structure itself. Attempts to further understand the relationship between precursor composition and structure and product formation in the material are currently underway.

Table VI.1: Representative compounds synthesized during the calibration process. Repeating unit (c parameter) for the as-deposited precursor and annealed structures, and the Bi/Ti ratio measured with EPMA are given.

Sample	Precursor C (Å)	Bi/Ti (EPMA)	Annealed C (Å)
A	12.1(2)	1.00(3)	11.778(5)
B	12.3(3)	1.06(3)	11.767(3)
C	12.3(3)	1.24(3)	11.776(4)
D	11.9(1)	0.91(3)	11.781(5)

Figure VI.1 contains diffraction data collected as one of the samples was annealed at a variety of temperatures to understand both the formation and transformations of the

target compound. Only 00*l* diffraction maxima are observed in the scans due to the intensely textured nature of the films as the 2-D structure of the constituents results in the c-axis being normal to the substrate surface. We used both intensity of the superlattice maxima and full width at half maximum (FWHM) to gauge the relative formation of the target superlattice. The as-deposited diffraction pattern in Figure VI.1 indicates that there is a significant amount of order in the as deposited film. As annealing temperature is increased up to 350°C, the superlattice maxima increase in intensity and the FWHM decreases. Above 350°C there is an increase in FWHM and a decrease in intensity, suggesting the decomposition of the superlattice. We also observe the growth of unidentified impurity phases, suggesting that the structure containing interleaved layers is rearranging to form other more thermodynamically favorable phases. The destruction of the target superlattice is consistent with the compound being metastable, as has been observed for other compounds synthesized by the modulated elemental reactant method, and the optimum formation temperature (350°C) is similar to the processing conditions for $(PbSe)_{1.16}TiSe_2$ reported previously. [15,17,19-22]

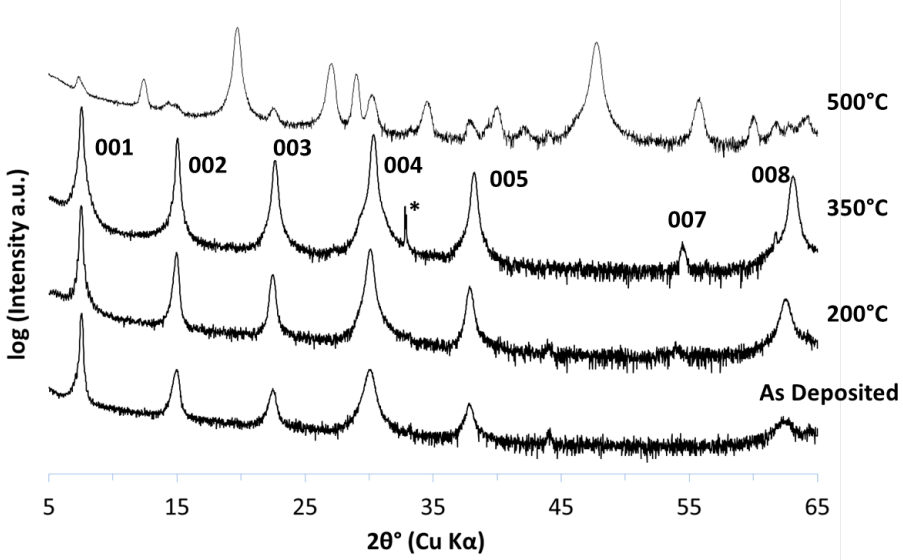

Figure VI.1: A series of 00*l* diffraction patterns collected as a function of annealing temperature (offset for clarity). All films were annealed for 30 min at the temperature indicated by the scan. Reflections are labeled with the 00*l* indices above the 350°C scan (*denotes substrate peak).

Electron microscopy data was collected to gain insight into the structure of the films, and a representative HAADF-STEM image is presented in Figure VI.2. The lower magnification images showed that the alternating layers prepared in the as deposited

precursor self assemble into two chemically unique layers in an alternating pattern in the annealed films. In the dark field images, the brighter layers can be attributed to the BiSe constituent by both the contrast difference expected for HAADF-STEM images and the appearance of (100) and (110) projections from a rocksalt-like structure (see inset Figure VI.2) expected from the structure reported for the MLC.[16] The dark layers are from the lower average Z $TiSe_2$, which is confirmed by the presence of (110) projections of the CdI_2 structure consistent with previous reports for $TiSe_2$.[11,15,17,24,25] The HAADF-STEM images show no sign of order in the 00l direction, suggesting that the supercell reported for the traditionally synthesized $(BiSe)_{1.13}TiSe_2$ is not present in the analogous compound reported here. This is not an unexpected result, as turbostratic disorder is typically observed in intergrowth compounds synthesized by the modulated elemental reactant method.[15,17,19-22]

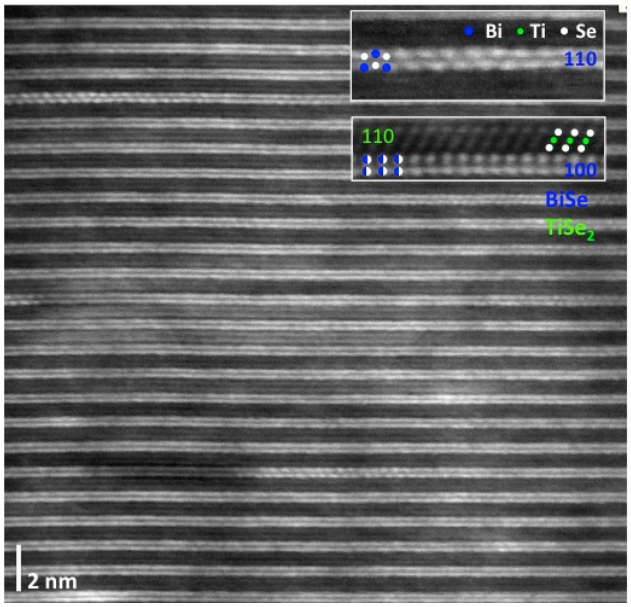

Figure VI.2: HAADF-STEM image at low and high (inset) magnification. Representations of the expected rocksalt and dichalcogenide structures along various projections are given in the high magnification images.

The in-plane diffraction pattern (Figure VI.3) of the $(BiSe)_{1+\delta}TiSe_2$ sample annealed at 350°C reveals *hk*0 reflections of both constituents only, which is consistent with several other ferecrystalline 1:1 compounds and the layered structure observed in the HAADF-STEM data.[19,20] The $TiSe_2$ can be indexed using the hexagonal basal plane lattice parameters of the bulk structure (CdI_2-type, a= 3.535 Å)[24] and reveals a slightly

larger value of 3.58(6) Å found for the intergrowth. The accuracy of the determined lattice parameter is relatively small as only two Bragg-peaks of $TiSe_2$ don't overlap with reflections stemming from BiSe. Attempts to index the remaining peaks using the basal plane parameters of a cubic unit cell failed, but reducing the symmetry to an orthorhombic structure allowed us to unambiguously explain all of the remaining Bragg-reflections. In contrast to the bulk structure of BiSe, which crystallizes in its own trigonal structure type[25] with an a-lattice parameter of 4.15(2) Å, within the ferecrystalline compound $(BiSe)_{1+\delta}TiSe_2$, the BiSe layer has slightly different a and b lattice parameters. The refined lattice parameters are a= 4.562(2) Å and b= 4.242(1) Å and the orthorhombic space group *Pcmn* that was previously used to explain the in-plane diffraction for $[(SnSe)_{1+\delta}]_m[MoSe_2]_n$[26] is consistent with our data for $(BiSe)_{1+\delta}TiSe_2$. The calculated misfit parameter, δ, for this compound is 0.15, which is close to the value of 0.13 reported recently for the corresponding misfit-layered compound.[16] The increase in the misfit parameter indicates a higher in-plane packing density of BiSe in the MER material, when compared to the MLC. This probably results from the independent constituent lattices, which are distinct from the distorted structures in MLCs that result in common lattice parameters in one or both in plane directions.[11,16]

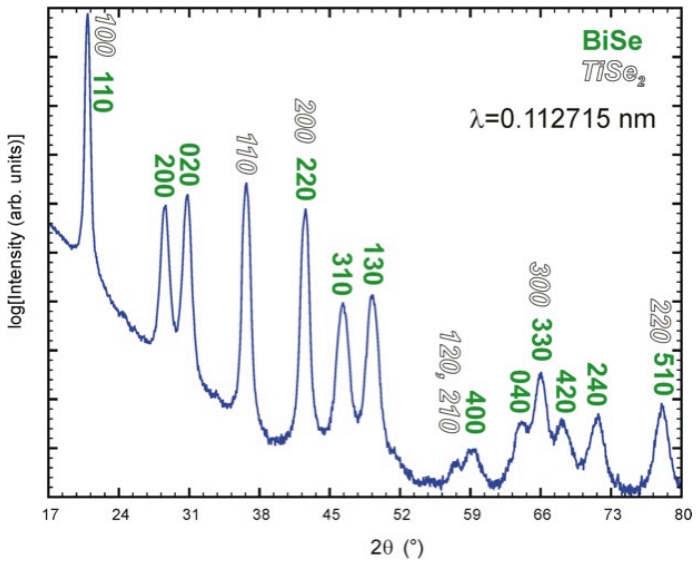

Figure VI.3: *hk*0 diffraction pattern displaying bragg peaks and associated indices from the independent lattice structures of both constituents.

SAED data was collected in order to compare the level of disorder in the $(BiSe)_{1.15}TiSe_2$ reported in this manuscript with the traditionally synthesized MLC analog reported previously. The SAED patterns (Figure VI.4) display clear, discreet maxima in the 00*l* and *hk*0 directions, which yield lattice parameters consistent with the 00*l* and *hk*0 XRD data discussed above. The films show no discrete *hkl* ($h, k \neq 0; l \neq 0$) reflections, but rather streaking in the *l* direction for each *hk* set of reflections, which is consistent with the turbostratic disorder evident in the STEM image discussed earlier. This streaking results from the low coherence length in *hkl* ($h, k \neq 0; l \neq 0$) directions and has been observed in turbostratically-disordered films reported previously.[15,17,19-22] The HAADF-STEM and SAED confirm the lack of any preferred interlayer orientation, in contrast to the MLC analog and to MLCs in general. The lack of a preferred orientation may contribute to the large difference in the in-plane lattice structures relative to the $(BiSe)_{1.13}TiSe_2$ MLC previously reported.[16]

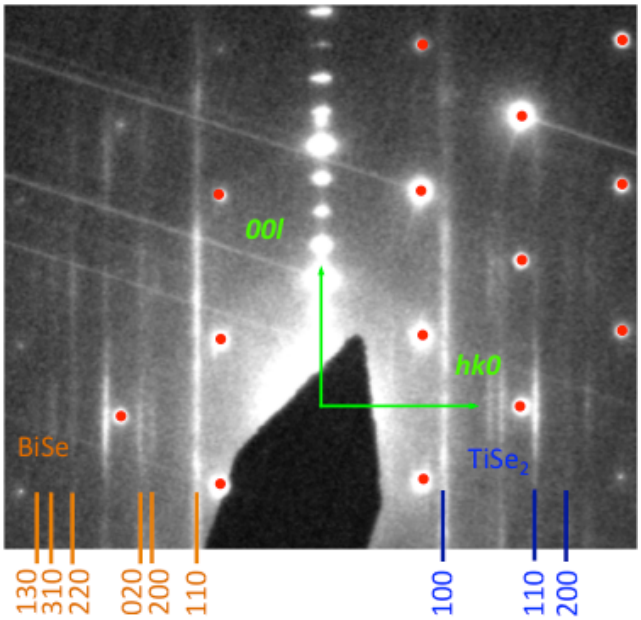

Figure VI.4: SAED pattern of $(BiSe)_{1.15}TiSe_2$. 00*l* and *hk*0 maxima consistent with XRD data. Streaking in l direction indicates the presence of turbostratic disorder. Si substrate maxima are denoted by red circles.

VI.3.2. Transport Properties

The electrical resistivity of a $(BiSe)_{1.15}TiSe_2$ film synthesized on a fused quartz substrate was obtained using the van der Pauw method and its temperature dependence is compared to the MLC analog in Figure VI.5.[16] Despite the significant structural

differences between the two compounds, the room temperature resistivities are strikingly similar, especially since different laboratories have reported order of magnitude differences between the resistivity of the same metallic compound.[27,28] For the MLC, the resistivity ratio $\rho(280)/\rho(20)$ is about 10, which is similar in magnitude to what is observed in common 3-D metals as a result of increased phonon scattering as temperature is raised. The $(BiSe)_{1.15}TiSe_2$ ferecrystal analog shows only a 30% decrease as the temperature is decreased to 20K. This suggests a different scattering mechanism in the ferecrystal compared to the crystalline analog. Although both compounds display metallic temperature dependence, the smaller change in magnitude observed in the ferecrystal is a direct result of the phonon disruption caused by turbostratic disorder. The lack of phonons caused by the short coherence lengths in the structure in directions other than 00*l* and *hk*0 in turbostratically disordered ferecrystals also results in very low thermal conductivity in the cross plane direction.[22,29,30]

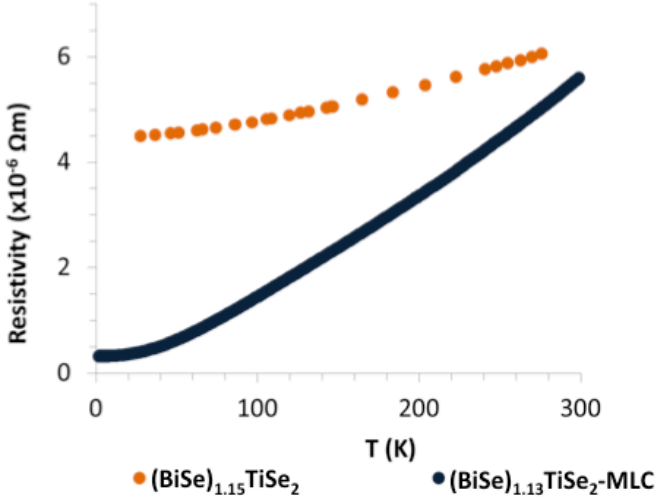

Figure VI.5: Temperature-dependent electrical resistivity comparison to the MLC[16] showing differences in magnitude of increase from 20-280K, attributed to differences in phonon transport in the films due to the presence of turbostratic disorder. The error bars fall within the marker for each data point.

Figure VI.6 contains the Hall coefficient as a function of temperature for both $(BiSe)_{1.15}TiSe_2$ and $(PbSe)_{1.16}TiSe_2$. In general, the Hall coefficient is a function of the electron and hole concentrations and the mobility of both the electrons and holes. Assuming a single band, and hence a single carrier type, the relationship simplifies to $R_H = 1/n_e$, where R_H is the Hall coefficient calculated from the measured Hall voltage and n

is the carrier concentration assuming a single band model. For both compounds the Hall coefficient was negative, indicating that electrons are the predominant carrier type. The lower absolute value of the Hall coefficient of $(BiSe)_{1.15}TiSe_2$ suggests that it has a higher carrier concentration. The carrier concentration increase of about 4 x 10^{21} carriers cm^{-3} at room temperature for the bismuth compound compared to the lead compound, assuming a single band model, is approximately equal to the number of rock salt cations in the same volume. This suggests that a bismuth atom in $(BiSe)_{1.15}TiSe_2$ donates one more electron to the conduction band than does a lead atom in $(PbSe)_{1.16}TiSe_2$, which agrees with the formal valance state of Pb^{2+} and Bi^{3+}.

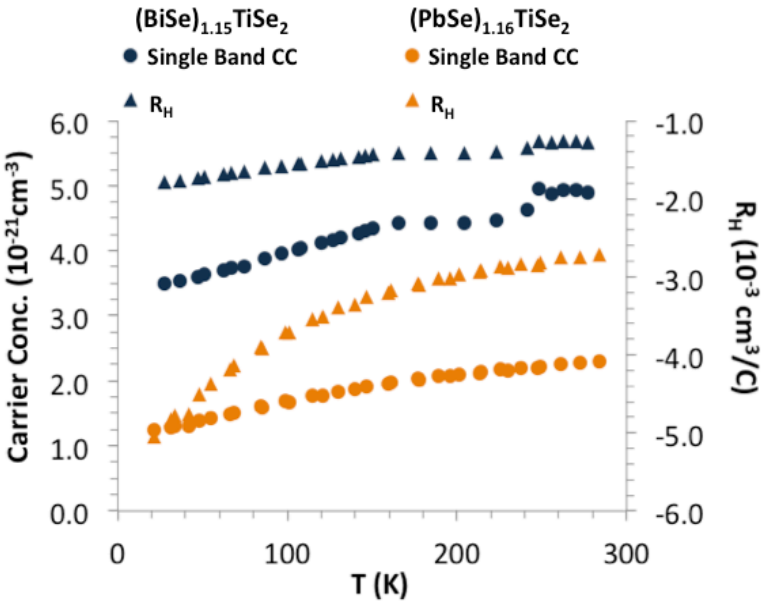

Figure VI.6: Temperature dependent Hall coefficient and carrier concentration calculated using a single band model for turbostratically disordered $(BiSe)_{1.15}TiSe_2$ and $(PbSe)_{1.16}TiSe_2$.The spread of the Hall coefficient data points with respect to a smooth curve reflects the error of the measurement.

The mobility values as a function of temperature, shown in Figure VI.7, were calculated for both $(BiSe)_{1.15}TiSe_2$ and $(PbSe)_{1.16}TiSe_2$ from the single band model carrier concentrations and the measured electrical resistivity. The mobility values are remarkably similar, supporting the idea in the literature that the metallic properties found in misfit layered compounds result from the properties of the dichalcogenide. If this idea is correct, then this combined with our measured carrier concentrations suggest that it

should be possible to systematically dope the conduction band in $(PbSe)_{1.16}TiSe_2$ by replacing Pb with Bi, and that conduction band should gain an electron for every Bi doped in to PbSe.

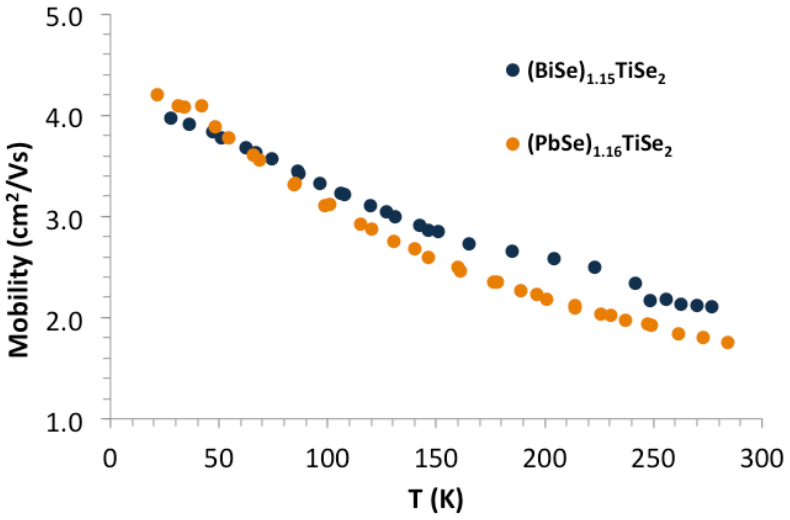

Figure VI.7: Temperature dependent mobility calculated using a single band model for $(BiSe)_{1.15}TiSe_2$ and $(PbSe)_{1.16}TiSe_2$ synthesized from MER. Similarity in magnitude suggests $TiSe_2$ is the conducting layer.

VI.4. Conclusions

The compound $(BiSe)_{1.15}TiSe_2$ was prepared from modulated elemental reactants, and was compared to the previously reported MLC analog. The presence of turbostratic disorder in $(BiSe)_{1.15}TiSe_2$ results in significant differences in the in-plane structure of the BiSe layers compared with that of the crystalline MLC. $(BiSe)_{1.15}TiSe_2$ is a metal, with similar room temperature resistivity to the MLC. It has a weaker temperature dependence, however, due to the disordered structure. Comparison of the Hall effect data with $(PbSe)_{1.16}TiSe_2$ suggests that the $TiSe_2$ layer is responsible for conduction in the materials with electrons transferred from the rocksalt constituent as majority carriers. The difference in carrier concentration between the PbSe and BiSe containing compounds suggests that the bismuth is a trivalent cation, donating one more electron to the $TiSe_2$ constituent than PbSe. This suggests that it should be possible to dope the $TiSe_2$ layer to a desired carrier concentration without lowering the mobility, by incorporating the dopant atoms into the non-conducting rocksalt structure.

VI.5. Bridge

The compound reported in this chapter is the first ferecrystal based on BiSe reported in literature. It offers the opportunity to understand the role of the rocksalt cation in both structural and electrical properties of the materials. This chapter provided motivation for the rest of this work, which explores making chemical substitutions to affect material properties. It also serves as the end member in a modulation doping study presented below.

CHAPTER VII

KINETICALLY CONTROLLED SITE-SPECIFIC SUBSTITUTIONS IN HIGHER ORDER HETEROSTRUCTURES

This work is published in volume 27 of *Chemistry of Materials* in 2015 with coauthors Duncan R. Sutherland, Jeffrey Ditto, Sage R. Bauers, Matthias Falmbigl, Douglas L. Medlin, and David C. Johnson. Duncan R. Sutherland assisted with sample synthesis and compositional studies, Jeffrey Ditto and Douglas L. Medlin provided electron microscopy analysis, Sage R. Bauers assisted with electrical characterization, Matthias Falmbigl assisted with diffraction characterization, David C. Johnson is my advisor and research group leader, and I am the primary author.

VII.1. Introduction

Perhaps the most common technique used to optimize or tune the properties of solids is to make a chemical substitution. For example, in thermoelectric materials solid solutions between two isostructural compounds are used to both lower thermal conductivity and to control carrier concentrations, resulting in improved zT values relative to the end members.[1] Substitutions are also a common method used to probe physical properties in the search for their fundamental underpinnings. Examples include superconducting compounds and magnetic materials, where substitutions have been used to probe the interaction that leads to the superconducting state and to explore magnetic coupling mechanisms between different sites, respectively.[2-6] In the electronics industry, trace amounts of an element are added to electronically dope semiconductors, for example As, P or B into silicon, to control material properties. Carrier concentrations increase as the doping concentration increases, with a subsequent decrease in carrier mobility due to increased impurity scattering. Typically substitutions are done during synthesis or crystal growth, where the high process temperatures enhance the incorporation of the substituting atom due to entropic considerations. However, these same high temperatures lead to random substitutions distributed across potential sites controlled by the segregation coefficients of each site at the temperatures used.

Preparing desired solid solutions or tuning carrier concentration by doping becomes more challenging as solids become more complex - either structurally, in the number of

constituent elements, or if a concentration gradient of the dopant is desired. For example, doping Si is rather straightforward with high activation percentages of 0.5 or more, due to preferred substitutions of dopants on lattice sites rather than other locations such as inclusions or defects.[7] Similar controlled substitutions in ternary and higher order tetrahedrally-based semiconductors, such as $CuInSe_2$, become more difficult as substitutions can occur in multiple sites and many different defects can form.[8-10] Higher order compounds with different structural motifs, such as misfit layer compounds that contain interleaved layers of a rock salt structured constituent with a transition metal dichalcogenide,[11] provide an even greater challenge. Processing conditions can also make substitutions difficult. While Si can be doped from a melt, where the segregation coefficients are known, growth conditions involving heterogeneous intermediates are difficult to control.[7] For example, compounds grown as single crystals via vapor transport reactions are notoriously difficult to dope, as the partition function between the vapor and solids are usually not known and the kinetics of the transport reaction are different for different elements.[12] As a result of these synthetic limitations, site specific alloys of complex materials, such as misfit layer compounds, remain relatively unexplored.

A potential solution to this challenge is provided by the modulated elemental reactant method. Modulated elemental reactants have been used to prepare many new misfit layer compounds and the nanoarchitecture of the precursor has been shown to be preserved in the self assembly of the targeted kinetically-stable product.[13-15] This synthetic approach has also been shown to provide a route to prepare solid solutions within just the transition metal dichalcogenide constituent, suggesting promise for control of material properties on a finer scale than previously possible in these compounds.[16] The literature on misfit layer compounds discusses them as being related to intercalation compounds,[11,17-19] with the rock salt (MX) constituent donating charge to the dichalcogenide (TX_2) and electrical transport occurring mainly in the TX_2 constituent. It should be possible to test this hypothesis by preparing solid solutions of the MX constituent. In principle, if the MX constituent contributes significantly to the conduction, then making a solid solution should decrease the overall mobility. However, if the TX_2 constituent dominates the conduction, the mobility should not be affected by the solid solution.

Here we report the synthesis of the alloyed intergrowth compounds $(Pb_xSn_{1-x}Se)_{1+\delta}TiSe_2$ using modulated elemental reactants. The compounds are shown to form a solid solution in the rock salt structured constituent over the entire range of $0 \leq x \leq 1$, confirmed via X-ray diffraction and electron microscopy experiments. The transport properties are also characterized and Hall mobility shows that the alloying of $Pb_xSn_{1-x}Se$ actually increases carrier mobility, providing direct evidence for conduction occurring mainly in the dichalcogenide constituent in misfit layer compounds. This suggests that modulation doping, i.e. adding doping atoms to the rock salt structured layer of a misfit compound, would be an effective approach to varying carrier concentration without decreasing mobility.

VII.2. Experimental

Amorphous layered precursors containing modulated elemental reactants were deposited in a custom built high-vacuum chamber at pressures lower than 5×10^{-7} torr. The elemental layers were deposited sequentially, in the order Ti, Se, Pb, Sn, Se, and repeated 42 times for ease of characterization. The deposition parameters were calibrated in a process described in detail elsewhere,[13] and were refined as discussed below. Si substrates were used for structural characterization. All samples were annealed in a N_2 atmosphere ($[O_2,H_2O] \leq 0.7$ ppm) for 30 minutes at 350°C, unless otherwise specified. Structural characterization was carried out using X-ray diffraction (XRD) and X-ray reflectivity (XRR), electron probe microanalysis (EPMA), and electron microscopy techniques. Standard θ/2θ and in-plane geometry XRD measurements were performed on a Bruker D8 Discover diffractometer and Rigaku SmartLab diffractometer, respectively (Cu Kα radiation). Standard geometry measurements were used to characterize the total film thickness (XRR) and the superlattice structure (XRD). In-plane geometry XRD was used to obtain structural information about the individual constituents. Composition data were obtained using EPMA via a thin-film technique described elsewhere.[20]

High angle annular dark field scanning transmission electron microscopy (HAADF-STEM) and energy dispersive X-ray spectroscopy (EDX) measurements were conducted using an aberration corrected FEI Titan G2 80-200 STEM equipped with *ChemiSTEM*™ technology. The STEM was operated at 200keV, 18.1 mrad convergence angle,110 mm camera length, and approximately 0.1 nA of current using a 50 μm condenser aperture.

EDX spectrum images were acquired with a 2.3 ms dwell time per pixel integrated over multiple drift-corrected frames. Thin cross-section lamellae were prepared on an FEI Helios 600i Dual-Beam FIB using wedge premilling methods.[21] EDX signal intensity profiles were extracted for Sn, Pb, Ti, and Se at energy windows of 3.34-3.99 keV, 2.23-2.56 keV, 4.37-4.67 keV, and 1.30-1.57 keV, respectively.

Transport measurements were conducted on samples deposited through a shadow mask onto fused quartz substrates. All measurements were performed on a lab-built system between 20 and 290 K, with measurements being made during both cooling and heating to identify any hysteresis. Film thicknesses were previously measured with XRR and contacts were made with pressed indium. Resistivity measurements were performed using the van der Pauw method[22,23] in a standard cross geometry while sourcing a current of ≤ 0.1mA. Hall effect measurements were made while sourcing 0.1 mA and were performed in the same cross geometry by measuring induced voltage while varying a perpendicular magnetic field between 0-16 kG. Carrier concentration and mobility calculations assume conduction via a single carrier and band.

VII.3. Results and Discussion

The compounds in this study were prepared using the modulated elemental reactants synthesis approach. This method relies on controlling local compositions to control reaction kinetics. To prepare the targeted alloy intergrowth compounds requires that precursor films have different regions corresponding to the compositions of the constituents with thickness of each region close to that of the targeted structural unit. For the $Pb_xSn_{1-x}Se$, the structural unit is a bilayer with a rock salt like structure. For the $TiSe_2$, the structural unit is a Se-Ti-Se trilayer with Ti octahedrally coordinated by Se. Initial deposition parameters were taken from the prior synthesis of the parent SnSe and PbSe containing compounds and scaled to prepare the three alloy compositions.[24,25] These initial precursors were annealed at the optimum temperature for the parent compounds (350°C) and x-ray diffraction patterns were collected to confirm that the targeted compounds formed. The ratio of Pb to Sn was modified slightly based on EPMA data until the targeted compositions were obtained. The thickness of the Pb/Sn layer was then adjusted until a maximum intensity and minimum line width of 00*l* reflections was obtained without any detectable impurity phases.

An annealing study was performed on the nominally x = 0.5 precursor to determine the optimal temperature for the formation of the alloys. Figure VII.1 contains diffraction patterns collected as a function of temperature. The as-deposited sample shows broad, low intensity 00*l* reflections due to the repeating electron density in the precursor. As the temperature was gradually increased up to 350°C, the reflections narrow, increase in intensity, and higher order 00*l* reflections appear indicating the formation of the desired superstructure. The maximum intensity and minimum line width was observed in the 350°C diffraction pattern. Above 350°C, the line widths increase, intensities of the 00*l* reflections decrease, and unidentified reflections are observed, suggesting the decomposition of the targeted compound and the formation of additional phases. 350°C was also found to be the optimal annealing temperature for the end members, and was therefore used for all of the samples in this study.

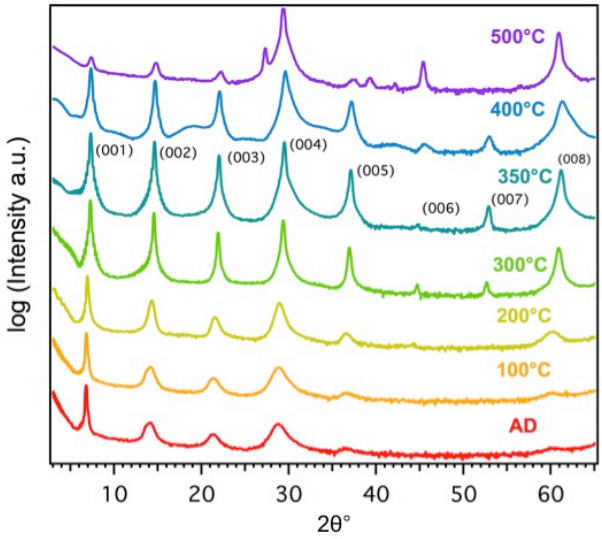

Figure VII.1: The evolution of the diffraction pattern during the self assembly of an as-deposited precursor designed to nominally form $(Pb_{0.5}Sn_{0.5}Se)_{1+\delta}TiSe_2$. The 00*l* indices for the superlattice reflections are given above the 350°C scan.

VII.3.1. Structural Properties

To track changes in lattice parameters as a function of Sn substitution for Pb, 00*l* diffraction patterns for both the alloys and end members were collected, and are shown in Figure VII.2. Due to the layered nature of the compound, the films display a high level of texturing, with the c-axis normal to the substrate surface. All the diffraction maxima can be indexed as 00*l* reflections of the targeted alloyed superlattices, with no observable

impurity phases or phase segregation. Qualitatively, the peaks shift continuously as a function of x from one end member to the other, which is especially obvious at higher angles (Figure VII.2b). The c lattice parameters calculated from the patterns (Table VII.1, inset Figure VII.2b) vary linearly as a function of the measured global composition, following Vegard's law.[26] The (007) reflection shows the largest variation in intensity between the two end members and its normalized intensity varies systematically with composition, resulting from the change in scattering power of the rock salt cation as a function of x, also supporting the formation of the targeted solid solution in the $Pb_xSn_{1-x}Se$ constituent (Figure VII.2b).

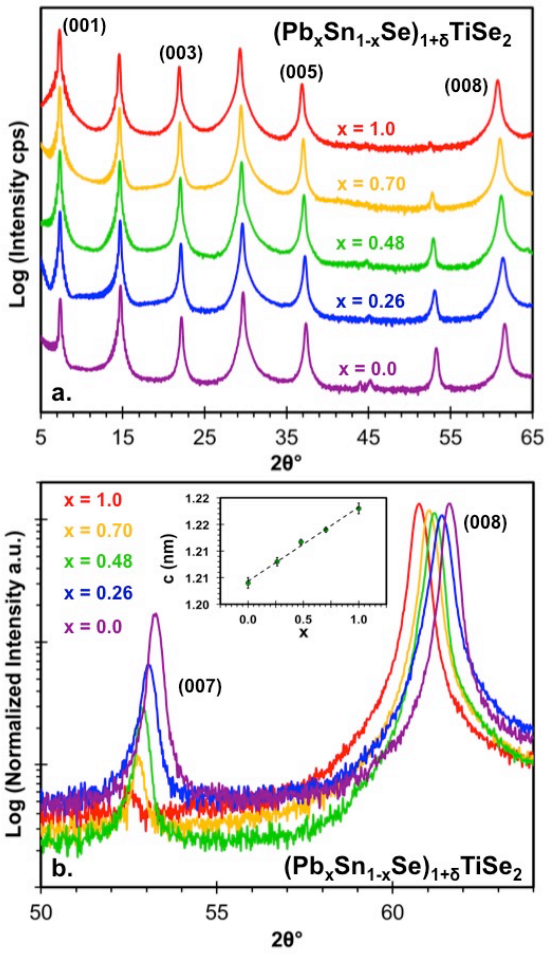

Figure VII.2: (a) The 00*l* diffraction pattern of the five $(Pb_xSn_{1-x}Se)_{1+\delta}TiSe_2$ compounds prepared in this investigation (offset for clarity), the peaks can be indexed to the superlattice (out-of-plane) structure. **(b)** A close up of the (007) and (008) reflections, showing the systematic shift in the position of the reflections and the systematic change in the intensity of the (007) reflection of the different compounds as x is varied. The inset shows the change in the lattice parameter as a function of composition.

Table VII.1: A summary of the measured composition and lattice parameter for the targeted $(Pb_xSn_{1-x}Se)_{1+\delta}TiSe_2$ compounds. The measured oxygen content partially results from the SiO_2 layer on the top of the substrate and is not used in calculating x.

Target Composition (x)	Fractional [O] Composition	Fractional [Se] Composition	Fractional [Ti] Composition	Fractional [Sn] Composition	Fractional [Pb] Composition	Measured Composition (x)	c-axis lattice parameter (nm)
1.0	0.04	0.59	0.18	0.00	0.19	1.00	1.218(1)
0.75	0.03	0.57	0.18	0.07	0.16	0.70	1.2140(5)
0.50	0.03	0.59	0.18	0.10	0.10	0.48	1.2117(5)
0.25	0.03	0.57	0.18	0.16	0.06	0.26	1.2080(8)
0.0	0.01	0.58	0.19	0.22	0.00	0.00	1.204(1)

The constituent structures can be characterized independently and the in-plane diffraction patterns of the compounds are shown in Figure VII.3a.[13-16,24,25] All of the reflections can be indexed as *hk*0 reflections from the expected constituent structures. For $TiSe_2$, the indexed reflections in Figure VII.3a are consistent with CdI_2 structure of bulk 1-T $TiSe_2$ and other $TiSe_2$-containing intergrowth compounds.[24,25,27-29,] The *a*-axis lattice parameters for the $TiSe_2$ constituent of the five compounds were calculated using a least squares fit and the space group *P-3m1*, (Table VII.2). The $TiSe_2$ lattice parameter does not systematically vary with composition changes in the rocksalt-like layer and is consistent with that measured for other $TiSe_2$ containing misfit compounds and is close to that of bulk $TiSe_2$, further supporting the targeted site-specific substitution.[24,25,27-29] The remaining peaks in the patterns could be indexed to a rocksalt-like structure as labeled in Figure VII.3a. The PbSe structure (x = 1) can be fit using a 2-D rocksalt structure (*p4gm*), with a square basal plane where a = b = 0.6125(2) nm. This agrees well with the lattice parameter reported previously.[24,27,28,29] The *hk*0 patterns for the SnSe structure (x = 0) shows a distortion from the square basal plane that can be fit using 2-D space group *p2gg*. This reduction in symmetry was not resolvable in the previously reported STEM data.[25] The reduced symmetry allows for the identification of all split reflections and yields an *a*-axis lattice parameter of 0.6094(3) nm and a *b*-axis lattice parameter of 0.5974(4) nm.

The intermediate compositions vary between the end members, with the lattice parameters decreasing and in-plane distortion increasing as a function of x (Figure VII.3b and Table VII.2). Both the a and b lattice parameters of the MSe constituent display Vegard's law behavior within error, and the in-plane area of the 2-D lattice along with the

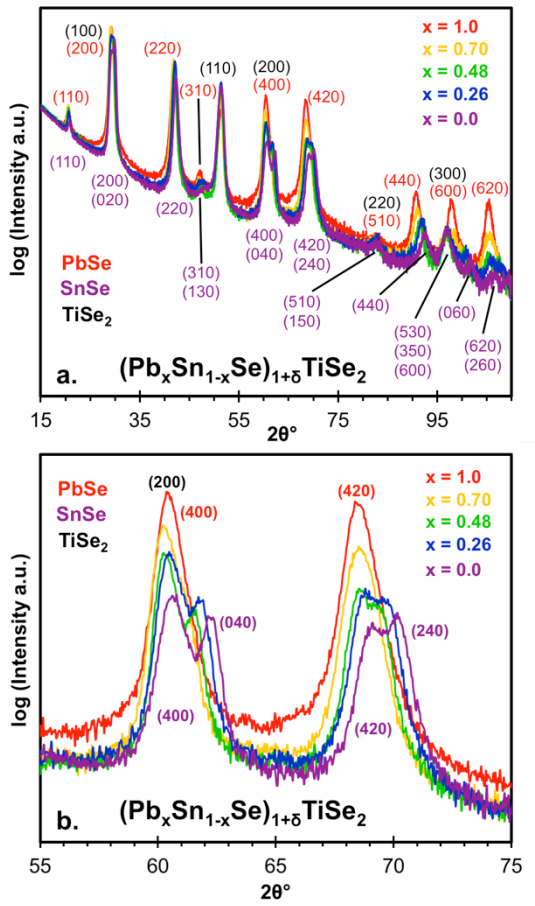

Figure VII.3: (a) In-plane diffraction patterns of the five $(Pb_xSn_{1-x}Se)_{1+\delta}TiSe_2$ compounds prepared in this investigation. All peaks can be indexed to *hk*0 reflections of the constituent structures. **(b)** A close up of two reflections that clearly show the rectangular in plane distortion of the rock salt constituent as it becomes more Sn rich.

resulting calculated misfit parameter (the difference in in-plane packing density that results from incommensurate constituent lattices, represented by the 1+δ ratio of constituent formula units) can be seen plotted in Figure VII.4 as a function of composition. The clear identification of all maxima observed in the patterns, the strong correlation between lattice parameter and measured global composition, and the lack of any impurity phases supports the conclusion drawn from the 00*l* diffraction that a $Pb_xSn_{1-x}Se$ solid solution of the rock salt constituent forms across the entire range of $0 \leq x \leq 1$. While the bulk $Pb_xSn_{1-x}Se$ solid solution has a miscibility gap such that the x = 0.26 and x = 0.48 compositions would be expected to disproportionate into Sn rich and Pb rich compounds, the kinetic approach used here provides a route to a single-phase metastable $Pb_xSn_{1-x}Se$ bilayer constituent. This solid solution behavior is perhaps not unexpected, as

the structure of the rock salt bilayers is significantly different from the bulk constituents.[30]

Table VII.2: In-plane lattice parameters for both constituents of $[(Pb_xSn_{1-x}Se)_{1+\delta}]TiSe_2$ and the calculated misfit parameter (1+δ).

x	$Pb_xSn_{1-x}Se$ *a* (nm)	$Pb_xSn_{1-x}Se$ *b* (nm)	$TiSe_2$ *a* (nm)	1+δ
1.0	0.6125(2)	0.6125(2)	0.3542(3)	1.158(3)
0.70	0.6116(8)	0.6073(7)	0.3550(4)	1.173(6)
0.48	0.6132(9)	0.6040(9)	0.3556(4)	1.183(6)
0.26	0.6110(9)	0.6010(9)	0.3547(6)	1.187(7)
0.0	0.6094(3)	0.5974(4)	0.3562(6)	1.207(5)

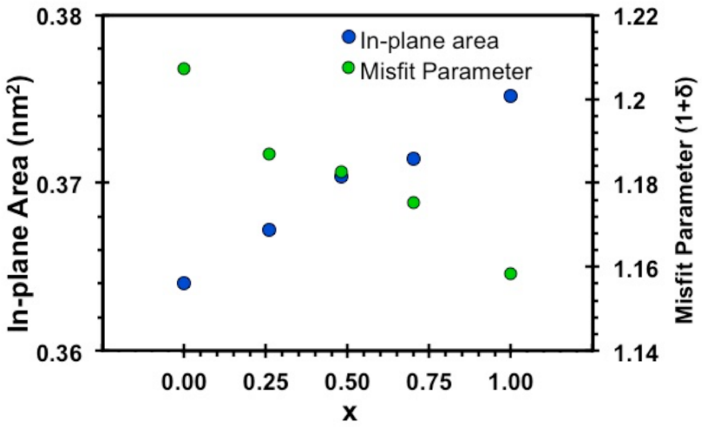

Figure VII.4: In-plane area of the $Pb_xSn_{1-x}Se$ constituent unit cell and the calculated misfit parameter, which results from the incommensurate constituent lattices. The error for both data sets is smaller than the markers for each point.

Additional evidence for the structure of the two constituents was obtained from HAADF-STEM data, with a representative example (x = 0.26) shown in Figure VII.5a. The image contains two constituent phases, with identifiable zone axes for a single phase rocksalt-like $Pb_xSn_{1-x}Se$ layer (brighter) and the octahedrally-coordinated CdI_2 structure expected for $TiSe_2$ (darker), consistent with the published parent compounds and the fits used in the *hk*0 diffraction data above. Turbostratic disorder is also observed, as is common in the kinetically stabilized class of compounds, synthesized from modulated elemental reactants.[13-16,24,25,29] EDX spectra images were also collected to qualitatively confirm the formation of the targeted constituents, and a map of the same representative

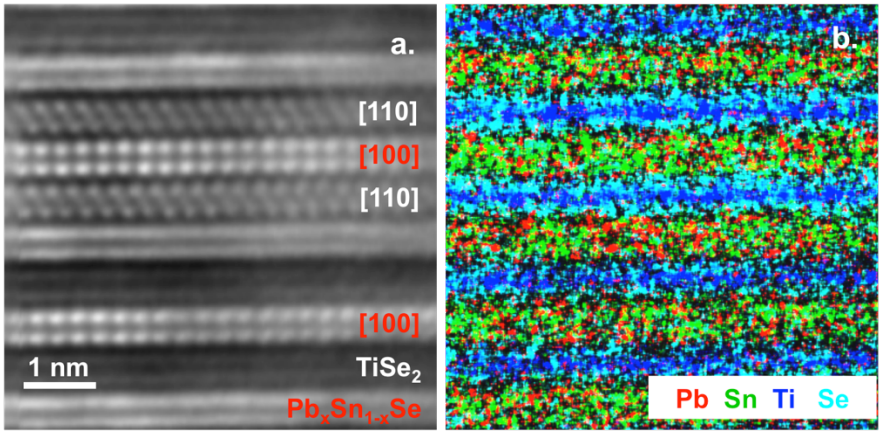

Figure VII.5: (a) HAADF-STEM data of a representative region (x = 0.26) showing superlattice structure. Visible zone axes are labeled for each constituent and **(b)** the corresponding EDX map, with Se-Ti-Se trilayers clearly visible.

region is shown in Figure VII.5b. The Spectra confirm the presence of Pb, Sn, and Se in the MX layer identified by STEM, further supporting the formation of a solid solution. The repeating unit is clearly resolved, and in some regions, the individual Se and Ti layers in the Se-Ti-Se trilayers expected for $TiSe_2$ can be seen. Spectra were integrated along the a-b plane to give intensity profiles in the c direction to assess the variation in relative local compositions with alloying. A representative sample area and the resulting profiles for the three alloy compounds are shown in Figure VII.6, with Se removed for clarity. The systematic variations in intensities for each elemental signal correspond quite well with the expectations from the EPMA and XRD results across the compositional series. In some cases the bilayer of the MX structure can even be resolved, providing further support for the presence of bilayers of a $Pb_xSn_{1-x}Se$ alloy separated by $TiSe_2$ trilayers.

VII.3.2. Electrical Transport Properties

Electrical transport measurements in the in-plane direction were conducted to understand the effect of the targeted substitution on the electronic structure of the compounds. The temperature dependent resistivity data for the mixed cation compounds can be seen in Figure VII.7 along with that previously published for the two end-members.[24,25] The magnitude of the resistivity is that of a poor metal and surprisingly the lowest resistivity was found for the tin-rich alloys. The magnitudes are similar to those reported previously for other $PbSe-TiSe_2$ and $SnSe-TiSe_2$ containing layered compounds

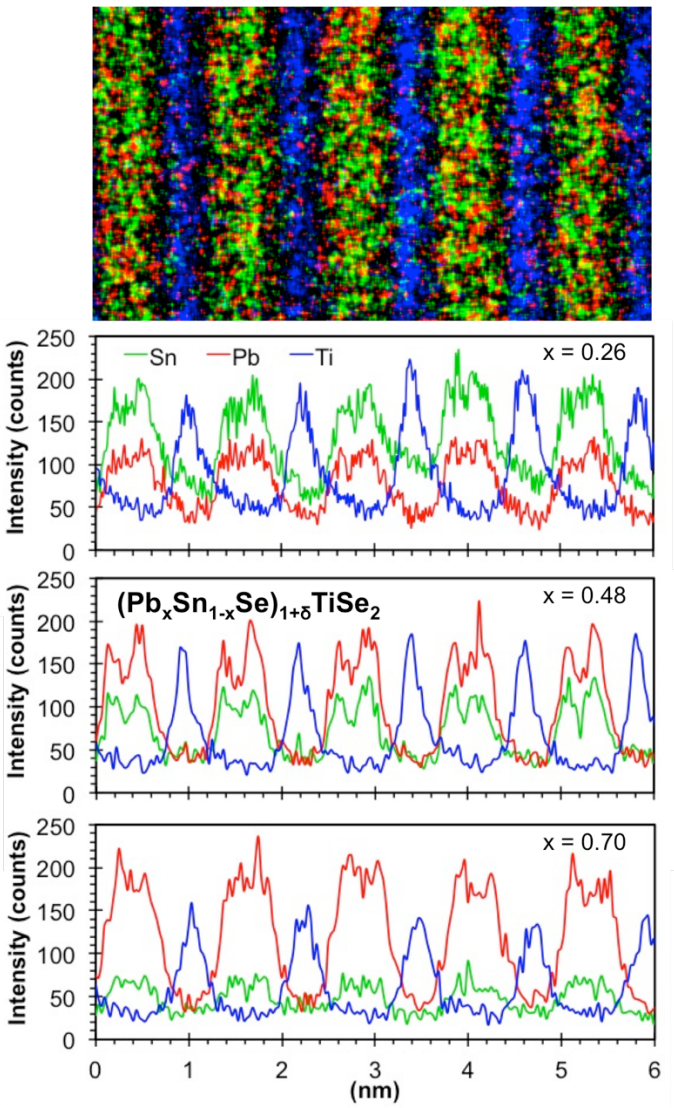

Figure VII.6: top - EDX map for the x = 0.70 sample with the Se signal removed for clarity. The bottom three graphs provide integrated intensity profiles for the three alloy compounds. Pixel resolution varies depending on the magnification used for the profile, but the compositionally distinct layers are clearly resolved for all three samples.

in the literature.[24,25,28,29] Given the isovalent nature of the substitution, and the variation seen in the Sn end member shown in Figure VII.7, the magnitudes measured on the compounds reported here likely fall within the reproducibility of samples. The very small temperature dependence of the intermediate compounds is very similar to that found for the parent compounds, suggesting a weak electron-phonon interaction. The presence of turbostratic disorder and the subsequent lack of phonons with a cross-plane component has been suggested as a cause of the small electron-phonon coupling.[25,29]

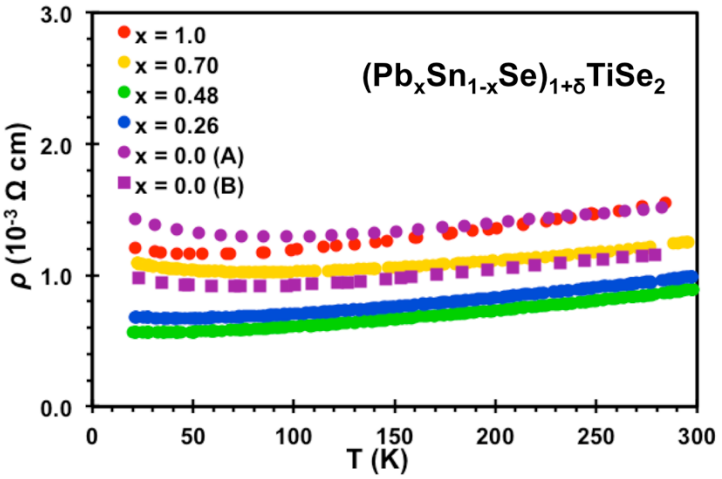

Figure VII.7: Temperature dependent resistivity. The magnitudes of the resistivity for all compounds fall within the range expected from sample to sample variation. The (A) and (B) labels for the two x = 0 data sets refer to two separate preparations of nominally the same sample, as previously reported.[25]

The Hall coefficient (R_H) was measured to be negative for all compounds, as reported for the parent compounds and other TiX_2 based misfit type compounds,[24,25,28,29,31,32] suggesting electrons are the majority carrier. Carrier concentration was calculated for each of the compounds assuming a single band model (Figure VII.8). The number of carriers calculated from R_H for the misfit type compounds here and in prior reports is far greater than those reported for bulk TiX_2 compounds, which has been attributed to charge transfer between constituents.[24,25,28,29,31,32] The carrier concentrations decrease linearly with decreasing temperature, which could be a result of carrier localization or a consequence of assuming a single band model. The calculated carrier concentration decreases with increasing Pb content and hence with decreasing misfit parameter. The trend in the carrier concentration is consistent with charge transfer from the rock salt layer to the $TiSe_2$, the magnitude of which would be expected to scale with the misfit parameter and the resulting change in stoichiometry between the two constituents. The spread of the values for the two $SnSe_{1.21}TiSe_2$ compounds prepared during different deposition runs indicate that the trend is at the limit of our resolution, given the sample to sample variation.[25] This lack of a strong variation in the carrier concentration as a function of x is not surprising considering the isovalent substitution of Pb for Sn.

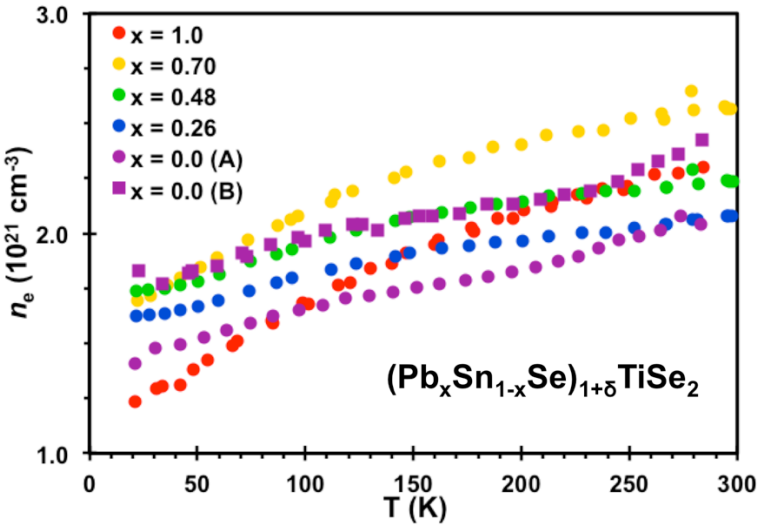

Figure VII.8: Carrier concentration calculated from the Hall coefficient, assuming a single band model.

From the carrier concentration and resistivity, the Hall mobility was calculated for the different samples and displayed in Figure VII.9. The highest mobility is found for the Sn rich alloys. In general, the mobility of charge carriers is influenced by defects, the presence of the interface between the constituents and by electron/phonon interactions cause by atomic displacement in the lattice due to thermal vibrations. At low temperatures, the density of impurities and defects determines the mean free path of charge carriers, and therefore mobility. Previously prepared solid solutions of both SnSe and PbSe material systems have shown decreased mobility, as expected, because the disorder present in the solid solution reduces the mean free path.[33,34] In the compounds presented here, the disorder in the rock salt layer would be expected to significantly decrease Hall mobility if the free carriers are conducting through states in the $Pb_xSn_{1-x}Se$ layer. However, the magnitude of the mobility is equal or greater than the end members, suggesting that little charge transport occurs through the $Pb_xSn_{1-x}Se$ constituent. This mobility data provides direct evidence that electrons in the $TiSe_2$ constituent are responsible for conduction, supporting the general assumption that the dichalcogenide constituent dominates the electrical transport in misfit layer compounds.[11,17-19] We speculate that the increase in mobility for the alloys might result from preferential site occupancy by Sn and Pb, which could reduce interfacial scattering. This would imply

surface segregation might occur in compounds with thicker, alloyed layers of the rock salt constituent.

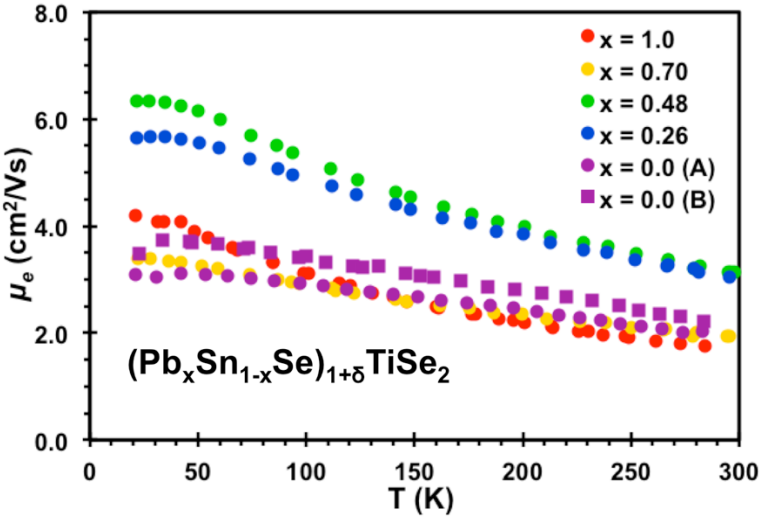

Figure VII.9: Hall mobility calculated from resistivity and carrier concentration. The magnitude of the mobility either remains constant or increases for the mixed cation compounds, providing the first direct evidence for the conduction mechanism in the compounds.

VII.4. Conclusions

$(Pb_xSn_{1-x}Se)_{1+\delta}TiSe_2$ compounds were successfully synthesized from modulated elemental reactants over the entire range of $0 \leq x \leq 1$, demonstrating that controlled substitution of the rocksalt cation site in a misfit layer compound is possible. The superlattice and constituent lattice parameters vary according to Vegard's law, supporting the formation of a solid solution. HAADF-STEM and EDX also support the conclusions drawn from the X-ray diffraction data. The mobility of the intermediate compounds is equal or greater than that of the end members, providing direct evidence that conduction of electrons in the $TiSe_2$ constituent is the mechanism of conduction in this family of compounds. If the appropriate substitutions can be identified, it may be possible to tune the Fermi energy in the MX layer to control charge transfer, carrier concentration and the subsequent properties of the material, without negatively impacting carrier mobility in the TX_2 structural unit. Such a modulation doping approach in a nanoscale composite material could provide a method for optimizing contradictory single-phase properties in complex materials applications, such as thermoelectric devices. More broadly, the ability to prepare complex materials with site-specific substitutions at lower reaction

temperatures suggests that the use of designed precursors that target specific local compositions could enable more efficient doping of semiconducting compounds.

VII.5. Bridge

The formation of a solid solution across the entire range of x in this chapter is somewhat surprising, as a miscibility gap is expected at intermediate concentrations. It suggests that new phases may be synthesized as intergrowth materials via the MER technique. It also suggests that the inclusion of an atom of different valencies may be possible, in which case modulation doping should occur. This chapter provides a platform for the following discussion of the Bi-Sn alloyed constituent, and the demonstration of modulation doping this class of compounds.

CHAPTER VIII
MODULATION DOPING IN METASTABLE CHALCOGENIDE HETEROSTRUCTURES VIA KINETICALLY-CONTROLLED SUBSTITUTION

This work is being prepared for publication, with coauthors Suzannah R. Wood, Alex Lygo, Jeffrey Ditto, and David C. Johnson. Suzannah R. Wood is providing minor assistance with sample synthesis as well as assistance with structural characterization, Alex Lygo is assisting with sample characterization, Duncan Sutherland provided electron microprobe analysis, Jeffrey Ditto is providing electron microscopy data, David C. Johnson is my advisor and research group leader, and I am the primary author.

VIII.1. Introduction

Chemical substitution has been a fundamental approach to affecting transport properties in compounds, yet these substitutions often result in ionized scattering and therefore a reduction in carrier mobility. Modulation doping, charge transfer between regions within a structure, has been demonstrated as a means to circumvent this detrimental effect, with improved mobility along semiconductor interfaces due to charge transfer from the non-conducting phase and the absence of dopant atoms in the conducting phase.[1,2] This approach has been suggested as a means of improving the thermoelectric figure of merit (zT) by increasing the conductivity in the material without significantly affecting the other contradictory properties and has been demonstrated in bulk composite[3,4] materials and superlattices.[5,6] The resulting composite materials display increased power factors ($S^2\sigma$), and are able to maintain low thermal conductivities thanks to the presence of interfaces between phases, which effectively scatter phonons.

Misfit layer compounds are an interesting class of thermodynamic layered compounds which represent an extreme case of a composite structure with two different structures that often do not lattice match in either one or two directions .[7–9] Early reports of these compounds suggest that compounds based on TiS_2[10] and NbS_2[11] may be interesting for thermoelectric materials, with more recent work showing zT values of 0.4 for reported for the unoptimized $(SnS)_{1.20}(TiS_2)_2$ compound.[12] The synthetic challenges associated with preparing and characterizing these materials make optimization difficult, and the ability to design nanoarchitecture via traditional solid state and vapor transport

reactions is limited. Recently metastable variants of these compounds have been prepared using amorphous layered precursors and low formation temperatures to nucleate the targeted superstructure with a variety of layering schemes.[13–15] Compounds synthesized via this route in the $(PbSe)_{1+\delta}(TiSe_2)_n$ family with high n values have promising $S^2\sigma$ values, suggesting the compounds in this family may be promising thermoelectric materials.[16] A family of $(Pb_xSn_{1-x}Se)_{1+\delta}TiSe_2$ compounds was synthesized, showing that the modulated elemental reactant synthesis technique is capable of making kinetically controlled site-specific substitutions. This suggests another route for affecting transport properties in these materials.[17]

Here we report the synthesis, structure and transport properties of compounds within the $(Bi_xSn_{1-x}Se)_{1+\delta}TiSe_2$ family. The end member compounds have different structures, with SnSe adopting a distorted rock salt structure and BiSe having a structure that has been described as a distorted rock salt structure with periodic antiphase boundaries to create a larger in-plane unit cell. The compound at x = 0.5, while forming the expected periodic structure along the c-axis, has in-plane diffraction data that is consistent with two distinct MX structures. The domain structure between these two MX structures is not known. All the samples are metallic, with resistivity values ~ 10^{-5} Ω m and very slight systematic changes in resistivity with temperature. The carrier concentration calculated from the Hall coefficient suggests that carriers can be added through the targeted substitution with minimal affect on mobility, but the change in transport properties as a function of Bi content is not linear, and suggests the doping efficiency of Bi drops as x increases. The drop in doping efficiency with increasing Bi content is likely due to an increase in the density of antiphase boundaries with Bi-Bi bonds that localize electrons.

VIII.2. Experimental

Precursor films were deposited using a designed physical vapor deposition system, at pressures below 5 x 10^{-7} Torr. The sources are isolated from one another by a baffle system designed to simultaneously deposit four sources, and the substrate via shutters sitting above a hole in the baffle architecture. The elemental layers were deposited in a Ti-Se-Bi-Sn-Se sequence using a PC-controlled labview program to control shutter delays to deliver calibrated thicknesses. Se was deposited using an effusion cell, while Bi, Sn, and Ti were deposited using electron beam guns, with rates were maintained at 0.1-

0.3 Å/s and monitored using quartz crystal microbalances. Films were deposited on <100> Si for structural characterization and fused silica for electrical measurements. Annealing was conducted in a N_2 environment ($[O_2,H_2O] \leq 0.8$ ppm), at the specified temperatures for 30 minute duration.

X-ray diffraction (XRD) experiments were conducting in both locked couple and in-plane geometries using a Bruker D8 Discover and Rigaku SmartLab diffractometer, respectively (Cu Kα radiation). Electron microprobe analysis experiments (EPMA) were performed using a Cameca SX50, equipped with 4 spectrometers, using a method described elsewhere.[18] Transport measurements were conducted using the van der Paaw method on a lab-built low temperature system. Fused silica substrates were masked during deposition to provide a cross geometry for the measurement. Electrical measurements were made using pressed indium contacts and and a custom built low-temperature system. Hall effect measurements were made with magnetic field varying from 0 – 16 kG.

VIII.3. Results and Discussion

The synthetic approach used to prepare the compounds requires calibration of the precursors to achieve the composition and similar structural unit to the target superstructure. In this case, the parent systems were calibrated separately, and the alloys synthesized by scaling the MX deposition parameters to match the targeted x value. Elemental layers were then adjusted slightly based on measured thickness and composition via XRR and EPMA, respectively. The two end members and three alloy precursors were synthesized and their as-deposited compositions are summarized in Table VIII.1. The measured rocksalt cation compositions match closely with the targeted values.

An annealing study was carried out on the x = 0.48 sample assuming it would be most representative of the alloyed compounds, and the resulting 00l diffraction patterns can be seen in Figure VIII.1. The as-deposited precursor displays the reflections resulting from the repeating electron density in the precursor, suggesting the precursor is uniformly layered throughout the film. As the annealing temperature is increased, reflections consistent with the targeted superstructure narrow and intensify, consistent with the formation of the designed compound. At 350°C, the reflections are most intense and

display the minimum full width at half maximum. Above 350°C, the reflections of the targeted superstructure are broader, less intense, and accompanied by the growth of maxima from impurity phases, most notably Bi_2Se_3. 350°C was therefore established as the optimum formation temperature of the compounds and was used for the remaining samples in this study.

Table VIII.1: Precursor composition and resulting annealed lattice parameters for the $[(BiSnSe)_{1+\delta}]TiSe_2$ compounds. the space group used to obtain the in-plane lattice parameters is also given.

Targeted x	Bi (at. %)	Sn (at. %)	Ti (at. %)	Se (at. %)	O (at. %)	Measured x	MX space group	MX a	MX b	$TiSe_2$ a	Misfit Paramter	C-lattice paramter (nm)
0.0	0	22	18	59	4	0.0	*p2gg*	0.6094(3)	0.5974(4)	0.356(1)	1.21	1.204(1)
0.25	5	17	19	57	1	0.24	*p2gg*	0.6146(3)	0.6006(3)	0.356(2)	1.19	1.195 (1)
0.5	11	12	19	56	3	0.48	*p2gg*	0.6153(3)	0.5990(3)	0.356(1)	1.19	1.188(1)
0.75	16	6	20	56	2	0.71	*Pcmn*	0.449(1)	0.426(1)	0.358(1)	1.16	1.185(1)
1.0	19	0	18	59	4	1.0	*Pcmn*	0.4562(2)	0.4242(1)	0.358(6)	1.15	1.177(1)

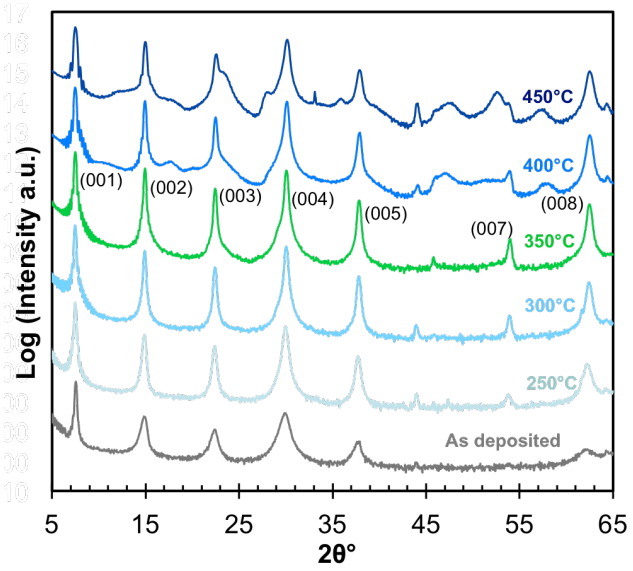

Figure VIII.1: Locked couple diffraction patterns for the x = 0.48 compound, as a function of annealing temperature (offset for clarity).

VIII.3.1. Structural Characterization

The 00l diffraction for the three intermediate compositions and the parent compounds are shown in Figure VIII.2. Each of the patterns can be indexed to the superstructure with no discernible impurity phases present. Figure VIII.2 also shows the (007) and (008) reflections, highlighting the systematic shift in lattice parameter as Bi replaces Sn. The c-

lattice parameter varies linearly with composition of the as-deposited precursor between the end members as expected from Vegard's law, changing from 1.177 nm for the Bi compound to 1.204 nm for the Sn compound. The systematic decay of the (007) peak's relative intensity as a function of x also suggests that the composition of the ferecrystal structure is changing as the targeted substitution is increased.

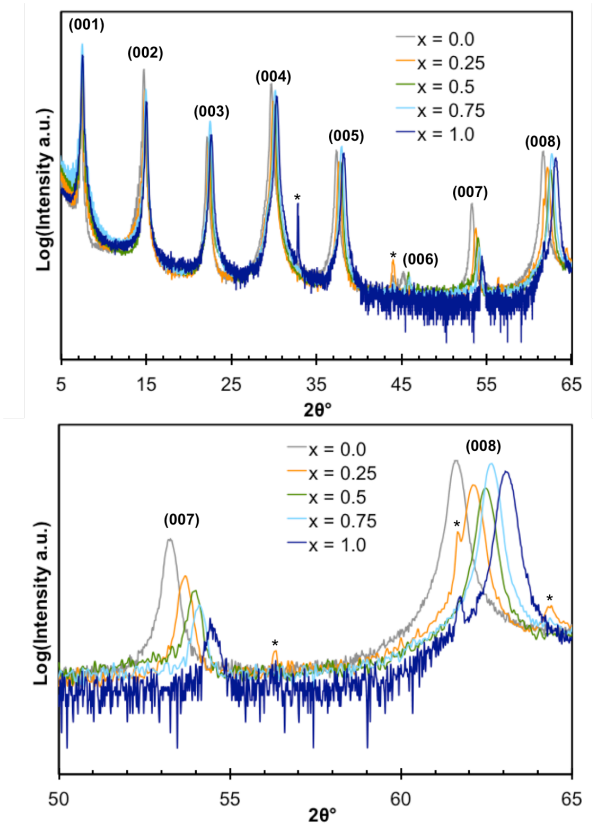

Figure VIII.2: (top) Overlay of the 00*l* diffraction patterns of the title compounds over the entire range of x and **(bottom)** zoomed in higher angle region, clearly showing the change in lattice parameter and superlattice composition through relative intensities as a function of x.

In-plane x-ray diffraction scans were collected to understand the evolution of the structure of the individual constituents and can be seen in Figure VIII.3. Lattice parameters were calculated from a least squares method and are summarized in Table VIII.1. The x = 1 sample's reflections can be indexed as $TiSe_2$ and BiSe.[19] The x = 0 sample's reflections can be indexed as $TiSe_2$ and SnSe.[17] The intermediate compositions displaying lattice parameters intermediate between the parent structures, with small x values consistent with adding Bi to the SnSe structure and large x values consistent with

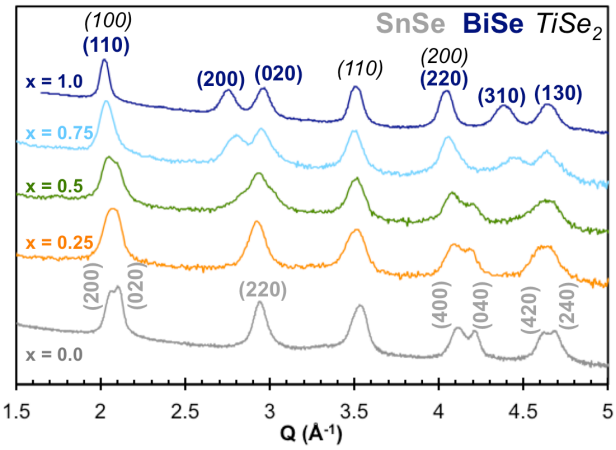

Figure VIII.3: In-plane diffraction parameters as a function of x (offset for clarity).

adding Sn to the BiSe structure. The x=0.5 sample is more complicated with evidence that regions of both the SnSe and BiSe structures might be present, with the SnSe reflections more intense as discussed further below. The $TiSe_2$ reflections remain consistent throughout the family of compounds In-plane parameters vary slightly from 0.356(1)-0.358(1) nm which is consistent with previous reports of $TiSe_2$ based metastable intergrowths[20] and the close to that reported for the bulk compound.[21]

The other reflections can be assigned to the two space groups expected from the SnSe and BiSe structures previously reported. SnSe parent was fit to 2-D space group *p2gg* with a = 0.6094(3) nm and b = 0.5974(3) nm.[17] The BiSe parent was fit using the space group *Pcmn* with a = 0.4562(2) nm and b = 0.4242(1) nm.[19] The targeted alloy compounds show structures intermediate between the end members, with the $x < 0.5$ displaying symmetry consistent with the SnSe consituent, and $x > 0.5$ consistent with that of BiSe. The calculated misfit parameter using the symmetry of the SnSe end member deviates strongly from the expected packing density, and away from Vegard's law as the structure changes to that of the BiSe end member. This behavior is different than observed in the $(Pb_xSn_{1-x}Se)_{1+\delta}TiSe_2$ alloys previously reported.[17] The x = 0.48 sample displays a broad background around the (220) SnSe reflection, as well as a shifting and broadening of the (420) and (240) peaks, suggesting the both symmetry types are present, with no observed disruption in the superstructure.

VIII.3.2. Electrical Transport Properties

Figure VIII.4 contains the measured resistivity as a function of temperature for the alloys, and the parent compounds.[19,22] The temperature dependence of the alloyed compounds is similar in behavior to the parents, and other materials synthesized from modulated elemental reactants. The small temperature dependence has been attributed to the turbostratic disorder observed between the layers, which decreases electron-phonon interactions at higher temperatures. The compounds trend as a function of Bi content as expected from the parent compounds, showing a systematic decrease in resistivity as the Bi content is increased. The upturn observed at low T has been attributed with weak localizations, and increases as a function of the magnitude of the resistivity, consistent with previous reports.[22,23]

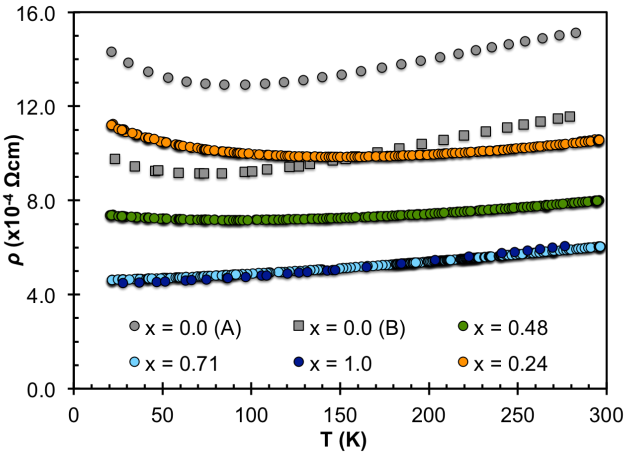

Figure VIII.4: In-plane resistivity as a function of temperature. The parent compounds are also given.[19,20]

The measured Hall voltage was negative indicating that electrons are the majority carriers, as seen in the previously reported TiX_2 based MLCs and ferecrystals.[12,16,17,24–26] Carrier concentration was calculated from the Hall coefficient assuming a single Ti 3d band in $TiSe_2$ was responsible for conduction, and can be seen along with the parents in Figure VIII.5. For compounds to date, this simplistic picture has successfully described the transport behavior of the materials. The compounds show marked increase in carrier concentration as Bi is added to the structure. Figure VIII.6 shows the number of carrier per rocksalt cation in the structure, as well as the calculated number of electrons added per Bi atom, by subtracting the number of electrons expected from the Sn structure, and

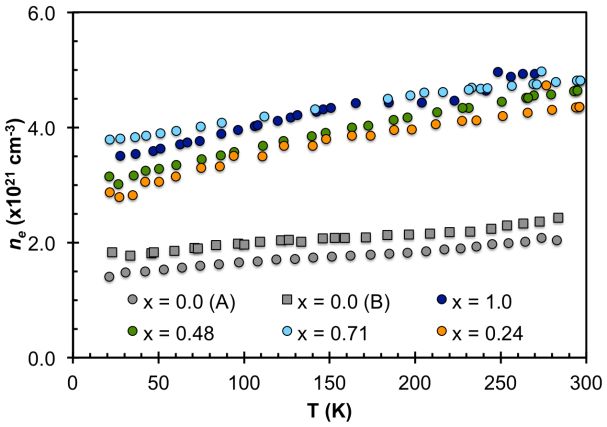

Figure VIII.5: Carrier concentration calculated from the Hall coefficient assuming a single band model.

normalizing the additional carriers to the concentration of Bi in the rocksalt cation site. It is clear from the hall data that the doping efficiency of the Bi atoms is changing as Bi content increases. We hypothesize this could be due in part to the complex structure reported for BiSe in MLCs,[8] where Bi-Bi bonds exist to partially stabilize the additional valence electron in the structure. In such a case, the increasing number of Bi-Bi bonds as a function of Bi concentration would be expected to decrease the doping efficiency of the Bi cations, which is consistent with the Hall effect data.

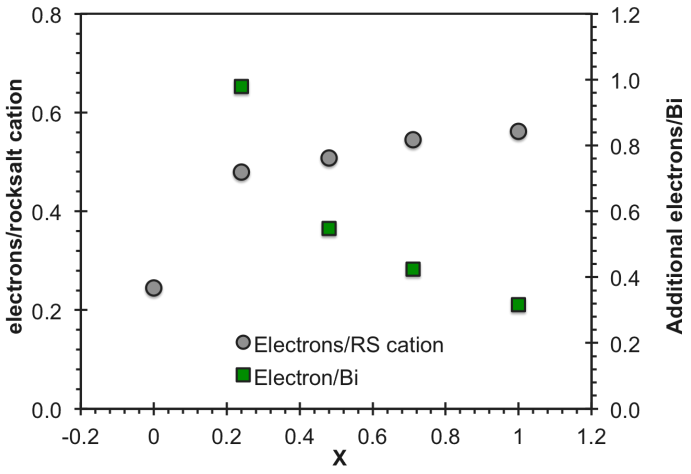

Figure VIII.6: The number of conducting electrons per rocksalt cation in the structure, and the number of additional electrons added to the conduction band from Bi.

The Hall mobility was calculated from the resistivity and carrier concentration and can be seen in Figure VIII.7. The mobility of the alloys increases with the Bi content. Surprisingly, the x = 0.24 and x = 0.48 compounds show lower mobility than the x = 0.71

compound, and the end members. The decrease observed in mobility is relatively small, considering the number of scattering sites incorporated by making substitutions on this scale, considering mobility can vary by an order of magnitude or more in bulk materials between the pure and alloyed compounds such as Si and GaAs are over an order of magnitude decrease for 10^{19} cm^{-3} carriers compared to 10^{15} cm^{-3} carriers.[27] Still, the decrease in mobility for high Sn content suggests that the substitution in the MX layer is affecting the mean free path of carriers, which is unexpected from the previously published reports for TiX_2 based materials.

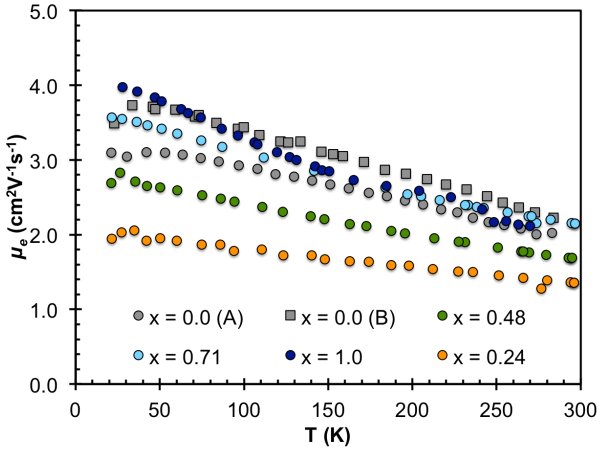

Figure VIII.7: The Hall mobility calculated from the resistivity and carrier concentration for the end members and intermediate compositions.

VIII.4. Conclusions

Superstructures can be formed over the entire range of x, with intermediate alloy concentrations resulting in a mix of grain symmetry in the $Bi_xSn_{1-x}Se$ layer. The resulting transport properties suggest that Bi cations provide extra charge carriers, as expected from the parent compounds. The observed properties confirm that modulation doping via controlled site-specific substitutions can be a useful mechanism for affecting materials properties in a manner not achievable through high temperature routes. The doping efficiency clearly changes as the Bi content increases, which would be expected as more Bi-Bi bonds reported for the BiS and BiSe based misfit layer compounds could be formed. The Hall mobility data suggests that there is more constituent interaction than previously hypothesized.

VIII.5. Bridge

The demonstration of modulation doping in metastable heterostructures provides a platform for further optimization of materials properties. It also highlights how little we know about the constituent interaction in the materials. It inspired the question as to other synthetic possibilities, and lead to attempts to synthesize 3 constituent heterostructures, reported in the following chapter.

CHAPTER IX

THE SYNTHESIS OF MULTI-CONSTITUENT HETEROSTRUCTURES FROM DESIGNED AMORPHOUS PRECURSORS

This work is in final preparation to be submitted to *Angewandte Chemie International Edition* with coauthors Duncan R. Sutherland, Jeffrey Ditto, Daniel B. Moore, Matthias Falmbigl, Douglas L. Medlin, and David C. Johnson. Duncan R. Sutherland assisted in sample synthesis, as well as structural and compositional analysis, Jeffrey Ditto and Douglas L. Medlin provided electron microscopy data and analysis, Daniel B. Moore assisted with sample synthesis, Matthias Falmbigl provided Rietveld and le Bail analyses, David C. Johnson is my advisor and research group leader, and I am the primary author.

IX.1. Introduction and Discussion

The number of unique properties discovered in single layer materials like graphene[1] and other 2-dimensional systems such as transition metal dichalcogenides have increased tremendously in the last decade,[2-4] and the opportunity to design and control properties via the stacking of 2-D layers in heterostructures has further increased the interest in this field.[5] The ability to predict the structure of multiple constituent heterostructures has enabled theorists to predict combinations of constituents with enhanced properties relative to those of the bulk constituents or isolated individual 2-D layer.[6] It has been proposed that graphene monolayers separated by high k dielectric materials might result in new materials with high superconducting critical temperatures, similar to the behavior observed between loosely coupled planes in copper oxide superconducting materials.[5,7,8] Novel optical properties in heterostructures of TX_2 compounds where T = Mo and W and X = S and Se have been predicted,[9] and the observed variation in electronic structure based on the number of adjacent TX_2 layers suggests further opportunity for material design.[2,6,10] There have also been a limited number of experimental demonstrations of enhanced properties of complex structures built from 2-D materials. Intercalation of atomic or molecular species has been used to adjust properties, such as superconductivity in Ca intercalated graphene,[11] and increased T_c in superconducting TaS_2.[12] Tuning both constituents and the interaction between constituents show promise for engineering properties tuned for specific applications.[5,13]

Synthetic challenges have prevented the broader exploration of higher order heterostructures. Approaches to large area films of single constituent 2-D materials are being developed using a variety of techniques, for example the recent work on the synthesis of 2-D MoS_2,[14] but it is generally not possible to use them sequentially to prepare heterostructures containing chemically different 2-D materials.[5] Therefore the most common approach to preparing heterostructures involves the cleaving of monolayers from bulk crystals or films with adhesive tape. The individual layers are then sequentially stacked together to form a heterostructure. This is a challenging approach, which requires layers to be individually manipulated. Only a few groups have developed the necessary expertise to successfully prepare multiconstituent films. Without pristine starting materials and formation conditions, the integrity of the film and its properties may also be compromised. The stability of the isolated 2-D constituents prepared by cleaving also presents challenges, as recently highlighted Geim et al.[5] New approaches are needed to enable the preparation of heterostructures containing layers that may not be stable on their own and that can be used to prepare homogenous multiconstituent 2-D structures over a large area.

Here we show that a kinetic approach for the synthesis of heterostructures enables the preparation of 3 constituent heterostructures in the $[(PbSe)_{1+\delta}]_m(TiSe_2)_n[(SnSe_2)_{1+\gamma}]_m(TiSe_2)_n$ family of compounds with a variety of m and n values by controlling the local composition and nanoarchitecture of designed amorphous precursors. To our knowledge, this is the first reported heterostructure containing $SnSe_2$ and among the first three-constituent heterostructures to be reported. Although structurally analogous to the thermodynamically stable misfit layer chalcogenide compounds[15] and the closely related tubular superstructures[16] including SnS-SnS_2 reported by Radovsky, et al,[17] the turbostratically-disordered products reported here consist of crystallographically independent layers with different constituent structures. The synthesis approach used enables sequences, layer thicknesses and combinations of structures to be prepared that cannot be synthesized using other techniques.[18,19]

The samples were prepared by depositing elemental layers in sequences resembling the structure of the desired products, for example a Pb-Se-Ti-Se-Sn-Se-Ti-Se sequence was used as a precursor for $[(PbSe)_{1+\delta}]_m(TiSe_2)_n[(SnSe_2)_{1+\gamma}]_m(TiSe_2)_n$. Individual

elemental layer thicknesses were adjusted based on composition data from electron probe microanalysis[20] and the repeat unit thickness determined from X-ray reflectivity to contain the correct number of atoms for the targeted constituent. The precursors were intentionally deposited with ~5% excess Se to compensate for losses during annealing.[21,22] An annealing study was conducted and 275°C was established as the optimal temperature for formation. This temperature is lower than previously reported for $[(MSe)_{1+\delta}]_m(TiSe_2)_n$ compounds (M=Sn or Pb), or alloyed $[(Sn_{1-x}Pb_xSe)_{1+\delta}]_m(TiSe_2)_n$ compounds.[21-24] Extended annealing above 275°C results in selenium loss and interdiffusion of the Sn and Pb layers to form the random alloy $[(Sn_{1-x}Pb_xSe)_{1+\delta}]_m(TiSe_2)_n$.[22]

Figure IX.1 contains the diffraction patterns resulting from annealing different precursors at 275°C for 15 minutes. All the diffraction maxima can be indexed as (00*l*) reflections indicating that the compounds are crystallographically aligned with their c-axis perpendicular to the substrate. The *c*-axis lattice parameters and in-plane lattice parameters for each of the constituents in the compounds derived from the data in Figure IX.1 are summarized in Table IX.1. The systematic changes in the *c*-axis lattice parameter as a function of *m* and *n* enable us to calculate the average thickness of the constituent layers. The thickness of a $TiSe_2$ layer was calculated to be 0.613 nm, which is larger than the thickness of the repeating Se-Ti-Se layer found in bulk $TiSe_2$ (0.6008 nm),[25] and the thickness of $TiSe_2$ layers found in ferecrystals (0.603 nm).[26] The sum of the thicknesses of the $SnSe_2$ and PbSe layers is 1.217 nm which is slightly lower than the sum of the bulk *c*-axis lattice parameters reported in the literature for $SnSe_2$ and PbSe (1.226 nm).[27,28] A structural model inferred from the changes in c-axis lattice parameter and the HAADF STEM data discussed below containing layers with thicknesses given by the m and n values reproduce the observed intensity patterns in the 00*l* diffraction patterns.

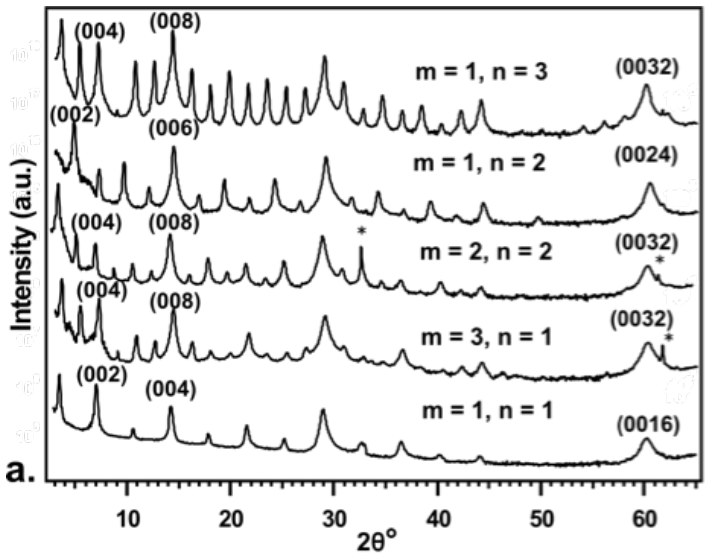

Figure IX.1: Out-of-plane (00*l*) diffraction patterns for compounds with different layering schemes. Indices are shown in parentheses above for selected reflections.

Table IX.1: Lattice Parameters obtained from the in and out of plane diffraction measurements.

m	n	Superstructure *c*-lattice parameter (nm)	PbSe *a*-axis lattice parameter (nm)	$TiSe_2$ *a*-axis lattice parameter (nm)	$SnSe_2$ *a*-axis lattice parameter (nm)
1	3	4.91 (1)	0.6115 (4)	0.357 (1)	0.377 (1)
1	2	3.66 (1)	0.607 (3)	0.353 (2)	0.374 (2)
2	2	4.87 (2)	0.606 (3)	0.354 (2)	0.376 (3)
3	1	4.90 (2)	0.6119 (2)	0.354 (1)	0.380 (1)
1	1	2.46 (1)	0.607 (2)	0.353 (3)	0.376 (1)

Diffraction experiments using in-plane geometry were collected to characterize the independent crystal lattices of the constituent materials, and the resulting patterns of three of the compounds are contained in Figure IX.2. Due to the textured nature of the film, only *hk*0 reflections of the independent constituent structures are present in the patterns. The lattice parameters calculated for the PbSe, $SnSe_2$ and $TiSe_2$ constituents (Table IX.1) are consistent with previously reported compounds, and display no clear trends as a function of the layering scheme. The PbSe constituent can be indexed using the 2-D rocksalt structure (*p*4*gm*), resulting in an *a*-axis lattice parameter ranging between 0.606(3) - 0.612(1) nm. This in-plane lattice parameter is slightly smaller than those reported for PbSe containing misfit compounds (0.614-0.620 nm) and agrees with

previously reported PbSe containing ferecrystals (0.603-0.618 nm).[29] $TiSe_2$ reflections can be fit using the CdI_2 structure (*P*-3*m*1) with an *a*-axis lattice parameter that varies between 0.353(3) nm and 0.357(1) nm for the heterostructures shown in Figure IX.1, also consistent with previous reports of ferecrystals (0.354-0.356 nm) containing $TiSe_2$ layers.[21-24,26] The remaining reflections can be indexed to a hexagonal CdI_2 structure (*P*-3*m*1) with the calculated *a*-axis lattice parameter varying between 0.374(2) nm and 0.380(1) nm for the heterostructures shown in Figure IX.2. These in-plane lattice parameters are close to the reported *a*-axis lattice parameter of bulk $SnSe_2$ of 3.81(1) nm.[27] The in-plane diffraction data suggests that the Sn constituent layer is predominately in the diselenide phase.

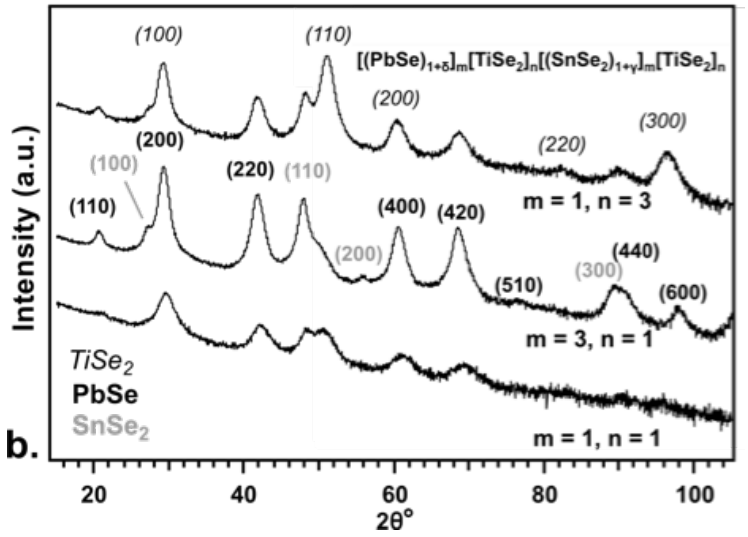

Figure IX.2: In-plane (*hk*0) diffraction patterns for compounds with different layering schemes. Indices are shown in parentheses above for selected reflections.

Scanning transmission electron microscopy (HAADF-STEM) and energy dispersive x-ray spectroscopy (EDX) mapping experiments were performed to obtain further structural and compositional information on the heterostructures formed. Representative HAADF-STEM images for the m = 1, n = 3 compound, shown in Figures IX.3a and b, support the formation of 3 unique constituents. The HAADF-STEM image (Figure IX.3a) shows a consistent repeating structure throughout the entirety of the film, with blocks of $TiSe_2$ separating the $SnSe_2$ and PbSe constituents as intended from the designed precursor. Higher magnification images like Figure IX.3b, show 3 unique constituents with different zone axes in different layers resulting from the turbostratic disorder

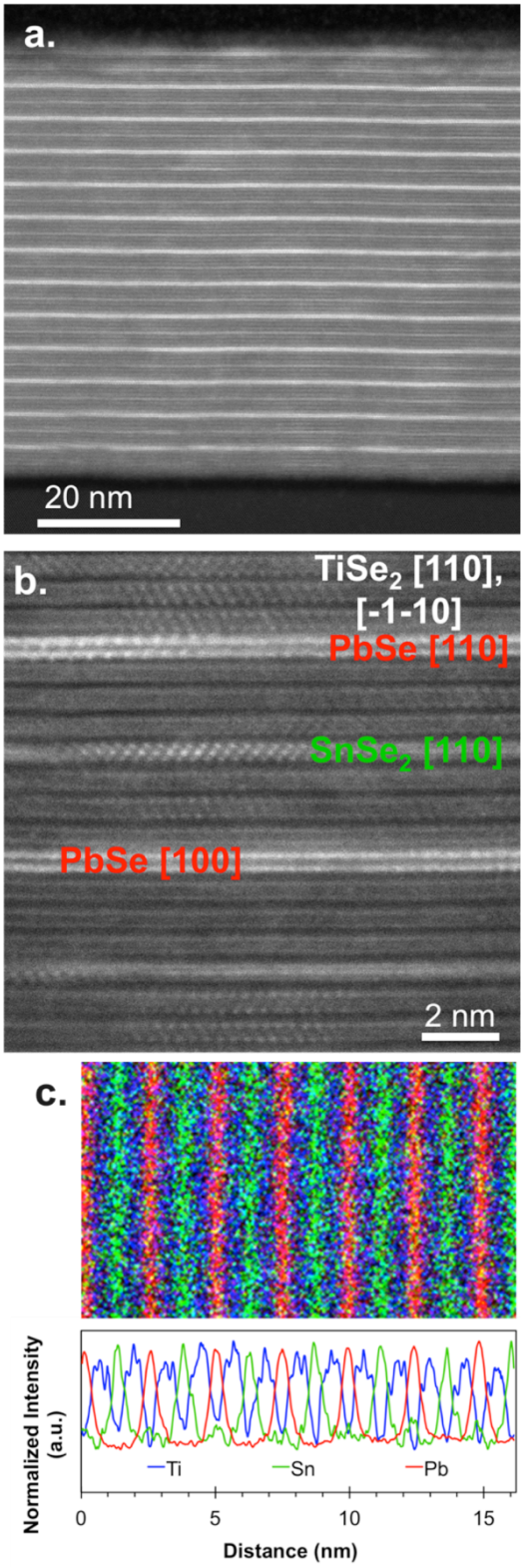

Figure IX.3: HAADF-STEM of the m = 1, n = 3 compound at low **(a)** and high **(b)** magnification, where the expected crystal faces for the constituents are observed. The EDS mapping data and the corresponing integrated profile can be found in pane **c**.

between constituents. The brightest layers, corresponding to high Z, contain regions with the expected zone axes of a rocksalt-like structure. This is consistent with the formation of a PbSe layer similar to that previously reported. The layers with the lowest intensity correspond to the 3 layer thick regions of $TiSe_2$ (CdI_2 structure) expected from the precursor structure. In the region displayed in Figure IX.3b, many identifiable zone axes in the $TiSe_2$ layers are clearly defined. While only a 1T stacking was observed in previous $[(PbSe)_{1+\delta}]_m(TiSe_2)_n$ ferecrystals, here we see several layers in which one of the layers in the $TiSe_2$ block has a different orientation, perhaps reflecting the asymmetry of the environment between the PbSe and $SnSe_2$ constituents, and the low formation temperatures. The intermediate z-contrast layers correspond to the single layer of the $SnSe_2$ constituent, which also has a CdI_2 structure type. The unique Z-contrast of the three layers, and observed patterns of the zone axes corroborate the formation of three unique constituent structures suggested by the diffraction data.

The EDX maps (Figure IX.3c) show the variation of the local composition and support the structural assignments made from the HAADF-STEM images. The EDX data also suggests that very little intermixing is occurring, with the constituent layers remaining unique. The slight upturn in Sn signal in the Pb layer suggests that some Sn atoms may have been incorporated into the PbSe layer. The $SnSe_2$ and $TiSe_2$ layers do not appear to intermix even though they have the same structure. The large difference between the atomic radii and therefore in-plane lattice parameters of these two constituents probably makes Sn/Ti substitutions enthalpically unfavorable.

The ability to vary the sequence of layers in the precursor to self assemble specific higher order heterostructures enables systematic investigations of structure-property relationships in these complex materials. These systematic studies combined with theory to understand the fundamental interactions will be needed to guide optimization of properties and performance of devices containing heterostructures, since the number of possible configurations increases rapidly as the number of constituents increase (Figure IX.4). We calculated the total number of uniquely layered compounds for varying constituents for up to a total of 20 constituent layers per unit cell using necklace combinatorics[30] and subtracted out the repeats that occur from the factors of larger unit

cells. The total number of compounds for n = 20 increases from almost 60,000 with two constituents to over 130 million with three constituents and to over 35 billion with four constituents. This illustrates the need to fundamentally understanding the interactions between constituents and how these interactions effect properties to predict how properties evolve with nanoarchitecture. The ability to prepare specific heterostructures with known structure enables predictions to be experimentally tested, enhancing the feedback between experiment and theory.

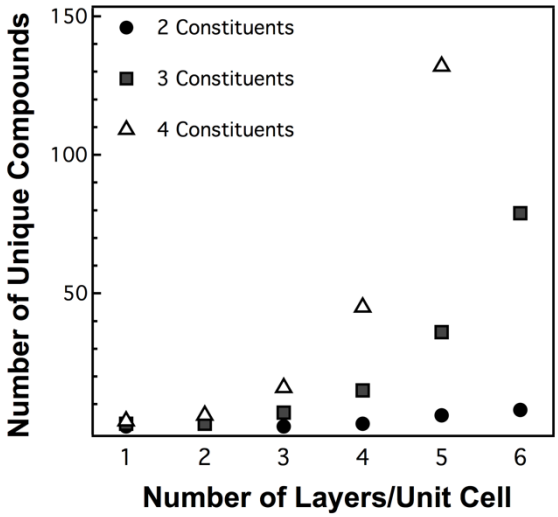

Figure IX.4: The calculated number of unique compounds based on the number of constituent layers, and the number of layers in the unit cell.

IX.2. Experimental Section

Samples were synthesized in a custom-built physical vapour deposition system, as described elsewhere.[21-24] Pressures were maintained below $5x10^{-7}$ Torr during the deposition, and rates were held between 0.1-0.3 Å/s at the substrate and monitored with quartz-crystal microbalances. Annealing was done in a N_2 environment ($[O_2,H_2O] \leq 0.8$ ppm). Out-of-plane and in-plane diffraction measurements were conducted on a Bruker D8 Discover and a Rigaku SmartLab diffractometer, respectively (Cu Kα). HAADF-STEM measurements were conducted at Pacific Northwest National Laboratory using a probe aberration-corrected Titan 80-300™ STEM and EDX maps were acquired using a probe aberration corrected JEOL ARM200CF.

IX.3. Bridge

The formation of 3 constituent heterostructures at low temperatures provides a route to produce complex materials. As highlighted above, the amount of imaginable compounds is nearly endless. The stability of such complex materials is not well understood, and of vital importance for their usefulness. Interestingly, higher temperature annealing of the compounds reported in this chapter showed a complex topotactic reaction, explored in greater detail the following chapter.

CHAPTER X
MULTISTEP TOPOTACTIC REACTIONS IN METASTABLE CHALCOGENIDE HETEROSTRUCTURES

This work is unpublished but was done in collaboration with Duncan R. Sutherland, Jeffrey Ditto, Douglas Medlin, and David C. Johnson. Duncan Sutherland assisted with in-situ and ex-situ annealing studies and data analysis, Jeffrey Ditto and Douglas Medlin provided electron microscopy data and analysis, David C. Johnson is my advisor and research group leader, and I am the primary author.

X.1. Introduction

Understanding the kinetics of solid state reactions is particularly important in the formation of metastable phases but it is challenging to obtain detailed information about most solid state reactions because reactants are typically powders and the reactions and structural changes occur at surfaces and interfaces. Solid state reactions are typically monitored by tracking changes in unit cell volume,[1] by tracking the ratio of reactants and products and their structural evolution using Rietveld refinements,[2–4] or via in-situ electron microscopy studies.[5] In-situ X-ray diffraction techniques have been used to understand solid state reactions,[6,7] and more complex synthesis methods such as the solvothermal approaches.[8,9] Attempts to combine in-situ scattering and spectroscopy techniques has further yielded useful insights into reaction pathways.[10,11] Yet obtaining direct information about the atomic level rate limiting step in a solid state reaction remains elusive.

Topotactic reactions via soft chemical reactions have been increasingly used to form metastable compounds and the preservation of basic structural features between reactants and products simplifies the reaction pathway. The simplest of these reactions are intercalation and ion exchange. These reactions are of vital importance for battery applications, where the longevity and consistency of the electrochemical reactions benefit from readily reversible, low-stress reaction pathways.[12,13] Synthetic examples include transition metal oxide reductions,[1] and redox synthesis of metastable magnetic phases.[4] There are fewer examples of multi-step reactions which can be performed sequentially to accomplish transformations that can not be done in a single one-step reaction.[3] Layered

compounds, because of the obvious diffusion pathways and preferred orientation that enhances signal, are particularly attractive for in situ studies of topotactic reactions.[14–16]

In this paper we explore the conversion of the ordered metastable $(PbSe)_m(TiSe_2)_n(SnSe_2)_m(TiSe_2)_n$ superstructures into higher entropy $(Pb_{0.5}Sn_{0.5}Se)_m(TiSe_2)_n$ random alloys at elevated temperatures using a variety of diffraction and STEM techniques. $(Pb_xSn_{1-x}Se)_m(TiSe_2)_n$ random alloys can be prepared at elevated temperatures[17] and $(PbSe)_m(TiSe_2)_n(SnSe_2)_m(TiSe_2)_n$ superstructures can be prepared at low temperatures by using precursors with different designed structures and have been structurally characterized using XRD and electron microscopy techniques. The topotactic nature of this reaction combined with the preferred orientation of both the reactants and products makes this an ideal system to probe the inter conversion using in-situ x-ray diffraction. The ability to systematically change the nanoarchitecture is an added advantage of this system, as it also allows diffusion to be independently probed as a rate limiting step in the reaction pathway. The studies outlined below are consistent with a three step reaction mechanism. The initial precursor consisting of a designed sequence of elemental layers self assembles into the $(PbSe)_m(TiSe_2)_n(SnSe_2)_m(TiSe_2)_n$ superstructure at low temperature. At higher temperatures, the $(PbSe)_m(TiSe_2)_n(SnSe_2)_m(TiSe_2)_n$ superstructure's Sn is reduced with the simultaneous loss of Se. The SnSe and PbSe layers intermix through the intervening $TiSe_2$ layers. The rate of the formation of the final $(Pb_{0.5}Sn_{0.5}Se)_m(TiSe_2)_n$ product does not depend on the number of $TiSe_2$ layers between the Sn and Pb constituents, indicating the rate determining step is the reduction of Sn with the concomitant loss of Se.

X.2. Experimental

Layered precursor films were synthesized using the modulated elemental reactants technique. This approach relies on the creation of a mostly amorphous film that mimics the targeted structure in both composition and structure. Precursors are deposited in a custom built physical vapor deposition system at pressures below 5×10^{-7} torr. Pb, Sn, and Ti were deposited using electron beam guns, and Se using an effusion cell. Rates were maintained at 0.1-0.3 Å/s at the substrate using quartz crystal microbalances (QCM) to monitor the rate and control the power of the electron beam sources. Elemental layers were deposited using a PC-controlled pneumatic shutter system to expose the substrate to

the plume of each source for a calibrated thickness measured by the QCM. Calibration of the deposition parameters is described further below. Precursor films were annealed in a N_2 environment ($[0_2,H_2O] \leq 0.8$ ppm) for ex-situ experiments.

Adjustments to deposition parameters during calibration were made using x-ray reflectivity (XRR) and diffraction (XRD) as well as compositional characterization from electron probe microanalysis (EPMA) using a method described elsewhere.[18] XRR, $\theta/2\theta$ XRD, and in-situ measurements were performed on a Bruker D8 Discover diffractometer (Cu Kα radiation). A Rigaku SmartLab diffractometer (Cu Kα) was used for in-plane XRD measurements to characterize the constituent phases independently. In-situ measurements were conducted using an Anton-Parr hot stage on the D8, with N_2 gas flowing through the polymer housing to prevent oxidation, which was confirmed via EPMA. High angle annular dark field scanning transmission electron microscopy (HAADF-STEM) and energy dispersive X-ray spectroscopy (EDX) experiments were conducted at Sandia National Laboratories using an aberration corrected FEI Titan G2 80-200 STEM equipped with *ChemiSTEM*™ technology. The STEM was operated at 200keV, 18.1 mrad convergence angle,110 mm camera length, and approximately 0.1 nA of current using a 50 μm condenser aperture.

X.3. Results

Precursors to $(PbSe)_m(TiSe_2)_n(SnSe_2)_m(TiSe_2)_n$ superstructures were prepared by depositing sequences of elemental layers to target a designed kinetic product following, procedures described previously.[19] Pairs of elements (shown in the square brackets below) were calibrated to produce specific compositions. For the [Pb|Se] and [Sn|Se] elemental bilayers, a 1 to 1 ratio of the elements was targeted with a ~5% excess of Se originally designed to account for losses due to sublimation during annealing. For [Ti|Se] elemental bilayer, a 1 to 2 + y ratio of the elements was chosen and y was adjusted to maximize the intensity of the diffraction pattern after low temperature annealing. The ratios between the elemental layers were adjusted to obtain cation ratios that matched the expected lattice mismatches between SnSe, PbSe and $TiSe_2$. The following sequence of elemental layers was deposited as a precursor to the $(PbSe)_1(TiSe_2)_1(SnSe_2)_1(TiSe_2)_1$ superstructure: [Pb|Se][Ti|(2+y)Se)][Sn|Se][Ti|(2+y)Se]. A second precursor was prepared by depositing three Ti|Se elemental bilayers twice in the same sequence of

bilayers as a precursor for the $(PbSe)_1(TiSe_2)_3(SnSe_2)_1(TiSe_2)_3$ superstructure. These precursors contain the correct amount of Sn to form an SnSe layer, but have an excess of Sn if a $SnSe_2$ layer is formed, which must leave the superstructured region for a sharp diffraction pattern to develop.

A sequence of diffraction patterns were collected as a function of time when the samples were annealed at different temperatures. Figure X.1 contains data collected while annealing the precursor for the $(PbSe)_1(TiSe_2)_1(SnSe_2)_1(TiSe_2)_1$ superstructure at 275°C. The sharpening of all peaks as well as an increase in intensity of the odd integer reflections in the 30 minute scan indicates that a super superstructure with the period of the precursor has self assembled. The scan after 2 hours already shows decreases in the odd integer reflections with increases in the even order reflection intensities, suggesting that the superstructure has already begun to transform into the $(Pb_{0.5}Sn_{0.5}Se)_1(TiSe_2)_1$ final product. This transformation continues with time, with the odd order reflections

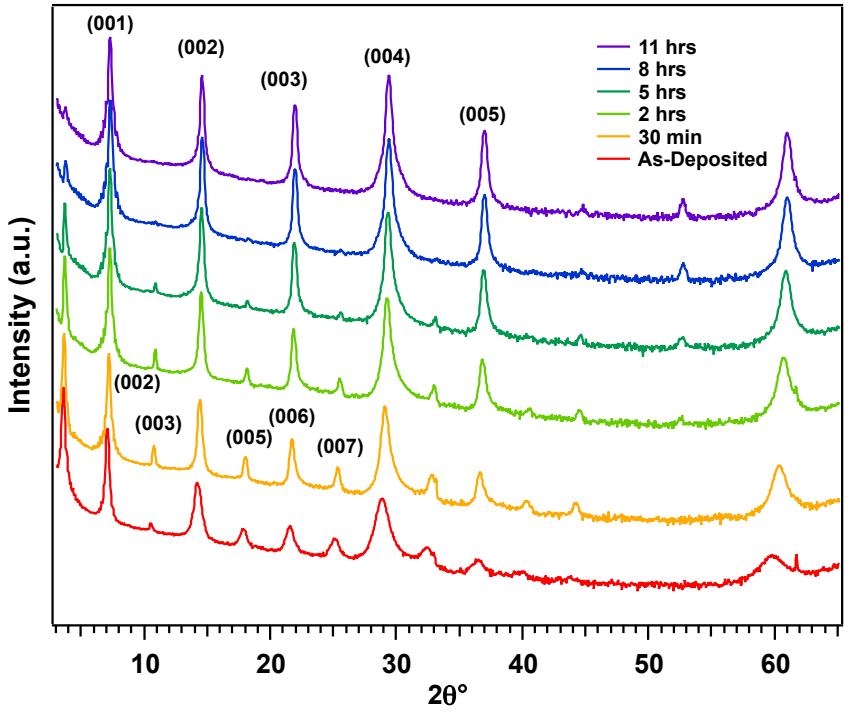

Figure X.1: The 00*l* diffraction data for a m = 1 n = 1 precursor annealed at 275°C. The structure is seen to form the 3 constituent structure first before converting to the alloyed $Pb_xSn_{1-x}Se$ constituent after extended annealing times, with a factor of 2 decrease in lattice parameter. The indices for each structure are given on the 30 minutes and 11 hour scans.

systematically decreasing in intensity until only the (001) reflection is barely visible after 11 hours, while the even order reflections grow in intensity (for example the (006) reflection, which converts to the (003) reflection). Along with the changes in intensity, there is a slight shift of the reflections to higher angle as a function of time, suggesting a slight decrease in the unit cell size. After additional annealing, only the even order reflections remain, suggesting that the *c*-axis lattice parameter has been decreased by a factor of two, which is consistent with the formation of $(Pb_{0.5}Sn_{0.5}Se)_1(TiSe_2)_1$. The relative intensities and the lattice parameter are consistent with that obtained for the compound $(Pb_{0.5}Sn_{0.5}Se)_1(TiSe_2)_1$ prepared without forming the superstructure as a precursor.

To support the interpretation of the specular diffraction patterns shown in Figure X.1, in-plane diffraction data as a function of annealing time was collected (Figure X.2). All the reflections in the in plane diffraction pattern of the superstructure can be indexed as reflections belonging to either $SnSe_2$, PbSe or $TiSe_2$. There is no evidence for SnSe, which shows a strong distortion in the a and b lattice parameters of the 2-D rocksalt structure.[17] As a function of time, the reflections for $SnSe_2$ lose intensity, as easily seen by the change in intensity of the (110) reflection at ~47°. The rock salt reflections gain in intensity, slightly shift their position and begin to broaden, suggesting a distortion of the in-plane structure is occurring. This is consistent with the formation of two layers each containing a $Pb_xSn_{1-x}Se$ alloy constituent structure.[17] The evolving constituent structures support the sequence of events inferred from the 00l diffraction data, and indicate that the initial superstructure has the formula $(PbSe)_1(TiSe_2)_1(SnSe_2)_1(TiSe_2)_1$. The suggested sequence of events requires the initial rearrangement of local structure to form the superstructure, including the extrusion of excess Sn. In the conversion of $(PbSe)_1(TiSe_2)_n(SnSe_2)_1(TiSe_2)_n$ into the final $(Pb_{0.5}Sn_{0.5}Se)_1(TiSe_2)_n$ compound, Se must diffuse out of the structure, Sn must diffuse in, and Pb and Sn must mix through the intervening $TiSe_2$ layers.

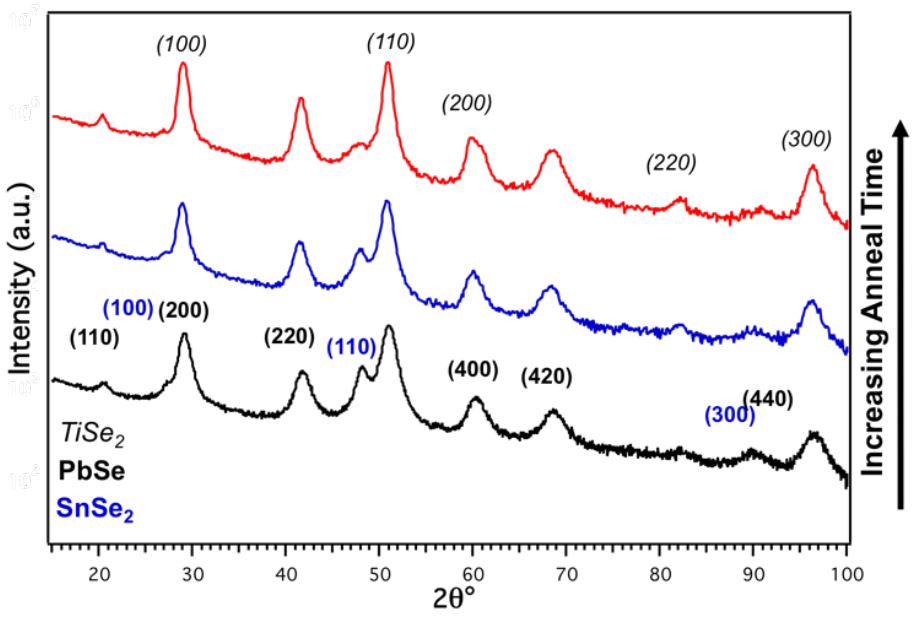

Figure X.2: The *hk*0 patterns for the m = 1, n = 3 compound as a function of annealing time. The $SnSe_2$ structure decays while the growth of the rocksalt structure occurs, and the distortion expected for the alloyed constituent structure begins to occur.

HAADF STEM data was collected on a sample that had formed the three constituent structure with m = 1 and n = 3 after a quick, low temperature anneal (Figure X.3). The image contains a repeating sequence of a bright PbSe bilayer, three consecutive dark $TiSe_2$ trilayers, an intermediate intensity $SnSe_2$ trilayer, and a second band of three consecutive dark $TiSe_2$ trilayers. The structure of the bright PbSe bilayers, suggested by the areas oriented down a zone axis, is consistent with a rock salt structure and with STEM images of other compounds containing a rock salt structured PbSe bilayer. The structure of the $SnSe_2$ layer determined from the zone axis images is consistent with layers in the bulk CdI_2 structure, with Sn octahedrally coordinated, centered between two Se layers. The structure of the $TiSe_2$ layers is also consistent the layers in the CdI_2 structure with octahedral coordination of the Ti, with Se layers on either side of the Ti layer. The stacking of the $TiSe_2$ layers is mostly consistent with the 1T polytype found for bulk $TiSe_2$, but occasionally a layer in the 3-layer blocks has a different orientation than the other two. The STEM data is consistent with the observed specular and in-plane X-ray data, supporting the initial formation of $(PbSe)_1(TiSe_2)_3(SnSe_2)_1(TiSe_2)_3$.

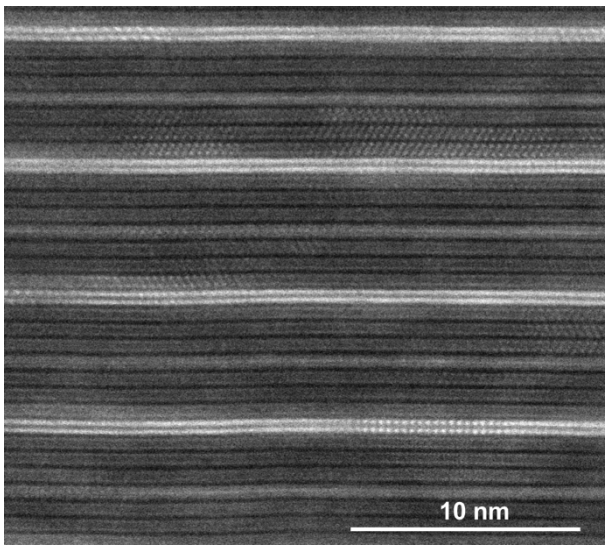

Figure X.3: HAADF-STEM image of the three constituent structure annealed at 275°C for 15 minutes. The crystal faces for the three expected phases are visible, and confirmed by the contrast in the image.

The topotactic nature of the observed transformation, which preserves the crystallographic alignment, makes this system ideal for in-situ diffraction measurements to monitor the reactions that occur. Based on the data presented above, two different transformations occur during the annealing. At low temperatures or for short times at higher temperatures, the precursor self assembles into the ordered $(PbSe)_m(TiSe_2)_n(SnSe_2)_n(TiSe_2)_n$ superstructure. At longer times at higher temperatures, the $(PbSe)_m(TiSe_2)_n(SnSe_2)_n(TiSe_2)_n$ superstructure transforms into the compound $(Pb_{0.5}Sn_{0.5}Se)_m(TiSe_2)_n$. To explore the self assembly of the precursor into the ordered superstructure, XRR data was collected as a function of time at temperatures at 200°C and below. Representative in-situ XRR measurements are shown in Figure X.4. The intensity changes seen in Figure X.4 as a function of time result from changing electron density in the repeating structure as it reorganizes to lower the free energy. The overall pattern changes very little, suggesting that there is little change in the overall superstructure. There is a slight shift in the position of the maxima of the first order reflection and subsidiary maxima to higher angles as a function of time, indicating that the size (thickness) of the diffracting entity is decreasing. The shift corresponds to less than a 1% decrease in thickness and the peak narrows, suggesting the sample is becoming more ordered. The second order Bragg reflection does not shift position, suggesting that it results from a different, more ordered aspect of the structure. The relative positions of

the first and second order Bragg reflections after annealing correspond more closely to that expected from Bragg's law (corrected for index of refraction changes). There also is a slight decrease in the intensity of the first order Bragg reflection while the intensity of the second order Bragg reflection remains constant. This indicates that the as deposited diffraction scan contains elements from regions containing the ordered superstructure and other regions that are more disordered or amorphous. Annealing causes the amorphous regions to self assemble into the ordered superstructure, which also causes the growth in intensity of the higher order odd Bragg reflections, as seen in Figure X.1. While the initial rate of decay of the (001) maxima increases as a function of temperature for temperatures 200°C and below, both the change in intensity and shift of position of the first order Bragg reflection with time trend towards the same intensity and thickness, as shown below in Figure X.5. This suggests that while the initial self assembly is faster at higher temperature, the same final structure, the $(PbSe)_m(TiSe_2)_n(SnSe_2)_n(TiSe_2)_n$ superstructure (where m=1, n=1, or m=1, n=3), self assembles during the low temperature annealing.

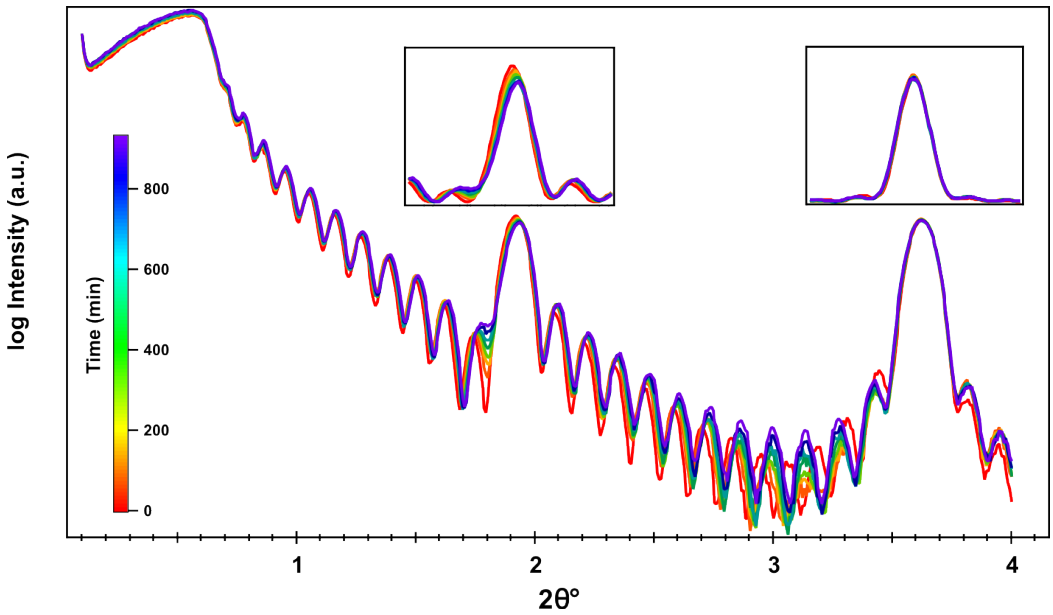

Figure X.4: XRR data collected as a function of time while a sample is annealed at 150°C. Each scan contains the first and second order Bragg reflections, and a sequence of subsidiary maxima (Kiessig fringes) resulting from the finite sample thickness and finite number of repeating sequences in the initial reactant.

The changes in the intensities of the higher temperature XRR data as a function of time are much different, as shown in Figure X.5, with some of the low temperature

annealing data also included for contrast. At higher temperatures, the intensity of the (001) reflection continuously decays as a function of time. The rate of decay of the (001) reflection increases dramatically as a function of temperature for temperatures above 200°C. Samples which were preannealed at temperatures below 250°C immediately have the intensity of the (001) reflection decrease when annealing at 250°C or above. Samples which have not been preannealed at lower temperatures have a different temperature dependence at short times, sometimes even increasing in intensity, reflecting the initial self assembly of the ordered superstructure. For longer times, not preannealed samples have the same decay rate of the (001) reflection, which is independent of the thickness of the $TiSe_2$ layer for small n values. If a sample is initially annealed for a period of time at 250°C or higher, and then annealed at lower temperatures, the (001) reflection does not change in intensity during the lower temperature anneals. This is consistent with the sample consisting of a metastable mixture of two products, the $(PbSe)_m(TiSe_2)_n(SnSe_2)_n(TiSe_2)_n$ superstructure and $(Pb_{0.5}Sn_{0.5}Se)_m(TiSe_2)_n$.

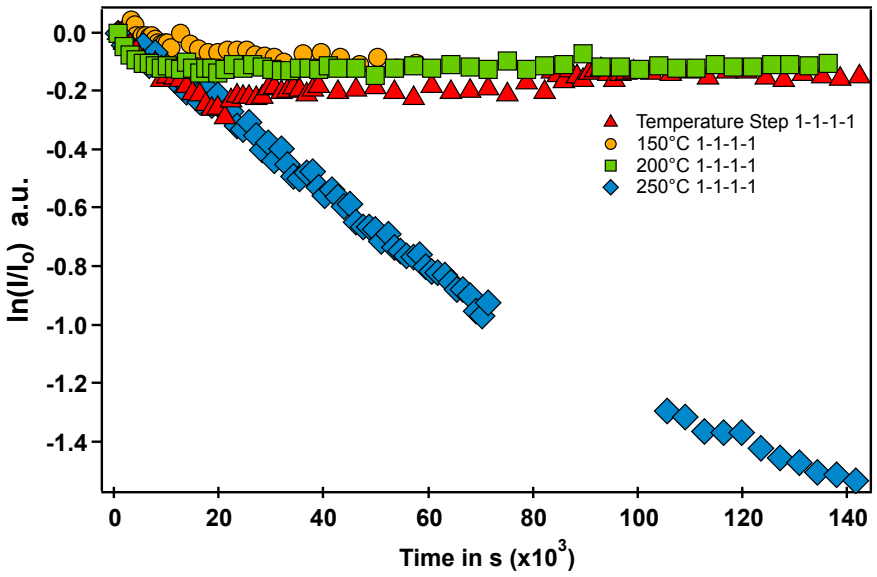

Figure X.5: The decay of intensity for the (001) diffraction maxima in a m = n = 1 precursor. At 250C a strong onset in the decay is observed, signaling significant reaction between constituents. The temperature step data represents a sample that was annealed at 250C, then again at lower temperatures, where no further reaction occurs.

The thickness of the films also changes during the transformations, as expected from the data presented in Figure X.1. Figure X.6 summarizes the changes in thickness as a function of annealing time and temperature for a representative set of samples. The

samples annealed at low temperatures all show a small decrease in thickness that trends to a common thickness change of less than 1%, which is consistent with the shift in the first order Bragg relection observed in Figure X.4. This change reflects the structural rearrangements that must occur during the self assembly of the ordered superstructure from the mostly amorphous precursor. The samples annealed at higher temperatures show a continuous and much larger decrease in thickness, reflecting the large changes that must occur for the ordered superstructure to decompose into the $(Pb_{0.5}Sn_{0.5}Se)_m(TiSe_2)_n$ compounds, and the loss of excess Se. The decrease in thickness is initially faster, with the slope in the decay equilibrating to approximately one tenth the initial slope. A sample annealed for ~20,000 seconds at 250°C was then annealed further at first 150°C and then 200°C. There is no change in sample thickness at these lower temperatures, consistent with the sample consisting of a metastable mixture of two products, the $(PbSe)_m(TiSe_2)_n(SnSe_2)_n(TiSe_2)_n$ superstructure and $(Pb_{0.5}Sn_{0.5}Se)_m(TiSe_2)_n$ without any reaction pathway accessible for the superstructure to convert to $(Pb_{0.5}Sn_{0.5}Se)_m(TiSe_2)_n$ at these lower temperatures.

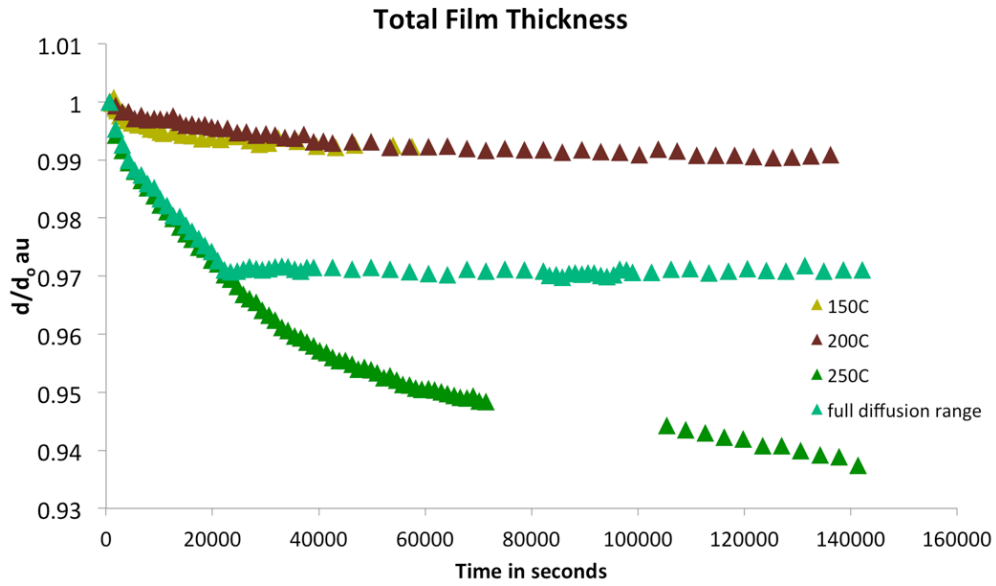

Figure X.6: Normalized film thickness as a function of time and temperature. The data correspnds to the observations in the decay of the (001) maxima.

Considering the changes that must occur during the conversion of the $(PbSe)_m(TiSe_2)_n(SnSe_2)_n(TiSe_2)_n$ superstructure into $(Pb_{0.5}Sn_{0.5}Se)_m(TiSe_2)_n$, two likely rate limiting steps are the intermixing of Sn and Pb, which is being directly monitored by

the previously discussed XRR data, or the reduction of Sn/loss of Se as the $SnSe_2$ converts into SnSe. To decouple these potential rate limiting steps, the annealing studies were done on two different precursors with different thicknesses for the $TiSe_2$ layers separating the Sn and Pb containing layers, and the decay in intensity can be seen in Figure X.7. As a first order approximation, the reduction of Sn/loss of Se as the $SnSe_2$ converts into SnSe is expected to be independent of the thickness of the $TiSe_2$ layers. The increase in the thickness of the $TiSe_2$ layer increases the diffusion length for the mixing of Sn and Pb by a factor of 3, which, if Fick's laws for diffusion hold, should decrease the interdiffusion rate by a factor of 9. As seen in Figure X.7, we observe the same decay rate in intensity for the n = 1 and n = 3 compounds when annealed at 250°C. This indicates that the interdiffusion of the cations across the $TiSe_2$ layers cannot be the rate limiting step in the reaction.

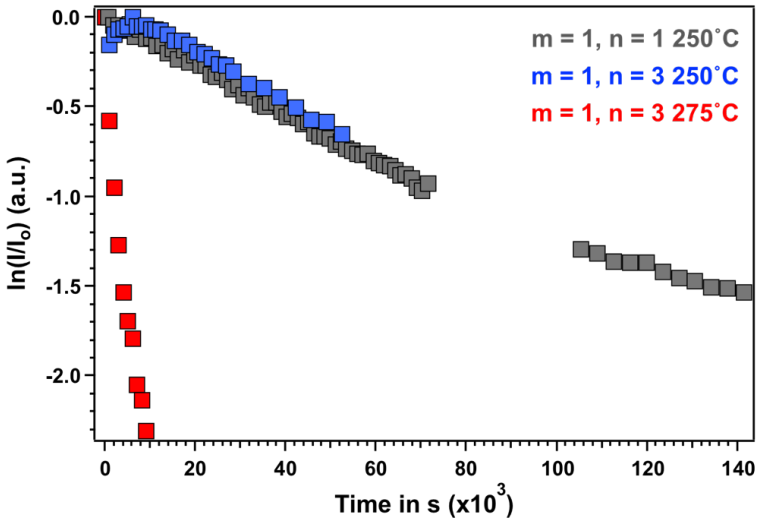

Figure X.7: The decay of the (001) maxima for the n =1 and n = 3 compounds. The same slope is observed for the two compounds at 250°C, suggesting that diffusion is not the rate-limiting step.

To obtain information of what happens at an atomic scale during the transformation of the $(PbSe)_m(TiSe_2)_n(SnSe_2)_n(TiSe_2)_n$ superstructure into $(Pb_{0.5}Sn_{0.5}Se)_m(TiSe_2)_n$, local EDS maps were obtained as shown in Figure X.8. The EDX maps confirm the

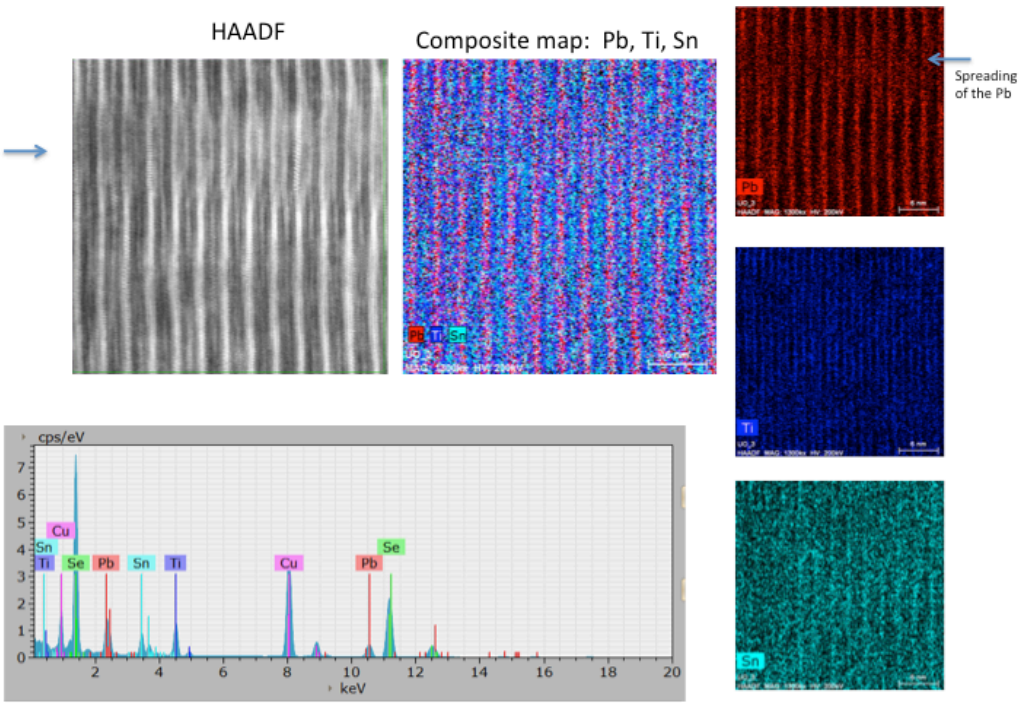

Figure X.8: HAADF-STEM and corresponding EDX spectra and maps for a m = n = 1 compound. Regions of the three constituent structure are observed. There are other regions where the decomposition of $SnSe_2$ has occurred, and subsequent layer mixing is occurring.

superstructure contains 3 distinct regions, each containing Sn, Pb or Ti as the predominant cation. The Pb and Sn containing layers are separated by the $TiSe_2$ layers.Interestingly, there are several regions where the structure appears to be transforming from $(PbSe)_m(TiSe_2)_n(SnSe_2)_n(TiSe_2)_n$ superstructure into $(Pb_{0.5}Sn_{0.5}Se)_m(TiSe_2)_n$. The higher intensity of the Pb signal makes Pb atoms diffusing into the Sn rich layer easier to observe. The conversion appears to preferentially occur at the same point in sequential layers.

X.4. Discussion

The studies outlined below are consistent with the following mechanism for this reaction:

$$\{m[Pb|Se]\}\{n[Ti|(2+y)Se)]\}\{m[Sn|Se]\}\{n[Ti|(2+y)Se]\} \xrightarrow{low\ \Delta} (PbSe)_m(TiSe_2)_n(SnSe_2)_m(TiSe_2)_n$$

$$(PbSe)_m(TiSe_2)_n(SnSe_2)_m(TiSe_2)_n \xrightarrow{\Delta} (PbSe)_m(TiSe_2)_n(SnSe)_m(TiSe_2)_n + Se$$

$$(PbSe)_m(TiSe_2)_n(SnSe)_m(TiSe_2)_n \xrightarrow{Diff.} 2\,(Pb_{0.5}Sn_{0.5}Se)_m(TiSe_2)_n$$

Since changing the thickness of the $TiSe_2$ layers does not change the rate of the reaction, the rate limiting step of the reaction is most likely the decomposition of $SnSe_2$ to SnSe. This decomposition requires the migration of Se out of the structure and Sn enter the structure from the surface, to obtain the required composition and to complete the rocksalt structure layer respectively. The strong onset of the reaction at 250°C and the associated decrease in film thickness suggests that this is the temperature required to liberate Se from the $SnSe_2$ layer. This creates vacancies in the structure through which Se and rock salt cations can diffuse, causing the diffusion fronts observed in the STEM data.

X.5. Conclusions

Here we present a topotactic reaction that occurs in a metastable layered system, with multiple steps and identifiable intermediates. The mostly amorphous precursor first assembles in the the three consistituent heterostructure $(PbSe)_m(TiSe_2)_n(SnSe_2)_m(TiSe_2)_n$ when annealed briefly, or at lower temperatures. At elevated temperatures and longer times, the structure rearranges to form $(Pb_{0.5}Sn_{0.5}Se)_m(TiSe_2)_n$, which maintains the superstructure, but decreases the unit cell size by a factor of two. In-situ diffraction, and ability to decouple diffusion from the reaction rate by increasing the number of $TiSe_2$ layers (n) in the precursor, allowing us to rule out diffusion as the rate limiting step. The data suggest that the decomposition of $SnSe_2$ to SnSe and Se, is rate determining step in the reaction pathway.

X.6. Bridge

The topotactic reaction observed here represents the first in-depth mechanistic study of the reaction of heterostructures materials, to our knowledge. It provides a foundation for thinking both about designing heterostructures, and also about how solid phases react with one another. The structural motif provides distinct advantages for studying solid state reactivity. In the following chapter, we expand upon this concept, using the structural motif to probe the stability of the alloy constituent structure.

CHAPTER XI

NANOSCALE SURFACE SEGREGATION AND MISCIBILITY IN INTERGROWTH ALLOY COMPOUNDS

This work is unpublished but was done in collaboration with Jeffrey Ditto and David C. Johnson. Jeffrey Ditto is responsible for electron microscopy data, David C. Johnson is my advisor and research group leader, and I am the primary author.

XI.1. Introduction

The solubility rules for solids and surface segregation described by William Hume-Rothery in the 1930s[1,2] provide a reasonable foundation for predicting solubility limits of binary alloys. Bulk models, however, do not necessarily predict segregation at surfaces, where the bonding arrangements differ from the bulk structure. Reductions in surface energy can provide a strong driving force for surface segregation in systems where favorable surface conditions differ from the bulk composition.[3] Conversely, the free energy of the bulk can also drive surface segregation.[4] The presence of segregation can have significant impact on material properties. Examples include changes in catalysis,[5] surface stability and reactivity,[6] and mechanical and electrical properties.[7]

Segregation becomes more pronounced in nanostructured materials, which have been shown to have solubility rules, structures and properties different from their bulk counterparts. Solubility in a nanomaterial system was recently shown to be more related to molar heat of vaporization than electronegativity.[8] It is possible to prepare solid solutions of nanomaterials within the miscibility gaps of the bulk phase diagram with properties that are not observed in phase segregated mixtures.[9] For example, the formation of nanoparticle alloys that are immiscible in bulk has been reported by Zlotea *et al.*[10], who observed unique size dependent Ir-Pd solubility and improved catalytic performance relative to the pure materials. Solid solution formation of alloyed SnSe-PbSe bilayers laminated between $TiSe_2$ films[11] from designed amorphous precursors has also been reported for compositions where the bulk phase diagram says they should be immiscibile. These size dependent differences in composition are thought to result from changes in the ratio of surface to bulk environments and/or changes in surface energy as a

function of curvature.[6,10] The ability to systematically investigate miscibility in nanomaterials has been hindered by the inability to prepare homogeneously sized constituents, and the analytical challenge of determining surface composition in three dimensional nanoparticles.

A layered structural motif combined with the ability to systematically alter the thickness of individual layers within in the superstructure through precursor design provides a platform to probe size related phenomena using electron microscopy techniques while eliminating effects from particle shape and curvature. Here we use scanning electron microscopy and energy dispersive X-ray spectroscopy to characterize the local composition the $[(Pb_xSn_{1-x}Se)_{1+\delta}]_mTiSe_2$ intergrowth alloy system. The data suggest that a homogeneous solid solution is formed, in agreement with the X-ray diffraction data.[11] A defect region is observed, where a $Pb_xSn_{1-x}Se$ layer is substituted for $TiSe_2$, resulting in 3 adjacent bilayers of the alloyed structure, and the energy dispersive X-ray spectroscopy maps suggests that phase segregation is occurring. We then synthesized 3 different starting precursors to show that Pb segregates to the surface of the $Pb_xSn_{1-x}Se$ layers when m = 3, and that the segregation is thermodynamically rather than kinetically driven.

XI.2. Experimental

Samples were prepared in a physical vapor deposition system capable of depositing Pb, Se, Sn, and Ti simultaneously, at pressures below 5×10^{-7} torr. Rates were maintained at 0.1-0.3 Å/s at the substrate and monitored by separate quartz crystal microbalances. A PC controlled pneumatic shutter system was used to create the modulated precursor by depositing calibrated thicknesses of elemental layers in a repeating pattern to a total thickness of 50 nm. All samples were annealed at 350°C in a N_2 environment ($[O_2]$,$[H_2O] \leq 0.8$ ppm). A more in-depth description of the synthesis approach for the alloy compounds is given elsewhere.[11] The synthesis of the compounds was confirmed by X-ray diffraction (XRD) and X-ray reflectivity (XRR) on a Bruker D8 Discover diffractometer (Cu Kα radiation). Electron probe microanalysis was used to report global composition of the films.[12]

Thin cross-sections of the films were prepared using a FEI Helios 600 dual-beam FIB for scanning transmission electron microscopy (STEM) using the in situ lift-out method and thinned to electron transparency using the wedge premilling method.[13] High angle annular dark field STEM (HAADF-STEM) and energy-dispersive X-ray spectroscopy (EDX) measurements were conducted using an aberration corrected FEI Titan G2 80-200 STEM equipped with ChemiSTEM technology. The STEM was operated at 200 keV, 18.1 mrad convergence angle,110 mm camera length, and approximately 0.1 nA of current using a 50 μm condenser aperture. EDX spectrum images were acquired with a 2.3 ms dwell time per pixel integrated over multiple drift-corrected frames. EDX signal intensity profiles were extracted for Sn, Pb, Ti, and Se at energy windows of 3.34−3.99, 2.23−2.56, 4.37−4.67, and 1.30−1.57 keV, respectively. Quantification was completed using the Cliff-Lorimer ratio technique, where k-factors were calculated from the end member compounds, which were used as standards for the alloys. To quantify the data from individual layers in the image, the k-factors used for the large areas were applied to each individual atomic layer of the EDX data. Ratios of Sn and Pb within the rock salt layer were calculated using k-factors determined from binary compounds of SnSe and PbSe synthesized from modulated elemental reactants.

XI.3. Results

We used EDX maps to explore the variation of local composition in a series of alloys containing a bilayer of a rock salt structured alloy $Pb_xSn_{1-x}Se$ through compositions where the bulk alloy has a miscibility gap.[14] Vegards law behavior of x-ray diffraction data suggests that a solid solution forms between SnSe and PbSe in the rock salt structured bilayers in $[(Pb_xSn_{1-x}Se)_{1+\delta}]_1(TiSe_2)_1$.[11] Figure XI.1 contains an EDX map for the x = 0.48 compound, and the corresponding integrated intensity profile from the spectra. The films are very stable under the electron beam. Even after 30 minutes of collecting data in a single area, no changes were observed in the sample.This allows sufficient time to accumulate enough counts to have clearly identifiable and resolved atomic planes in the cross-plane direction with elemental specificity. The global composition of the films was determined from the integrated EDX signals in the map by using the Cliff-Lorimer quantification method.[15] This composition (see Table XI.1)

closely matches both that inferred from the observed Vegard's Law behavior and that measured with EPMA.[11]

Table XI.1: Local (EDX) and global[11] (EPMA) composition of the alloy compounds. The oxygen content in the EPMA measurement is due to slight surface oxidation and the native substrate oxide.

Target Composition (x)	Technique	Fractional [O] Composition	Fractional [Se] Composition	Fractional [Ti] Composition	Fractional [Sn] Composition	Fractional [Pb] Composition	Measured Composition (x)
0.75	EPMA	0.03	0.57	0.18	0.07	0.16	0.70
	EDX	-	0.59	0.17	0.08	0.16	0.68
0.50	EPMA	0.03	0.59	0.18	0.10	0.10	0.48
	EDX	-	0.58	0.16	0.13	0.12	0.49
0.25	EPMA	0.03	0.57	0.18	0.16	0.06	0.26
	EDX	-	0.60	0.16	0.17	0.07	0.28

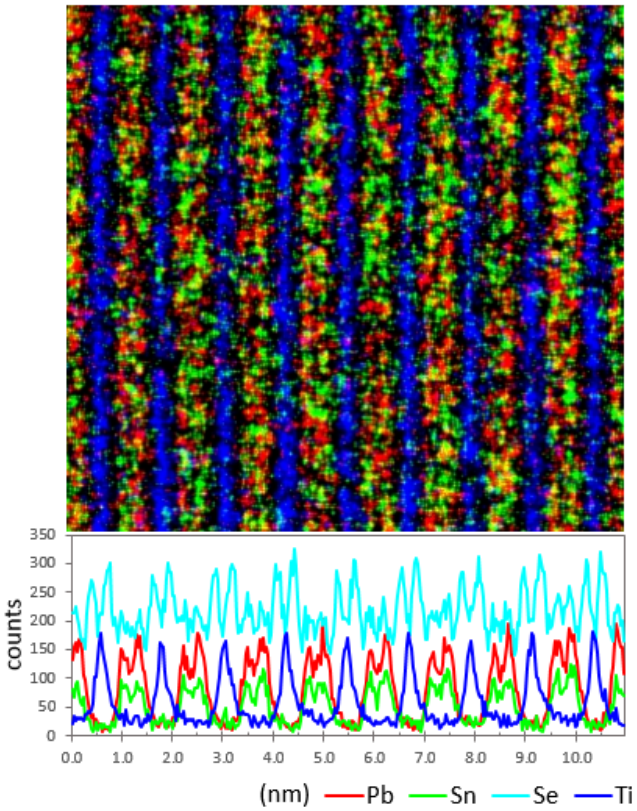

Figure XI.1: Top: HAADF STEM image of a representative area of a $[(Pb_xSn_{1-x}Se)_{1+\delta}]_1(TiSe_2)_1$ sample. Middle: EDX map of a representative area. Bottom: Integrated intensity of the respective elemental signals showing the average distribution of elements corresponds to Se-Ti-Se trilayers separated by bilayers of $Pb_xSn_{1-x}Se$.

In order to quantify the local homogeneity, we take a statistical approach where we examine the variation of the ratio of integrated counts for the different elements for areas of different sizes across the EDX map (Figure XI.2). It has been experimentally determined X-ray counts in the spectrum obey Gaussian statistics.[16] The standard deviation (σ) in counts is equal to $N^{1/2}$ where N equals the number of counts in the peak. The characteristic peak chosen for Pb exhibits the largest k value of the elements in this study, and therefore has the smallest σ. For maximum sensitivity we will therefore focus on compositional changes in Pb. Examining the compositions within each of the $(Pb_xSn_{1-x}Se)_{1+\delta}TiSe_2$ layers within the area mapped, we find an average Pb composition of 11% with σ = 0.9%. For the number of counts analyzed in each square, Gaussian statistics estimate that the standard deviation would be between 0.6% and 0.9%, which is quite

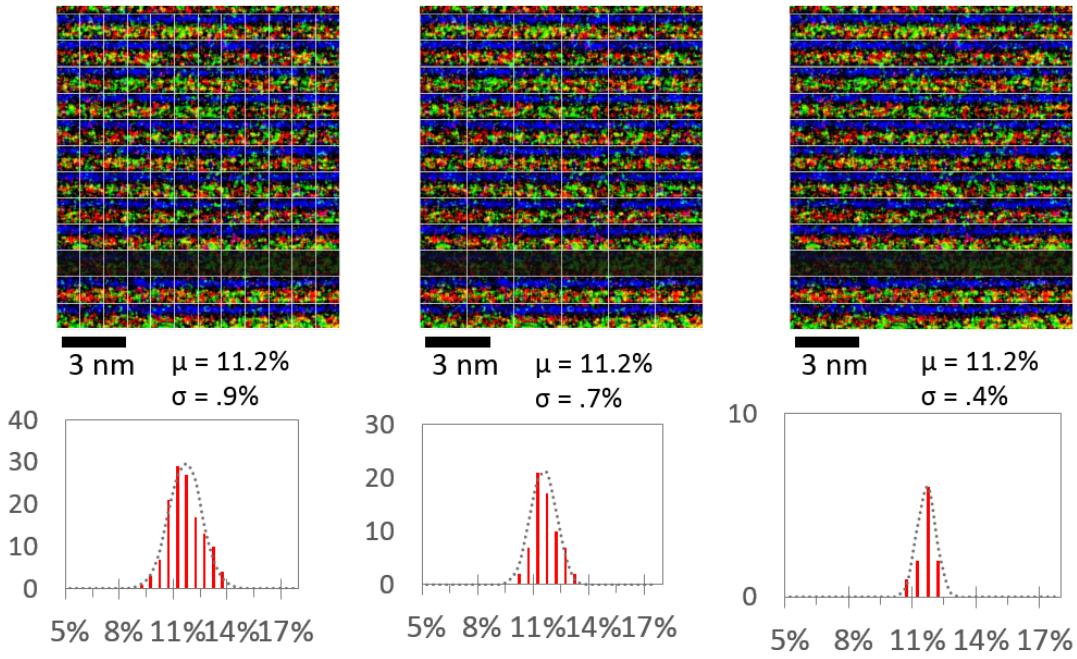

Figure XI.2: Quantitative analysis of the Pb composition in different particians of a spectrum image are displayed as a histogram. Variance in the composition is distributed normally (Gaussian fit shown with grey dotted line). (left) Compositions of 12x11 rectangluar regions, (middle) 6x11 regions, 1x11 regions (exluding a layer with a defect, darkened). Given that the composition distributions are approximately normal and that the standard deviation is decreases consistantly with $1/N^{1/2}$ (where N=counts of signal) indicates that there is no evidence for phase separation within the layers and that a solid solution of SnSe and PbSe was formed within the layers.

close to the experimentally determined σ and is consistent with each of the layers having equivalent composition. Dividing each layer into 12 equal sized regions, resulting in 132 boxes, and examining the integrated intensity in each area, we obtain the distribution shown in Figure XI.2. The statistical broadening of the widths as the counting statistics decrease in smaller areas is consistent with a homogeneous distribution of Pb and Sn throughout the bilayers, supporting the conclusion from XRD that a solid solution has been formed.

While the bilayer alloys appear to be homogeneous, as the thickness of the $Pb_{1-x}Sn_xSe$ layer is increased from a bilayer the bulk phase diagram[14] indicates that at some layer thickness the system should show a miscibility gap, at intermediate compostions. Figure XI.3 shows a defect region with 6 planes of rock salt structure. Qualitatively the compositions of the outer layers of the defect are enriched in lead. At this concentration, the bulk structures would be immiscible.[14] The observed inhomogeneity within this

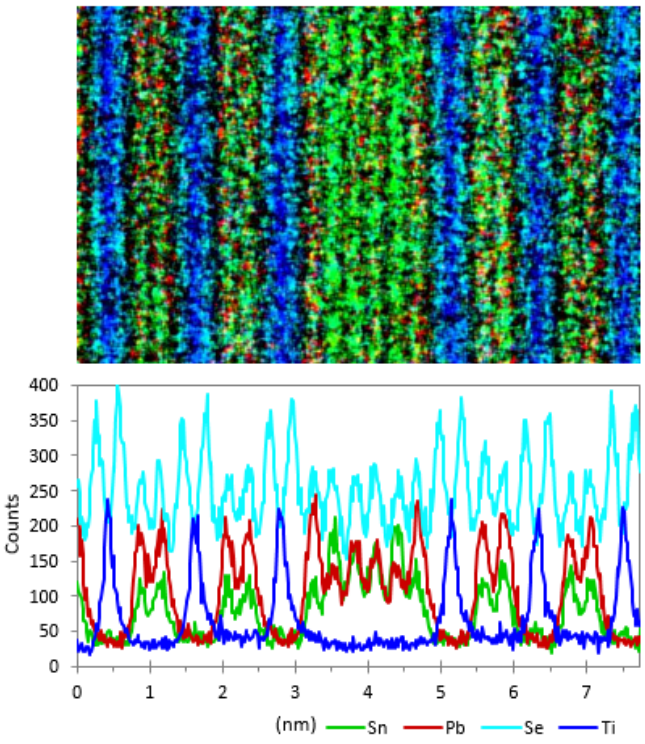

Figure XI.3: top. HAADF STEM image of a defect area within the $[(Pb_xSn_{1-x}Se)_{1+\delta}]_1(TiSe_2)_1$ sample. Middle: EDX map of this area indicating the non-uniform distribution of Pb and Sn in the 6 rock salt planes. Bottom: Integrated intensity of the respective elemental signals showing the average distribution of elements.

defect suggest that as the surface to volume ratio changes, so does the distribution of the cations within the rock salt layer. The segregation of Pb to the surface layer would decrease the entropy of the system which must be offset by an enthalpic stabilization. It is not clear if the segregation observed in the defect results from a variation in local precursor composition (kinetically stabilized), or enthalpic effects in the structure (thermodynamically stabilized).

To determine if this segregation is a result of kinetic limitations or thermodynamic stability, three different $[(Pb_{1/3}\,Sn_{2/3}Se)_{1+\delta}]_3(TiSe_2)_1$ precursors were prepared using the MER technique and annealed to form the same compound, and schematics of these precursors are shown in Figure XI.4. The three different precursors distribute the Pb and Sn differently within the Pb | Sn | Se layer, with a homogenous distribution, and with lead concentrated on either the interior or exterior of the structure. If the distribution of Pb and Sn in the final product is a kinetic effect, we expect to see different distributions in the self-assembled products, with the ferecrystalline product reflecting the arrangement of the precursor. However, if the distribution is a thermodynamic phenomenon, then we expect to see similar distribution of Pb and Sn in the final product.

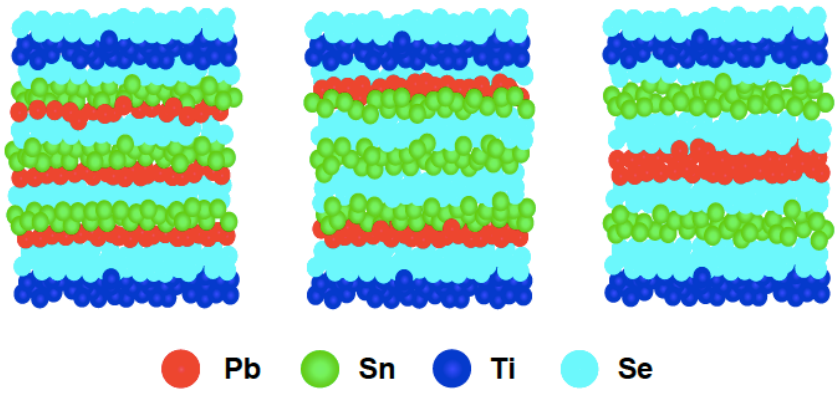

Figure XI.4: Schematic structures of the three different repeating units of precursors to probe whether surface segregation is a thermodynamic or kinetic phenomenon.

A representative HAADF STEM image for the three compounds is shown in Figure XI.5. All the annealed compounds display the same basic structure, with blocks of rocksalt six monolayers thick interleaved between single trilayers of $TiSe_2$. The rocksalt [110] and [100] faces are clearly present in the figure. CdI_2 type [110] and [100],

consistent with the structure reported for $TiSe_2$, are also visible. The contrast suggests the higher Z Pb and Sn atoms are present in the rocksalt structure, and that the darker CdI_2 layer contains the low Z Ti atoms as expected from the previously reported alloys.[11] The unit cell measured with XRD was found to be the same within error ranging between 2.38(1)-2.39(1) nm. The samples display the characteristic rotational or turbostratic disorder between the layers, as expected for metastable compounds formed from amorphous precursors.[17–19] Qualitatively EDX maps confirm the formation of distinct $Pb_xSn_{1-x}Se$ and $TiSe_2$ phases, and further indicate enhanced Pb concentration at the interface layers for all of the precursors, with a representative map shown inset in Figure XI.5.

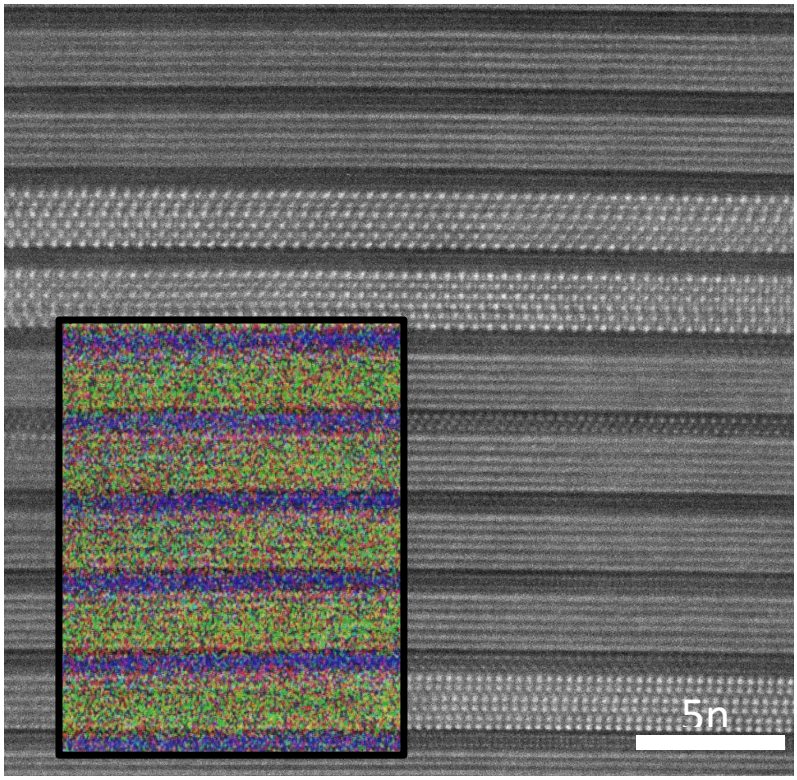

Figure XI.5: Representative HAADF-STEM image and corresponding EDX map (inset) for the disperse precursor. Crystallographic alignment for the expected phases are observed.

To quantify the local composition, a large area of data was integrated and analyzed using the approach described above. The overall composition in the 3 samples from EDX over a large area is consistent with the deposition parameters used in preparing the

precursors and the targeted composition of the samples (Table XI.2). All samples are about 66%Sn leading to a measured stoichiometry of $[(Pb_{0.34}\ Sn_{0.66}Se)_{1.17}]_3(TiSe_2)_1$ for the self assembled products which is consistent with the deposition parameters used to prepare them. Figure XI.6 contains the compositions of each atomic rock salt plane in the samples prepared with different precursors. The results show that all three precursors have similar enhanced Pb composition in the outer most layers, with the variation of these layers from the interior layers being statistically significant. The spectra suggest that the rock salt structure in homogenous in the in-plane direction. Atomic plane quantification results in a partially background subtracted quantification as true quantification has not yet been accomplished at atomic resolution due to signal overlapping caused by probe tails, surface amorphization, and a broadening interaction volume.

Table XI.2: STEM-EDX quantitative results using k-factors calculated from SnSe and PbSe films prepared via MER, as well as the c-lattice parameter calculated from the XRD patterns.

Element	Stoichiometric (at. %)	Disperse (at. %)	Interior (at. %)	Surface (at. %)
Se	55	54	56	56
Pb	12	13	13	12
Sn	23	25	23	25
Ti	10	8	8	8
c (nm)	-	2.38(1)	2.39(1)	2.39(1)

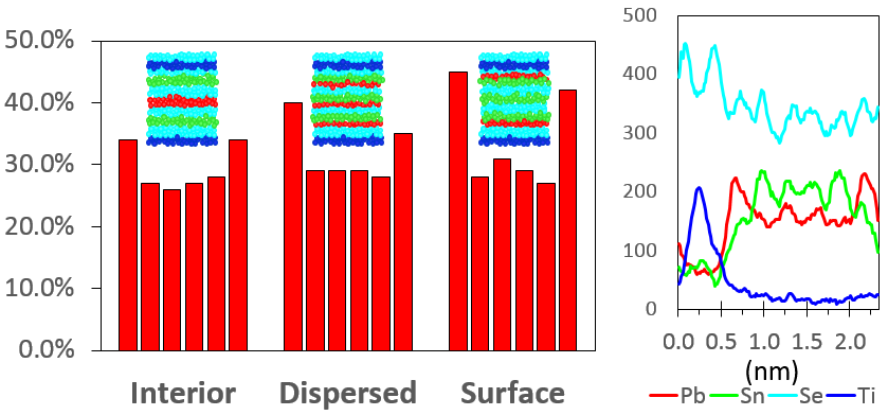

Figure XI.6: The histograms displaying the Pb content for each of the $Pb_xSn_{1-x}Se$ monolayers (left) and a representative integrated profile for the unit cell (right).

XI.4. Discussion

The formation of similar self assembled product from three unique precursors suggests that the surface segregation observed is a thermodynamic effect, rather than kinetic. The precursor was deposited outside of the miscibility gap for the bulk compounds, which further suggests that the surface segregation is the result of a surface energy stabilization. The low temperature formation of $SnSe_2$ in the superstructure reported in Chapter 9 suggests that the formation could also be a result of a more complex reaction mechanism. DFT calculations would be helpful to understand the relative stability of the structures and surfaces. Collaborators from the University of Florida have begun these calculations, with the goal of commenting on the stability of the structures, and the root of the observed surface segregation.

XI.5. Conclusions

Electron microscopy, and more specifically EDX measurements were used to characterize local composition in the $[(Pb_xSe_{1-x}Se)_{1+\delta}]_1(TiSe_2)_1$ intergrowth compounds using a statistical approach. The compounds were found to have a homogeneous composition, confirming the formation of a solid solution suggested from previous X-ray diffraction experiments. The observation of the a defect region suggests that surface segregation occurs in thicker blocks of the alloyed rock salt structure. Variation of the precursor films resulted in the formation of similar products and suggests the observed segregation is thermodynamically driven.

CHAPTER XII

CONCLUSIONS AND SUMMARY

The formation of several ternary metastable misfit layer compounds based on $TiSe_2$ are reported. These compounds were synthesized via modulated elemental reactants, which employs the use of a designed precursor to synthesize targeted heterostructures by controlling local composition and annealing in a diffusion-limited regime to allow the precursor to self assemble in the local free energy minima. Compounds with the basic formula $[(MSe)_{1+\delta}]_mTiSe_2$ were explored, where M = Sn and Bi. The m = n = 1 compounds suggest that charge transfer between constituents is responsible for the n-type behavior observed, with the Bi compound donating more electrons to the conduction band than Sn, as expected based on their formal valencies. Unexpected structural behavior was observed in$[(SnSe)_{1.21}]_mTiSe_2$, where there is evidence of long range order, and in-plane distortions to create a lattice match, suggesting the compounds is more apptly described as a misfit layer compound with considerable rotational defects. The transport properties observed in the $[(SnSe)_{1+\delta}]_mTiSe_2$ compounds ($m \leq 4$) suggests more complicated constituent interaction in this system than previously observed.

In order to optimize the materials, the ability to make site-specific substitutions was explored. First a series of $(Pb_xSn_{1-x}Se)_{1+\delta}TiSe_2$ compounds were synthesized, which showed the formation of the targeted $Pb_xSn_{1-x}Se$ over the entire range of $0 \leq x \leq 1$ even though a miscibility gap is expected from the bulk SnSe and PbSe phase diagram. The compounds showed increased mobility when compared to the end members. This approach was then used to demonstrate modulation doping in Heterostructures through the synthesis of the $(Bi_xSn_{1-x}Se)_{1+\delta}TiSe_2$ series of compounds. The superstructures were shown to form for the entirety of the range $0 \leq x \leq 1$, with the intermediate x values showing evidence of two symmetry types in the $Bi_xSn_{1-x}Se$ constituent, suggesting the two parent structures are present. The doping efficiency of the Bi atoms was observed to decrease as the concentration of Bi atoms increased, and the mobility of the compounds increased as the Bi content increased as well. This work combined suggests that targeted substitutions and subsequent modulation doping may be a way to optimize material properties in this class of compounds at a deeper level than previously demonstrated.

The synthesis of multi-constituent heterostructures is reported. The formation of a 3 constituent phase is reported containing PbSe, $SnSe_2$, and $TiSe_2$, and is demonstrated for several different layering schemes. The formation of the compounds occurs at a far lower temperature than the compounds reported above. Interestingly, these precursors annealed at higher temperatures undergo a topotactic reaction, converting to the higher entropy $(Pb_xSn_{1-x}Se)_{1+\delta}(TiSe_2)_n$ structure. Through in-situ diffraction and designed precursor structures, diffusion is decoupled from the reaction rate, and the decomposition of the $SnSe_2$ is suggested as the rate limiting step in the multistep reaction.

Finally, the stability of the alloy constituent phase $Pb_xSn_{1-x}Se$ is explored. In thicker blocks of the structure, Pb is observed to segregate to the surface. Three precursors were designed to test whether this was a kinetic or thermodynamic effect, which all resulted in the same metastable structure. The synthesis of these precursors outside the miscibility gap suggests that the observed surface segregation is a thermodynamic effect likely driven by a surface energy gain. The work understanding the reactivity of metastable solids should serve as a starting place for more fundamental chemical studies, using layered compounds as a model system for the ease of characterization, and the ability to control structure to systematically study solid state reaction.

REFERENCES CITED

Chapter I

1. Seebeck, T. J., **1826**, Ann. Phys. 82, 253.

2. Peltier, J. C., **1834**, Ann Chim. Phys. 56, 371.

3. Ioffe, A. F., **1932**, in The socialist reconstruction and science, No.1, p.23.

4. Ioffe, A. F., in Semiconductor Thermoelements and Thermoelectric Cooling, (Infosearch Ltd, London), pp.1-183. **1958**

5. Spaldin, N. A. Computational design of contraindicated multifunctional materials. 230th ACS National Meeting, Washington, DC, United States, Aug. 28-Sept. 1, 2005.

6. Wiedemann, G. and Franz, R. **1853**, Ann. Phys. 89, 497.

7. Goldsmid, H. J.; Douglas, R. W. The Use of Semiconductors in Thermoelectric Refrigeration. *Br. J. Appl. Phys.* **1954**, *5*, 386–390.

8. Ioffe, A. V. and A. F. Ioffe, **1956**, Izv. Akad. Nauk. SSSR, Ser. Fiz. 20, 65.

9. Hicks, L. D.; Dresselhaus, M. S. Effect of Quantum-Well Structures on the Thermoelectric Figure of Merit. *Phys. Rev. B* **1993**, *47*, 727–731.

10. Hicks, L. D.; Dresselhaus, M. S. Thermoelectric Figure of Merit of a One-Dimensional Conductor. *Phys. Rev. B* **1993**, *47*, 16631–16634.

11. Slack, G.A. New Materials and Performance Limits for Thermoelectric Cooling. In CRC Handbook of Thermoelectrics; Rowe, D.M., Ed.; CRC Press: Boca Raton, FL, USA, **1995**; pp. 407-440

12. Harman, T. C.; Taylor, P. J.; Walsh, M. P.; LaForge, B. E. Quantum Dot Superlattice Thermoelectric Materials and Devices. *Science* **2002**, *297*, 2229–2232.

13. Venkatasubramanian, R.; Siivola, E.; Colpitts, T.; O'Quinn, B. Thin-Film Thermoelectric Devices with High Room-Temperature Figures of Merit. *Nature* **2001**, *413*, 597–602.

14. Winkler, M.; Liu, X.; Schürmann, U.; König, J. D.; Kienle, L.; Bensch, W.; Böttner, H. Current Status in Fabrication, Structural and Transport Property Characterization, and Theoretical Understanding of Bi2Te3 / Sb2Te3 Superlattice Systems. *Zeitschrift fur Anorg. und Allg. Chemie* **2012**, *638*, 2441–2454.

15. Rogl, G.; Grytsiv, a.; Rogl, P.; Peranio, N.; Bauer, E.; Zehetbauer, M.; Eibl, O. N-Type Skutterudites (R,Ba,Yb)yCo4Sb12 (R = Sr, La, Mm, DD, SrMm, SrDD) Approaching ZT ??? 2.0. *Acta Mater.* **2014**, *63*, 30–43.

16. Saramat, A.; Svensson, G.; Palmqvist, A. E. C.; Stiewe, C.; Mueller, E.; Platzek, D.; Williams, S. G. K.; Rowe, D. M.; Bryan, J. D.; Stucky, G. D. Large Thermoelectric Figure of Merit at High Temperature in Czochralski-Grown Clathrate Ba 8Ga 16Ge 30. *J. Appl. Phys.* **2006**, *99*, 023708.

17. Brown, S. R.; Kauzlarich, S. M.; Gascoin, F.; Snyder, G. J. Yb 14 MnSb 11 : New High Efficiency Thermoelectric Material for Power Generation. *Chem. Mater.* **2006**, *18*, 1873–1877.

18. Kauzlarich, S. M.; Brown, S. R.; Snyder, G. J. Zintl Phases for Thermoelectric Devices. *Dalton Trans.* **2007**, 2099–2107.

19. Rhyee, J.-S.; Lee, K. H.; Lee, S. M.; Cho, E.; Kim, S. Il; Lee, E.; Kwon, Y. S.; Shim, J. H.; Kotliar, G. Peierls Distortion as a Route to High Thermoelectric Performance in In(4)Se(3-Delta) Crystals. *Nature* **2009**, *459*, 965–968.

20. Zhang, Y.; Morelli, D.; Ozolins, V.; Wolverton, C. Prediction of New Stable Compounds and Promising Thermoelectrics in the Cu − Sb − Se System. *Chem. Mater.* **2014**, *26*, 3427–3435.

21. Zhao, L. D.; Lo, S. H.; He, J.; Li, H.; Biswas, K.; Androulakis, J.; Wu, C. I.; Hogan, T. P.; Chung, D. Y.; Dravid, V. P.; et al. High Performance Thermoelectrics from Earth-Abundant Materials: Enhanced Figure of Merit in PbS by Second Phase Nanostructures. *J. Am. Chem. Soc.* **2011**, *133*, 20476–20487.

22. Snyder, G. J.; Toberer, E. S. Complex Thermoelectric Materials. *Nat. Mater.* **2008**, *7*, 105–114.

23. Rowe, D. M.; Min, G. Alpha-plot in sigma-plot as a thermoelectric-material performance indicator. *J. Mater. Sci. Lett.* **1995**, 14, 617-619.

24. Mott, N. F. Electrons in disordered structures. *Advan. Phys*. **1967,** 16 :49-144.

25. Mott N. F.The minimum metallic conductivity in 3 dimensions. *Philosophical Magazine Part B.* **1981,** 44, 2, 265-284.

26. Gaultois, M. W.; Sparks, T. D.; Borg, C. K. H.; Seshadri, R.; Bonificio, W. D.; Clarke, D. R. Data-Driven Review of Thermoelectric Materials: Performance and Resource Considerations BT - Chemistry of Materials. *Chem. Mater.* **2013**, *25*, 2911–2920.

27. Goldsmid, H. J. Bismuth Telluride and Its Alloys as Materials for Thermoelectric Generation *Materials.* **2014**, *7*, 2577-2592.

28. Nolas, G. S., G. A. Slack, T. M. Tritt, and D. T. Morelli, 1995, in Proceedings of the 14th International conference on Thermoelectrics, edited by M. V. Vedernikov (A.F. loffe Physical-Technical Institute, St. Petersburg, Russia) 236.

29. Sales, B. C.; Mandrus D.; Williams R. K. Filled Skutterudite Antimonides: A New Class of Thermoelectric Materials**.** *Science.* **1996** 272, 1325.

30. Li, S.; Funahashi, R.; Matsubara, I.; Ueno, K.; Yamada, H. High Temperature Thermoelectric Properties of Oxide Ca9Co12O28. *J. Mater. Chem.* **1999**, *9*, 1659–1660.

31. Masset, A.; Michel, C.; Maignan, A.; Hervieu, M.; Toulemonde, O.; Studer, F.; Raveau, B.; Hejtmanek, J. Misfit-Layered Cobaltite with an Anisotropic Giant Magnetoresistance: Ca3Co4O9. *Phys. Rev. B* **2000**, *62*, 166–175.

32. Miyazaki, Y.; Kudo, K.; Akoshima, M.; Ono, Y.; Koike, Y.; Kajitani, T. Low-Temperature Thermoelectric Properties of the Composite Crystal [Ca 2CoO 3.34] 0.614[CoO 2]. *Jpn. J. Appl. Phys.* **2000**, *39*, L531–L533.

33. Jones, C. D. W.; Regan, K. A.; DiSalvo, F. J. Thermoelectric Properties of the Doped Kondo Insulator: NdxCe3-xPt3Sb4. *Phys. Rev. B* **1998**, *58*, 16057–16063.

34. DiSalvo, F. J. Thermoelectric Cooling and Power Generation. *Science.* **1999**, *285*, 703–706.

35. Sugiyama, J.; Itahara, H.; Brewer, J. H.; Ansaldo, E. J.; Dohmae, K.; Xia, C.; Seno, Y.; Hitti, B.; Tani, T. A Common Behavior of Thermoelectric Layered Cobaltites: An Incommensurate Spin Density Wave State. *Proc. ICT'03. 22nd Int. Conf. Thermoelectr. (IEEE Cat. No.03TH8726)* **2003**.

36. Heremans, J. P.; Jovovic, V.; Toberer, E. S.; Saramat, A.; Kurosaki, K.; Charoenphakdee, A.; Yamanaka, S.; Snyder, G. J. Enhancement of Thermoelectric Efficiency in PbTe by Distortion of the Electronic Density of States. *Science (80-.).* **2008**, *321*, 1457–1461.

37. Pei, Y.; Shi, X.; LaLonde, A.; Wang, H.; Chen, L.; Snyder, G. J. Convergence of Electronic Bands for High Performance Bulk Thermoelectrics. *Nature* **2011**, *473*, 66–69.

38. Martin, J.; Wang, L.; Chen, L.; Nolas, G. S. Enhanced Seebeck Coefficient through Energy-Barrier Scattering in PbTe Nanocomposites. *Phys. Rev. B - Condens. Matter Mater. Phys.* **2009**, *79*, 1–5.

39. Liu, W.; Jie, Q.; Kim, H. S.; Ren, Z. ScienceDirect Current Progress and Future Challenges in Thermoelectric Power Generation : From Materials to Devices. *ACTA Mater.* **2015**, *87*, 357–376.

40. Ohta, H.; Sugiura, K.; Koumoto, K. Recent Progress in Oxide Thermoelectric Materials: P-Type Ca 3 Co 4 O 9 and N-Type SrTiO 3 -. *Inorg. Chem.* **2008**, *47*, 8429–8436.

41. Takeuchi, T.; Kondo, T.; Takami, T.; Takahashi, H.; Ikuta, H.; Mizutani, U.; Soda, K.; Funahashi, R.; Shikano, M.; Mikami, M.; et al. Contribution of Electronic Structure to the Large Thermoelectric Power in Layered Cobalt Oxides. *Phys. Rev. B* **2004**, *69*, 1–9.

42. Wiegers, G. A. Misfit Layer Compounds: Structure and Physical Properties. *Prog. Solid St. Chem.* **1996**, *24*, 1–139.

43. Meerschaut, A. Misfit Layer Compounds. *Curr. Opin. Solid State Mater. Sci.* **1996**, *1*, 250–260.

44. Rouxel, J.; Meerschaut, a.; Wiegers, G. a. Chalcogenide Misfit Layer Compounds. *J. Alloys Compd.* **1995**, *229*, 144–157.

45. Wiegers, G. a. Charge Transfer between Layers in Misfit Layer Compounds. *J. Alloys Compd.* **1995**, *219*, 152–156.

46. van Smaalen, S. Superspace Description of Incommensurate Intergrowth Compounds and the Application to Inorganic Misfit Layer Compounds. *Mater. Sci. Forum* **1992**, *100-101*, 173–222.

47. Wan, C.; Wang, Y.; Wang, N.; Koumoto, K. Low-Thermal-Conductivity (MS)1+x(TiS2)2 (M = Pb, Bi, Sn) Misfit Layer Compounds for Bulk Thermoelectric Materials. *Materials (Basel).* **2010**, *3*, 2606–2617.

48. Miyazaki, Y.; Ogawa, H.; Kajitani, T. Preparation and Thermoelectric Properties of Misfit-Layered Sulfide [Yb 1.90 S 2] 0.62 NbS 2. *Jpn. J. Appl. Phys.* **2004**, *43*, L1202–L1204.

49. Jood, P.; Ohta, M.; Nishiate, H.; Yamamoto, A.; Lebedev, O. I.; Berthebaud, D.; Suekuni, K.; Kunii, M. Microstructural Control and Thermoelectric Properties of Misfit Layered Sulfides (LaS)1+ mTS2 (T = Cr, Nb): The Natural Superlattice Systems. *Chem. Mater.* **2014**, *26*, 2684–2692.

50. Wan, C.; Wang, Y.; Norimatsu, W.; Kusunoki, M.; Koumoto, K. Nanoscale Stacking Faults Induced Low Thermal Conductivity in Thermoelectric Layered Metal Sulfides. *Appl. Phys. Lett.* **2012**, *101913*, 1–5.

51. Di Salvo, F. J.; Moncton, D. E.; Waszczak, J. V. Electronic Properties and Superlattice Formation in Semimetal TiSe2. *Phys. Rev. B* **1976**, *14*, 4321.

52. Bhatt, R.; Basu, R.; Bhattacharya, S.; Singh, A. Low Temperature Thermoelectric Properties of Cu Intercalated TiSe2: A Charge Density Wave Material. *Appl. Phys. A* **2013**, 465–470.

53. Giang, N.; Xu, Q.; Hor, Y.; Williams, A.; Dutton, S.; Zandbergen, H.; Cava, R. Superconductivity at 2.3 K in the Misfit Compound (PbSe)1.16(TiSe2)2. *Phys. Rev. B* **2010**, *82*, 1–5.

54. Wiegers, G.; Haange, R. Electrical Transport Properties of the Misfit Layer Compounds (SnS) 1.20 TiS2 and (PbS) 1.18 TiS2. *Eur. J. solid state Inorg. Chem.* **1991**, *28*, 1071–1078.

55. Lin, Q.; Smeller, M.; Heideman, C. L.; Zschack, P.; Koyano, M.; Anderson, M. D.; Kykyneshi, R.; Keszler, D. a.; Anderson, I. M.; Johnson, D. C. Rational Synthesis and Characterization of a New Family of Low Thermal Conductivity Misfit Layer Compounds [(PbSe) 0.99] M (WSe 2) N †. *Chem. Mater.* **2010**, *22*, 1002–1009.

56. Heideman, C.; Nyugen, N.; Hanni, J.; Lin, Q.; Duncombe, S.; Johnson, D. C.; Zschack, P. The Synthesis and Characterization of New [(BiSe)1.10]m[NbSe2]n, [(PbSe)1.10]m[NbSe2]n, [(CeSe)1.14]m[NbSe2]n and [(PbSe)1.12]m[TaSe2]n Misfit Layered Compounds. *J. Solid State Chem.* **2008**, *181*, 1701–1706.

57. Atkins, R.; Wilson, J.; Zschack, P.; Grosse, C.; Neumann, W.; Johnson, D. C. Synthesis of [(SnSe) 1.15]m((TaSe2)n Ferecrystals: Structurally Tunable Metallic Compounds. *Chem. Mater.* **2012**, *24*, 4594–4599.

58. Beekman, M.; Cogburn, G.; Heideman, C.; Rouvimov, S.; Zschack, P.; Neumann, W.; Johnson, D. C. New Layered Intergrowths in the Sn-Mo-Se System. *J. Electron. Mater.* **2012**, *41*, 1476–1480.

59. Heideman, C. L.; Tepfer, S.; Lin, Q.; Rostek, R.; Zschack, P.; Anderson, M. D.; Anderson, I. M.; Johnson, D. C. Designed Synthesis , Structure , and Properties of a Family of Ferecrystalline Compounds [(PbSe)1.00]m(MoSe2)n. *J. Am. Chem. Soc.* **2013**, *135*, 11055–11062.

60. M. Falmbigl, M. B. Alemayehu, D. R. Merrill, M. Beekman, D. C. Johnson, In-plane Structure of Ferecrystalline Compounds, *Crystal Research +Technology*, 2015, submitted.

61. Nguyen, N. T.; Berseth, P. a.; Lin, Q.; Chiritescu, C.; Cahill, D. G.; Mavrokefalos, A.; Shi, L.; Zschack, P.; Anderson, M. D.; Anderson, I. M.; et al. Synthesis and Properties of Turbostratically Disordered, Ultrathin WSe 2 Films. *Chem. Mater.* **2010**, *22*, 2750–2756.

62. Kertesz, M.; Hoffmann, R. Octahedral vs. Trigonal-Prismatic Coordination and Clustering in Transition-Metal Dichalcogenides. *J. Am. Chem. Soc.* **1984**, *106*, 3453–3460.

63. Wilson, J. A.; Yoffe, A. D. The transition metal dichalcogenides discussion and interpretation of the observed optical, electrical and structural properties. Advances in Physics, vol. 18, Issue 73, p.193-335.

64. Atkins, R.; Moore, D. B.; Johnson, D. C. Insights into the Self-Assembly of Ferecrystalline Compounds from Designed Amorphous Precursors. *Chem. Mater.* **2013**, *25*, 1744–1750.

65. Anderson, M. D.; Heideman, C. L.; Lin, Q.; Smeller, M.; Kokenyesi, R.; Herzing, A. a; Anderson, I. M.; Keszler, D. a; Zschack, P.; Johnson, D. C. Size-Dependent Structural Distortions in One-Dimensional Nanostructures. *Angew. Chem. Int. Ed. Engl.* **2013**, *52*, 1982–1985.

66. Chiritescu, C.; Cahill, D. G.; Nguyen, N.; Johnson, D.; Bodapati, A.; Keblinski, P.; Zschack, P. Ultralow Thermal Conductivity in Disordered, Layered WSe2 Crystals. *Science* **2007**, *315*, 351–353.

67. Chiritescu, C.; Cahill, D. G.; Heideman, C.; Lin, Q.; Mortensen, C.; Nguyen, N. T.; Johnson, D.; Rostek, R.; Böttner, H. Low Thermal Conductivity in Nanoscale Layered Materials Synthesized by the Method of Modulated Elemental Reactants. *J. Appl. Phys.* **2008**, *104*, 033533.

68. Moore, D. B.; Beekman, M.; Disch, S.; Zschack, P.; Häusler, I.; Neumann, W.; Johnson, D. C. Synthesis, Structure, and Properties of Turbostratically Disordered (PbSe) 1.18 (TiSe 2) 2. *Chem. Mater.* **2013**, *25*, 2404–2409.

69. Alemayehu, M. B.; Mitchson, G.; Hanken, B. E.; Asta, M.; Johnson, D. C. Charge Transfer between PbSe and NbSe 2 in [(PbSe) 1.14]. *Chem. Mater.* **2014**, *26*, 1859–1866.

70. Merrill, D. R.; Moore, D. B.; Coffey, M. N.; Jansons, A. W.; Falmbigl, M.; Johnson, D. C. Synthesis and Characterization of Turbostratically Disordered (BiSe) 1.15 TiSe 2. *Semicond. Sci. Technol.* **2014**, *29*, 064004.

71. Alemayehu, M. B.; Falmbigl, M.; Ta, K.; Grosse, C.; Westover, R. D.; Bauers, S. R.; Fischer, S. F.; Johnson, D. C. Structural and Electrical Properties of ([SnSe] 1+x)m(NbSe2)1 Compounds: Single NbSe2 Layers Seprated by Increasing Thickness of SnSe. *Chem. Mater.* **2015**.

72. Dingle, R.; Störmer, H. L.; Gossard, A. C.; Wiegmann, W. Electron mobilities in modulation-doped semiconductor heterojunction superlattices. *Applied Physics Letters*. **1978,** 33, 665-667.

73. Falmbigl, M.; Fiedler, A.; Atkins, R. E.; Fischer, S. F.; Johnson, D. C. Suppressing a Charge Density Wave by Changing Dimensionality in the Ferecrystalline Compounds ([SnSe] 1.15) 1 (VSe 2) with N = 1,2,3,4. *Nano Lett.* **2014**.

74. Lin, Q.; Tepfer, S.; Heideman, C.; Mortensen, C.; Nguyen, N.; Zschack, P.; Beekman, M.; Johnson, D. C. Influence of Selenium Vapor Postannealing on the Electrical Transport Properties of PbSe–WSe2 Nanolaminates. *J. Mater. Res.* **2011**, *26*, 1866–1871.

75. Moore, D. B.; Stolt, M. J.; Atkins, R.; Sitts, L.; Jones, Z.; Disch, S.; Matt, B.; Johnson, D. C. Structural and Electrical Properties of (PbSe)1·16TiSe2. *Emerg. Mater. Res.* **2012**, *1*, 292–298.

76. Merrill, D. R.; Moore, D. B.; Ditto, J.; Sutherland, D. R.; Falmbigl, M.; Winkler, M.; Pernau, H.; Johnson, D. C. The Synthesis , Structure , and Electrical Characterization of (SnSe)1.2TiSe2. *Eur. J. Inorg. Chem.* **2015**, 83–91.

77. Phung, T.; Jensen, J.; Jonshon, D.; Donovan, J.; McBurnett, B. Determination of the Composition of Ultra-thin Ni-Si Films on Si: Constrained Modeling of Electron Probe Microanalysis and X-ray Reflectivity Data. *X-Ray Spectrom.* **2008**, *37*, 608–614.

78. Leventi-Peetz, A.; Krasovskii, E. E.; Schattke, W. Dielectric Function and Local-Field Effects of TiSe2. *Phys. Rev. B* **1995**, *51*, 17965–17971.

79. Hummer, K.; Grüneis, A.; Kresse, G. Structural and Electronic Properties of Lead Chalcogenides from First Principles. *Phys. Rev. B* **2007**, *75*, 1–9.

80. Altshuler, B.; Khmel'Nitzkii, D.; Larkin, A.; Lee, P. Magnetoresistance and Hall Effect in a Disordered Two-Dimensional Electron Gas. *Phys. Rev. B* **1980**, *22*, 5142–5153.

Chapter II

1. Wiegers, G. A. Misfit Layer Compounds: Structure and Physical Properties. *Prog. Solid St. Chem.* **1996**, *24*, 1–139.

2. Heideman, C. L.; Tepfer, S.; Lin, Q.; Rostek, R.; Zschack, P.; Anderson, M. D.; Anderson, I. M.; Johnson, D. C. Designed Synthesis, Structure, and Properties of a Family of Ferecrystalline Compounds [(PbSe)1.00]m(MoSe2)n. *J. Am. Chem. Soc.* **2013**, *135*, 11055–11062.

3. Lin, Q.; Smeller, M.; Heideman, C. L.; Zschack, P.; Koyano, M.; Anderson, M. D.; Kykyneshi, R.; Keszler, D. a.; Anderson, I. M.; Johnson, D. C. Rational Synthesis and Characterization of a New Family of Low Thermal Conductivity Misfit Layer Compounds [(PbSe) 0.99] M (WSe 2) N †. *Chem. Mater.* **2010**, *22* (3), 1002–1009.

4. Atkins, R.; Wilson, J.; Zschack, P.; Grosse, C.; Neumann, W.; Johnson, D. C. Synthesis of [(SnSe) 1.15]m((TaSe2)n Ferecrystals: Structurally Tunable Metallic Compounds. *Chem. Mater.* **2012**, *24*, 4594–4599.

5. Alemayehu, M. B.; Mitchson, G.; Hanken, B. E.; Asta, M.; Johnson, D. C. Charge Transfer between PbSe and NbSe 2 in [(PbSe) 1.14]. *Chem. Mater.* **2014**, *26*, 1859–1866.

6. Phung, T.; Jensen, J.; Jonshon, D.; Donovan, J.; McBurnett, B. Determination of the Composition of Ultra-thin Ni-Si Films on Si: Constrained Modeling of Electron Probe Microanalysis and X-ray Reflectivity Data. *X-Ray Spectrom.* **2008**, *37*, 608–614.

Chapter III

1. Hicks, L.; Dresselhaus, M. *Phys. Rev. B* 1993, *47*, 727–731.

2. Slack GA., CRC Handbook of Thermoelectrics, ed. DM Rowe, Boca Raton, FL: CRC Press (1995) ISBN 0-8493-0146-7.

3. Nolas, GS; Morelli, DT; Tritt, TM. *Annu. Rev. Mater. Sci*. **1999**, *29*, 89–116.

4. Terasaki, I.; Sasago, Y.; Uchinokura, K. *Phys. Rev. B* **1997**, *56*, 685–687.

5. Wan, C.; Wang, Y.; Wang, N.; Koumoto, K. *Materials (Basel)*. **2010**, *3*, 2606–2617.

6. Guilmeau, E.; Bréard, Y.; Maignan, a. *Appl. Phys. Lett.* **2011**, *99*, 052107.

7. de Boer, D.; Bruggen, C. Van; Bus, G. *Phys. Rev. B* **1984**, *29*, 6797.

8. Klipstein, P.; Bagnall, A. *J. Phys. C ...* **1981**, *14*, 4067–4081.

9. Rasch, J.; Stemmler, T.; Müller, B.; Dudy, L.; Manzke, R. *Phys. Rev. Lett.* **2008**, *237602*, 2–5.

10. R. D. Barnard. Thermoelectricity in Metals and Alloys (Wiley, New York, **1972**).

11. Bhatt, R.; Basu, R.; Bhattacharya, S.; Singh, A. *Appl. Phys. A* **2013**, 465–470.

12. Bhatt, R.; Bhattacharya, S.; Patel, M.; Basu, R.; Singh, A.; Sürger, C.; Navaneethan, M.; Hayakawa, Y.; Aswal, D. K. *J. Appl. Phys.* **2013**, *114*, 114509.

13. Giang, N.; Xu, Q.; Hor, Y.; Williams, A.; Dutton, S.; Zandbergen, H.; Cava, R. *Phys. Rev. B* **2010**, *82*, 1–5.

14. Moore, D. B.; Stolt, M. J.; Atkins, R.; Sitts, L.; Jones, Z.; Disch, S.; Matt, B.; Johnson, D. C. *Emerg. Mater. Res.* **2012**, *1*, 292–298.

15. Moore, D. B.; Beekman, M.; Disch, S.; Zschack, P.; Häusler, I.; Neumann, W.; Johnson, D. C. *Chem. Mater.* **2013**, *25*, 2404–2409.

16. Chiritescu, C.; Cahill, D. G.; Nguyen, N.; Johnson, D.; Bodapati, A.; Keblinski, P.; Zschack, P. *Science* **2007**, *315*, 351–353.

17. Chiritescu, C.; Cahill, D. G.; Heideman, C.; Lin, Q.; Mortensen, C.; Nguyen, N. T.; Johnson, D.; Rostek, R.; Böttner, H. *J. Appl. Phys.* **2008**, *104*, 033533.

18. Roisnel, T.; Rodríquez-Carvajal, J. *Mater. Sci. Forum* **2001**, *378-381*, 118–123.

19. Phung, T.; Jensen, J.; Jonshon, D.; Donovan, J.; McBurnett, B. *X-Ray Spectrom.* **2008**, *37*, 608–614.

20. Heideman, C.; Nyugen, N.; Hanni, J.; Lin, Q.; Duncombe, S.; Johnson, D. C.; Zschack, P. *J. Solid State Chem.* **2008**, *181*, 1701–1706.

21. Atkins, R.; Disch, S.; Jones, Z.; Haeusler, I.; Grosse, C.; Fischer, S. F.; Neumann, W.; Zschack, P.; Johnson, D. C. *J. Solid State Chem.* **2013**, *202*, 128–133.

22. Atkins, R.; Wilson, J.; Zschack, P.; Grosse, C.; Neumann, W.; Johnson, D. C. *Chem. Mater.* **2012**, *24*, 4594–4599.

23. Wiegers, G.; Meetsma, A. *J.Phys. Condens. Matter* **1991**, 2603.

24. Grosse, C.; Atkins, R.; Kirmse, H.; Mogilatenko, A.; Neumann, W.; Johnson, D. C. *Alloy. Compd.* **2013**, *579*, 507–515.

25. Parratt, L. *Phys. Rev.* **1954**, *95*, 359–362.

26. Greenaway, D. L.; Nitsche, R. *J. Phys. Chem. Solids* **1965**, *26*, 1445–1458.

27. Chattopadhyay, T.; Pannetier, J.; von Schnering, H. *J. Phys. Chem. Solids* **1986**, *47*, 879–885.

28. Beekman, M.; Cogburn, G.; Heideman, C.; Rouvimov, S.; Zschack, P.; Neumann, W.; Johnson, D. C. *J. Electron. Mater.* **2012**, *41*, 1476–1480.

29. Smeller, M. M.; Heideman, C. L.; Lin, Q.; Beekman, M.; Anderson, M. D.; Zschack, P.; Anderson, I. M.; Johnson, D. C. *Zeitschrift für Anorg. und Allg. Chemie* **2012**, *638*, 2632–2639.

30. Wiegers, G.; Haange, R. *Eur. J. Solid State Inorg. Chem.* **1991**, *28*, 1071–1078.

31. Di Salvo, F. J.; Moncton, D. E.; Waszczak, J. V. *Phys. Rev. B* **1976**, *14*, 4321.

32. Moore, D. B.; Sitts, L.; Stolt, M. J.; Beekman, M.; Johnson, D. C. *J. Electron. Mater.* **2012**, *42*, 1647–1651.

33. Altshuler, B.; Khmel'Nitzkii, D.; Larkin, A.; Lee, P. *Phys. Rev. B* **1980**, *22*, 5142–5153.

34. Wiegers, G. A. *Prog. Solid St. Chem.* **1996**, *24*, 1–139.

35. Merrill, D. R.; Moore, D. B.; Coffey, M. N.; Jansons, A. W.; Falmbigl, M.; Johnson, D. C. *Semicond. Sci. Technol.* **2014**, *29*, 064004.

36. Heideman, C. L.; Johnson, D. C. *Semicond. Sci. Technol.* **2014**, *29*, 064007.

37. Lin, Q.; Tepfer, S.; Heideman, C.; Mortensen, C.; Nguyen, N.; Zschack, P.; Beekman, M.; Johnson, D. C. *J. Mater. Res.* **2011**, *26*, 1866–1871.

38. Blatt FJ. Physics of electronic conduction in solids. New York: McGraw-Hill; 1968. p. 210.

39. Snyder, G.; Toberer, E. *Nat. Mater.* **2008**, *7*, 105–114.

40. Schaffer, M.; Schaffer, B.; Ramasse, Q. *Ultramicroscopy* **2012**, 114, 62–71.

Chapter IV

1. Wiegers, G. A. Misfit Layer Compounds: Structure and Physical Properties. Prog. Solid St. Chem. 1996, 24, 1–139.

2. Rouxel, J.; Meerschaut, a.; Wiegers, G. a. Chalcogenide Misfit Layer Compounds. J. Alloys Compd. 1995, 229, 144–157.

3. Wiegers, G. a. Charge Transfer between Layers in Misfit Layer Compounds. J. Alloys Compd. 1995, 219, 152–156.

4. Heideman, C.; Nyugen, N.; Hanni, J.; Lin, Q.; Duncombe, S.; Johnson, D. C.; Zschack, P. The Synthesis and Characterization of New [(BiSe)1.10]m[NbSe2]n, [(PbSe)1.10]m[NbSe2]n, [(CeSe)1.14]m[NbSe2]n and [(PbSe)1.12]m[TaSe2]n Misfit Layered Compounds. J. Solid State Chem. 2008, 181, 1701–1706.

5. Nguyen, N. T.; Howe, B.; Hash, J. R.; Liebrecht, N.; Johnson, D. C. Synthesis of [(VSe2)n]1.06[(TaSe2)n] Superlattices Using a Hybrid Approach: Self-Assembly of Amorphous Nanostructured Reactants. Adv. Mater. 2006, 18 (1), 118–122.

6. Lin, Q.; Smeller, M.; Heideman, C. L.; Zschack, P.; Koyano, M.; Anderson, M. D.; Kykyneshi, R.; Keszler, D. a.; Anderson, I. M.; Johnson, D. C. Rational Synthesis and Characterization of a New Family of Low Thermal Conductivity Misfit Layer Compounds [(PbSe) 0.99] M (WSe 2) N †. Chem. Mater. 2010, 22 (3), 1002–1009.

7. Beekman, M.; Cogburn, G.; Heideman, C.; Rouvimov, S.; Zschack, P.; Neumann, W.; Johnson, D. C. New Layered Intergrowths in the Sn-Mo-Se System. J. Electron. Mater. 2012, 41 (6), 1476–1480.

8. Beekman, M.; Disch, S.; Rouvimov, S.; Kasinathan, D.; Koepernik, K.; Rosner, H.; Zschack, P.; Neumann, W. S.; Johnson, D. C. Controlling Size-Induced Phase Transformations Using Chemically Designed Nanolaminates. Angew. Chemie - Int. Ed. 2013, 52 (50), 13211–13214.

9. Alemayehu, M. B.; Mitchson, G.; Hanken, B. E.; Asta, M.; Johnson, D. C. Charge Transfer between PbSe and NbSe 2 in [(PbSe) 1.14]. Chem. Mater. 2014, 26, 1859–1866.

10. Alemayehu, M. B.; Falmbigl, M.; Ta, K.; Grosse, C.; Westover, R. D.; Bauers, S. R.; Fischer, S. F.; Johnson, D. C. Structural and Electrical Properties of ([SnSe]1+δ)m(NbSe2)1 Compounds: Single NbSe2 Layers Separated by Increasing Thickness of SnSe. Chem. Mater. 2015, 27 (3), 867–875.

11. Anderson, M. D.; Heideman, C. L.; Lin, Q.; Smeller, M.; Kokenyesi, R.; Herzing, A. a; Anderson, I. M.; Keszler, D. a; Zschack, P.; Johnson, D. C. Size-Dependent Structural Distortions in One-Dimensional Nanostructures. Angew. Chem. Int. Ed. Engl. 2013, 52 (7), 1982–1985.

12. Heideman, C. L.; Tepfer, S.; Lin, Q.; Rostek, R.; Zschack, P.; Anderson, M. D.; Anderson, I. M.; Johnson, D. C. Designed Synthesis, Structure, and Properties of a Family of Ferecrystalline Compounds [(PbSe)1.00]m(MoSe2)n. J. Am. Chem. Soc. 2013, 135, 11055–11062.

13. Atkins, R.; Moore, D. B.; Johnson, D. C. Insights into the Self-Assembly of Ferecrystalline Compounds from Designed Amorphous Precursors. Chem. Mater. 2013, 25, 1744–1750.

14. Moore, D. B.; Beekman, M.; Disch, S.; Zschack, P.; Häusler, I.; Neumann, W.; Johnson, D. C. Synthesis, Structure, and Properties of Turbostratically Disordered (PbSe) 1.18 (TiSe 2) 2. Chem. Mater. 2013, 25, 2404–2409.

15. Atkins, R.; Disch, S.; Jones, Z.; Haeusler, I.; Grosse, C.; Fischer, S. F.; Neumann, W.; Zschack, P.; Johnson, D. C. Synthesis, Structure and Electrical Properties of a New Tin Vanadium Selenide. J. Solid State Chem. 2013, 202, 128–133.

16. Merrill, D. R.; Moore, D. B.; Ditto, J.; Sutherland, D. R.; Falmbigl, M.; Winkler, M.; Pernau, H.; Johnson, D. C. The Synthesis, Structure, and Electrical Characterization of (SnSe)1.2TiSe2. Eur. J. Inorg. Chem. 2015, No. 1, 83–91.

17. Moore, D. B.; Stolt, M. J.; Atkins, R.; Sitts, L.; Jones, Z.; Disch, S.; Matt, B.; Johnson, D. C. Structural and Electrical Properties of (PbSe)1·16TiSe2. Emerg. Mater. Res. 2012, 1, 292–298.

18. Merrill, D. R.; Moore, D. B.; Coffey, M. N.; Jansons, A. W.; Falmbigl, M.; Johnson, D. C. Synthesis and Characterization of Turbostratically Disordered (BiSe) 1.15 TiSe 2. Semicond. Sci. Technol. 2014, 29 (6), 064004.

19. Merrill, D. R.; Sutherland, D. R.; Ditto, J.; Bauers, S. R.; Falmbigl, M.; Medlin, D. L.; Johnson, D. C. Kinetically Controlled Site-Specific Substitutions in Higher-Order Heterostructures. Chem. Mater. 2015, 27 (11), 4066–4072.

20. Greenaway, D. L.; Nitsche, R. Preparation and Optical Properties of IV-VI2 Chalcogenides Having the CdI2 Structure. J. Phys. Chem. Solids 1965, 26, 1445–1458.

21. Falmbigl, M.; Alemayehu, M. B.; Merrill, D. R.; Beekman, M.; Johnson, D. C. In-Plane Structure of Ferecrystalline Compounds. Cryst. Res. Technol. 2015, 50 (6), 464–472.

Chapter V

1. Fiebig, M. Revival of the Magnetoelectric Effect. J. Phys. D. Appl. Phys. 2005, 38 (8), R123–R152.

2. Spaldin, N. A.; Fiebig, M. The Renaissance of Magnetoelectric Multiferroics. Science 2005, 309 (5733), 391–392.

3. Ramesh, R.; Spaldin, N. a. Multiferroics: Progress and Prospects in Thin Films. Nat. Mater. 2007, 6 (1), 21–29.

4. Fabbri, E.; Licoccia, S.; Traversa, E.; Wachsman, E. D. Composite Cathodes for Proton Conducting Electrolytes. Fuel Cells 2009, 9 (2), 128–138.

5. Fabbri, E.; Bi, L.; Pergolesi, D.; Traversa, E. Towards the next Generation of Solid Oxide Fuel Cells Operating below 600 °c with Chemically Stable Proton-Conducting Electrolytes. Adv. Mater. 2012, 24 (2), 195–208.

6. Yaroslavtsev, a. B. Ion Conductivity of Composite Materials on the Base of Solid Electrolytes and Ion-Exchange Membranes. Inorg. Mater. 2012, 48 (13), 1193–1209.

7. Snyder, G. J.; Toberer, E. S. Complex Thermoelectric Materials. Nat. Mater. 2008, 7 (2), 105–114.

8. Toberer, E. S.; Baranowski, L. L.; Dames, C. Advances in Thermal Conductivity. Annu. Rev. Mater. Res. 2012, 42 (1), 179–209.

9. Geim, a K.; Grigorieva, I. V. Van Der Waals Heterostructures. Nature 2013, 499 (7459), 419–425.

10. Di Salvo, F. J.; Moncton, D. E.; Waszczak, J. V. Electronic Properties and Superlattice Formation in Semimetal TiSe2. Phys. Rev. B 1976, 14 (10), 4321.

11. Guilmeau, E.; Bréard, Y.; Maignan, a. Transport and Thermoelectric Properties in Copper Intercalated TiS2 Chalcogenide. Appl. Phys. Lett. 2011, 99 (5), 052107.

12. Rasch, J.; Stemmler, T.; Müller, B.; Dudy, L.; Manzke, R. 1 T-TiSe 2: Semimetal or Semiconductor? Phys. Rev. Lett. 2008, 237602 (December), 2–5.

13. Bhatt, R.; Bhattacharya, S.; Patel, M.; Basu, R.; Singh, A.; Sürger, C.; Navaneethan, M.; Hayakawa, Y.; Aswal, D. K. Thermoelectric Performance of Cu Intercalated Layered TiSe 2 above 300 K. J. Appl. Phys. 2013, 114 (May 2014), 114509.

14. Wan, C.; Wang, Y.; Wang, N.; Koumoto, K. Low-Thermal-Conductivity (MS)1+x(TiS2)2 (M = Pb, Bi, Sn) Misfit Layer Compounds for Bulk Thermoelectric Materials. Materials (Basel). 2010, 3 (4), 2606–2617.

15. Giang, N.; Xu, Q.; Hor, Y.; Williams, A.; Dutton, S.; Zandbergen, H.; Cava, R. Superconductivity at 2.3 K in the Misfit Compound (PbSe)1.16(TiSe2)2. Phys. Rev. B 2010, 82 (2), 1–5.

16. Wiegers, G.; Haange, R. Electrical Transport Properties of the Misfit Layer Compounds (SnS) 1.20 TiS2 and (PbS) 1.18 TiS2. Eur. J. solid state Inorg. Chem. 1991, 28, 1071–1078.

17. Bauers, S. R.; Merrill, D. R.; Moore, D. B.; Johnson, D. C. Carrier Dilution in TiSe 2 Based Intergrowth Compounds for Enhanced Thermoelectric Performance. J. Mater. Chem. C 2015.

18. Merrill, D. R.; Moore, D. B.; Coffey, M. N.; Jansons, A. W.; Falmbigl, M.; Johnson, D. C. Synthesis and Characterization of Turbostratically Disordered (BiSe) 1.15 TiSe 2. Semicond. Sci. Technol. 2014, 29 (6), 064004.

19. Moore, D. B.; Stolt, M. J.; Atkins, R.; Sitts, L.; Jones, Z.; Disch, S.; Matt, B.; Johnson, D. C. Structural and Electrical Properties of (PbSe)1·16TiSe2. Emerg. Mater. Res. 2012, 1, 292–298.

20. Wood, S. R.; Merrill, D. R.; Falmbigl, M.; Moore, D. B.; Ditto, J.; Esters, M.; Johnson, D. C. Tuning Electrical Properties through Control of TiSe2 Thickness in (BiSe)1+δ(TiSe2)nCompounds. Chem. Mater. 2015, 27 (17), 6067–6076.

21. Chiritescu, C.; Cahill, D. G.; Heideman, C.; Lin, Q.; Mortensen, C.; Nguyen, N. T.; Johnson, D.; Rostek, R.; Böttner, H. Low Thermal Conductivity in Nanoscale Layered Materials Synthesized by the Method of Modulated Elemental Reactants. J. Appl. Phys. 2008, 104 (3), 033533.

22. Lin, Q.; Smeller, M.; Heideman, C. L.; Zschack, P.; Koyano, M.; Anderson, M. D.; Kykyneshi, R.; Keszler, D. a.; Anderson, I. M.; Johnson, D. C. Rational Synthesis and Characterization of a New Family of Low Thermal Conductivity Misfit Layer Compounds [(PbSe) 0.99] M (WSe 2) N †. Chem. Mater. 2010, 22 (3), 1002–1009.

23. Merrill, D. R.; Moore, D. B.; Ditto, J.; Sutherland, D. R.; Falmbigl, M.; Winkler, M.; Pernau, H.; Johnson, D. C. The Synthesis, Structure, and Electrical Characterization of (SnSe)1.2TiSe2. Eur. J. Inorg. Chem. 2015, No. 1, 83–91.

24. Phung, T.; Jensen, J.; Jonshon, D.; Donovan, J.; McBurnett, B. Determination of the Composition of Ultra- thin Ni- Si Films on Si: Constrained Modeling of Electron Probe Microanalysis and X- ray Reflectivity Data. X-Ray Spectrom. 2008, 37, 608–614.

25. Atkins, R.; Wilson, J.; Zschack, P.; Grosse, C.; Neumann, W.; Johnson, D. C. Synthesis of [(SnSe) 1.15]m((TaSe2)n Ferecrystals: Structurally Tunable Metallic Compounds. Chem. Mater. 2012, 24, 4594–4599.

26. Alemayehu, M. B.; Falmbigl, M.; Ta, K.; Grosse, C.; Westover, R. D.; Bauers, S. R.; Fischer, S. F.; Johnson, D. C. Structural and Electrical Properties of ([SnSe]1+δ)m(NbSe2)1 Compounds: Single NbSe2 Layers Separated by Increasing Thickness of SnSe. Chem. Mater. 2015, 27 (3), 867–875.

27. Beekman, M.; Cogburn, G.; Heideman, C.; Rouvimov, S.; Zschack, P.; Neumann, W.; Johnson, D. C. New Layered Intergrowths in the Sn-Mo-Se System. J. Electron. Mater. 2012, 41 (6), 1476–1480.

28. Moore, D. B.; Beekman, M.; Disch, S.; Zschack, P.; Häusler, I.; Neumann, W.; Johnson, D. C. Synthesis, Structure, and Properties of Turbostratically Disordered (PbSe) 1.18 (TiSe 2) 2. Chem. Mater. 2013, 25, 2404–2409.

29. Merrill, D. R.; Sutherland, D. R.; Ditto, J.; Bauers, S. R.; Falmbigl, M.; Medlin, D. L.; Johnson, D. C. Kinetically Controlled Site-Specific Substitutions in Higher-Order Heterostructures. Chem. Mater. 2015, 27 (11), 4066–4072.

30. Falmbigl, M.; Alemayehu, M. B.; Merrill, D. R.; Beekman, M.; Johnson, D. C. In-Plane Structure of Ferecrystalline Compounds. Cryst. Res. Technol. 2015, 50 (6), 464–472.

31. Beekman, M.; Disch, S.; Rouvimov, S.; Kasinathan, D.; Koepernik, K.; Rosner, H.; Zschack, P.; Neumann, W. S.; Johnson, D. C. Controlling Size-Induced Phase Transformations Using Chemically Designed Nanolaminates. Angew. Chemie - Int. Ed. 2013, 52 (50), 13211–13214.

32. Bauers, S. R.; Moore, D. B.; Ditto, J.; Johnson, D. C. Phase Width of Kinetically Stable ([PbSe]1+δ)1(TiSe2)1 Ferecrystals and the Effect of Precuror Compostion on Electrical Properties. J. Alloys Compd. 2015, 645, 118–124.

33. Atkins, R.; Moore, D. B.; Johnson, D. C. Insights into the Self-Assembly of Ferecrystalline Compounds from Designed Amorphous Precursors. Chem. Mater. 2013, 25, 1744–1750.

Chapter VI

1. Geim, a K.; Novoselov, K. S. *Nat. Mater.* **2007**, *6*, 183–91.

2. Geim, a K. *Science* **2009**, *324*, 1530–4.

3. Radisavljevic, B.; Radenovic, a; Brivio, J.; Giacometti, V.; Kis, a *Nat. Nanotechnol.* **2011**, *6*, 147–50.

4. Zhang, Y.; Tan, Y.-W.; Stormer, H. L.; Kim, P. *Nature* **2005**, *438*, 201–4.

5. Alet, F.; Walczak, A. M.; Fisher, M. P. a. *Phys. A Stat. Mech. its Appl.* **2006**, *369*, 122–142.

6. Limelette, P.; Georges, a; Jérome, D.; Wzietek, P.; Metcalf, P.; Honig, J. M. *Science* **2003**, *302*, 89–92.

7. Goli, P.; Khan, J.; Wickramaratne, D.; Lake, R. K.; Balandin, A. a *Nano Lett.* **2012**, *12*, 5941–5.

8. Fuhrer, M. S.; Hone, J. *Nat. Nanotechnol.* **2013**, *8*, 146–7.

9. Guilmeau, E.; Bréard, Y.; Maignan, a. *Appl. Phys. Lett.* **2011**, *99*, 052107.

10. Morosan, E.; Zandbergen, H. W.; Dennis, B. S.; Bos, J. W. G.; Onose, Y.; Klimczuk, T.; Ramirez, a. P.; Ong, N. P.; Cava, R. J. *Nat. Phys.* **2006**, *2*, 544–550.

11. Wiegers, G. A. *Prog. Solid St. Chem.* **1996**, *24*, 1–139.

12. Miyazaki, Y.; Ogawa, H.; Kajitani, T. *Jpn. J. Appl. Phys.* **2004**, *43*, L1202–L1204.

13. Wan, C.; Wang, Y.; Wang, N.; Koumoto, K. *Materials (Basel).* **2010**, *3*, 2606–2617.

14. Heideman, C. L.; Tepfer, S.; Lin, Q.; Rostek, R.; Zschack, P.; Anderson, M. D.; Anderson, I. M.; Johnson, D. C. *J. Am. Chem. Soc.* **2013**, *135*, 11055–11062.

15. Moore, D. B.; Beekman, M.; Disch, S.; Zschack, P.; Häusler, I.; Neumann, W.; Johnson, D. C. *Chem. Mater.* **2013**, *25*, 2404–2409.

16. Trump, B. a.; Livi, K. J. T.; McQueen, T. M. *J. Solid State Chem.* **2014**, *209*, 6–12.

17. Moore, D. B.; Stolt, M. J.; Atkins, R.; Sitts, L.; Jones, Z.; Disch, S.; Matt, B.; Johnson, D. C. *Emerg. Mater. Res.* **2012**, *1*.

18. Phung, T.; Jensen, J.; Jonshon, D.; Donovan, J.; McBurnett, B. *X-Ray Spectrom.* **2008**, *37*, 608–614.

19. Atkins, R.; Wilson, J.; Zschack, P.; Grosse, C.; Neumann, W.; Johnson, D. C. *Chem. Mater.* **2012**, *24*, 4594–4599.

20. Atkins, R.; Disch, S.; Jones, Z.; Haeusler, I.; Grosse, C.; Fischer, S. F.; Neumann, W.; Zschack, P.; Johnson, D. C. *J. Solid State Chem.* **2013**, *202*, 128–133.

21. Heideman, C. L.; Tepfer, S.; Lin, Q.; Rostek, R.; Zschack, P.; Anderson, M. D.; Anderson, I. M.; Johnson, D. C. *J. Am. Chem. Soc.* **2013**.

22. Lin, Q.; Heideman, C. L.; Nguyen, N.; Zschack, P.; Chiritescu, C.; Cahill, D. G.; Johnson, D. C. *Eur. J. Inorg. Chem.* **2008**, *2008*, 2382–2385.

23. Di Salvo, F. J.; Moncton, D. E.; Waszczak, J. V. *Phys. Rev. B* **1976**, *14*, 4321.

24. McTaggart, F. K.; Wadsley, A. D. *Australian J. Chem.* **1958**, *11*, 445-457.

25. Gobrecht, H.; Boeters, K. E.; Pantzer, G. *Zeitschrift für Physik* **1964**, *177*, 68-83.

26. Beekman, M.; Cogburn, G.; Heideman, C.; Rouvimov, S.; Zschack, P.; Neumann, W.; Johnson, D. C. *J. Electron. Mater.* **2012**, *41*, 1476–1480.

27. Nader, A.; Briggs, A.; Meerschaut, A.; A, L. *Solid State Commun.* **1997**, *102*, 401–403.

28. Oosawa, Y.; Gotoh, Y.; Akimoto, J.; Tsunoda, T.; Sohma, M.; Onoda, M. *Jpn. J. Appl. Phys.* **1992**, *31*, 1096–1099.

29. Chiritescu, C.; Cahill, D. G.; Nguyen, N.; Johnson, D.; Bodapati, A.; Keblinski, P.; Zschack, P. *Science* **2007**, *315*, 351–3.

30. Chiritescu, C.; Cahill, D. G.; Heideman, C.; Lin, Q.; Mortensen, C.; Nguyen, N. T.; Johnson, D.; Rostek, R.; Böttner, H. *J. Appl. Phys.* **2008**, *104*, 033533.

Chapter VII

1. Snyder, G. J.; Toberer, E. S. Complex Thermoelectric Materials. *Nat. Mater.* **2008**, *7*, 105–114.

2. Stewart, G. R. Superconductivity in Iron Compounds. *Rev. Mod. Phys.* **2011**, *83*.

3. Orenstein, J.; Millis, A. J. Advances in the Physics of High-Temperature Superconductivity. *Science.* **2000**, *288*, 468–474.

4. Havinga, E. E.; Damsma, H.; van Maaren, M. H. Oscillatory Dependence of Superconductive Critical Temperature on Number of Valency Electrons in Cu3Au-Type Alloys. *J. Phys. Chem. Solids* **1970**, *31*, 2653–2662.

5. Pickett, W. E.; Singh, D. J. Electronic Structure and Half-Metallic Transport in the $La_{1-x}Ca_xMnO_3$ System. *Phys. Rev. B* **1996**, *53*, 1146–1160.

6. Li, C.; Hu, Q.; Yang, R.; Johansson, B.; Vitos, L. Magnetic Ordering and Physical Stability of $X_2Mn_{1+X}Sn_{1-X}$ (X = Ru, Os, Co, Rh, Ni, Pd, Cu, and Ag) Heusler Alloys from a First-Principles Study. *Phys. Rev. B* **2013**, *88*, 014109.

7. Wolf, S.; Tauber, R. N. *Silicon Processing for the VLSI Era - Volume 1: Process Technology*; Second ed.; Lattice Press: Sunset Beach, CA, **2000**; pp. 1–32.

8. Park, J.-S.; Yang, J.-H.; Ramanathan, K.; Wei, S.-H. Defect Properties of Sb- and Bi-Doped $CuInSe_2$: The Effect of the Deep Lone-Pair S States. *Appl. Phys. Lett.* **2014**, *105*, 243901.

9. Cahen, D.; Abecassis, D.; Soltz, D. Doping of $CuInSe_2$ Crystals: Evidence for Influence of Thermal Defects. *Chem. Mater.* **1989**, 202–207.

10. Chen, S.; Walsh, A.; Gong, X. G.; Wei, S. H. Classification of Lattice Defects in the Kesterite Cu_2ZnSnS_4 and $Cu_2ZnSnSe_4$ Earth-Abundant Solar Cell Absorbers. *Adv. Mater.* **2013**, *25*, 1522–1539.

11. Wiegers, G. A. Misfit Layer Compounds: Structure and Physical Properties. *Prog. Solid St. Chem.* **1996**, *24*, 1–139.

12. Schafer, H. *Chemical Transport Reactions*; Academic Press: New York, 1964.

13. Atkins, R.; Wilson, J.; Zschack, P.; Grosse, C.; Neumann, W.; Johnson, D. C. Synthesis of $[(SnSe)_{1.15}]_m((TaSe_2)_n$ Ferecrystals: Structurally Tunable Metallic Compounds. *Chem. Mater.* **2012**, *24*, 4594–4599.

14. Heideman, C.; Nyugen, N.; Hanni, J.; Lin, Q.; Duncombe, S.; Johnson, D. C.; Zschack, P. The Synthesis and Characterization of New $[(BiSe)_{1.10}]_m[NbSe_2]_n$, $[(PbSe)_{1.10}]_m[NbSe_2]_n$, $[(CeSe)_{1.14}]_m[NbSe_2]_n$ and $[(PbSe)_{1.12}]_m[TaSe_2]_n$ Misfit Layered Compounds. *J. Solid State Chem.* **2008**, *181*, 1701–1706.

15. Heideman, C. L.; Tepfer, S.; Lin, Q.; Rostek, R.; Zschack, P.; Anderson, M. D.; Anderson, I. M.; Johnson, D. C. Designed Synthesis, Structure, and Properties of a Family of Ferecrystalline Compounds $[(PbSe)_{1.00}]_m(MoSe_2)_n$. *J. Am. Chem. Soc.* **2013**, *135*, 11055–11062.

16. Westover, R.; Atkins, R.; Ditto, J. J.; Johnson, D. C. Synthesis of $[(SnSe)_{1.16-1.09}]_1[(Nb_xMo_{1-x})Se_2]_1$ Ferecrystal Alloys. *Chem. Mater.* **2014**, *26*, 3443–3449.

17. Wiegers, G. a. Charge Transfer between Layers in Misfit Layer Compounds. *J. Alloys Compd.* **1995**, *219*, 152–156.

18. Rouxel, J.; Meerschaut, a.; Wiegers, G. a. Chalcogenide Misfit Layer Compounds. *J. Alloys Compd.* **1995**, *229*, 144–157.

19. Meerschaut, A. Misfit Layer Compounds. *Curr. Opin. Solid State Mater. Sci.* **1996**, *1*, 250–260.

20. Phung, T.; Jensen, J.; Jonshon, D.; Donovan, J.; McBurnett, B. Determination of the Composition of Ultra-thin Ni-Si Films on Si: Constrained Modeling of Electron Probe Microanalysis and X-ray Reflectivity Data. *X-Ray Spectrom.* **2008**, *37*, 608–614.

21. Schaffer, M.; Schaffer, B.; Ramasse, Q. Sample Preparation for Atomic-Resolution STEM at Low Voltages by FIB. *Ultramicroscopy* **2012**, *114*, 62–71.

22. van der Pauw, L.J. A method of measuring specific resistivity and Hall effect of discs of arbitrary shape. *Philips Research Reports*. **1958,** *13*, 1–9.

23. van der Pauw, L. J. A method of measuring the resistivity and Hall coefficient on lamellae of arbitrary shape. *Philips Tech. Rev.* **1958**, 20, 220.

24. Moore, D. B.; Stolt, M. J.; Atkins, R.; Sitts, L.; Jones, Z.; Disch, S.; Matt, B.; Johnson, D. C. Structural and Electrical Properties of $(PbSe)_{1.16}TiSe_2$. *Emerg. Mater. Res.* **2012**, *1*, 292–298.

25. Merrill, D. R.; Moore, D. B.; Ditto, J.; Sutherland, D. R.; Falmbigl, M.; Winkler, M.; Pernau, H.; Johnson, D. C. The Synthesis, Structure, and Electrical Characterization of $(SnSe)_{1.2}TiSe_2$. *Eur. J. Inorg. Chem.* **2015**, 83–91.

26. Vegard, L. Die Konstitution der Mischkristalle und die Raumfüllung der Atome. *Zeitschrift für Physik* **1921** *5*, 1, 17–26.

27. Greenaway, D. L.; Nitsche, R. Preparation and Optical Properties of IV-VI2 Chalcogenides Having the CdI2 Structure. *J. Phys. Chem. Solids* **1965**, *26*, 1445–1458.

28. Giang, N.; Xu, Q.; Hor, Y.; Williams, A.; Dutton, S.; Zandbergen, H.; Cava, R. Superconductivity at 2.3 K in the Misfit Compound (PbSe)1.16(TiSe2)2. *Phys. Rev. B* **2010**, *82*, 1–5.

29. Moore, D. B.; Beekman, M.; Disch, S.; Zschack, P.; Häusler, I.; Neumann, W.; Johnson, D. C. Synthesis, Structure, and Properties of Turbostratically Disordered (PbSe) 1.18 (TiSe 2) 2. *Chem. Mater.* **2013**, *25*, 2404–2409.

30. Corso, S. D.; Liautard, B.; Tedenac, J. C. The Pb-Sn-Se system: Phase equilibria and reactions in the PbSe-SnSe-Se subternary *J. Phase Equilibria* **1995**, *16*, 308–314.

31. Wiegers, G.; Haange, R. Electrical Transport Properties of the Misfit Layer Compounds $(SnS)_{1.20}TiS_2$ and $(PbS)_{1.18}TiS_2$. *Eur. J. solid state Inorg. Chem.* **1991**, *28*, 1071–1078.

32. Wan, C.; Wang, Y.; Wang, N.; Koumoto, K. Low-Thermal-Conductivity $(MS)_{1+x}(TiS_2)_2$ (M = Pb, Bi, Sn) Misfit Layer Compounds for Bulk Thermoelectric Materials. *Materials (Basel).* **2010**, *3*, 2606–2617.

33. Hohnke, D. K.; Kaiser, S. W. Epitaxial PbSe and $Pb_{1-x}Sn_xSe$: Growth and Electrical Properties. *J. Appl. Phys.* **1974**, *45*, 892–897.

34. Chen, C.-L.; Wang, H.; Chen, Y.-Y.; Day, T.; Snyder, J. Thermoelectric Properties of P-Type Polycrystalline SnSe Doped with Ag. *J. Mater. Chem. A* **2014**, *2*, 11171–11176.

Chapter VIII

1. Dingle, R.; Störmer, H. L.; Gossard, a. C.; Wiegmann, W. Electron Mobilities in Modulation-Doped Semiconductor Heterojunction Superlattices. Appl. Phys. Lett. 1978, 33 (7), 665–667.

2. Stormer, H. L.; Dingle, R.; Gossard, A. C.; Wiegmann, W.; Sturge, M. D. Two-Dimensional Electron Gas at a Semiconductor-Semiconductor Interface. Solid State Commun. 1979, 29, 705–709.

3. Zebarjadi, M.; Joshi, G.; Zhu, G.; Yu, B.; Minnich, A.; Lan, Y.; Wang, X.; Dresselhaus, M.; Ren, Z.; Chen, G. Power Factor Enhancement by Modulation Doping in Bulk Nanocomposites. Nano Lett. 2011, 11 (6), 2225–2230.

4. Yu, B.; Zebarjadi, M.; Wang, H.; Lukas, K.; Wang, H.; Wang, D.; Opeil, C.; Dresselhaus, M.; Chen, G.; Ren, Z. Enhancement of Thermoelectric Properties by Modulation-Doping in Silicon Germanium Alloy Nanocomposites. Nano Lett. 2012, 12 (4), 2077–2082.

5. Samarelli, a.; Ferre Llin, L.; Cecchi, S.; Frigerio, J.; Etzelstorfer, T.; Müller, E.; Zhang, Y.; Watling, J. R.; Chrastina, D.; Isella, G.; et al. The Thermoelectric Properties of Ge/SiGe Modulation Doped Superlattices. J. Appl. Phys. 2013, 113 (23), 233704.

6. Venkatasubramanian, R.; Siivola, E.; Colpitts, T.; O'Quinn, B. Thin-Film Thermoelectric Devices with High Room-Temperature Figures of Merit. Nature 2001, 413, 597–602.

7. Rouxel, J.; Meerschaut, a.; Wiegers, G. a. Chalcogenide Misfit Layer Compounds. J. Alloys Compd. 1995, 229, 144–157.

8. Wiegers, G. A. Misfit Layer Compounds: Structure and Physical Properties. Prog. Solid St. Chem. 1996, 24, 1–139.

9. Wiegers, G. a. Charge Transfer between Layers in Misfit Layer Compounds. J. Alloys Compd. 1995, 219, 152–156.

10. Wiegers, G.; Haange, R. Electrical Transport Properties of the Misfit Layer Compounds (SnS) 1.20 TiS2 and (PbS) 1.18 TiS2. Eur. J. solid state Inorg. Chem. 1991, 28, 1071–1078.

11. Miyazaki, Y.; Ogawa, H.; Kajitani, T. Preparation and Thermoelectric Properties of Misfit-Layered Sulfide [Yb 1.90 S 2] 0.62 NbS 2. Jpn. J. Appl. Phys. 2004, 43, L1202–L1204.

12. Wan, C.; Wang, Y.; Wang, N.; Koumoto, K. Low-Thermal-Conductivity (MS)1+x(TiS2)2 (M = Pb, Bi, Sn) Misfit Layer Compounds for Bulk Thermoelectric Materials. Materials (Basel). 2010, 3 (4), 2606–2617.

13. Atkins, R.; Wilson, J.; Zschack, P.; Grosse, C.; Neumann, W.; Johnson, D. C. Synthesis of [(SnSe) 1.15]m((TaSe2)n Ferecrystals: Structurally Tunable Metallic Compounds. Chem. Mater. 2012, 24, 4594–4599.

14. Heideman, C.; Nyugen, N.; Hanni, J.; Lin, Q.; Duncombe, S.; Johnson, D. C.; Zschack, P. The Synthesis and Characterization of New [(BiSe)1.10]m[NbSe2]n, [(PbSe)1.10]m[NbSe2]n, [(CeSe)1.14]m[NbSe2]n and [(PbSe)1.12]m[TaSe2]n Misfit Layered Compounds. J. Solid State Chem. 2008, 181, 1701–1706.

15. Heideman, C. L.; Tepfer, S.; Lin, Q.; Rostek, R.; Zschack, P.; Anderson, M. D.; Anderson, I. M.; Johnson, D. C. Designed Synthesis , Structure , and Properties of a Family of. J. Am. Chem. Soc. 2013, 135, 11055–11062.

16. Bauers, S. R.; Merrill, D. R.; Moore, D. B.; Johnson, D. C. Carrier Dilution in TiSe 2 Based Intergrowth Compounds for Enhanced Thermoelectric Performance. J. Mater. Chem. C 2015.

17. Merrill, D. R.; Sutherland, D. R.; Ditto, J.; Bauers, S. R.; Falmbigl, M.; Medlin, D. L.; Johnson, D. C. Kinetically Controlled Site-Specific Substitutions in Higher-Order Heterostructures. Chem. Mater. 2015, 27 (11), 4066–4072.

18. Phung, T.; Jensen, J.; Jonshon, D.; Donovan, J.; McBurnett, B. Determination of the Composition of Ultra- thin Ni- Si Films on Si: Constrained Modeling of Electron Probe Microanalysis and X- ray Reflectivity Data. X-Ray Spectrom. 2008, 37, 608–614.

19. Merrill, D. R.; Moore, D. B.; Coffey, M. N.; Jansons, A. W.; Falmbigl, M.; Johnson, D. C. Synthesis and Characterization of Turbostratically Disordered (BiSe) 1.15 TiSe 2. Semicond. Sci. Technol. 2014, 29 (6), 064004.

20. Falmbigl, M.; Alemayehu, M. B.; Merrill, D. R.; Beekman, M.; Johnson, D. C. In-Plane Structure of Ferecrystalline Compounds. Cryst. Res. Technol. 2015, 50 (6), 464–472.

21. Greenaway, D. L.; Nitsche, R. Preparation and Optical Properties of IV-VI2 Chalcogenides Having the CdI2 Structure. J. Phys. Chem. Solids 1965, 26, 1445–1458.

22. Merrill, D. R.; Moore, D. B.; Ditto, J.; Sutherland, D. R.; Falmbigl, M.; Winkler, M.; Pernau, H.; Johnson, D. C. The Synthesis, Structure, and Electrical Characterization of (SnSe)1.2TiSe2. Eur. J. Inorg. Chem. 2015, No. 1, 83–91.

23. Altshuler, B.; Khmel'Nitzkii, D.; Larkin, A.; Lee, P. Magnetoresistance and Hall Effect in a Disordered Two-Dimensional Electron Gas. Phys. Rev. B 1980, 22 (11), 5142–5153.

24. Moore, D. B.; Stolt, M. J.; Atkins, R.; Sitts, L.; Jones, Z.; Disch, S.; Matt, B.; Johnson, D. C. Structural and Electrical Properties of (PbSe)1·16TiSe2. Emerg. Mater. Res. 2012, 1, 292–298.

25. Wood, S. R.; Merrill, D. R.; Falmbigl, M.; Moore, D. B.; Ditto, J.; Esters, M.; Johnson, D. C. Tuning Electrical Properties through Control of TiSe2 Thickness in (BiSe)1+δ(TiSe2)nCompounds. Chem. Mater. 2015, 27 (17), 6067–6076.

26. Giang, N.; Xu, Q.; Hor, Y.; Williams, A.; Dutton, S.; Zandbergen, H.; Cava, R. Superconductivity at 2.3 K in the Misfit Compound (PbSe)1.16(TiSe2)2. Phys. Rev. B 2010, 82 (2), 1–5.

27. Sze, S. M.; Lee, M. K. Semiconductor Devices: Physics and Technology, 3rd ed.; John Wiley & Sons, Inc.: New York, 2012.

Chapter IX

1. Geim, A. K.; Novoselov, K. S. *Nat. Mater.* **2007**, *6*, 183–191, and reference therein.

2. Wang, Q. H.; Kalantar-Zadeh, K.; Kis, A.; Coleman, J. N.; Strano, M. S. *Nat. Nanotechnol.* **2012**, *7*, 699–712.

3. Lv, R.; Robinson, J. a; Schaak, R. E.; Sun, D.; Sun, Y.; Mallouk, T. E.; Terrones, M. *Acc. Chem. Res.* **2015**, *48*, 56–64.

4. Heine, T. *Acc. Chem. Res.* **2015**, *48*, 65–72.

5. Geim, a K.; Grigorieva, I. V. *Nature* **2013**, *499*, 419–425 and references therein.

6. Zeng, Q.; Wang, H.; Fu, W.; Gong, Y.; Zhou, W.; Ajayan, P. M.; Lou, J.; Liu, Z. *Small* **2015**, *11*, 1868–1884.

7. Kastner, M.; Birgeneau, R.; Shirane, G.; Endoh, Y. *Rev. Mod. Phys.* **1998**, *70*, 897–928.

8. Orenstein, J.; Millis, A. J. *Science (80-.).* **2000**, *288*, 468–474.

9. Terrones, H.; López-Urías, F.; Terrones, M. *Sci. Rep.* **2013**, *3*, 1549.

10. Lee, H. S.; Min, S. W.; Chang, Y. G.; Park, M. K.; Nam, T.; Kim, H.; Kim, J. H.; Ryu, S.; Im, S. *Nano Lett.* **2012**, *12*, 3695–3700.

11. Yang, S.-L.; Sobota, J. a; Howard, C. a; Pickard, C. J.; Hashimoto, M.; Lu, D. H.; Mo, S.-K.; Kirchmann, P. S.; Shen, Z.-X. *Nat. Commun.* **2014**, *5*, 3493.

12. Murphy, D. W. *J. Chem. Phys.* **1975**, *62*, 967.

13. Fang, H.; Battaglia, C.; Carraro, C.; Nemsak, S.; Ozdol, B.; Kang, J. S.; Bechtel, H. A.; Desai, S. B.; Kronast, F.; Unal, A. A.; et al. *Proc. Natl. Acad. Sci. U. S. A.* **2014**, *111*, 6198–6202.

14. Lin, Y.-C.; Lu, N.; Perea-Lopez, N.; Li, J.; Lin, Z.; Peng, X.; Lee, C. H.; Sun, C.; Calderin, L.; Browning, P. N.; et al. *ACS Nano* **2014**, *8*, 3715–3723.

15. Wiegers, G. A. *Prog. Solid St. Chem.* **1996**, *24*, 1–139.

16. Tenne, R. Recent. *Front. Phys.* **2013**, *9*, 370–377.

17. Radovsky, G.; Popovitz-biro, R.; Tenne, *Chem. Mater.* **2012**, *24*, 3004–3015.

18. Atkins, R.; Wilson, J.; Zschack, P.; Grosse, C.; Neumann, W.; Johnson, D. C. *Chem. Mater.* **2012**, *24*, 4594–4599.

19. Heideman, C. L.; Tepfer, S.; Lin, Q.; Rostek, R.; Zschack, P.; Anderson, M. D.; Anderson, I. M.; Johnson, D. C. *J. Am. Chem. Soc.* **2013**, *135*, 11055–11062.

20. Phung, T.; Jensen, J.; Jonshon, D.; Donovan, J.; McBurnett, B.. *X-Ray Spectrom.* **2008**, *37*, 608–614.

21. Merrill, D. R.; Moore, D. B.; Ditto, J.; Sutherland, D. R.; Falmbigl, M.; Winkler, M.; Pernau, H.; Johnson, D. C. *Eur. J. Inorg. Chem.* **2015**, 83–91.

22. Merrill, D. R.; Sutherland, D. R.; Ditto, J.; Bauers, S. R.; Falmbigl, M.; Medlin, D. L.; Johnson, D. C. *Chem. Mater.* **2015**, *27*, 4066–4072.

23. Moore, D. B.; Stolt, M. J.; Atkins, R.; Sitts, L.; Jones, Z.; Disch, S.; Matt, B.; Johnson, D. C. *Emerg. Mater. Res.* **2012**, *1*, 292–298.

24. Moore, D. B.; Beekman, M.; Disch, S.; Zschack, P.; Häusler, I.; Neumann, W.; Johnson, D. C. *Chem. Mater.* **2013**, *25*, 2404–2409.

25. Riekel, C. *J. Solid State Chem.* **1976**, *17*, 389–392.

26. Bauers, S. R.; Merrill, D. R.; Moore, D. B.; Johnson, D. C. *J. Mater. Chem. C* **2015**.

27. Pałosz, B.; Salje, E. *J. Appl. Crystallogr.* **1989**, *22*, 622–623.

28. Oosawa, Y.; Gotoh, Y.; Akimoto, J.; Tsunoda, T.; Sohma, M.; Onoda, M. Jpn. J. Appl. Phys. 1992, 31, 1096−1099.

29. Falmbigl, M.; Alemayehu, M. B.; Merrill, D. R.; Beekman, M.; Johnson, D. C. *Cryst. Res. Technol.* **2015**, *50*, 464–472 and references therein.

30. Faticoni, T. G. Combinatorics: An Introduction; John Wiley & Sons, **2014**.

Chapter X

1. Hernden, B. C.; Lussier, J. a.; Bieringer, M. Topotactic Solid-State Metal Hydride Reductions of Sr 2 MnO 4. *Inorg. Chem.* **2015**, *54* (9), 4249–4256.

2. Neilson, J. R.; McQueen, T. M. Bonding, Ion Mobility, and Rate-Limiting Steps in Deintercalation Reactions with ThCr 2Si 2-Type KNi 2Se 2. *J. Am. Chem. Soc.* **2012**, *134* (18), 7750–7757.

3. Masese, T.; Orikasa, Y.; Tassel, C.; Kim, J.; Minato, T.; Arai, H.; Mori, T.; Yamamoto, K.; Kobayashi, Y.; Kageyama, H.; et al. Relationship between Phase Transition Involving Cationic Exchange and Charge-Discharge Rate in Li2FeSiO4. *Chem. Mater.* **2014**, *26* (3), 1380–1384.

4. Bridges, C. a; Darling, G. R.; Hayward, M. a; Rosseinsky, M. J. Electronic Structure, Magnetic Ordering, and Formation Pathway of the Transition Metal Oxide Hydride LaSrCoO3H0.7. *J. Am. Chem. Soc.* **2005**, *127* (207402), 5996–6011.

5. Streller, F.; Agarwal, R.; Mangolini, F.; Carpick, R. W. Novel Metal Silicide Thin Films by Design via Controlled Solid-State Diffusion. *Chem. Mater.* **2015**, 150523102340004.

6. Zhou, Y.; Pienack, N.; Bensch, W.; Patzke, G. R. The Interplay of Crystallization Kinetics and Morphology in Nanostructured W/Mo Oxide Formation: An in Situ Diffraction Study. *Small* **2009**, *5* (17), 1978–1983.

7. Pienack, N.; Bensch, W. In-Situ Monitoring of the Formation of Crystalline Solids. *Angew. Chemie Int. Ed.* **2011**, *50* (9), 2014–2034.

8. Zhou, Y.; Antonova, E.; Bensch, W.; Patzke, G. R. In Situ X-Ray Diffraction Study of the Hydrothermal Crystallization of Hierarchical Bi_2WO_6 Nanostructures. *Nanoscale* **2010**, *2* (11), 2412–2417.

9. Millange, F.; Medina, M. I.; Guillou, N.; Férey, G.; Golden, K. M.; Walton, R. I. Time-Resolved In Situ Diffraction Study of the Solvothermal Crystallization of Some Prototypical Metal-Organic Frameworks. *Angew. Chemie Int. Ed.* **2010**, *49* (4), 763–766.

10. Kiebach, R.; Pienack, N.; Ordolff, M.; Studt, F.; Bensch, W. Combined In Situ EDXRD / EXAFS Investigation of the Crystal Growth of [Co (C6H18N4)][Sb2S4] under Solvothermal Conditions : Two Different Reaction Pathways Leading to the Same Product. *Chem. Mater.* **2006**, *18* (11), 1196–1205.

11. Michailovski, A.; Grunwaldt, J.-D.; Baiker, A.; Kiebach, R.; Bensch, W.; Patzke, G. R. Studying the Solvothermal Formation of MoO3 Fibers by Complementary in Situ EXAFS/EDXRD Techniques. *Angew. Chem. Int. Ed. Engl.* **2005**, *44* (35), 5643–5647.

12. Gnanavel, M.; Pralong, V.; Lebedev, O. I.; Caignaert, V.; Bazin, P.; Raveau, B. Lithium Intercalation into the Jarosite-Type Hydroxysulfate: A Topotactic Reversible Reaction from a Crystalline Phase to an Inorganic Polymer-like Structure. *Chem. Mater.* **2014**, *26*, 4521–4527.

13. Zhang, W.; Duchesne, P. N.; Gong, Z.; Wu, S.; Ma, L.; Jiang, Z.; Zhang, S.; Zhang, P.; Mi, J.; Yang, Y. In Situ Electrochemical XAFS Studies on an Iron Fluoride High Capacity Cathode Material for Rechargeable Lithium Batteries. *J. Phys. Chem. C* **2013**, No. 1, 130513154755006.

14. Road, M. In Situ Intercalation of the Layered Compounds TiS2 , ZrSe 2 and V G E 2. *Surf. Sci.* **1995**, *333*, 419–424.

15. Evans, J. S. O.; Price, S. J.; Wong, H. V.; O'Hare, D. Kinetic Study of the Intercalation of Cobaltocene by Layered Metal Dichalcogenides with Time-Resolved in Situ X-Ray Powder Diffraction. *J. Am. Chem. Soc.* **1998**, *120* (42), 10837–10846.

16. Du, G.; Guo, Z.; Wang, S.; Zeng, R.; Chen, Z.; Liu, H. Superior Stability and High Capacity of Restacked Molybdenum Disulfide as Anode Material for Lithium Ion Batteries. *Chem. Commun. (Camb).* **2010**, *46* (7), 1106–1108.

17. Merrill, D. R.; Sutherland, D. R.; Ditto, J.; Bauers, S. R.; Falmbigl, M.; Medlin, D. L.; Johnson, D. C. Kinetically Controlled Site-Specific Substitutions in Higher-Order Heterostructures. *Chem. Mater.* **2015**, *27* (11), 4066–4072.

18. Phung, T.; Jensen, J.; Jonshon, D.; Donovan, J.; McBurnett, B. Determination of the Composition of Ultra-thin Ni-Si Films on Si: Constrained Modeling of Electron Probe Microanalysis and X-ray Reflectivity Data. *X-Ray Spectrom.* **2008**, *37*, 608–614.

19. Atkins, R.; Wilson, J.; Zschack, P.; Grosse, C.; Neumann, W.; Johnson, D. C. Synthesis of [(SnSe) 1.15]m((TaSe2)n Ferecrystals: Structurally Tunable Metallic Compounds. *Chem. Mater.* **2012**, *24*, 4594–4599.

Chapter XI

1. Hume-Rothery, W.; Mabbott, G. W.; Channel Evans, K. M. The Freezing Points, Melting Points, and Solid Solubility Limits of the Alloys of Silver and Copper with the Elements of the B Sub-Groups. *Philos. Trans. R. Soc. London, Ser. A* **1934**, *233*, 1–97.

2. Hume-Rothery, W. *Structure of Metals and Alloys*, 1st ed.; Institute of Metals: London, 1939.

3. Barnett, R. N.; Landman, U.; Clevelend, C. L. Surface Segregation in Simple Metal Alloys: An Electronic Theory. *Phys. Rev B*. 1983, pp 6647–6658.

4. Jr., Egelhoff, W. F. Thermochemical Values for Cu-Ni Surface and Interface Segregation Deduced from Core Level Binding-Energy Shifts. *Phys. Rev. Lett.* **1983**, *50* (8), 587–590.

5. Park, J. Y.; Zhang, Y.; Joo, S. H.; Jung, Y.; Somorjai, G. a. Size Effect of RhPt Bimetallic Nanoparticles in Catalytic Activity of CO Oxidation: Role of Surface Segregation. *Catal. Today* **2012**, *181* (1), 133–137.

6. Huxter, V. M.; Lee, A.; Lo, S. S.; Scholes, G. D. CdSe Nanoparticle Elasticity and Surface Energy. *Nano Lett.* **2009**, *9*, 405–409.

7. Nongjai, R.; Khan, S.; Asokan, K.; Ahmed, H.; Khan, I. Magnetic and Electrical Properties of In Doped Cobalt Ferrite Nanoparticles. *J. Appl. Phys.* **2012**, *112* (8), 084321.

8. Miyajima, K.; Fukushima, N.; Himeno, H.; Yamada, a; Mafune, F. Breakdown of the Hume-Rothery Rules in Sub-Nanometer-Sized Ta-Containing Bimetallic Small Clusters. *J. Phys. Chem. A* **2009**, *113* (48), 13448–13450.

9. Rodriguez, J. Physical and Chemical Properties of Bimetallic Surfaces. *Surf. Sci. Rep.* **1996**, *24* (7-8), 223–287.

10. Zlotea, C.; Morfin, F.; Nguyen, T.; Nguyen, N. Nanoalloying Bulk-Immiscible Iridium and Palladium Inhibits Hydride Formation and Promotes Catalytic Performances. *Nanoscale* **2014**, *6*, 9955–9959.

11. Merrill, D. R.; Sutherland, D. R.; Ditto, J.; Bauers, S. R.; Falmbigl, M.; Medlin, D. L.; Johnson, D. C. Kinetically Controlled Site-Specific Substitutions in Higher-Order Heterostructures. *Chem. Mater.* **2015**, *27* (11), 4066–4072.

12. Phung, T.; Jensen, J.; Jonshon, D.; Donovan, J.; McBurnett, B. Determination of the

Composition of Ultra-thin Ni-Si Films on Si: Constrained Modeling of Electron Probe Microanalysis and X-ray Reflectivity Data. *X-Ray Spectrom.* **2008**, *37*, 608–614.

13. Schaffer, M.; Schaffer, B.; Ramasse, Q. Sample Preparation for Atomic-Resolution STEM at Low Voltages by FIB. *Ultramicroscopy* **2012**, *114*, 62–71.

14. Corso, S. D.; Liautard, B.; Tedenac, J. C. The Pb-Sn-Se System: Phase Equilibria and Reactions in the PbSe-SnSe-Se Subternary. *J. Phase Equilibria* **1995**, *16* (4), 308–314.

15. Watanabe, M.; Williams, D. B. The Quantitative Analysis of Thin Specimens: A Review of Progress from the Cliff-Lorimer to the New ζ-Factor Methods. *J. Microsc.* **2006**, *221* (2), 89–109.

16. Williams, D. B.; Carter, C. B. *Transmission Electron Microscopy*, 2nd ed.; Springer: Newyork, 2009.

17. Moore, D. B.; Beekman, M.; Disch, S.; Zschack, P.; Häusler, I.; Neumann, W.; Johnson, D. C. Synthesis, Structure, and Properties of Turbostratically Disordered (PbSe) 1.18 (TiSe 2) 2. *Chem. Mater.* **2013**, *25*, 2404–2409.

18. Alemayehu, M. B.; Falmbigl, M.; Ta, K.; Grosse, C.; Westover, R. D.; Bauers, S. R.; Fischer, S. F.; Johnson, D. C. Structural and Electrical Properties of ([SnSe]1+δ)m(NbSe2)1 Compounds: Single NbSe2 Layers Separated by Increasing Thickness of SnSe. *Chem. Mater.* **2015**, *27* (3), 867–875.

19. Heideman, C. L.; Tepfer, S.; Lin, Q.; Rostek, R.; Zschack, P.; Anderson, M. D.; Anderson, I. M.; Johnson, D. C. Designed Synthesis , Structure , and Properties of a Family of. *J. Am. Chem. Soc.* **2013**, *135*, 11055–11062.